

Copyright

by

Agnès Kim

2007

The Dissertation Committee for Agnès Kim
certifies that this is the approved version of the following dissertation:

Probing exotic Physics with Pulsating White Dwarfs

Committee:

D.E. Winget, Supervisor

S.D. Kawaler

P. Kumar

M.H. Montgomery

E.L. Robinson

Probing exotic Physics with Pulsating White Dwarfs

by

Agnès Kim, B.S.; M.S.

Dissertation

Presented to the Faculty of the Graduate School of

The University of Texas at Austin

in Partial Fulfillment

of the Requirements

for the Degree of

Doctor of Philosophy

The University of Texas at Austin

May 2007

Acknowledgments

I am grateful first and foremost to my Mom, for never revealing the fact that I was a girl and that as such, I was supposed to have modest ambitions. When I was 3, I figured out on my own that I was different from my brothers and I demanded little girls' cloths, but aside from that, I always enjoyed the same freedom and opportunities as my brothers did and carried similar duties. I had my Mom's full support when I decided, at the age of 16, to live for a year in the US and when I decided to major in science in high school. I also had her full support when I left home nearly 11 years ago to study in the US. I know it was not easy for her to let her only daughter go, and I want to make her proud. None of my dreams would have been possible without my Dad's support and I want him to be proud too. I am also fortunate to have three great brothers, Antoine, Jean-Louis, and François. They have been there for me as well.

I probably would not have considered attending college in the US if it had not been for encouragements from Mrs. Bettridge. Mrs. Bettridge was my English teacher and mentor while I was an exchange student in the US during high-school. She is one of the upbeat people in my life from whom I have drawn strength.

Steve Kawaler is responsible for my decision to pursue a degree in Astronomy. I took my first astronomy class from him at Iowa State University, as a freshman. Though he will never admit it, Steve is an amazing teacher and the class blew me away. I came back to him a year later to start on the first research project of my career.

I was also blessed to have the opportunity to work with Lee Anne Willson for my

master's project. Under her supervision, I learned that fluffy stars were interesting too, and I grew as a researcher. Both Lee Anne and Steve offered me their unwavering support and played a big role in my decision to come to UT for my Ph.D.

At UT, I met many wonderful people. I found a great adviser in Don Winget. Don's optimism and enthusiasm never weakened, even in the face of illness. Don was like a good parent. He provided me with all the freedom I wanted, while sharing his wisdom when needed, both serious and less serious. Don described the defense process in the following words:

"We have the public humiliation, err ... defense ... then we have a secret conclave with the student wherein the committee attempts to dazzle the candidate with their own brilliance at the same time demonstrating the candidate's woeful inadequacy with a series of increasingly obscure questions; all this is sort of like a presidential debate. Somehow these attempts usually backfire – also eerily reminiscent of a presidential debate. In the end the student emerges more or less unscathed and the faculty excuses the candidate from the room to build suspense, and lick their own wounds. After some discussion a puff of smoke (of the appropriate color) emerges from the room and the candidate is recalled, congratulated, and presented with their secret decoder ring. All of this is generally followed by a party at Don's place to celebrate the poor committee's survival, and the student's grace, wisdom, and mercy."

I missed the emergence of the puff of smoke after the closed door session so I do not know what color it was, but Karen Winget did throw a great party that night, complete with delicious, stinky cheese from right around where I grew up. It was a very special evening, made more special by all those present.

This work would not be what it is without Mike Montgomery. When I met Mike for the first time my very first semester at UT, I was impressed by the depth of his physical understanding of nature and by his ability to convey that understanding. Mike is among the few smart people I know who manage to make people around them feel smart as well. I

learned a lot from Mike. He never allowed me to take shortcuts or be lazy, always encouraging me to understand my work at a deeper level and work things out for myself when I was unsure. He was always there when I had questions and never lost patience with me. For that, I am deeply grateful.

I also wish to thank the other members of my committee, Rob Robinson, and Pawan Kumar. I met Rob when I took a class from him. He is an amazing teacher and under his rough appearance, I knew he would be a valuable member of my committee. When I asked him whether he would accept to be on my committee and told him about my plans to do my second year defense a year early, Rob very seriously replied “I would love to, but you do understand that I tend to flunk students under those circumstances”. I knew Rob well enough to know that he was joking, but my heart sank nonetheless and it must have showed on my face. Rob quickly added that he was kidding. Rob’s ability to do objective science allowed him to provide some very valuable feedback for the present work. Pawan has been delightful as always and pushed me to gain a better physical understanding of the processes I was studying. Ted von Hippel was involved with the project early on and remains a source of advice.

I would also like to thank Eiichiro Komatsu for helping me learn basic Cosmology and for his unbreakable faith in axions. I live in the comfort of knowing I have an expert to whom I can go and ask questions any time I want.

Paul Bradley is one of the few people alive who understand the inner workings of the White Dwarf Evolution Code (WDEC). He was kind enough to allow me to benefit from his wisdom, even sending copies of detailed, colorfully written, notes of his. He also provided the new equation of state tables I used. Travis Metcalfe is behind the idea of using a simplex search to zero in on best fit models in section 5.6.5. We started working on the coding together. He also provided the neatly packaged version of the WDEC I modified and used for much of the work presented in this thesis. And it was during a conversation with him that I realized that the goal of a scientific study was not to find *the* answer, but the

best scientifically sound answer.

I was fortunate to join a great research group. I overlapped with senior students Anjum Mukadam and Mukremin Kilic. Anjum showed me how work under pressure was done, with grace. Mukremin scared us a bit with the amount of work he could produce. I had a good time on the road and at the observatory with Elizabeth Jeffery. She has some great stories. Steve DeGennaro was the latest addition to the group. We shared our interest in teaching and public outreach. Fergal Mullally had the misfortune of sharing an office with me, which gave me the right to disturb him at any time to help me when my computer and I were unable to communicate, or to ask him random questions. I thank him for always being willing to help gracefully.

I am thankful to Stephanie Crouch, our graduate coordinator. She never got angry at me once for problems I caused with the paperwork because of my ignorance or forgetfulness. It was nice to have someone who always knew what to do and who to call.

And last but not least, there is the unsung hero of it all, my dear friend and husband, Ryan. Ryan knew that I had what it took to complete a Ph.D., even before I even considered going on to graduate school. He was always there to tell me how awesome I was, especially when I needed to hear it. He took care of life while I was taking care of my studying. Magically, bills were paid, the car was fixed, the house kept, and there was food on the table when I got home. He forgave me for not being home very often and for not earning as much as I could have with a real job. He patiently waited for me to finally end my student career so he could start his life.

AGNÈS KIM

Probing exotic Physics with Pulsating White Dwarfs

Publication No. _____

Agnès Kim, Ph.D.

The University of Texas at Austin, 2007

Supervisor: D.E. Winget

In the present work, I combine observations of pulsating white dwarf stars with theoretical models of these stars to constrain the mass of axions and the emission rate of plasmon neutrinos (neutrinos that result from the decay of a photon coupled to a plasma). Axions, while hypothetical, are of great interest in Astrophysics because they are good candidates for the mysterious dark matter that pervades our universe. Measuring plasmon neutrino emission rates gives us a unique way to test the theory of weak interactions in the Standard Model of particles physics.

Axions arise from an elegant solution to a problem with the Standard Model of particle physics. Along with supersymmetric particles, axions are currently favored candidates for dark matter. But they have not been discovered (neither have supersymmetric

particles) and the theory of axions fails to place any constraint on their mass. The possible contribution of axions to dark matter depends of course on their mass. The mass of axions determines how strongly they interact with the matter we know, with more massive axions interacting more strongly. In turn, the stronger the interaction of axions with matter or light, the larger their emission rate. With pulsating white dwarfs, we can constrain the axion emission rates and therefore their mass.

While we know a lot about neutrinos produced in nuclear reactions inside the Sun, plasmon decay has never been detected. This is because plasmon neutrino emission rates are expected to be significant only in very dense plasmas, such as in the degenerate interiors of white dwarfs. We cannot reproduce those conditions in the lab, and they are also not present in our nearest neutrino emitter, the Sun.

Both axions and plasmon neutrinos should stream freely out of white dwarfs, contributing efficiently to their cooling. We can measure the cooling rate of pulsating white dwarfs by measuring the rate at which the pulsation period of a given mode slows down with time (\dot{P}). The faster the cooling, the larger \dot{P} is. By comparing the \dot{P} theoretically expected from the cooling with the \dot{P} we actually measure, we can deduce the emission the emission rates of plasmon neutrinos and axions and the mass of axions.

I begin by providing useful background information. I talk about non-radial stellar oscillations, give an overview of the observational methods behind the determination of \dot{P} 's, and list the \dot{P} 's we have so far. Then I describe the approach I took to asteroseismology. Computers have become powerful enough that I was able for the first time to perform a brute force, systematic fine grid search of the relevant stellar parameter space. Next I present the theory behind axions, connect them to the dark matter problem through axion cosmology, and describe experiments and astrophysical observations (other than pulsating white dwarfs) that have already helped place upper limits on the axion mass. None of those attempts measures up to the method presented in the present work, where I use my own best fit models of G117-B15A (fit in parallel with R548) and the \dot{P} measured by Kepler et

al. (2005c) to place a strong upper limit on the axion mass of 26.5 meV. I conclude with a detailed discussion of plasmon neutrinos and derive constraints we can very soon hope to place on their production rates, using the hot DBV EC20058. Along the way, I perform detailed asteroseismological analyses of G117-B15A, her sister R548, and of EC20058 and gain further physical insight into what determines the pulsation periods in those stars.

Contents

Acknowledgments	iv
Abstract	viii
List of Tables	xvii
List of Figures	xix
Chapter 1 Introduction	1
Chapter 2 Some background: Non-radial oscillations and \dot{P}'s	7
2.1 Non-radial oscillations	7
2.1.1 Equations of oscillations	8
2.1.2 The Brunt-Väisälä frequency	13
2.1.3 Mode trapping	17
2.1.4 Propagation diagram and asymptotic theory	19
2.2 Rates of period change (\dot{P} 's)	23
2.2.1 Measuring \dot{P} 's	23
2.2.2 Measured \dot{P} 's - A status report	26
Chapter 3 Models and methods	31
3.1 The White Dwarf Evolution Code	32

3.2	The models - choices to make	33
3.2.1	Chemical Composition Profiles	33
3.2.2	Input Physics	35
3.2.3	Numerical Artifacts	37
3.3	A quantitative analysis of the uncertainties	37
3.3.1	G117-B15A and R548	37
3.3.2	EC20058	39
3.4	A new approach to white dwarf asteroseismology	42
3.4.1	The problem and a solution	42
3.4.2	Fine grid search	44
Chapter 4	Axions and the missing universe	46
4.1	Introduction	46
4.2	Cosmology primer	47
4.3	The dark matter problem	48
4.3.1	Astrophysical evidence for the presence of dark matter	49
4.3.2	Evidence for non-baryonic dark matter	52
4.4	Where is the rest of the universe? The dark energy question	54
4.4.1	Einstein's biggest blunder - The cosmological constant	55
4.4.2	The resurrection of the cosmological constant	56
4.4.3	The nature of dark energy and where axions come in	56
4.5	Dark matter candidates	57
4.5.1	How about neutrinos?	57
4.5.2	Supersymmetric dark matter	58
4.5.3	Weakly Interacting Massive Particles (WIMPs)	59
4.6	What are axions	59
4.6.1	Particle physics motivation for axions	60
4.6.2	Axion models	63

4.7	Axion Cosmology and Dark Matter	65
4.7.1	Inflationary scenario	66
4.7.2	Standard thermal scenarios	66
4.7.3	Cosmological lower limit on m_a	68
4.8	Non white dwarf axions searches and limits	69
4.8.1	Microwave cavity experiments	69
4.8.2	Solar axions	70
4.8.3	“Telescope” searches	72
4.8.4	Constraints from the Sun’s known properties	74
4.8.5	Constraints from post Main Sequence evolution	75
4.8.6	SN 1987A	77
4.8.7	Constraints from white dwarfs not based on \dot{P} ’s	77
4.9	Summary	79
Chapter 5 Axion limits from G117-B15A and R548		82
5.1	Introduction	82
5.2	The stars	83
5.3	Axion production in White Dwarfs	84
5.4	Review of work done on the subject	85
5.5	The observables: periods, temperature and mass	87
5.6	Four-parameter fit to G117-B15A and R548	89
5.6.1	Broad search on a not so fine grid	89
5.6.2	Constraints from mode identification	91
5.6.3	Zooming in - A finer, narrower grid	94
5.6.4	Summary of the results	97
5.6.5	Breaking free from grid points - Simplex search	99
5.7	Constraint on the axion mass from \dot{P} ’s	101
5.7.1	A sanity check: 0 meV axion results	103

5.7.2	Axion mass limit	106
Chapter 6	EC20058 and Plasmon neutrinos	109
6.1	Introduction	109
6.2	Plasmon neutrinos	110
6.2.1	Description of the basic physical process	110
6.2.2	Plasma frequency inside white dwarfs	111
6.2.3	Approximate expressions for plasmon neutrino rates	114
6.2.4	Plasmon neutrino rates in white dwarfs - A physical understanding .	117
6.3	Plasmon neutrino rates used in code	121
6.3.1	Outline of how plasmon neutrino rates are evaluated	121
6.4	Observed properties of EC20058	124
6.5	Asteroseismological analysis of EC20058	125
6.5.1	Broad 4 parameter grid search	126
6.5.2	Fine grid search	127
6.5.3	Results	128
6.6	Prospective limits on plasmon neutrino rates	133
6.6.1	Method	133
6.6.2	Results	135
Chapter 7	Conclusions	140
7.1	The big picture	140
7.2	What we found	141
7.2.1	Asteroseismology of G117-B15A and R548 and the axion mass . .	141
7.2.2	Asteroseismology of EC20058 and plasmon neutrino rates	142
7.3	What now?	144
Appendix A	Axions in the White Dwarf Evolution Code	148
A.1	Modifications to the WDEC to include axions	148

A.2	Subroutine axions	152
Appendix B Smoothing of abundance profiles and Salaris-like profiles		164
B.1	Overview	164
B.2	Smoothing of the core abundance profiles	164
B.2.1	Introduction	164
B.2.2	Results	166
B.2.3	Code	167
B.3	Salaris-like core abundance profiles	171
B.3.1	Code	173
Appendix C Smoothing of the Brunt-Väisälä frequency		185
C.1	Overview of the problem and quick solution	185
C.2	Implementation	188
Appendix D Period fitting		199
D.1	Overview	199
D.2	How the routine works with an example	200
D.3	Fitness routine	201
Appendix E Simplex method		217
E.1	Brief description of the downhill simplex method and implementation . . .	217
E.1.1	Input	218
E.1.2	Convergence criterion	219
E.2	Code and input files	220
E.2.1	Main program	220
E.2.2	The minimizing routine	225
E.2.3	Input file	230

Appendix F	New Plasmon Neutrino Rates	232
F.1	Comparison between the older rates and the new ones	232
F.2	Relevant subroutines	235
Bibliography		238
Vita		248

List of Tables

2.1	Time evolution of the measurements of \dot{P} for the 215s mode in G117-B15A	28
3.1	Uncertainties for DAV models	38
3.2	Uncertainties for DBV models	40
5.1	Observed properties of G117-B15A and R548	84
5.2	Region of parameter space covered in the broad four-parameter fit and step sizes.	90
5.3	Region of parameter space covered in the narrowed four-parameter fit and step sizes.	94
5.4	Regions of the 4 parameter space occupied by the best fit models for G117-B15A and R548 and mode identification.	98
5.5	Average periods and \dot{P} 's for G117-B15A and R548, without axions.	104
6.1	Observed properties for EC20058	124
6.2	Region of parameter space covered in the broad four-parameter fit and step sizes	126
6.3	Region of parameter space covered in the fine four-parameter fit and step sizes	128
6.4	The two families of best fit solutions for EC20058	131

6.5	Average periods and \dot{P} 's for EC20058, with plasmon neutrino rates given in Itoh et al. (1996a).	136
B.1	Coordinates of the points that make up the chemical abundance profile. The second column header line lists the names each variable is given in the code.	172
B.2	Parameters that fit the Salaris profiles best. w_1 and w_2 are limited by the smoothing done by subroutine <code>profsm</code> . Any value smaller than 0.01 does not do anything as we cannot make the profile any steeper than <code>profsm</code> will allow. The $0.606 M_{\odot}$ profile and above meet the r_{\max} limit (see text) and so the value of w_3 for those models is irrelevant. This is what “saturated” means.	172

List of Figures

1.1	An HR diagram with the location of the two cooler white dwarf instability strips (Bennett et al., 2004). The hottest pulsating white dwarfs are off the diagram, to the left.	4
1.2	Time evolution of different sources of energy loss in a typical white dwarf model. The vertical dashed lines mark the location of the DBV and DAV instability strips. The neutrino luminosity remains significant near the hot (blue) edge of the DBV instability strip. The contribution to energy loss from axions depends strongly on their mass, but if present, remains significant into the DAV instability strip.	5
2.1	An illustration of $\ell = 3$ spherical harmonics. Figure 4.1 in Unno et al. (1989).	12
2.2	The log of the Brunt-Väisälä frequency (squared) and chemical composition transition zones in a white dwarf model, at two different effective temperatures.	15

2.3	An example of mode trapping, from Montgomery et al. (2003). The top panel shows the bumps in the Brunt-Väisälä frequency. The higher bump corresponds to the transition between the homogeneous carbon and oxygen core and the pure carbon layer. The lower bump further out in the model corresponds to the transition between the pure helium layer and the pure hydrogen layer. The $k = 11$ mode is trapped in the hydrogen layer, while the $k = 21$ mode (bottom panel) is trapped between the two transition zones.	18
2.4	Period spacing for the modes observed in GD358, a DBV (solid curve), from Metcalfe (2001). The 540 s and 700 s modes are trapped. The dashed curve is a fit to the period spacing performed by Metcalfe.	19
2.5	Propagation diagram for the 11000K DAV model of figure 2.2. The Lamb frequency curve shown corresponds to $\ell = 1$. The curve moves up for higher ℓ modes.	22
2.6	Amplitude variation of a hypothetical mode (dashed curve) and what we would expect it to look like if the period were constant (solid curve). The real period (P) increases with time, while the expected period (P_1) is kept constant. The first maximum after fiducial time T_0 marks epoch $E = 1$, the second $E = 2$ and so on. Note that the drift is slow enough that we are not missing any cycles. For clarity, I have greatly exaggerated the rate of period change. This is <i>not</i> an actual example.	25
2.7	A real O-C diagram (figure 1 from Kepler et al., 2005c). This O-C diagram is for G117-B15A, a DAV for which we have a well measured \dot{P} .	26
3.1	A variety of possible oxygen abundance profiles. The thin line represents a basic profile, the dashed line the same profile except smoothed, and the line with the hump, a profile based on Salaris et al. (1997) (see Appendix B).	34
3.2	A single layer helium profile (thin curve) and a double layer profile (bold curve) and the associated parameters.	36

3.3	An example of a model with a poorly chosen stop mass compared to one with a better stop mass.	41
4.1	Rotation curve for the Milky Way (figure 2 in Englmaier & Gerhard, 2006). The solid line is the observed rotation curve, the dashed line the contribution from the visible matter, and the dotted line the contribution from a dark matter halo.	50
4.2	Big Bang Nucleosynthesis abundances from Coc et al. (2005). The curves correspond to BBN abundances computed from nucleosynthesis models. The horizontal shaded regions reflect the observed abundances (see text).	53
4.3	A CP conserving model of a neutron.	61
4.4	A CP violating model of a neutron.	61
4.5	Feynman diagrams of the production of axions through the Primakoff effect and the reverse reaction (from Lazarus et al., 1992).	64
4.6	Figure 2 from Kinion et al. (2005). The excluded region lies above the curve. The horizontal line (added) shows the relation between $g_{\gamma\gamma}$ and m_a for KVSZ axions (see equation 4.9). Microwave experiments do not place any limits on DFSZ axions.	70
4.7	Figure 3 from Bradley et al. (2003). Exclusion regions for early microwave cavity experiments (Rochester-Brookhaven-Fermilab and University of Florida).	71
4.8	The region of parameter space excluded by the CAST experiment. The excluded region lies above the curve labeled “CAST phase I”. The slanted region indicates axion models for which $ E/N - 1.95 $ lies between 0.07 and 7. DFSZ axions ($E/N = 8/3$) lie on a line within that region, below the KSVZ axion model line. None of the solar axion experiments have the required sensitivity to place any limit on those two axion models.	72

4.9	Excluded region from telescope search. The telescope searches fails to place any limit on KFSZ or DFSZ axions (for $m_a \sim 300\mu\text{eV}$, $g_{a\gamma\gamma} \sim 10^{-14}$)	73
4.10	A summary of the allowed axion mass range according to the three cosmological models presented in this chapter (top part of the figure) along with the limits set in the $g_{a\gamma\gamma} - m_a$ plane by a variety of searches, also presented in this chapter. The shaded regions are exclusion regions. “ADMX” stands for the Axion Dark Matter Experiment and “MWC” for older microwave cavity experiments (see figure 4.7). “Telescope” refers to the most recent telescope search (figure 4.9). The two slanted lines mark the location in this parameter space of the KSFZ and DFSZ axion models (see equation 4.9). The horizontal dashed line labeled “HB” corresponds to the limit found by Raffelt & Dearborn (1987) using observations of Horizontal Branch stars. The dark, narrow vertical region is the allowed mass range for axions to account for dark energy (de Vega & Sanchez, 2007).	81
5.1	Feynman diagram of the production of axions through electron-ion bremsstrahlung (figure 2.a in Raffelt, 1986a)	85
5.2	Value the quantity $F(\rho, T)$ in equation 5.1 takes on in the interior of a typical DAV white dwarf model ($0.6 M_\odot$, 11000K).	86
5.3	Core composition profiles for the models in the four-parameter grid.	90

5.4	The valley of best fit models (4 parameters) for G117-B15A and R548 in the $M_* - T_{\text{eff}}$ plane. The dashed circles mark the location of the subset of models that fit the $\ell = 1$ mode identification criterion (see text). Of those, the progressively filled-in circles indicate better and better fits ($\Phi < 2.5s$, $2s$, $1.5s$, $1s$ respectively) . For G117-B15A, the one model that fits to better than 1 second is not significantly better than the next model down the list. The colored squares indicate the spectroscopically determined temperatures and mass for G117-B15A and R548, according to the legend. Koester et al. 1994 and Robinson et al. 1995 do not quote a mass, but both find an average $\log g$ for G117-B15A so I placed their values at the average white dwarf mass ($0.6 M_{\odot}$).	92
5.5	The valley of best fit models (4 parameters) for G117-B15A and R548 in the $\log(M_H) - \log(M_{He})$ plane. Like in figure 5.4, the dashed circles mark the location of the subset of models that fit the $\ell = 1$ mode identification criterion (see text) and the progressively filled-in circles indicate better and better fits.	93
5.6	Same as figure 5.4 for the finer grid.	95
5.7	Same as figure 5.5 for the finer grid.	96
5.8	Best fit models in the $M_* - T_{\text{eff}}$ plane for different layer masses. For G117-B15A, I isolated the solutions for which $\Phi < 1s$ and for R548, those for which $\Phi < 1.5s$. The open circles correspond to thick hydrogen solutions ($-\log(M_H) < 6.4$), while the filled circles correspond to thin hydrogen solutions ($-\log(M_H) > 6.4$).	97
5.9	The migration of the best solutions for a model like G117-B15A after a simplex search. The filled squares correspond to solutions that satisfy $\Phi < 1 s$ and the filled circles to those that satisfy $\Phi < 0.1 s$	100

5.10	The value of the function Φ (equation 3.1) for the 50 best fit models from the grid, before and after a simplex search for a nearby true minimum. . . .	101
5.11	Best fit models after the simplex search in the $M_H - T_{\text{eff}}$ plane and the $M_{\text{He}} - T_{\text{eff}}$ planes. The filled circles, like in figure 5.9 mark the location of the models for which $\Phi < 0.1$ s.	102
5.12	A sample simulated random population within the bounds defined in table 5.4 for G117-B15A. The small circles show the location in parameter space of the simulated population, while the squares and diamonds are best fit grid models. In the $M_* - T_{\text{eff}}$ plane, family 1 and 2 lie on top of each other.	105
5.13	A sample simulated random population within the bounds defined in table 5.4 for R548. The small circles show the location in parameter space of the simulated population, while the squares are best fit grid models.	106
5.14	Period of the 215.2s mode as a function of axion mass for all three families of fit to G117-B15A's period spectrum. Family 1's period is too low and I did not use that family to place a constraint on the axion mass. Family 2 has a low \dot{P} and as a result, can accommodate higher mass axions before the calculated \dot{P} becomes too large to be consistent with the observed value. . .	107
5.15	\dot{P} 's as a function of axion mass for G117-B15A and R548. The observed \dot{P} for G117-B15A is indicated by the horizontal solid line and its 1 sigma error bars by the dashed lines above and below it. The shaded regions inside the dashed horizontal lines indicates the range of calculated \dot{P} 's consistent with the observed value (to 1 sigma). For R548, the symbols with error bars indicate the \dot{P} calculated for each family of fits listed in table 5.5, and are labeled in the legend. The bold curve and shaded region combines all three families.	108
6.1	Fermi-dirac distribution for different values of Ef/kT (values listed next to the curves.)	112

6.2	Degree of degeneracy of a $0.6 M_{\odot}$, 28000K model. The thin solid black curve is the ρ/μ_e profile. The horizontal lines correspond to the right hand side of equation 6.7, evaluated for different values of E_f/kT (corresponding E_f/kT listed for each above the line). The bold curve is a plot of the plasmon neutrino emission in the model. Full degeneracy becomes a poorer approximation out at $M_r \simeq 0.98M_*$, where neutrino rates are small and do not contribute much to the neutrino luminosity.	114
6.3	A comparison of approximate emissivities with the exact result for a $0.6 M_{\odot}$, 28000K model. The vertical dashed lines were borrowed from figure 6.2 and indicate the degree of degeneracy of the model. The assumption of full degeneracy is very good out to the rightmost vertical dashed line. . . .	117
6.4	The $x = \frac{\hbar\omega_0}{kT}$ profiles for different mass and effective temperature models. The horizontal line corresponds to $x = 7.5$ (see text).	118
6.5	Temperature and density profiles for different mass models. Both are 28000K models.	119
6.6	Plasmon neutrino rates (according to Itoh et al., 1996a) for different mass models at different effective temperatures. The neutrino luminosity is simply $L_v = \int_0^{M_*} \epsilon_n dM$. The horizontal axis was chosen so that the area under each curve is proportional to the neutrino luminosity.	120
6.7	Neutrino luminosity as a function of effective temperature for two different mass models.	121
6.8	Plasmon neutrino rates for the same models as figure 6.6, but for a higher effective temperature (70000K). The $0.9 M_{\odot}$ model has a slightly higher neutrino luminosity than the $0.6 M_{\odot}$ model, only because the integration gets carried out over a larger mass range, not because the neutrino rates are higher.	122

6.9	The best fit solutions in the $M_* - T_{\text{eff}}$ plane for EC20058. The dotted circles mark the location of the grid points. The progressively filled in circles correspond to better and better fits ($\Phi < 1.75\text{s}$, 1.50s , 1.25s , and 1.00s) respectively, where Φ is defined by equation 3.1.	127
6.10	Same as figure 6.9, but in the $\log(M_{\text{He}}) - T_{\text{eff}}$ plane.	128
6.11	Same as figure 6.9, but in the $X_{\text{fm}} - T_{\text{eff}}$ plane.	129
6.12	The location of the best fit models in the $M_* - T_{\text{eff}}$ plane. The dotted circles indicate the location of the grid points. Only the very best fit models are shown ($\Phi < 1\text{s}$). The circles are color coded by the models' X_{fm} value. The solid circles correspond to thin helium solutions ($-\log(M_{\text{He}}) > 3.6$) while the shaded circles correspond to thick helium solutions ($-\log(M_{\text{He}}) < 3.6$).	130
6.13	Same as figure 6.12, but in the $\log(M_{\text{He}}) - T_{\text{eff}}$ plane.	131
6.14	Same as figure 6.12, but in the $X_{\text{fm}} - T_{\text{eff}}$ plane.	132
6.15	The simulated populations (small circles) for each family of best fit models listed in table 6.4 in the $M_* - T_{\text{eff}}$ plane. Each population contains 500 members. The big squares are the best fit models from the grid search ($\Phi \leq 1\text{s}$).	134
6.16	Same as figure 6.15 in the $\log(M_{\text{He}}) - T_{\text{eff}}$ plane	135
6.17	Same as figure 6.15 in the $X_{\text{fm}} - T_{\text{eff}}$ plane	136
6.18	The average period for the 257s mode and 281s mode for each family of best fit models. The horizontal lines show the observed values of those two modes. Each point is shown with 1 sigma error bars.	137
6.19	The \dot{P} 's predicted for each mode with 1 sigma error bars. The filled symbols correspond to family 1 best fit models and the open symbols to family 2. The horizontal lines are an example of a measured \dot{P} we could obtain for EC20058.	138

B.1	Oxygen abundance profile for a $0.606 M_{\odot}$ white dwarf model according to Salaris et al. 1997 (black dashed curve) and a WDEC chemical profile (solid red curve). The WDEC chemical profile is defined by two parameters: X_o , the central oxygen abundance, and q_o , the point in the star at which the oxygen abundance drops to zero.	165
B.2	The oxygen abundance profile (solid curve on top) and the Brunt-Väisälä frequency both for the original abundance profile (dashed with circles) and the smoothed profile (bold line).	166
B.3	Basic structure of an evolved chemical profile. XO and XOfm are input parameters that may be changed in order to obtain a best fit to the periods. One can also set them to the values that best correspond to the Salaris chemical profiles (see table B.2). All other parameters on the figure are fixed for a given mass range. Table 1 lists the coordinates of each of the points in terms of the parameters.	171
B.4	173
B.5	174
B.6	174
B.7	175
B.8	175
B.9	176
B.10	176
B.11	177
C.1	The Brunt-Väisälä frequency and composition profiles for an average DA model (11500K , $0.6 M_{\odot}$, $M_{He} = 10^{-2}$, $M_H = 10^{-4}$). The dotted line shows the original curve, while the solid line shows the smoothed version of the curve. The region inside the box is blown up in figure C.2.	186
C.2	A blow up of the smoothed part of the Brunt-Väisälä frequency.	187

C.3	Illustration of the smoothing algorithm. The program averages the slope right before and right after the discontinuity (in this case $\frac{1/3+2/3}{2} = \frac{1}{2}$) and moves the point to the right of the discontinuity on the line that has that average slope. It repeats the process until it rejoins the original curve or after a set number of iterations have occurred.	188
F.1	New plasmon neutrino rates (solid lines) compared with old rates (dashed lines) for a low mass model ($0.5 M_{\odot}$, bold), a medium mass model ($0.6 M_{\odot}$, grey), and a high mass model ($0.9 M_{\odot}$, lowest curves). All models have $T_{eff} = 18000K$	233
F.2	Same as figure F.1 for hotter models (28000K)	233
F.3	Same as figure F.1 for even hotter models (60000K)	234
F.4	The plasmon neutrino luminosity for the same 3 different mass models as a function of effective temperature.	234

Chapter 1

Introduction

“Le ciel prétend qu’il te connais. *The sky boasts that it knows you.*
Il est si beau, c’est sûrement vrai. *It’s so beautiful, that must be true.*
Lui qui ne s’approche jamais, *While it never comes close,*
Je l’ai vu pris dans tes filets.” *I saw it caught in your nets.*

Francis Cabrel in “Je t’aimais, je t’aime, et je t’aimerai”

White dwarfs are the end product in the life of most stars. They are not born in a catastrophic explosion, they do not emit relativistic jets of particles and radiation, they do not warp space-time to the same extent neutron stars do, they are not the brightest things in our sky, they do not present exotic shapes and colors, and to many astronomers today are all in all pretty boring.

Needless to say, this is not the way I feel. I first read about white dwarfs when I was very young and was intrigued. To me, just the fact that they packed nearly as much matter as the entire Sun in a volume nearly the size of the Earth seemed amazing. I knew white dwarf matter must be very strange, though I could not imagine in what way exactly. It took me a long time to begin to grasp the physical nature of the matter inside white dwarfs. Much of the work presented here has to do with the strange nature of white dwarf interiors.

As I mentioned earlier, white dwarfs are the end product of the evolution of the vast

majority of stars. The whole purpose in the life of a star is to maintain itself against gravity. It gets the energy it needs from nuclear fusion. The most efficient available nuclear reaction is hydrogen fusing into helium. When there is no more hydrogen left in the core, helium becomes the next best thing, yielding carbon and oxygen. Fusing heavier and heavier elements requires higher and higher temperatures and densities. Stars under about $8 M_{\odot}$ never achieve the conditions needed in their core to ignite carbon and oxygen fusion. When they run out of helium, they quickly blow away their envelope in a wind, leaving their naked core, now inert, behind. Like a hot piece of charcoal taken out of the furnace, the core, a white dwarf, proceeds to cool.

With nuclear fusion no longer available as a pressure source against the push of gravity, a white dwarf should contract and finally collapse to a point. While it does start out its life with significant contraction, a white dwarf very quickly reaches a state where much of its mass is supported against further collapse by electron degeneracy pressure, a purely quantum mechanical effect. Electrons are sort of like neurotic cats. They do not like sharing the same home and there can only be one electron per energy state. In a white dwarf, all the available energy states are each occupied by an electron. We say the matter is degenerate. Further collapse would force the electrons to share the same energy state and they refuse to do that. Because this effect prevents the white dwarf from contracting any further, we call it a "pressure", and hence the term "electron degeneracy pressure". As it turns out the dense, degenerate interior is a good place to study exotic predictions of particle physics, such as plasmon neutrinos and axions.

The challenge is to collect observational data that teaches us about the interior. We learn about the interior of the Earth (composition, temperature, density, whether it is solid or liquid ...) by studying seismic waves. Some white dwarfs undergo "starquakes" naturally, saving us the trouble of launching gigantic hammers onto white dwarfs and listen to them ring. Unlike earthquakes, which occur occasionally when a tectonic plate slips suddenly, starquakes on white dwarfs are happening continuously in a predictable pattern

and result in a periodic sloshing back and forth of material at the surface of the white dwarf. Where material comes together, it heats up and becomes brighter. Where it flows apart, it cools down and grows dimmer. This results in luminosity variations that we can observe. The study of these starquakes is called “asteroseismology”. White dwarfs that undergo starquakes are called pulsating white dwarfs.

The luminosity variations vary with periods ranging between 2 and 20 minutes (100 s - 1200 s). We find pulsating white dwarfs in three instability strips. In the present work, we are interested in the two cooler ones: the DBVs and the DAVs (figure 1.1). Pulsating DB’s (DBVs), which have helium atmospheres, range in temperature from 21,000 K to 29,000 K (Beauchamp et al., 1999; Castanheira et al., 2005). Pulsating DA’s (DAVs), which have hydrogen atmospheres are found in a narrow temperature range between 10900 K and 12,300 K (Gianninas et al., 2006; Castanheira et al., 2006).

As white dwarfs cool, they become more and more degenerate and the periods of stable modes increase. The reason why this is true is not trivial and I discuss it in chapter 3. It is mainly a result of the interior becoming less and less compressible. By measuring the rate at which the period of a given mode increases (\dot{P}), we can measure the rate at which the star cools, e.g. the rate at which it is losing energy.

In addition to the energy loss we can measure directly (photon luminosity), there could be an additional source of cooling, in the form of weakly interacting particles produced inside white dwarfs that carry energy away as they stream out of the star. Those particles include neutrinos and, if one is not afraid to go out on a limb, axions. Measuring \dot{P} ’s for DBVs helps place constraints on the neutrino rates and axion mass, while \dot{P} ’s measured for DAVs place constraints on the axion mass.

According to models, loss of neutrinos overwhelmingly dominates cooling in the hottest white dwarfs and continues to dominate cooling well into the DBV instability strip, down to a temperature of about 24,000 K (figure 1.2). At this point, one might wonder about the value of studying neutrinos produced in white dwarfs. After all, we learned a lot

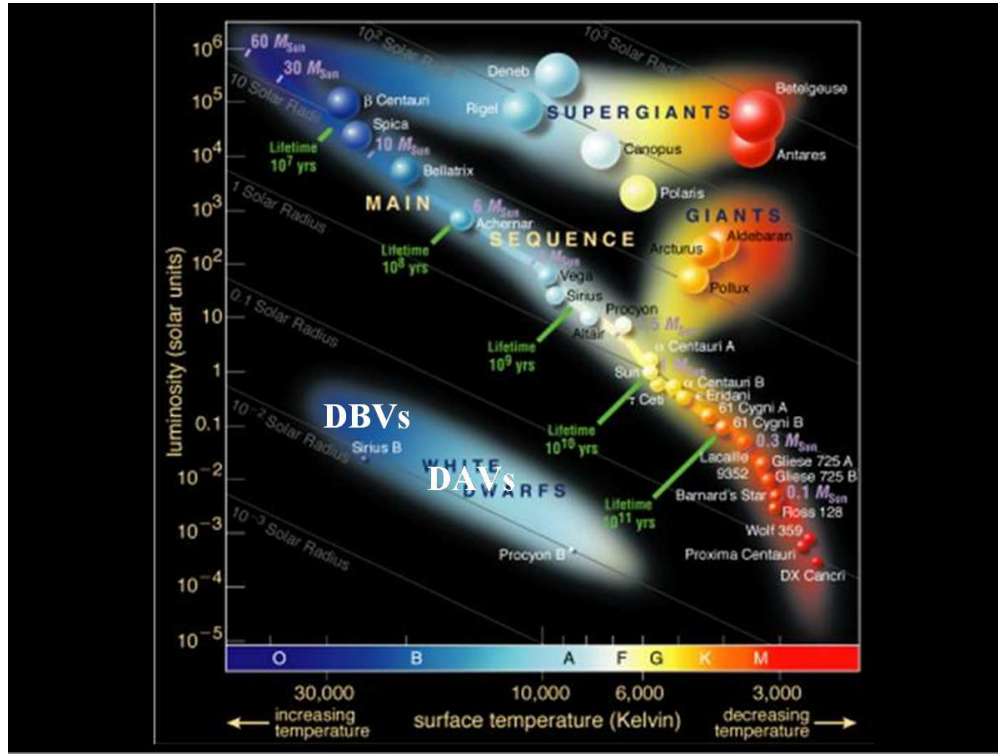


Figure 1.1: An HR diagram with the location of the two cooler white dwarf instability strips (Bennett et al., 2004). The hottest pulsating white dwarfs are off the diagram, to the left.

about neutrinos already from the Sun. But unlike solar neutrinos, neutrinos in white dwarf interiors must be produced in a process which does not involve nuclear reactions.

The Standard Model of particle physics, specifically the theory of weak interactions, predicts the existence of plasmon neutrinos. Such neutrinos result from the decay of a photon in a plasma (a “plasmon”) into a neutrino-antineutrino pair (Adams et al., 1963). Emission rates are expected to be significant only in very dense plasmas, such as in the degenerate interiors of white dwarfs. Indeed, according to theory, the dominant process by which neutrinos are produced in most white dwarfs is plasmon decay (Winget et al., 2004). No measurements, either direct or indirect, have ever demonstrated the existence of neutrinos produced in this way.

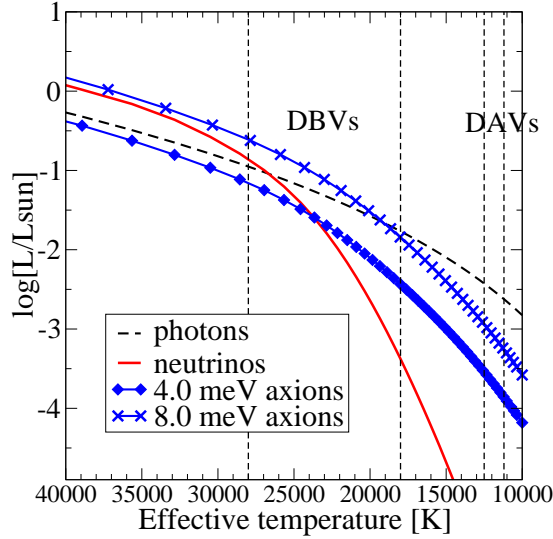


Figure 1.2: Time evolution of different sources of energy loss in a typical white dwarf model. The vertical dashed lines mark the location of the DBV and DAV instability strips. The neutrino luminosity remains significant near the hot (blue) edge of the DBV instability strip. The contribution to energy loss from axions depends strongly on their mass, but if present, remains significant into the DAV instability strip.

The contribution to the energy loss from axions is heavily dependent on their mass (figure 1.2). If massive enough, axions could contribute not only to the cooling of DBVs, but also DAVs. Along with supersymmetric particles, axions are currently favored candidates for dark matter. They arise from an elegant solution to a problem with the Standard Model of particle physics. There are at least two problems with axions. They have not been discovered (neither have supersymmetric particles) and the theory of axions fails to place any constraint on their mass.

In chapter 2, I provide background information useful to appreciate the rest of the present work. I talk about non-radial stellar oscillations, give an overview of the observational methods behind the determination of \dot{P} 's, and list the \dot{P} 's we have so far.

In chapter 3, I describe the approach I took to asteroseismology. Computers have

become powerful enough that I was able for the first time to perform a brute force, systematic fine grid search of the relevant stellar parameter space.

In chapter 4, I present the theory behind axions, connect them to the dark matter problem through axion cosmology, and describe experiments and astrophysical observations (other than pulsating white dwarfs) that have already helped place upper limits on the axion mass. None of those attempts measures up to the method presented in chapter 5, where I use my own best fit models of G117-B15A (fit in parallel with R548) and the \dot{P} measured by Kepler et al. (2005c) to place an upper limit on the axion mass. I devote chapter 6 to a detailed discussion of plasmon neutrinos and discuss constraints we can hope to place on their production rates, using the hot DBV EC20058.

Chapter 2

Some background: Non-radial oscillations and \dot{P} 's

2.1 Non-radial oscillations

Much of the work in this thesis is based on the observation of the pulsations of white dwarfs and on how we understand them. In this section I give an overview of white dwarf pulsations and how they tell us about their inner structure.

White dwarfs are non-radial pulsators. Much of the motion occurs as a sloshing of material back and forth at very nearly constant radius. Because of the high surface gravity, there is very little radial motion, at least for gravity modes. White dwarfs do not "breathe". There are different kinds of non-radial oscillations, which depend on the properties (e.g. temperature, pressure, density) of the interior. Each type of pulsation occurs as a result of different restoring forces. The pulsations we observe in DAVs and DBVs are a result of gravity or buoyancy. In what follows, I describe those pulsation modes in detail, and I also talk briefly about other types of non-radial oscillations, as they come naturally out of the framework.

2.1.1 Equations of oscillations

In this section, I give an introduction to the equations of stellar oscillations. Much of what follows is covered extensively in Cox (1980) and Unno et al. (1989). To arrive at the equations of oscillations, we consider the unperturbed equilibrium state of a star and we superimpose small perturbations. The small perturbations allow us to use the linear theory, where we only retain first order perturbations. For most pulsating white dwarfs, the luminosity variations are observed to be $\sim 1 - 2$ % of the average luminosity and so linear theory is appropriate (Mukadam, 2004). We assume that the transport of fluid elements occurs sufficiently fast so that there is negligible heat exchange between them and the surroundings; e.g. the transport occurs adiabatically. We further assume a stratified, spherically symmetric equilibrium stellar interior.

We ignore complications such as rotation, convection, and magnetic fields. We can comfortably ignore rotation as the vast majority of pulsating white dwarfs are known to be slow rotators (e.g., see Kawaler, 2003 for a review). Non-rotating models are perfectly adequate for slow-rotating white dwarfs. We believe convection is responsible for non-linear effects in higher amplitude pulsators, such as the cool DAVs (e.g. Montgomery, 2005), but those are second order effects and linear theory is still able to give us useful insights. Magnetic fields would also introduce complications. Only about 10-20% of all white dwarfs are known to have magnetic fields ($B > 1$ kG, Jordan et al., 2007). Weaker magnetic fields are not observable at present and we have hints that magnetic fields may play a role in the pulsations of the cooler DAVs (Bischoff-Kim et al., 2007), but our theoretical understanding is still in its infancy in that area.

The equilibrium state satisfies the basic equations of stellar structure; the equation of conservation of mass, momentum and energy. The only assumption we make for now is that there is no convection present. In DAVs and DBVs, convection is confined to the very outer layers of the model (the outer 10^{-10} at most by mass). While convection plays an essential role in driving pulsations in white dwarfs, it has a negligible effect on their

structure. Without convection, the basic equations of stellar structure are (Unno et al., 1989, equations 13.1, 13.4, 13.3):

$$\frac{\partial \rho}{\partial t} + \nabla \cdot (\rho \mathbf{v}) = 0 \quad (2.1)$$

$$\rho \left(\frac{\partial}{\partial t} + \mathbf{v} \cdot \nabla \right) \mathbf{v} = - \nabla p - \rho \nabla \Phi \quad (2.2)$$

$$\rho T \left(\frac{\partial}{\partial t} + \mathbf{v} \cdot \nabla \right) S = \rho \varepsilon - \nabla \cdot \mathbf{F}_R, \quad (2.3)$$

as well as Poisson's equation and the equation of radiative diffusion (Unno et al., 1989, equations 13.5-13.7)

$$\nabla^2 \Phi = 4\pi G \rho \quad (2.4)$$

$$\mathbf{F}_R = -K \nabla T, \quad (2.5)$$

where

$$K = \frac{4ac_*}{3\kappa\rho} T^3. \quad (2.6)$$

The bold quantities in the equations above are vectors. ρ is the density, p the pressure, \mathbf{v} the fluid velocity, S the specific entropy, Φ the gravitational potential, ε the energy generation rate, and \mathbf{F}_R the radiative flux. In white dwarfs, the energy generation includes simply the cooling (due to photons, neutrinos or other weakly interacting particles such as axions). K is the radiative conductivity, a the radiation density constant, and c_* the speed of light. To fully define the problem, one needs in addition an equation of state $p(\rho, T)$ and an equation describing the opacity $\kappa(\rho, T)$.

Next we apply Eulerian perturbations to each variable ($\rho \rightarrow \rho + \rho'$, $p \rightarrow p + p' \dots$). An Eulerian perturbation is the difference between the perturbed and the equilibrium solution at a given time and position. Here we introduce two more assumptions. We ignore rotation so that $\mathbf{v} = \mathbf{v}'$ (e.g. the velocity field is zero in the equilibrium state). We also assume that the perturbations are small, so that any higher order terms (e.g. $\rho' T'$) may be

ignored. We linearize the equations. We also introduce a new variable, the displacement $\xi = \mathbf{r} - \mathbf{r}_0$, where \mathbf{r}_0 is the equilibrium position and \mathbf{r} the new position of a disturbed fluid element. From this definition, $\mathbf{v} = \mathbf{v}' = \frac{\partial \xi'}{\partial t}$.

We obtain the Eulerian linearized basic equations of stellar oscillations (Unno et al., 1989, equations 13.28 - 13.32):

$$\frac{\partial \rho'}{\partial t} + \nabla \cdot (\rho \mathbf{v}) = 0, \quad (2.7)$$

$$\rho \frac{\mathbf{v}}{\partial t} + \nabla p' + \rho \nabla \Phi' + \rho' \nabla \Phi = 0, \quad (2.8)$$

$$\rho T \frac{\partial}{\partial t} (\mathbf{S}' + \xi \cdot \nabla \mathbf{S}) = (\rho \epsilon)' - \nabla \cdot \mathbf{F}', \quad (2.9)$$

and

$$\mathbf{F}' = -K_0 \nabla T' - K' \nabla T. \quad (2.10)$$

If we now assume spherical symmetry of the *equilibrium* quantities, we can write each variable as $f' = f'(\mathbf{r})e^{i\sigma t}$, where \mathbf{r} is the position vector $\mathbf{r}(r, \theta, \phi)$, and rewrite the equations above in terms of the radial component of ξ . In spherical coordinates we write the fluid element's displacement vector ξ as:

$$\xi = \left[\xi_r(r) \hat{r} + \xi_h(r) \frac{\partial}{\partial \theta} \hat{\theta} + \xi_h(r) \frac{\partial}{\sin \theta \partial \phi} \hat{\phi} \right] Y_\ell^m(\theta, \phi) e^{i\sigma t}, \quad (2.11)$$

where the horizontal displacement ξ_h is given by

$$\xi_h = \frac{1}{\sigma^2 r} \left(\frac{p'}{\rho} + \Phi' \right). \quad (2.12)$$

After a whole lot of algebra, we obtain (Unno et al., 1989, equations 13.47-13.50 and 13.52):

$$\frac{1}{\rho} \left(\frac{\partial}{\partial r} + \frac{\rho g}{\Gamma_1 p} \right) p' + (N^2 - \sigma^2) \xi_r + \frac{\partial \Phi'}{\partial r} = g \nabla_{ad} \frac{\rho T}{p} \delta S, \quad (2.13)$$

$$\frac{1}{r^2} \frac{\partial}{\partial r} (r^2 \xi_r) + \frac{1}{\Gamma_1} \frac{d \ln p}{dr} \xi_r + \left(\frac{\rho}{\Gamma_1 p} + \frac{\nabla_\perp^2}{\sigma^2} \right) \frac{p'}{\rho} + \frac{1}{\sigma^2} \nabla_\perp^2 \Phi' = \nabla_{ad} \frac{\rho T}{p} \delta S, \quad (2.14)$$

$$\left(\frac{\partial}{r^2 \partial r} r^2 \frac{\partial}{\partial r} + \nabla_\perp^2 \right) - 4\pi G \rho \left(\frac{p'}{\Gamma_1 p} + \frac{N^2}{g} \xi_r \right) = -4\pi G \nabla_{ad} \frac{\rho^2 T}{p} \delta S, \quad (2.15)$$

$$F_r' = -K \frac{\partial T'}{\partial r} - K' \frac{dT}{dr}, \quad (2.16)$$

and

$$i\sigma \rho T \delta S = (\rho \epsilon)' - \frac{1}{r^2} \frac{\partial}{\partial r} (r^2 F_r') + \nabla_\perp^2 (KT'), \quad (2.17)$$

where ∇_\perp is the horizontal component of the gradient operator in spherical polar coordinates, $\Gamma_1 = \left(\frac{\partial \ln p}{\partial \ln \rho} \right)_S$ and $\nabla_{ad} = \left(\frac{\partial \ln T}{\partial \ln p} \right)_S$ are thermodynamic derivatives, δS is now the Lagrangian perturbation to the entropy, and $N^2 = -g \left(\frac{d \ln p}{dr} - \frac{1}{\Gamma_1} \frac{d \ln p}{dr} \right)$ is the Brunt-Väisälä frequency. The Brunt-Väisälä frequency is the frequency at which a fluid element displaced from its equilibrium position oscillates as a result of buoyant/gravitational return forces. This frequency plays an important role in white dwarf asteroseismology and deserves its own section (2.1.2).

Next we write each unknown as $f'(r, \theta, \phi) = f'(r) Y_\ell^m(\theta, \phi)$, where Y_ℓ^m are spherical harmonics. I give a visual example of spherical harmonics with $\ell = 3$ in figure 2.1. The positive integer ℓ indicates the number of boundaries between regions where the phase velocity of the oscillation goes in opposite directions. The integer m can take on any value between $-\ell$ and $+\ell$. The absolute value of m indicates how many of the ℓ boundaries are in the longitudinal direction. The sign of m is related to the sign of the phase velocity of the wave in the different regions. Reversing the sign of m reverses the sign of the phase velocity in each region.

After we separate out the azimuthal components, we finally obtain the equations for linear, non-adiabatic, non-radial oscillations (Unno et al., 1989, equations 13.62 - 13.66):

$$\frac{1}{\rho} \frac{dp'}{dr} + \frac{g}{\rho c^2} p' + (N^2 - \sigma^2) \xi_r + \frac{d\Phi'}{dr} = g \nabla_{ad} \frac{\rho T}{p} \delta S, \quad (2.18)$$

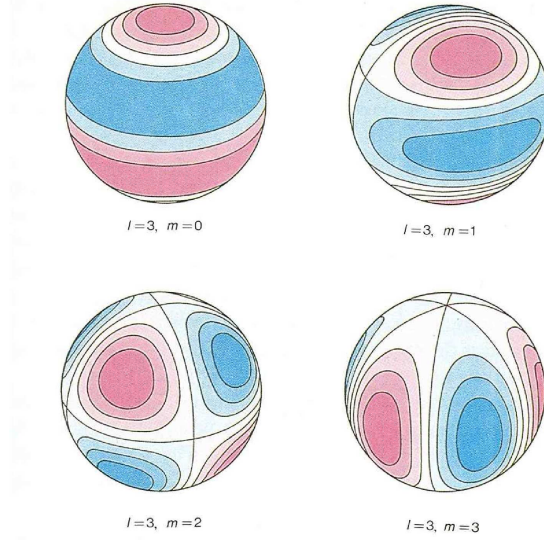


Figure 2.1: An illustration of $\ell = 3$ spherical harmonics. Figure 4.1 in Unno et al. (1989).

$$\frac{1}{r^2} \frac{d}{dr} (r^2 \xi_r) + \frac{1}{\Gamma_1} \frac{d \ln p}{dr} \xi_r + \left(1 - \frac{L_\ell^2}{\sigma^2} \right) \frac{p'}{\rho c^2} - \frac{\ell(\ell+1)}{\sigma^2 r^2} \Phi' = \nabla_{ad} \frac{\rho T}{p} \delta S, \quad (2.19)$$

$$\frac{1}{r^2} \frac{d}{dr} \left(r^2 \frac{d\Phi'}{dr} \right) - \frac{\ell(\ell+1)}{r^2} \Phi' - 4\pi G \rho \left(\frac{p'}{\rho c^2} + \frac{N^2}{g} \xi_r \right) = -4\pi G \nabla_{ad} \frac{\rho^2 T}{p} \delta S, \quad (2.20)$$

$$K \frac{dT'}{dr} = -F_r' - K' \frac{dT}{dr}, \quad (2.21)$$

and

$$i\sigma \rho T \delta S = (\rho \epsilon)' - \frac{1}{r^2} \frac{d(r^2 F_r')}{dr} - \frac{\ell(\ell+1)}{r^2} K T', \quad (2.22)$$

where $c^2 = \frac{\Gamma_1 p}{\rho}$ is the speed of sound and $L_\ell = \left[\frac{\ell(\ell+1)c^2}{r^2} \right]^{1/2}$ is the acoustic or Lamb frequency. The Lamb frequency is the inverse of the time it would take a sound wave to cross one horizontal wavelength of the disturbance along the circumference of a circle of radius r (Cox, 1980).

If we now assume that the fluid elements are displaced adiabatically, we have $\delta S = 0$

and only 3 equations remain (Unno et al., 1989, equations 14.2 - 14.4):

$$\frac{1}{r^2} \frac{d}{dr} (r^2 \xi_r) - \frac{g}{c^2} \xi_r + \left(1 - \frac{L_\ell^2}{\sigma^2}\right) \frac{p'}{\rho c^2} = \frac{\ell(\ell+1)}{\sigma^2 r^2} \Phi', \quad (2.23)$$

$$\frac{1}{\rho} \frac{dp'}{dr} + \frac{g}{\rho c^2} p' + (N^2 - \sigma^2) \xi_r = -\frac{d\Phi'}{dr}, \quad (2.24)$$

and

$$\frac{1}{r^2} \frac{d}{dr} \left(r^2 \frac{d\Phi'}{dr} \right) - \frac{\ell(\ell+1)}{r^2} \Phi' = 4\pi G \rho \left(\frac{p'}{\rho c^2} + \frac{N^2}{g} \xi_r \right). \quad (2.25)$$

Those are the basic equations for linear, adiabatic, non-radial oscillations with three unknowns (ξ_r , p' and Φ'). We shall come back to those equations in section 2.1.4, after we learn more about the Brunt-Väisälä frequency and discuss how we infer the internal structure of white dwarfs from a pulsation spectrum.

2.1.2 The Brunt-Väisälä frequency

Cox (1980) gives a clear treatment of the Brunt-Väisälä frequency (based on Tolstoy 1963; 1973). I reproduce his discussion in what follows. One motivation for the discussion of the Brunt-Väisälä frequently is the question: what happens to a displaced fluid element, initially at equilibrium with its surroundings? Does it keep going in the direction we nudged it or does it come back toward its original position?

Consider a stratified fluid where p , ρ , and $\Gamma_1 = \left(\frac{d \ln P}{d \ln p} \right)_S$ are functions of radius only. Imagine we take a fluid element initially at position r_0 and move it to a new position $r_0 + \delta r$. We assume the fluid element does not mix with its surroundings. Let

$$\Delta \rho(r_0 + \delta r) = \rho_{\text{el}}(r_0 + \delta r) - \rho_{\text{surr}}(r_0 + \delta r) \quad (2.26)$$

be the difference between the density of the fluid element and the density of the immediate surroundings. At the original position r_0 , $\Delta \rho = 0$. The fluid element shares the properties of its surroundings. At the new position $r_0 + \delta r$, the change in the density of the fluid element

has two components, both related to the surroundings.

The first contribution comes from the fact that the surroundings at the new position have a different density than they had at the original position:

$$\rho_{\text{surr}}(r_0 + \delta r) = \rho(r_0) + \frac{d\rho}{dr}(r_0)\delta r. \quad (2.27)$$

$\frac{d\rho}{dr}$ applies to the surroundings and is evaluated at r_o .

The second contribution comes from the fact that if the fluid is compressible, it will adjust its volume to remain in pressure equilibrium with its surroundings. In order for the fluid element to remain in pressure equilibrium with its surroundings, it needs to move sufficiently slowly. On the other hand, we also assume that it moves quickly enough not to exchange heat with its surroundings. If that is true, then

$$\rho_{\text{el}}(r_0 + \delta r) = \rho(r_0) + \left(\frac{d\rho}{dp}\right)_{\text{ad}} \frac{dp}{dr} \delta r = \rho(r_0) + \frac{\rho}{p} \frac{1}{\Gamma_1} \frac{dp}{dr} \delta r. \quad (2.28)$$

Again, $\frac{dP}{dr}$ applies to the surroundings and is evaluated at r_o .

The total change in the density of the displaced fluid element is then simply

$$\Delta\rho = \rho_{\text{el}}(r_0 + \delta r) - \rho_{\text{surr}}(r_0 + \delta r) = -\rho \left(\frac{1}{\rho} \frac{d\rho}{dr} - \frac{1}{\Gamma_1 P} \frac{dP}{dr} \right) \delta r \equiv -\rho A \delta r, \quad (2.29)$$

where A is called “Schwarzschild A”.

To first order, the buoyant force per unit volume acting on the fluid element is

$$f_B = -g\Delta\rho = \rho g A \delta r. \quad (2.30)$$

Now we come to the question “will the fluid element keep going or come back toward its equilibrium position?”. In order for the fluid to come back to its original position, f_B must have the opposite sign of δr . In other words, $f_B/\delta r$ must be negative, and so A must be negative.

If the fluid comes back to its original position, and there is no energy loss, then it will overshoot and execute a simple harmonic oscillation about its original position. The angular frequency of this motion is the Brunt-Väisälä frequency, given by

$$N^2 = -Ag \quad (2.31)$$

If the motion is oscillatory, then N^2 is positive and N is real.

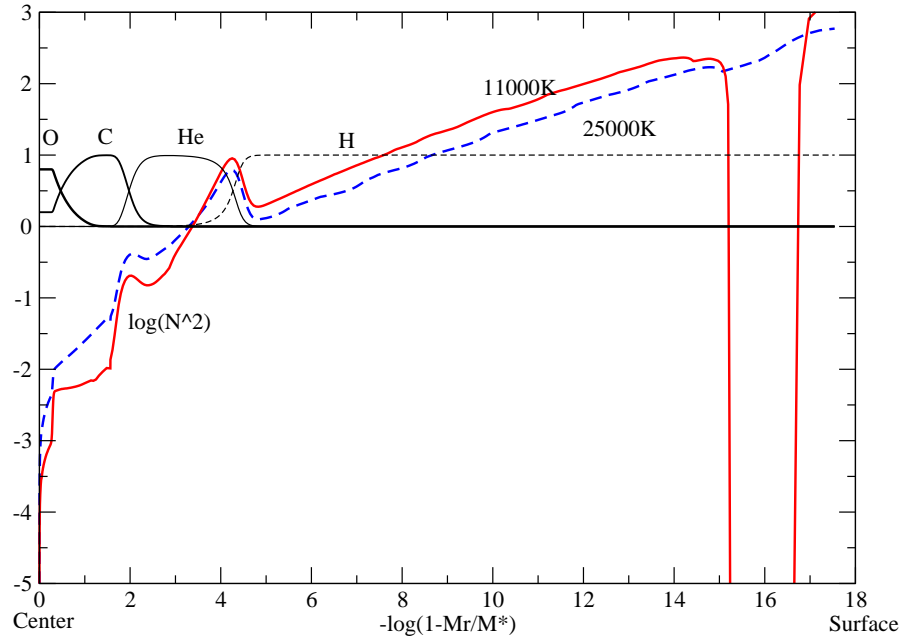


Figure 2.2: The log of the Brunt-Väisälä frequency (squared) and chemical composition transition zones in a white dwarf model, at two different effective temperatures.

In figure 2.2, I plotted the log of the Brunt-Väisälä frequency in a DA model, for two different temperatures: 25000K and 11000K. DAVs are observed to pulsate at 11000K and not at 25000K. In general, the Brunt-Väisälä frequency increases from the center to

the surface because both the density and degeneracy decrease and the matter becomes more compressible as we move closer to the surface. To understand why that is, imagine we have complete degeneracy, so that the pressure is completely independent of the temperature ($P = P(\rho)$). If we move a fluid element to a lower density region, it will remain in equilibrium with its surroundings both in pressure and in density and stay wherever we put it (and so the Brunt-Väisälä frequency would be zero in this ideal case). The closer to complete degeneracy we are, the closer the Brunt-Väisälä frequency is to zero.

The Brunt-Väisälä frequency peaks in transition zones because there is a density gradient between the different composition regions. Imagine we move a fluid element from the core composed mostly of oxygen, to a layer closer to the surface made up of pure carbon. For simplicity assume again complete degeneracy (P independent of temperature). Like before, the fluid element expands just enough to maintain pressure equilibrium with its surroundings and if it had the same composition as the surroundings, it would remain in density equilibrium as well. But this time, it is made up mostly of oxygen, while the surroundings are made up of a lighter element, carbon (remember we assume there is no mixing). Because it is heavier, the fluid element sinks back down and we get a non-zero Brunt-Väisälä frequency. In a model, composition transition zones enhance a non-zero Brunt-Väisälä frequency.

One striking feature in figure 2.2 is the drop in the Brunt-Väisälä curve for the 11000K model around $\log(1 - M_r/M_*) \sim -16$. This corresponds to a convectively unstable region in the model, where N^2 is negative.

As the model cools, the interior becomes more and more degenerate so that we come closer and closer to the complete degeneracy case described above. The pressure is independent of temperature and displaced fluid elements tend to stay in density equilibrium with their surroundings. As a result the Brunt-Väisälä comes closer and closer to zero. We notice that behavior in figure 2.2 in the core, but when we get further out, the Brunt-Väisälä frequency actually *increases*. If the model is contracting as it cools and becoming more and

more degenerate, how could that be? Let us not forget the fact that the model is shrinking in radius as it cools. The horizontal axis is like a mass axis and does not reflect that fact faithfully. We have to remember that at a given mass point, we are looking at a point that is closer to the surface for the cooler model (the star is more compact). This is a very small effect deep in the core, where the star is already very degenerate at 25000K, but it matters further out. At $\log(1 - M_r/M_*) = -6$, we are comparing a region of the 11000K model that is close to the surface to a region of the 25000K model that is deeper down, and hence denser and less compressible.

2.1.3 Mode trapping

Mode trapping is what allows us to infer the structure of a white dwarf from a set of pulsation periods. Montgomery et al. (2003) showed that one could go a long way toward understanding vibrations in a white dwarf by considering the vibrations of a (not so simple) string. The pulsations we observe in white dwarfs are standing waves. Think of how one sets up standing waves on a string. One end of the string needs to be tied down, while the other goes up and down at just the right frequency (or harmonics thereof) so that the outbound wave interferes constructively and destructively with the reflected wave in a very special way. They interfere with each other so that the sum of the two does not travel along the string (the nodes remain fixed along the string).

For a uniform string, the fundamental mode and its harmonics are evenly spaced ($\omega_n = n\omega_0$). If we now place a bead on the string, this is no longer true. The new (uneven) spacing of the harmonics and the resulting period spectrum is sensitive to the location, the mass, and the physical extent of the bead. Realistic white dwarf models are chemically layered and are like strings with beads on them.

In a white dwarf, a mode is trapped if it has just the right frequency so that it gets strongly reflected at a chemical composition transition zone. In this case, its amplitude past the transition zone is much smaller than its amplitude before (see figure 2.3, taken

from Montgomery et al., 2003). If a mode is trapped by a transition zone, its frequency is strongly affected by the location of that transition zone. The mode becomes very useful asteroseismologically, as it carries a lot of information about the exact location and physical nature of the transition zone. In general, modes are influenced by more than one transition zone and a combination of modes is necessary in order to learn about the interior of the star.

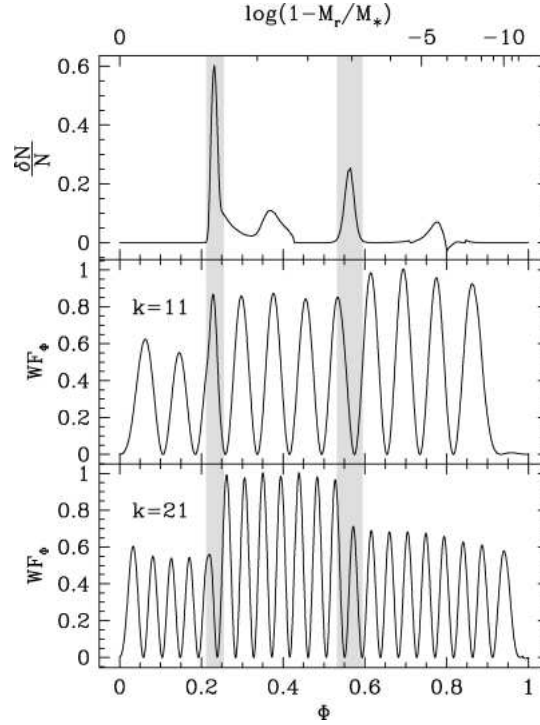


Figure 2.3: An example of mode trapping, from Montgomery et al. (2003). The top panel shows the bumps in the Brunt-Väisälä frequency. The higher bump corresponds to the transition between the homogeneous carbon and oxygen core and the pure carbon layer. The lower bump further out in the model corresponds to the transition between the pure helium layer and the pure hydrogen layer. The $k = 11$ mode is trapped in the hydrogen layer, while the $k = 21$ mode (bottom panel) is trapped between the two transition zones.

Mode trapping has a potentially observable effect on the periods. Modes trapped in the outer layers of the star, such as the $k = 11$ mode in figure 2.3 have small amplitudes in the core. The core is where most of the mass lies and if it does not participate much in the

oscillation, the mode has a smaller kinetic energy compared to adjacent modes. Bradley & Winget (1991) showed that adjacent modes also tend to be pulled toward the trapped resonance so that the period spacing between the trapped mode and the adjacent mode is smaller than that of other modes. The signature of a trapped mode is a minimum in period spacing (figure 2.4).

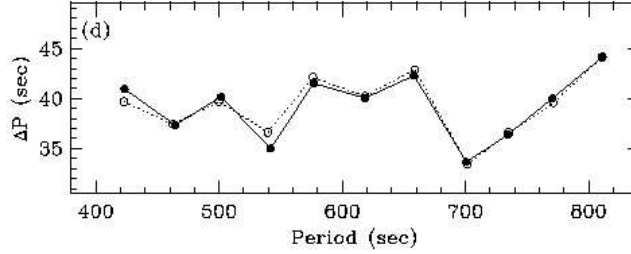


Figure 2.4: Period spacing for the modes observed in GD358, a DBV (solid curve), from Metcalfe (2001). The 540 s and 700 s modes are trapped. The dashed curve is a fit to the period spacing performed by Metcalfe.

2.1.4 Propagation diagram and asymptotic theory

Now let us come back to where we left off in section 2.1.1. To gain further physical insight, we make one more simplifying assumption. We ignore the perturbations to the gravitational potential ($\Phi' = 0$) in equations 2.23-2.25. This is called the Cowling approximation (Cowling, 1941). It is a very good approximation for modes with large values of ℓ and k . Those modes have short wavelength so changes in the potential over one wavelength for those modes are very small and may be ignored. All the modes of interest in the present work are low ℓ , low k . Those modes penetrate deep in the core and can sample most of the star in one single wavelength, but with white dwarfs, we are redeemed by the fact that their interior is not very compressible. In the core, ρ'/ρ is small so that Φ'/Φ is also small ($\Phi \sim \rho$ according to Poisson's equation).

If we apply the Cowling approximation, equations 2.23-2.25 reduce to (Unno et al.,

1989, equations 15.1 and 15.2):

$$\frac{1}{r^2} \frac{d}{dr} (r^2 \xi_r) - \frac{g}{c^2} \xi_r + \left(1 - \frac{L_\ell^2}{\sigma^2}\right) \frac{p'}{\rho c^2} = 0 \quad (2.32)$$

and

$$\frac{1}{\rho} \frac{dp'}{dr} + \frac{g}{\rho c^2} p' + (N^2 - \sigma^2) \xi_r = 0. \quad (2.33)$$

Changing the variables from ξ_r and p' to $\tilde{\xi}$ and $\tilde{\eta}$ where (Unno et al., 1989, equations 15.3 and 15.4)

$$\tilde{\xi} \equiv r^2 \xi_r \exp\left(-\int_0^r \frac{g}{c^2} dr\right) \quad (2.34)$$

and

$$\tilde{\eta} \equiv \frac{p'}{\rho} \exp\left(-\int_0^r \frac{N^2}{g} dr\right), \quad (2.35)$$

we recast equations 2.32-2.33 in their normal form (Unno et al., 1989, equations 15.5 and 15.6)

$$\frac{d\tilde{\xi}}{dr} = h(r) \frac{r^2}{c^2} \left(\frac{L_\ell^2}{\sigma^2} - 1\right) \tilde{\eta} \quad (2.36)$$

and

$$\frac{d\tilde{\eta}}{dr} = \frac{1}{r^2 h(r)} (\sigma^2 - N^2) \tilde{\xi}, \quad (2.37)$$

where

$$h(r) \equiv \exp\left[\int_0^r \left(\frac{N^2}{g} - \frac{g}{c^2}\right) dr\right]. \quad (2.38)$$

We gain further physical insight by performing a local analysis, where we hold the coefficients in equations 2.36 and 2.37 constant. This is a crude, but valid approximation if the background state (e.g. p and ρ) changes little over one wavelength of the mode. This works for short wavelength modes (high k modes) and/or for modes that do not penetrate deep in the star and remain in the outer layers, where the pressure and the density level off (high ℓ modes). A slightly less crude approximation is to allow the coefficients in equations 2.36 and 2.37 to vary a little. This is the JWKB approximation, presented nicely in Gough

(2007). All we want to do here is understand the propagation of oscillations in white dwarfs and ultimately why the periods get longer as white dwarfs cool. The crude approximation is good enough for those purposes.

If we hold the coefficients in equations 2.36 and 2.37 constant, the functions $\tilde{\xi}(r)$ and $\tilde{\eta}(r)$ are each proportional to $\exp(ik_r r)$. Inserting solutions of that form into equations 2.36 and 2.37, we find that the constant (in the local treatment) k_r is equal to (Unno et al., 1989 equation 15.9)

$$k_r^2 = \sigma^{-2} c^{-2} (\sigma^2 - L_\ell^2) (\sigma^2 - N^2). \quad (2.39)$$

In order to have spatially oscillatory solutions (purely imaginary exponent), k_r needs to be real. This requires that k_r^2 be positive. This in turns means that the two terms in parentheses in equation 2.39 should have the same sign (positive or negative). A wave will be able to propagate if its angular frequency σ is either below both the Lamb and the Brunt-Väisälä frequency or above both. In regions where k_r is imaginary, the oscillation amplitude either grows or decays exponentially with radius. In those regions, we say the wave is “evanescent”.

Modes that satisfy $\sigma < N$ and $\sigma < L_\ell$ are called gravity or g-modes and modes that satisfy $\sigma > N$ and $\sigma > L_\ell$ are pressure modes or p-modes (see figure 2.5 for a visual representation). For g-modes, the dominant restoring force is gravity, as described in section 2.1.2. For p-modes, the restoring force is pressure.

The pulsations periods we observe in white dwarfs range from just under 100 seconds to over 1000 seconds. In general, for the same radial overtone, $\ell = 2$ modes can have lower periods than $\ell = 1$ modes, as the Lamb frequency is higher for higher ℓ modes. g-modes (figure 2.5) propagate in convection zones and are evanescent in radiative zones.

Asymptotic theory

We conclude this section with the asymptotic theory for g-modes. Our ultimate goal is to understand why pulsation periods are observed to get longer as white dwarfs cool. Again,

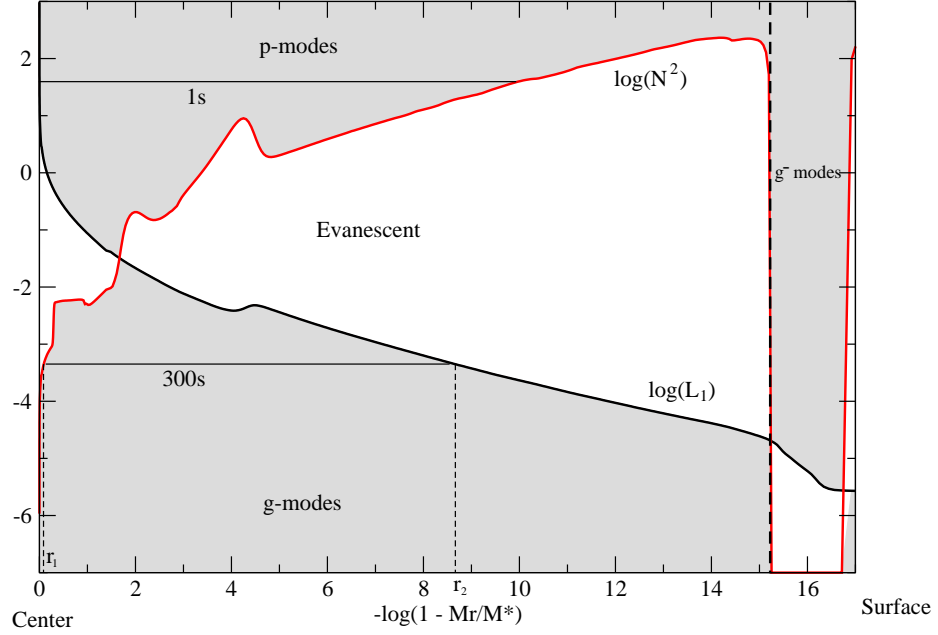


Figure 2.5: Propagation diagram for the 11000K DAV model of figure 2.2. The Lamb frequency curve shown corresponds to $\ell = 1$. The curve moves up for higher ℓ modes.

we assume that the background state varies slowly compared to the wavelength of the mode so that we can use the dispersion relation given by equation 2.39.

In any asymptotic theory, one assumes a given quantity is becoming very large or very small. Since we are interested in g-modes (low frequency, long period modes), we consider what happens if σ becomes very small (i.e. $\sigma \ll L_\ell^2$ and $\sigma \ll N^2$). For very small σ , the dispersion relation (2.39) reduces to

$$k_r^2 = \left(\frac{L_\ell N}{\sigma c} \right)^2. \quad (2.40)$$

By requiring that the radial component of the wave disappears at the inner and outer

turning points r_1 and r_2 (e.g. 300s mode in figure 2.5), we obtain the eigenvalue condition

$$\int_{r_1}^{r_2} k_r dr = k\pi. \quad (2.41)$$

Unfortunately, k_r and k are completely different entities. k_r is the radial wave number, and k is an integer that has to do with how many complete wavelengths fit between r_1 and r_2 . If we substitute k_r given in equation 2.40 into equation 2.41, solve for σ_k (the subscript indicating that we are now dealing with eigenvalues) and express the result in terms of periods, we find:

$$P_k = \frac{k\pi}{[\ell(\ell+1)^{1/2}]} \left[\int_{r_1}^{r_2} \frac{N}{r} dr \right]^{-1}. \quad (2.42)$$

The Brunt-Väisälä frequency decreases as the interior becomes denser and more degenerate, which causes the period P_k (equation 2.42) to increase as the star cools. The asymptotic theory is only a limit, which works well for high k modes (low frequency, long periods). Low k modes, dominant in the observed period spectra, are not well approximated by equation 2.42, but qualitatively, they depend on the Brunt-Väisälä frequency in a similar way.

Theoretically then, we expect the period of a given mode to increase as a result of the star cooling. We define $\frac{dP}{dt} \equiv \dot{P}$. \dot{P} is an observable that is key in constraining axion and plasmon neutrino emission rates. In the next section, I give an overview of how we measure \dot{P} 's and of what \dot{P} 's we have at our disposal so far.

2.2 Rates of period change (\dot{P} 's)

2.2.1 Measuring \dot{P} 's

The best method to determine \dot{P} 's is the O-C method, presented in detail by Kepler et al. (1991b). I reproduce their derivation here, with a few added details for clarity. O-C stands for “Observed - Calculated”. The idea, illustrated in figure 2.6, is very simple. Knowing that

a particular mode of pulsation is stable over the years, we can make a prediction of when the star will reach its peak brightness (for instance) at some point in the future. This is the calculated time. We then look at data collected around this calculated time and determine at what time the star actually reached its peak brightness. This is the observed time. If they do not match and we have strong reasons to believe we measured the initial period accurately, it means that the period did not remain absolutely constant since the last time we measured it. The result gives \dot{P} . The method works for a slow change in periods (or else requires more frequent data), because we need to guess the correct number of cycles between the starting time and calculated time. Typical period variations are $\sim 10^{-15}$ s/s for DAVs and $\sim 10^{-14}$ s/s for DBVs. Very slow indeed.

We begin by assuming a periodic variation of the form $T_{\max}(E) = T_o + PE$, where T_{\max} is the time of maximum brightness at epoch E , P is the period, and T_o is a starting point, chosen when we know the star was at a maximum (see figure 2.6). If the period is constant, then T_{\max} will recur at fixed intervals. We assume P changes slowly with time and expand T_{\max} in a Taylor series around epoch $E_o = T_o/P$, keeping only the first three terms:

$$T_{\max} = T_{\max}(E_o) + \left. \frac{\partial T_{\max}}{\partial E} \right|_{E_o} (E - E_o) + \frac{1}{2} \left. \frac{\partial^2 T_{\max}}{\partial E^2} \right|_{E_o} (E - E_o)^2 \quad (2.43)$$

Taking the derivative of T_{\max} with respect to E , we have (chain rule):

$$\frac{\partial T_{\max}}{\partial E} = \frac{\partial P}{\partial E} E + P \quad (2.44)$$

Assuming P changes very slowly with epochs ($\frac{\partial P}{\partial E}$ small), we take $\frac{\partial T_{\max}}{\partial E} \simeq P$ so that:

$$\frac{\partial^2 T_{\max}}{\partial E^2} = \frac{\partial P}{\partial E} = \frac{\partial t}{\partial E} \frac{dP}{dt} = P\dot{P}. \quad (2.45)$$

Equation 2.43 becomes:

$$T_{\max} = T_{\max}^o + P(E - E_o) + \frac{1}{2} P\dot{P}(E - E_o)^2 \quad (2.46)$$

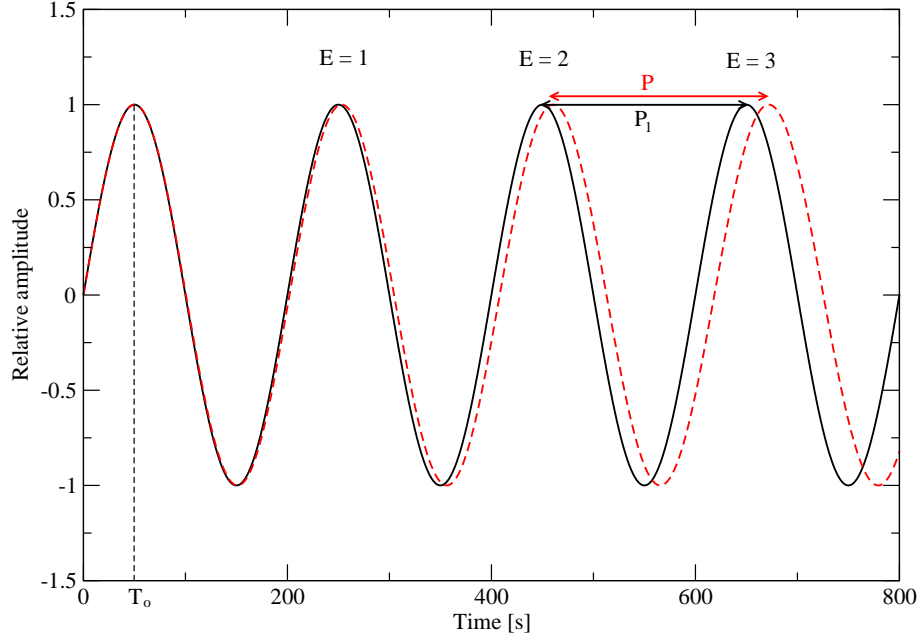


Figure 2.6: Amplitude variation of a hypothetical mode (dashed curve) and what we would expect it to look like if the period were constant (solid curve). The real period (P) increases with time, while the expected period (P_1) is kept constant. The first maximum after fiducial time T_0 marks epoch $E = 1$, the second $E = 2$ and so on. Note that the drift is slow enough that we are not missing any cycles. For clarity, I have greatly exaggerated the rate of period change. This is *not* an actual example.

After a large number of cycles, we have $E \gg E_0$ and we get

$$T_{\max} = T_{\max}^0 + PE + \frac{1}{2}P\dot{P}E^2. \quad (2.47)$$

We now define $O \equiv T_{\max}^{\text{obs}} = T_{\max}^0 + PE + \frac{1}{2}P\dot{P}E^2$ and $C \equiv T_{\max}^1 + P_1E$, where T_{\max}^0 is the observed time of maximum at epoch $E = 0$ (measured to the best of our abilities, and T_{\max}^1 is the actual time of maximum at the same epoch (point T_0 in figure 2.6). From our

ideal figure, it seems like they should be identical, but in reality, we have scatter in the data points and so $T_{\max}^1 \neq T_{\max}^0$. We finally obtain

$$(O - C) = (T_{\max}^0 - T_{\max}^1) + (P - P_1)E + \frac{1}{2}P\dot{P}E^2 \quad (2.48)$$

$$= \Delta T_o + \Delta PE + \frac{1}{2}P\dot{P}E^2. \quad (2.49)$$

ΔT_o corresponds to the uncertainty in measuring the time of maximum, and ΔP is the difference between the assumed period and the actual period at the time of maximum. If \dot{P} is non-zero, a plot of $(O-C)$ versus the epoch number E (the “O-C diagram”) is a parabola. The value of \dot{P} is found by plotting the observed O-C values vs epoch E and after having removed the linear trend ($\Delta T_o + \Delta PE$), fitting a parabola through the data points (figure 2.7). \dot{P} is given by the amount of curvature of the parabola.

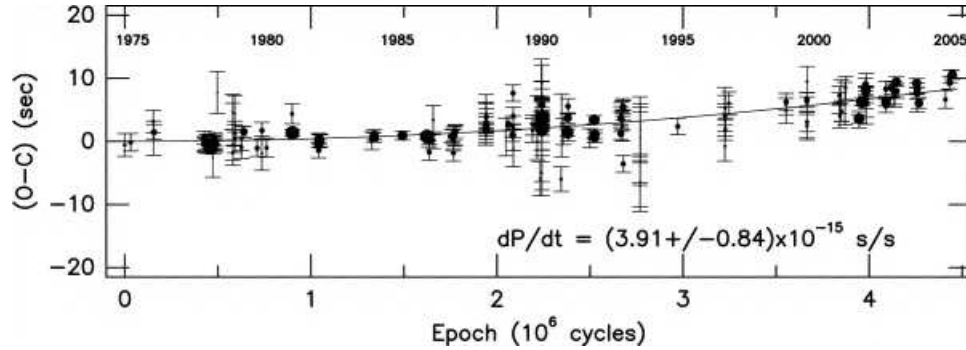


Figure 2.7: A real O-C diagram (figure 1 from Kepler et al., 2005c). This O-C diagram is for G117-B15A, a DAV for which we have a well measured \dot{P} .

2.2.2 Measured \dot{P} 's - A status report

Measuring \dot{P} 's is not just a dream of what we can do in the future. We have a well measured value for the 215s mode in G117-B15A, and are converging on one for the 213s doublet mode in R548. Both R548 and G117-B15A are blue edge DAVs. There is an active observing program under way for blue edge DAVs, that is rapidly yielding a growing number of

\dot{P} 's for those stars. In the framework of a planet search around white dwarfs, Mullally et al. (2006) have identified 30 stable pulsators at the blue edge of the DAV instability strip.

Stable pulsating white dwarfs are very precise clocks. For instance, G117-B15A loses one second every 8 million years as it cools ($\dot{P} \sim 10^{15}$ s/s), or one "tick" (a full 215s period) every 1.7 billion years. A planet around a pulsating white dwarf would cause it to wobble around a common center of mass, which would in turn delay or advance the arrival time of peaks in the light curve (because the light would have to travel more and less in turn as the white dwarf lies further or closer to us). The result would be a periodic signal in the O-C diagram, as opposed to a parabola (though each trough may still be approximated by a parabola so that the method to measure \dot{P} outlined above still works).

A 1 Jupiter mass planet 5 AU from the white dwarf would correspond to a $\dot{P} \sim 10^{-12}$ s/s (Kepler et al., 1990), 3 orders of magnitude larger than the evolutionary timescale for DAVs similar to G117-B15A. If the search fails and there is no planet, we eventually measure an evolutionary timescale, useful for the present study. In addition to \dot{P} 's for DAVs, we have the data in hand to measure a \dot{P} for one DBV, EC20058. For EC20058, we expect $\dot{P} \sim 10^{-14}$ s/s. I review below the status of the measurement of \dot{P} 's for pulsating white dwarfs.

G117-B15A

Richer & Ulrych (1974) first observed G117-B15A in may 1973. McGraw & Robinson (1976) confirmed that it was a pulsator and found that the 215s mode was very stable. They provided the first data point in figure 2.7, taken a few months before I was born. Kepler observed G117-B15A for over 30 years and published in 2005 a 4σ measurement of G117-B15A's \dot{P} (Kepler et al., 2005c). In table 2.1, I detail the time evolution of the measurement of \dot{P} for G117-B15A. Until year 2000, most measurements of \dot{P} were upper limits (in the absolute value). In chapter 5, we use $\dot{P} = (3.57 \pm 0.82) \times 10^{-15}$ s/s to place limits on the axion mass.

Table 2.1: Time evolution of the measurements of \dot{P} for the 215s mode in G117-B15A

Year	\dot{P} [10^{-15} s/s]	Confidence level	Reference
1982	$56. \pm 47.$	Upper limit	Kepler et al., 1982
1988	-5.7 ± 7.8	“	Kepler et al., 1988
1989	12.5 ± 5.5	“	Kepler et al., 1989
1990	8.3 ± 5.0	“	Kepler et al., 1990
1991	12.0 ± 3.5	3.4σ	Kepler et al., 1991a,b
1992	3.2 ± 3.0	Upper limit	Kepler et al., 2000
1995	1.2 ± 2.9	Upper limit	Kepler et al., 1995
1998	1.2 ± 2.2	Upper limit	Kepler et al., 1998
2000	2.3 ± 1.4	1σ	Kepler et al., 2000
2005	4.12 ± 0.83		Kepler et al., 2005b
2005	3.57 ± 0.82	4σ	Kepler et al., 2005c

R548

R548, also known as ZZ Ceti, was the first DAV discovered (Lasker & Hesser, 1971) and DAVs are still sometimes called “ZZ Ceti stars”. R548 has four dominant pulsation periods, a doublet around 213s and another one around 274s (Mukadam et al., 2003). Because the two dominant modes are doublets, measuring their \dot{P} is challenging. The members of the doublets produce signals that can interact with each other in the Fourier transform and introduce phase uncertainties. As a result, 31 years of data on R548 do not allow as precise a measurement on \dot{P} as 30 years of data on G117-B15A did. The latest published \dot{P} ($5.5 \pm 1.9 \times 10^{-15}$ s/s) for the 213s mode (Mukadam et al., 2003) is only an upper limit.

L19-2

L19-2 is another blue edge DAV, visible from the southern hemisphere (its declination being -81°). The largest amplitude mode is found near 192s. Unfortunately, it is a rotationally split triplet, with a definite asymmetry in frequency. The fact that those frequencies do not

stay in phase (and we do not know how they change in phase relative to each other) makes it difficult to accurately measure a \dot{P} for this mode. O'Donoghue & Warner (1987) used 8 years of data to place an upper limit on the 192 s mode \dot{P} of 3.0×10^{-14} s/s. Sullivan (1998) conducted follow-up observations of L19-2 from New-Zealand from 1994 to the time he published his 1998 paper. In 1995, L19-2 was the object of a 3-site Whole Earth Telescope run. Sullivan (1998) proposes ways to reduce the uncertainties due to phase variations (such as averaging over data sets taken during the same observing season). The 3.0×10^{-14} s/s limit is the last published result on L19-2.

GD66 and more

More recently, Mullally et al. (2007) determined a \dot{P} of order 10^{-12} for the 302 s singlet mode of GD66, another blue edge DAV. This \dot{P} is 3 orders of magnitudes too large to be due to the cooling of the star (according to any reasonable model). The most likely explanation is that this high \dot{P} is due to the reflex motion of GD66 about a center of mass shared with an unseen Jupiter-like companion. Mullally has determined upper limits of 10^{-13} s/s for an additional 9 white dwarfs (private communication) and has identified more blue edge DAVs with stable modes.

In the past 6 or 7 years, the high-speed photometry data at McDonald Observatory in West Texas has been collected using Argos, an instrument built to do white dwarf high speed photometry (Mukadam & Nather, 2005). Argos produces high signal to noise CCD data by minimizing timing errors. With Argos quality data, it no longer takes 30 years to determine \dot{P} 's as precisely as we have for G117-B15A. The on-going observation of hot DAVs should begin to yield measurements of \dot{P} 's for those stars within the next 3 to 5 years.

EC20058

All the \dot{P} 's I have presented so far were determined for DAVs. Today there are 124 known DAVs. Of those, 30 are known to have stable modes (Mullally et al., 2006). For DBVs,

the situation is quite different. There are only 13 known DBVs. Of those, 8 have no stable modes, 4 require follow-up observations to determine whether they are stable or not, and one, EC20058 is known to have two stable modes, one at 257 seconds and one at 281 seconds. EC20058 is a southern hemisphere object (-52° declination) like L19-2. Dennis Sullivan has been observing it from New Zealand and has collected a decade of high speed photometry data, enough to determine a precise \dot{P} for EC20058. EC20058 is hotter than G117-B15A (28000K vs 12500K) and its evolutionary \dot{P} should be an order of magnitude greater. This makes it easier to measure. I describe what we know observationally of EC20058 in section 6.4 and I make a prediction of how tightly we should be able constrain plasmon neutrino rates once we have measured \dot{P} for EC20058 in section 6.7.

Now that we have laid down the foundations, we proceed to a presentation of the method used in chapters 5 and 6 to perform the asteroseismological analysis of the DAVs G117-B15A, R548 and the DBV EC20058.

Chapter 3

Models and methods

Don still talks affectionately about the good old days when he and fellow students would punch cards and take stacks of them to the computing center for processing. In a few hours, the main frame computer would spit out a converged white dwarf model. Computing technology improved quickly and it was not long before desktop computers could easily run the White Dwarf Evolutionary Code (WDEC, described below) in a few minutes. White dwarf asteroseismology entered an era of trial and error. Travis Metcalfe 2001 revolutionized asteroseismology by taking for the first time a systematic approach, using a parallel code based on a Genetic Algorithm (GA). With the GA, Metcalfe was attempting to find not just “a” good fit to an observed period spectrum, but the best fits in all of parameter space. In the same spirit, I took another kind of systematic approach to asteroseismology: a fine grid search.

I begin this chapter with a brief description of the WDEC. Next I describe the two classes of models I used: DAV models for G117-B15A and R548, and DBV models for EC20058. In each case, I perform a quantitative analysis of the modeling uncertainties that guided the asteroseismological analysis of all 3 stars. The purpose of such fits is to constrain the equilibrium models of these stars, with the ultimate goal of determining their neutrino and/or axion emission rates. I conclude with a section on the fine grid search method and

contrast it with the GA method.

3.1 The White Dwarf Evolution Code

The original version of the WDEC was written by Martin Schwarzschild and later modified by a variety of people, including Kutter & Savedoff (1969), Lamb & van Horn (1975), Winget (1981), Kawaler (1986), Wood (1990), Bradley (1993), and Montgomery (1998). It is described in detail in Lamb & van Horn (1975) and Wood (1990). I provide a brief description here.

The WDEC evolves hot starter models to an effective temperature of our choice. The starter model can be the result of the full evolution of a stellar model from the Main Sequence, but for DAVs and DBVs, this is not necessary, if one starts with a hot enough model ($\sim 100,000$ K). By the third model in the evolutionary sequence (where the DAV or DBV model we want is typically number 20 or higher, depending upon the time steps we choose), we already obtain models that are thermally relaxed solutions to the stellar structure equations. The starter models I used are simple polytropes ($P \propto \rho^{5/3}$), computed by Travis Metcalfe for his thesis (2001).

In its original form, the WDEC contains three components, which need to be run each in turn if one wants to obtain pulsation periods for the models. First, the program `evol` computes a white dwarf evolutionary model. Next, the `prep` code adds shells to the model and smooths out a few quantities that are important to calculate the pulsation periods. Last, the `pulsation` code computes pulsation periods for the model by solving the adiabatic or non-adiabatic equations of stellar pulsations. To run the GA efficiently, Travis recast all three programs into a single fortran function, which takes in the same input as WDEC, and outputs a number, a measure of how well the model fits the periods we are trying to match. I adopted his function (one for DAVs called `makeda` and one for DBVs called `makedb`). The two functions mainly differ in how they accept input. `makeda` accepts a hydrogen layer mass parameter, while `makedb` does not. This allowed me to run grids of models without

having to write complicated file manipulation scripts and sped up computing time.

3.2 The models - choices to make

There is a wide variety of ingredients that go into making a model of a white dwarf. Each ingredient is a source of uncertainty. In this section I identify a number of those sources. They fall into three categories: chemical make-up of the interior of the model, input physics, and numerical artifacts. I discuss each in turn below and then show the quantitative effect of each source of uncertainty.

3.2.1 Chemical Composition Profiles

The internal composition of a white dwarf depends on post Main Sequence evolution, which is not all fully understood (e.g. mass loss). All we really know from single stellar evolution models is that white dwarf interiors should be made up primarily of carbon and oxygen, a result of post-Main sequence nucleosynthesis. Indeed, most white dwarfs are best modeled with a carbon and oxygen core. The carbon and oxygen mixture is homogeneous out to a certain radius, corresponding to a phase of nuclear burning in a convective core. Above that, the model is differentiated due to the strong gravity and one finds in turn a layer of pure carbon, a layer of pure helium, and in the case of DAVs such as G117-B15A and R548, a layer of pure hydrogen. We do not know beforehand the relative abundance of carbon and oxygen in the homogeneous region of the core, where the pure carbon layer begins, nor the exact shape of the transitions from one chemical composition to the next.

There are a number of decisions we have to make regarding the shape of the chemical abundance profiles in the core of the model. Figure 5.3 gives an illustration of each. We can change:

1. the central oxygen abundance (X_o)
2. at what mass point the oxygen abundance starts dropping (X_{fm})

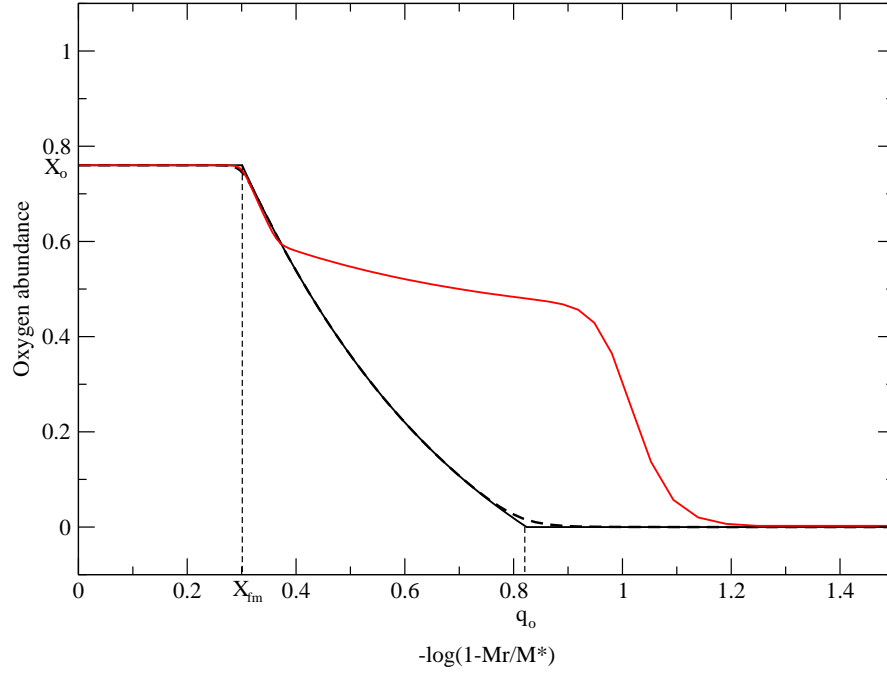


Figure 3.1: A variety of possible oxygen abundance profiles. The thin line represents a basic profile, the dashed line the same profile except smoothed, and the line with the hump, a profile based on Salaris et al. (1997) (see Appendix B).

3. at what mass point the oxygen abundance drops down to zero (q_0)
4. how smooth the chemical abundance profiles are
5. the general shape of the chemical abundance profiles

For the DAV models, I fixed the core composition profiles to those calculated by Salaris et al. (1997) because I already had 4 parameters to fit and did not have the luxury to meaningfully vary core composition profiles. The results of the asteroseismological analysis of G117-B15A and R548 did not convince me that those profiles were significantly

better than the simpler ones and I did not use them for EC20058. Instead, I used simple core composition profiles and varied the related parameter that mattered most (among X_o , X_{fm} , and q_o).

Double layer helium abundance profiles

Dehner & Kawaler (1995) included time-dependent diffusion of the elements in evolutionary models of the hot pulsating white dwarf PG 1159 down to a temperature within the DBV range. They discovered that diffusion led to a double layered helium abundance profile. Fontaine & Brassard (2002) included double layer profiles in an asteroseismological fit of DBV GD 358 and were able to match its 11 periods spectrum as well as Metcalfe et al. (2003) did, with a single-layer helium layer. Metcalfe et al. (2003) included double layered helium abundance profiles in asteroseismological fits to GD 358 and CBS 114. They found that double-layered models were not quite as successful as single-layer models in finding fits consistent with the spectroscopy to both CBS 114 and GD 358. I decided to try both single-layer and double-layer models for EC20058. I show an example of each in figure 3.2. I fixed the shapes and varied the locations of the composition transitions, following the parametrization used by Metcalfe et al. (2003).

3.2.2 Input Physics

Another category of uncertainties to consider is the input physics. These include among other things:

6. equations of state
7. treatment of convection
8. neutrino rates

In the core of the star, we use the Lamb (1974) equation of state. In the less strongly degenerate parts of the model (the outer 3-5% of the model), we use the Saumon et al.

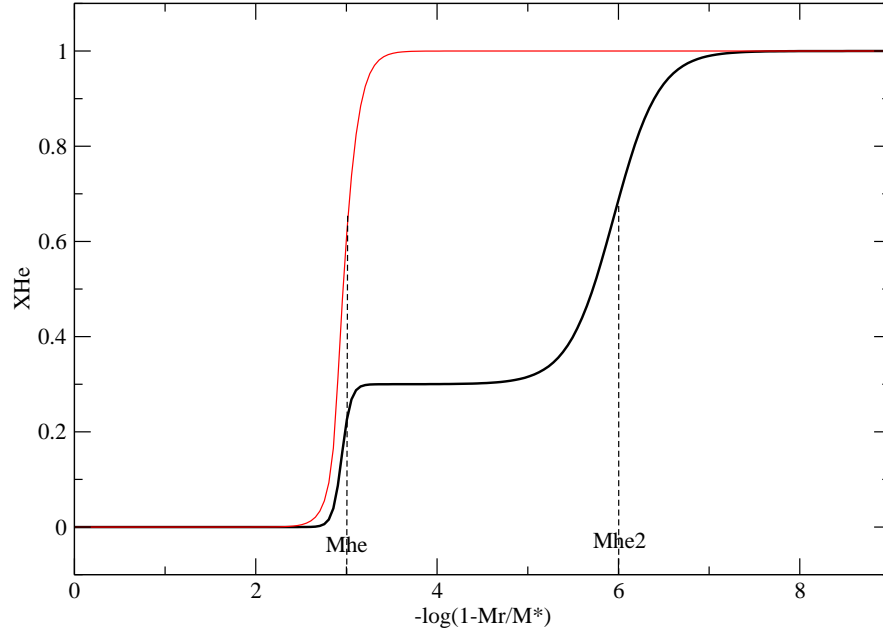


Figure 3.2: A single layer helium profile (thin curve) and a double layer profile (bold curve) and the associated parameters.

(1995) equation of state. Convection is treated through Mixing Length Theory (MLT) according to Bohm & Cassinelli (1971). For DAVs, I fixed the ratio of the pressure scale height to the mixing length (α) to 0.6, consistent with model atmosphere calculations by Bergeron et al. (1995a) and DAV light curve fitting work by Montgomery (2005). For DBVs, I fixed α to 1.0, consistent with $\alpha = 1.1$ found by Montgomery (2007) and $\alpha = 1.25$ found in model atmosphere calculations by Beauchamp et al. (1999). As we shall see, the exact value of α matters little for fitting the periods of the models. The models include the latest plasmon neutrino rates computed by Itoh et al. (1996a).

3.2.3 Numerical Artifacts

And finally, there are uncertainties due to the way the code works. The code makes a model of the core of the white dwarf, and a model of the envelope. In the envelope, we assume that energy generation is non-existent ($L(r)$ held constant), and we do not include any carbon or oxygen. The two models are then matched at the core-envelope boundary. The matching is not perfect and depends on the specified location of that boundary. This introduces a small discontinuity (if we do things right) in the Brunt-Väisälä frequency, which in turn affects the computed periods. To determine the effect of the core-envelope discontinuity on the periods, we can:

9. change the location of the core-envelope boundary (the “stop mass”)
10. smooth the Brunt-Väisälä frequency after the fact (see Appendix C)

For my grids of models, I set the stop mass at $M_r = 0.97 M_*$. For most chemical compositions, this location minimizes the discontinuity in the B-V frequency. I found that artificially smoothing the B-V frequency had a relatively small effect on the periods of the model (see section below) and I decided not to smooth it for the models in my grids, therefore minimizing the amount of non-physical manipulations.

3.3 A quantitative analysis of the uncertainties

3.3.1 G117-B15A and R548

To get an idea of the effect of the sources of uncertainties listed in the previous section on our fit to G117-B15A and R548, I considered a number of models that differed from one another by one of the factors mentioned above and compared their periods and \dot{P} 's. The fiducial model has $T_{\text{eff}} = 12,200$ K, $M_* = 0.6 M_{\odot}$, $M_{\text{He}}/M_* = 10^{-2}$, and $M_{\text{H}}/M_* = 10^{-7}$. From now on, I shall simply designate the helium and the hydrogen layer mass by M_{He} and M_{H} respectively, and the $1/M_*$ will be implicit.

I list the results in order of decreasing significance for the period fit in table 3.1. In column 1, I list the item number according to the previous section, in column 2 the properties of the fiducial model, in column 3 the changes I made in each case, in column 4 the average difference between the periods of the fiducial model and the modified model (equation 3.1, with $A = 1$), and in column 5 the fractional change in \dot{P} 's. I considered the \dot{P} of a particular mode, in this case one close to 215 s (the mode in G117-B15A for which we have measured a \dot{P}).

Table 3.1: Uncertainties for DAV models

Item	Fiducial model	Change	$\langle \Delta P \rangle$ [s]	$\Delta \dot{P} / \dot{P}$ [%]
5	$T_{\text{eff}} = 12200 \text{ K}$	$T_{\text{eff}} = 10980 \text{ K} (-10\%)$	18.9	-22.83
	$M_* = 0.6 M_{\odot}$	$M_* = 0.54 M_{\odot} (-10\%)$	15.9	79.55
	basic chemical profiles	Salaris profiles	11.0	50.40
	$M_{\text{H}} = 10^{-7}$	$M_{\text{H}} = 10^{-6.3} (-10\% \text{ in the log})$	9.58	87.93
	$M_{\text{He}} = 10^{-2}$	$M_{\text{He}} = 10^{-2.2} (-10\% \text{ in the log})$	5.28	-11.57
3	$q_0=0.85$	$q_0=0.95$	3.53	1.93
2	$X_{\text{fm}}=0.50$	$X_{\text{fm}}=0.55 (-10\%)$	1.97	0.47
1	$X_0=0.80$	$X_0=0.72 (-10\%)$	1.81	-2.51
6	Saumon et al.(1995) envelope EOS	old EOS	0.974	1.66
9	$\frac{M_c}{M_*} = 0.98$	$\frac{M_c}{M_*} = 0.95$	0.370	-0.06
4	non-smoothed chemical profiles	smoothed	0.317	-0.21
10	non-smoothed BV frequency	smoothed	0.0829	-0.21
7	$\alpha = 0.6$	$\alpha = 2$	0.0155	0.18
7	ML2	ML1	0.00210	0.03

In general, factors that matter most for the period fit (the asteroseismology) also matter most for the \dot{P} 's, but not always. I approached the problem in two steps. The first

step is to find a best fit model for the observed set of periods we have to match. In that step, I considered what factors influenced $\langle \Delta P \rangle$ most. As was already well known from previous studies (e.g. Bradley, 1998, Benvenuto et al., 2002), the 4 free parameters that influence the calculated period spectrum most are T_{eff} , M_* , M_H , and M_{He} . Salaris chemical profiles produce very different bumps in the Brunt-Väisälä frequency (see Appendix B) and as a result also have a large effect on the periods. As I stated earlier, I decided to use those profiles in my DAV models, because I did not have the luxury to vary the three core composition parameters.

The first block in table 3.1 includes the 4 parameters I varied in the asteroseismological analysis of G117-B15A and R548. The next block indicates parameters that matter to a lesser extent. They are the three core composition parameters; I did not vary those parameters. The last block includes factors that have a negligible effect, for my current purpose, on the asteroseismology (I adopted $\langle \Delta P \rangle = 1\text{ s}$ as the significance limit).

The second step is to look at the factors that influence the calculated \dot{P} 's most. By and large, the factors that matter for \dot{P} 's matter as well for the periods, with a few differences in ranking. One striking example is the effect of the hydrogen layer mass on \dot{P} . In chapter 5 we shall see that this is because the 215s mode is particularly sensitive to M_H . This fact will prove very useful.

3.3.2 EC20058

I follow the same method as in the section above to assess the importance of each source of uncertainty in the DBV models. I describe the fiducial model in the second column of table 3.2. I list the changes made in column 3, their effect on the periods in column 4, and their effect on the \dot{P} 's in column 5. I calculated \dot{P} for a mode close to 257s, one of the stable modes observed in EC20058.

Again, factors that influence the periods most also tend to have a large effect on the \dot{P} 's. The notable exception is the inclusion or non-inclusion of neutrino emission in the

Table 3.2: Uncertainties for DBV models

Item	Fiducial model	Change	$\langle \Delta P \rangle$ [s]	$\Delta \dot{P} / \dot{P} [\%]$
	$T_{\text{eff}} = 28000\text{K}$	$T_{\text{eff}} = 25200\text{K} (-10\%)$	6.66	-36.21
	$M_* = 0.60M_{\odot}$	$M_* = 0.54M_{\odot} (-10\%)$	6.48	19.08
	$M_{\text{He}} = 4.0$	$M_{\text{He}} = 3.6 (-10\%)$	2.57	-25.42
	Double layered He profile	Single layer	2.45	7.86
	$M_{\text{He}2} = 6.0$	$M_{\text{He}2} = 5.4 (-10\%)$	1.27	-0.31
2	$X_{\text{fm}} = 0.50$	$X_{\text{fm}} = 0.55 (+10\%)$	0.715	0.75
3	$q_0 = 0.85$	$q_0 = 0.95$	0.452	1.96
8	Itoh et al. 1996 ν rates	no neutrinos	0.415	-71.00
9	$\frac{M_c}{M_*} = 0.98$	$\frac{M_c}{M_*} = 0.97$	0.403	8.48
		$\frac{M_c}{M_*} = 0.95$	2.40	44.69
1	$X_0 = 0.80$	$X_0 = 0.72 (-10\%)$	0.210	-1.61
7	$\alpha = 1$	$\alpha = 2$	0.00988	-0.11
7	ML2	ML1	0.00187	0.08

models. Not including them reduces \dot{P} by 71%. This shows the importance of neutrino emission on the cooling. After all, at 28000K, they carry away more energy than photons. On the other hand, the period spectrum remains relatively unchanged ($\langle \Delta P \rangle = 0.415$ s). The small effect on $\langle \Delta P \rangle$ may come as a surprise. It is however fortunate, and not so surprising. Córscico et al. (2001) note the small dependence of the periods on the axion luminosity. Changing the axion luminosity by a factor of 900 leads to a 1% drift in the periods of their best fit model to G117-B15A. One would expect the neutrino luminosity to have a similar effect on the periods of a model. We saw that neutrinos and axions had the same function: to carry energy away from the core of the star.

The reason for this small dependence is that neutrinos are emitted deep in the star, though slightly suppressed deep in the core as we shall see. Degenerate material does not respond to changes in temperature (due to energy loss) by contracting and as a result, the structure of the star remains mostly unaffected by the emission of neutrinos. Since the modes respond to structural changes in the star, they too remain mostly unaffected. In addi-

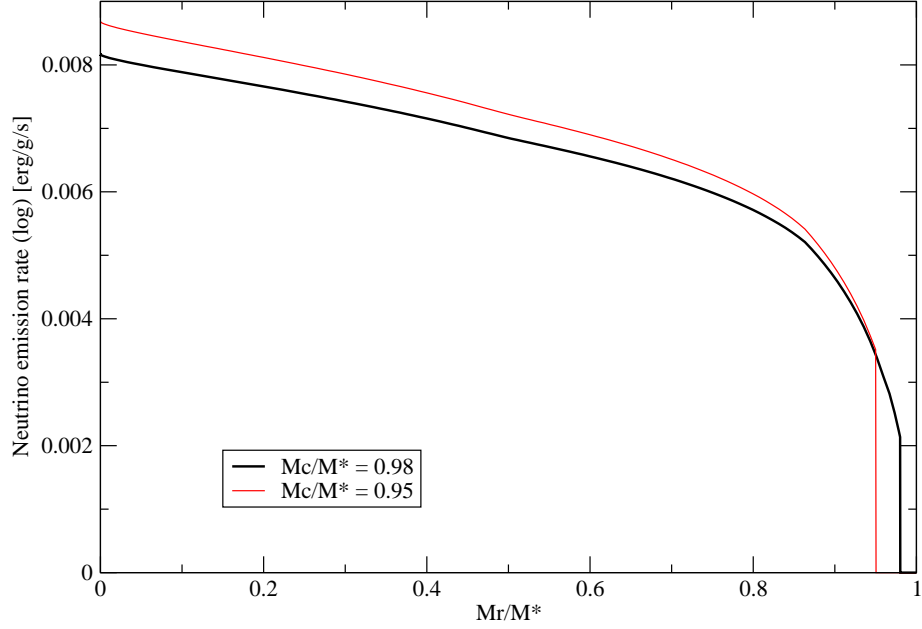


Figure 3.3: An example of a model with a poorly chosen stop mass compared to one with a better stop mass.

tion, neutrino emission does not introduce any "bumps" into the Brunt-Väisälä frequency. It merely slightly lowers it throughout the degenerate core.

This is a fortunate situation because it allows us to vary the plasmon neutrino rates by factors of 10 and still be able to compute \dot{P} 's for a barely changing mode, allowing meaningful comparisons. According to the models I discuss in chapter 6, the change in the 257s and 281s modes for EC20058 is of order 0.1% if I vary the plasmon neutrino emission rates by a factor of 10. That and the large effect of the neutrinos on \dot{P} is what will allow us to place strong constraints on plasmon neutrino emission rates.

I also found that the location of the stop mass is much more sensitive in DBV models than it is in DAV models. This is because ignoring energy production in the outer 5% of

the star is OK for DAV models, but not for DBV models. DBV models are hotter than DAV models and are still extracting a non-negligible amount of potential energy in their outer layers from contraction. In addition, we have to take into account neutrino production. In figure 3.3 I show the neutrino emission rate in the fiducial model described in table 3.1, for two different stop masses: one chosen as far out as possible ($\frac{M_c}{M_*} = 0.98$) and one with a stop mass too far in ($\frac{M_c}{M_*} = 0.95$). Because neutrino emission is not taken into account in the envelope, it gets cut short at the core-envelope boundary and the whole model is affected. This is most likely the cause of the large $\langle \Delta P \rangle$ for the case where $\frac{M_c}{M_*} = 0.95$.

The repercussion on \dot{P} is even more dramatic. The reason \dot{P} is 45% *higher* when we cut the neutrino emission short is apparent in figure 3.3. While the neutrino emission is cut short in the envelope, it is higher in the core, where it contributes more to the total energy loss, and therefore leads to a higher \dot{P} . We did not have that problem for DAV models, as neutrino emission is negligible in those models. I used $\frac{M_c}{M_*} = 0.97$ for all the models in the grids described in section 6.6, with a high success rate of models converging properly. If we push the stop mass further out, we start introducing a discontinuity in the helium abundance profile at the carbon/helium transition zone.

Choosing the same significance limit as in the previous section ($\langle \Delta P \rangle = 1\text{s}$), I separated table 3.2 into two blocks. For EC20058, I tried both single layer helium profiles and double layer helium profiles. I had the luxury to include an additional free parameter, and I chose the next one down the list, X_{fm} , the location of the edge of the homogeneous carbon and oxygen core.

3.4 A new approach to white dwarf asteroseismology

3.4.1 The problem and a solution

In essence, the problem we have to solve in white dwarf asteroseismology is the simple minimization of a function (the average difference between the calculated periods and the

observed periods) with n variables, where n is usually 4. Those variables include T_{eff} , M_* , M_{He} , and an additional one that depends on the situation. Expressed mathematically:

$$\Phi(T_{\text{eff}}, M_*, M_{\text{He}}, \dots) = \langle \Delta P \rangle = \frac{A}{N} \sum_{i=1}^N |P_i^{\text{calc}} - P_i^{\text{obs}}| \quad (3.1)$$

where N is the number of observed periods and A is a normalizing factor to account for the fact that at higher effective temperatures and higher masses, the period spacing decreases, artificially increasing our chances of finding a good period match (see Appendix D). For the regions of parameter space considered in chapter 5 and 6, $A \sim 1$.

The simplest way to minimize Φ is to compute it for all conceivable values of the n variables and pick the smallest value we find. But the number of times we have to evaluate Φ can quickly become astronomical. To make matters worse, each evaluation of the function requires running a full evolutionary sequence of white dwarf models and computing a set of periods for the last model in each sequence (the one that converged to the chosen effective temperature). Calculating a single evolutionary sequence used to be computationally time consuming and building a detailed map of Φ over all the relevant parameter space was out of the question.

Metcalf (2001) developed a scheme which allowed him to minimize Φ without having to build a full map of parameter space. His method was based on a genetic algorithm (GA) which could find a global minimum by evaluating Φ at cleverly chosen points in parameter space. The GA requires evolving a population of 138 models for 200 generations, which adds up to $\sim 10^5$ evaluations of Φ or a function like it. With synthetic data, Metcalf determined that given a list of 11 periods to match, the GA would find the correct solution 65% of the time. In order to bring the efficiency up to 99% required running the GA 5 times on the average. Metcalf built his own cluster of 24 nodes (Darwin) to run the parallelized GA algorithm. On Darwin, one run of the GA took 6 hours.

In addition to fitting the periods themselves, one can also use the period spacings, as they are manifestations of trapped modes, which in turn carry information about the

location of the transition zones between layers in the model that have different composition (see section 2.2). Metcalfe performed such a fit for GD358, the brightest DBV. GD358 was the object of extensive observing campaigns and presents a rich period spectrum that includes 11 independent modes. As we shall see in chapter 5, G117-B15A offers us a paltry 3 periods to match and R548, five. For EC20058, I also used 5 solidly measured periods. EC20058 was the object of a 4 site Whole Earth Telescope run in 1997 (Sullivan, 2005). The results of the run have not been published yet, though Sullivan states that a total of 11 modes were identified as a result of the extended coverage. It may be worth attempting a more sophisticated asteroseismological fit to EC20058's period spectrum once the data is fully reduced.

3.4.2 Fine grid search

I took a different approach from Metcalfe and decided to perform a brute force fine grid search for best fits to the observed periods of G117-B15A, R548, and EC20058. The advantage of a fine grid search is that for the first time, it allowed me to build a full map of parameter space both for models of DAVs like G117-B15A and models of DBVs like EC20058. My limited grids can easily be expanded to include more of parameter space. Once a grid of periods is calculated, one can very rapidly fit any set of periods. Such a grid therefore can be used to fit other stars. The disadvantage is that one is “stuck” with the physics I included in my models. Changing the physics requires the computation of an entirely new grid. In order to have a useful grid, I had to make sure I had included all the relevant physics in a sensible way (this took more than one trial).

For the DAV grid (relevant for G117-B15A and R548) and the DBV grid (useful for EC20058), I followed the same procedure. First I built a low resolution grid that covered a broad region of parameter space. For that grid, I determined that step sizes of 400K in T_{eff} , $0.02 M_{\odot}$ in M_{\star} , 0.4 in $\log(M_{\text{He}})$ and $\log(M_{\text{H}})$, and 0.1 in X_{fm} were sufficient to locate likely minima of Φ . Using the results of the broad grid search, I narrowed down my search

to smaller areas of parameter space and built a finer grid. I found that a resolution of 200K in T_{eff} , $0.01 M_{\odot}$ in M_* , 0.2 in $\log(M_{\text{He}})$ and $\log(M_{\text{H}})$, and 0.05 in X_{fm} was sufficient to clearly define the minima of Φ . The broad DAV grid contains about 20000 models, the fine grid 6000; the broad DBV grid is 28000 models strong (half of them single layer helium and half double layer helium models) and the fine grid is 70000 models strong (all single layer helium models). I detail the regions of parameter space covered by each grid in sections 5.7 and 6.6. I ran most of the models on two dual processor machines. On average, each machine was able to process 30000 models in 24 hours.

Chapter 4

Axions and the missing universe

“Does the axion actually exist? I do not know. However, I am very certain that if it does, it will be found in the heavens and not on earth!”

Michael S. Turner in “Windows on the axion”, (1990).

“[Astronomers] are spherical bastards. No matter how you look at them they are just bastards.”

Fritz Zwicky

Swiss spherical bastard, discoverer of dark matter

4.1 Introduction

Axions became very interesting to astrophysicists when Weinberg (1989) suggested that they could account for the mysterious dark matter that pervades our universe. Since then, both physicists and astrophysicists have been looking for the elusive particle. There are really two questions we would like to answer. The first one is “Do axions exist?”. So far, we have not detected any. The second one is “If axions exist, can they account for dark matter?” The answer to this second question is far from trivial. First of all, we do not know how massive axions should be. The theory does not constrain this particular property of

axions. Much of the searches for axions, including the one I present in the next chapter, seek to place limits on the axion mass. But even if we knew the axion mass, whether those axions could account for dark matter depends on the axion model we adopt *and* the cosmological model of their formation in the early universe.

I start this chapter with a very brief primer on cosmology. In section 4.3 I review the evidence we have that 84% of the *matter* in the universe is in the form of dark matter. In section 4.4 we make a brief excursion into the twilight zone as I present very recent results on axions and dark energy. In section 4.5, I mention some dark matter candidates other than axions. I describe axion models in section 4.6, and review axion cosmology in section 4.7. In section 4.8, I give an overview of the different axion searches done to date and their results. I summarize the constraints on axion models from those searches and how they relate to the missing part of the universe in section 4.9.

4.2 Cosmology primer

The main purpose of this section is to give the background to the dimensionless mass densities used in Cosmology, Ω_i . Much of what follows is reviewed very clearly in Bergstroem (2000). We start with the spatial metric for the universe, which can be written

$$ds^2 = a^2 \left(\frac{dr^2}{1 - kr^2} + r^2 d\Omega^2 \right), \quad (4.1)$$

where $d\Omega$ is the usual solid angle, a is a length scale parameter, and $k = -1, 0, 1$ for an open, flat, and closed universe respectively. A basic task of Cosmology is to determine k and compute $a(t)$ both in the past and future.

The time dependence of a is given by the Friedmann equation:

$$\left(\frac{\dot{a}}{a} \right)^2 + \frac{k}{a^2} = \frac{8\pi G}{3} \rho_{\text{tot}}, \quad (4.2)$$

where $\frac{\dot{a}}{a} = H(t)$ (e.g. $v = Hd$). Cosmologists often use the dimensionless Hubble constant h , which is defined as $H \equiv h \cdot 100 \text{ km s}^{-1} \text{ Mpc}^{-1}$. Recent cosmological observations suggest that in today's universe, $h_0 = 0.735 \pm 0.032$ (Limon et al. , 2006).

The critical density is the density the universe would have if it were flat. With $k = 0$, equation 4.2 gives $\rho_c = \frac{3H^2}{8\pi G}$. Plugging in the numerical values, one obtains: $\rho_c = 1.9 \times 10^{-38} \text{ h}^2 \text{ kg/m}^3$. Now define $\Omega_i \equiv \rho_i/\rho_c$, where the subscript “i” may be “M” for matter, “B” for baryons etc ... For a flat universe, $\rho_{tot} = \rho_c$, and so $\Omega_{tot} = 1$. Plugging $k = -1$ and $k = 1$ in equation 4.2 for an open and closed universe respectively, we also find $\Omega < 1$ for an open universe and $\Omega > 1$ for a closed universe. In plain terms, the universe is open if its density is lower than the critical density, and closed if it is higher.

Before looking at axions as dark matter candidates, let us review the evidence for dark matter, why baryonic matter cannot account for all of it, and what could account for it.

4.3 The dark matter problem

Dark matter is one of the greatest problems today in Astrophysics. Dark matter is invisible matter that has a gravitational effect on the matter we know well (baryonic matter). The nature of dark matter is heavily debated. Some believe that the “existence” of dark matter is a result of our lack of understanding of gravity and are exploring alternatives. Alternatives include the famous Modified Newtonian Dynamics (MOND) (Milgrom, 1983), general relativistic approaches (Cooperstock & Tieu, 2006) and more exotic gravitational theories based on general relativity (Reuter & Weyer, 2004).

This is a direction that is surely worth pursuing, but the present work contributes to the other approach. The majority of the projects currently underway to solve the dark matter problem assume that our understanding of gravity is correct (or at least not that flawed), and that dark matter really does exist. The problem then becomes, “what is dark matter?”

4.3.1 Astrophysical evidence for the presence of dark matter

Dark matter manifests itself by the gravitational effect it has on the matter that we can see. Dark matter influences the way stars orbit in galaxies, as well as how galaxies themselves move in galactic clusters. There is evidence that most matter in the universe is in the form of dark matter.

Rotation curves of galaxies

The velocities of stars orbiting in a galaxy are related to the mass interior to their orbit through simple Newtonian physics by:

$$v(r) = \sqrt{\frac{GM_r}{r}}. \quad (4.3)$$

By surveying the amount of luminous matter, one can make a prediction of what $v(r)$ should look like, based on what one can see. Figure 4.1 shows the rotation curve for the Milky Way (Englmaier & Gerhard, 2006). The matter contained in the luminous matter alone should first cause $v(r)$ to rise in the denser parts of the galaxy and then decrease as the disk tapers off (dashed curve in 4.1). The observed rotation curve (solid line) is flat in the outer parts of the galaxy. To account for the higher than expected $v(r)$ in the outer parts of the galaxy, one needs to include a halo of dark matter (dotted line).

From equation 4.3 one can readily derive the following ratio between the mass of visible matter present in a galaxy and the mass of dark matter:

$$\frac{M_{DM}}{M_{LUM}} = \left(\frac{v_{DM}}{v_{LUM}} \right)^2, \quad (4.4)$$

where “LUM” for “luminous” refers to all the known contributions. Velocities are taken at the known edge of the galaxy, so that the masses are total masses. Using this simple treatment, we can derive $\frac{M_{DM}}{M_{LUM}} \simeq 2.8$ from 4.1. Therefore according to this data, 73% of the mass of our galaxy is in the form of dark matter.

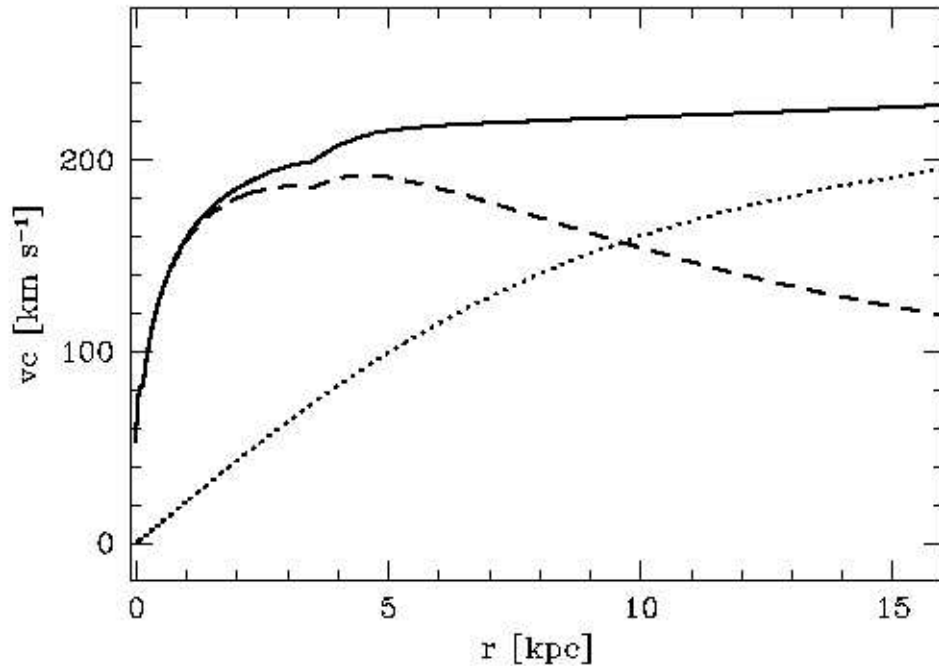


Figure 4.1: Rotation curve for the Milky Way (figure 2 in Englmaier & Gerhard, 2006). The solid line is the observed rotation curve, the dashed line the contribution from the visible matter, and the dotted line the contribution from a dark matter halo.

There are some uncertainties in such analyses. One lies in the measured velocities. This is a bigger problem for the Milky Way than it is for other galaxies. For other galaxies, the only difficulty lies in measuring the proper inclination. The vast majority of galaxies also show a significant amount of dark matter. The main source of uncertainty, however lies in deriving the mass of the visible matter. The velocity curve tells us the total mass present and photometry tells us how luminous the galaxy is. To get the mass of the luminous matter, one has to assume a “mass to light” ratio, which is usually an educated guess based on stellar formation and galaxy formation models.

Also if one plays the game all the way, there is no reason why the dark matter halo would terminate where the visible galaxy ends. There is no detectable limit to the dark

matter halo if there is no visible matter there to reveal the dark matter density. In that respect, 73% of dark matter in our galaxy is a lower limit. We can get an idea of how much dark matter there is between galaxies by studying galactic clusters.

Galactic clusters

In galactic clusters, the galaxies themselves become tracers of dark matter. It is actually in a galactic cluster, the Coma cluster, that the first hint of dark matter was discovered, from the velocity dispersion of the Coma galaxies (Zwicky, 1933).

Additional evidence for dark matter in galactic clusters arises from gravitational lensing, where the images of background galaxies are distorted by the foreground cluster. From the lenses, the total mass of the cluster can be inferred and then compared with visible images (which show the galaxies in the cluster) and X-ray images, which show emission from the hot intergalactic gas that makes up most of the visible mass of the cluster (e.g. Fabian & Allen, 2003). Fabian & Allen looked at 9 galactic clusters and for all 9 of them, find $M_{\text{gas}}/M_{\text{tot}} \sim 0.1$. Their result is typical.

At even larger scales, the Wilkinson Microwave Anisotropy Map (WMAP) measures the total amount of dark matter in the universe.

Evidence from WMAP

The WMAP (Wilkinson Microwave Anisotropy Map) satellite measured fluctuations in the Cosmic Microwave Background down to angular scales of $10'$. The best model to explain those fluctuations is the Big Bang model. In that model, those fluctuations are the results of early acoustic oscillations. The angular size spectrum of the fluctuations in the CMB gives a precise measurement of Ω_{tot} and shows that it is very nearly 1. The universe is flat. The addition of large extragalactic surveys such as the SDSS help determine the different contributions to Ω_{tot} and show that $\Omega_{\text{M}} = 0.237 \pm 0.034$ (total matter density in the universe) and $\Omega_{\text{B}} = 0.0436 \pm 0.00701$ (baryonic matter density in the universe). Again, dark matter

is needed to explain the fact that $\Omega_B \ll \Omega_M$ (Limon et al. , 2006).

4.3.2 Evidence for non-baryonic dark matter

There are (at least) two different arguments based on observations that rule out regular matter as a possibility for all that unseen matter. The first argument is based on nucleosynthesis in the first minute after the Big Bang and measurements of the abundance of light elements in today's universe. The second piece of evidence comes from the WMAP satellite and extragalactic surveys.

Light element abundances

Nucleosynthesis started as soon as deuterons were able to survive for some extent of time. This was possible only after the universe had cooled down enough that UV photons capable of breaking up deuterons ($E > 2.2 \text{ keV}$) became scarce relative to the number of deuterons. Nucleosynthesis stopped when the temperature was so “low” that the nuclei no longer had sufficient kinetic energy to overcome their mutual electrostatic repulsion. In that first minute, the elements made were Hydrogen, Deuterium, Tritium, Helium 3, Helium 4, and Lithium.

The question we are trying to answer is, “how much matter was there in the universe in the beginning?” (and therefore, “how much matter should we expect to see today?”) Assuming that stars have contributed minimally to the nucleosynthesis of light elements since then, we should find today the same abundances there were when the primordial nucleosynthesis ceased. The amount of light elements produced right after the Big Bang depends on how long the synthesis of those elements took place, how many building blocks (nucleons) were available, the reaction cross sections, and on how many photons there were.

Reaction cross sections are known from laboratory experiments. For the rest, one needs to assume an initial relative abundance of nucleons to photons. This abundance determines when nucleosynthesis started (and therefore how long it took place). It also deter-

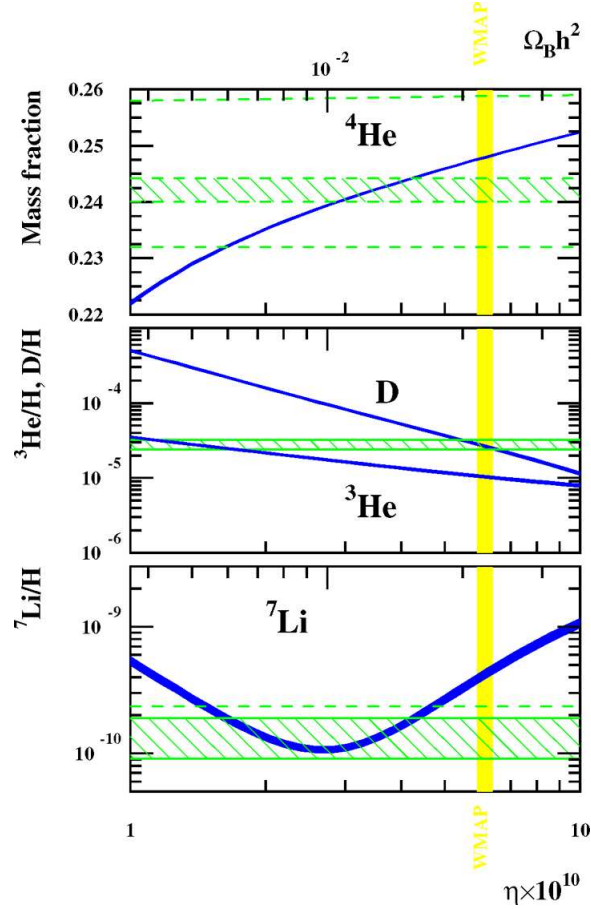


Figure 4.2: Big Bang Nucleosynthesis abundances from Coc et al. (2005). The curves correspond to BBN abundances computed from nucleosynthesis models. The horizontal shaded regions reflect the observed abundances (see text).

mines the number density of photons and nucleons as time progresses. Figure 4.2 shows the relative abundances predicted as a function of the initial relative abundance of nucleons to photons (Coc et al., 2005). Coc et al. give a good review of the current status of Big Bang Nucleosynthesis and much of the information that follows comes from their review.

All that is left to do is to measure the relative abundances in today's universe and compare with the models to see which value of $\Omega_b h^2$ is right. For the deuterium relative abundance, we use the Lyman Alpha Forest. The Lyman Alpha Forest is a series of Lyman

Alpha hydrogen absorption lines produced at different red shifts in the intergalactic medium between us and distant quasars. Integrated spectroscopy of those lines reveals the relative abundance of deuterium in the universe (Kirkman et al., 2003). The abundance of deuterium is well constrained (horizontal hashed region in the middle panel of figure 4.2).

The relative abundance of helium 4 is determined from the observation of metal-poor intergalactic HII regions and is not as simple to determine observationally. The horizontal hashed region in the top panel of figure 4.2 reflects results found by Luridiana et al. (2003) and Izotov et al. (1999). The horizontal dashed lines include more conservative results by Olive & Skillman (2004).

The relative abundance of Lithium 7 comes from the observation of halo Main Sequence stars. The horizontal hashed region in the bottom panel of figure 4.2 reflects work done by Ryan et al. (2000). The dashed line represents a more recent result by Meléndez & Ramírez (2004). The determination of the helium 3 abundances is problematic. We assume that none has been produced since the Big Bang or if it has, we know how much breaks down.

The vertical stripes in figure 4.2 correspond to the WMAP value of $\Omega_B h^2$ (Limon et al. , 2006). If one looks at figure 4.2 naively, one notes that the WMAP and the BBN results agree only for the deuterium abundance. Coc et al. give a variety of arguments that indicate that the observed deuterium abundance is the only one that can be trusted. Even if one does not believe those arguments, the observed abundances tell the same story as WMAP: $\Omega_B \ll 1$. Baryonic matter makes up only a small portion of the universe.

4.4 Where is the rest of the universe? The dark energy question

The attentive reader will have noticed a serious discrepancy. In section 4.3.1 I stated that the universe was flat ($\Omega_{\text{tot}} = 1$) and that the total matter density in the universe (including dark matter) was $\Omega_M = 0.237 \pm 0.034$. Where is the rest of the universe? Cosmologists have come to the unsettling conclusion that 76% of our universe is in the form of a mysterious

dark energy.

4.4.1 Einstein's biggest blunder - The cosmological constant

When Albert Einstein was developing the theory of General Relativity early in the 20th century, he firmly believed in a static universe. That is a universe that was neither expanding nor contracting. This was a natural assumption to make in the absence of data showing whether or not the universe was changing and if it was, how. With that assumption he ran into a problem. The only long-range force that acts on uncharged heavenly bodies we know is gravity. Gravity does only one thing: it brings masses together. In order to maintain a static universe, Einstein had to introduce an additional (repulsive) force term in the equation, the cosmological constant Ω_Λ :

$$\Omega_{tot} = \Omega_M + \Omega_\Lambda. \quad (4.5)$$

In the 1920's, Edwin Hubble discovered that distant galaxies were receding from us at increasing speed the further away they were ($V=Hd$). His observations suggested a new cosmological model of the universe: the Big Bang theory. In the Big Bang theory, the universe was produced in an initial burst of energy, an explosion of space time, and what we witnessed today was simply galaxies coasting away from one another as a result. There were two possible scenarios possible for the future of the universe. If there was enough matter in the universe, gravity would eventually be able to rein in the expanding universe and would bring it back together ($\Omega_{tot} > \Omega_c$, closed universe). If, on the other hand, the universe was too empty, gravity would fail to bring it back together and it would keep expanding *at its present expansion rate*. Edwin Hubble had shown that the universe was not static and the need for the cosmological constant went away. Ω_Λ became known as Einstein's greatest blunder.

4.4.2 The resurrection of the cosmological constant

In the 1980's cosmologists were elated and a little sad at the same time. They had a simple problem left to solve on their hand: measure the density of the universe Ω_{tot} . They were elated because by the late 1980's COBE, the predecessor of WMAP, was about to launch and they would obtain precise values for all the cosmological constants of the Big Bang model. Soon, they would know the answer. They were a little sad because once the answer was found, an active field of research would end.

But in the late 1990's, just when the value of the Hubble constant H_0 was pinned down to 70 Mpc/km/s, type Ia supernova measurements revealed that H was not the same in the past as it was today (Type Ia supernovae are powerful distance indicators, as they are standard candles that can be seen from hundreds of megaparsecs away). The universe is not expanding at a constant rate, it is not slowing down, it is *accelerating*. While the supernova data suggest that $\Omega_M < 1$, WMAP data suggest that $\Omega_{\text{tot}} = 1$. This means that Ω_Λ is not equal to zero (equation 4.5). Cosmologists called this additional unseen component of our universe “dark energy”.

4.4.3 The nature of dark energy and where axions come in

Following the discovery of dark energy, there was a debate about its nature. Is Ω_Λ truly a constant? If we express the equation of state of the universe as $p = w\rho$, a constant Ω_Λ would imply $w=-1$. The third year WMAP data released recently strongly suggest $w \simeq -1$ (Spergel et al. , 2007). It appears that the dark energy is due to a cosmological constant after all. In that model, dark energy results from a quantum vacuum of light particles that fill the universe with an additional pressure and add to the energy density.

Based on that observation, de Vega & Sanchez (2007) propose that dark energy could be produced by a scalar particle provided the particle has a mass of order 1 meV, interacts weakly with matter we know, and is stable on the timescale of the age of the universe. Axions fulfill those requirements beautifully. de Vega & Sanchez conclude that in

order to account for dark energy, axions should have a mass between 4 and 5 meV. This is a very interesting result because we are very close to being able to tell whether or not such axions exist (at least given a particular axion model).

4.5 Dark matter candidates

4.5.1 How about neutrinos?

Early nucleosynthesis and WMAP rule out protons and neutrons and anything made out of protons and neutrons as viable candidates for dark matter. So what could it be? How about neutrinos? Neutrinos escape detection very easily and we now know that at least one kind has a mass of around 0.01 eV (Atre et al., 2005). It turns out that neutrinos are not likely candidates for dark matter either, for two reasons.

First of all, theory predicts that neutrinos in the early universe froze out at temperatures close to 1 MeV, which means that neutrinos were relativistic as the structures in the universe were being formed. Neutrinos would therefore constitute hot dark matter. But structure formation models, such as N-body simulations, all show that dark matter triggered small structure formation, which then grew into larger and larger structures. If one starts out with hot dark matter, one never gets the smaller structures observed in the CMB. If we believe those models, then neutrinos are not good dark matter candidates (Bergstroem, 2000).

Perhaps a stronger argument against neutrinos is the fact that they are fermions and not very massive. As fermions, they cannot be “packed” too closely together, but on the other hand, one needs a lot of them in a small space in order to reach a high density. Tremaine & Gunn (1979) estimate that to account for the dark matter of a dwarf galaxy of velocity dispersion σ (usually of order 100 km/s) and core radius r_c (typically 1 kpc), the

neutrino mass has to fulfill:

$$m_\nu \geq 120 \text{ eV} \left(\frac{100 \text{ km/s}}{\sigma} \right)^{1/4} \left(\frac{1 \text{ kpc}}{r_c} \right). \quad (4.6)$$

On the other hand, the neutrino density is given by (Bergstroem, 2000)

$$\Omega_\nu h^2 = \frac{\sum m_{\nu_i}}{93 \text{ eV}}, \quad (4.7)$$

where the summation applies to the number of kinds of neutrinos (which is 3 in the Standard Model). Assuming $(\Omega_\nu h^2)_{\text{max}} \sim 1$, the equation above yields a maximum mass for the neutrino of $\sim 30 \text{ eV}$, which is too small for the neutrinos to account for (all) the dark matter in a dwarf galaxy.

There is no particle that we know of (predicted by the Standard Model) that seems to account for all of dark matter. One needs at least an extension of our current theories and new particles.

4.5.2 Supersymmetric dark matter

The Standard Model (SM) of particle Physics predicts the existence of the “Higgs boson”, which has not yet been discovered. If the Higgs boson exists, then each fundamental particle in the SM must have a supersymmetric (SUZY) counterpart, (electron - selectron, quark - squark, neutrino - neutralino, photon - photino,...), otherwise the mass of the Higgs boson is infinite. The supersymmetric particles must have the same charge as their SM counterparts, and a different spin. The other quantum numbers may or may not be the same.

The simplest SUZY models assume that the supersymmetric particles are identical in every way to their SM counterpart, except for their spin. Those theories are R parity conserving. In R parity conserving SUZY, the lightest supersymmetric particle (LSP) is stable, and is a dark matter candidate. The most likely one is the neutralino, which has spin 0 (so it is a boson, unlike the neutrino). The R parity conserving SUZY model is considered

by many physicists as the most likely one.

4.5.3 Weakly Interacting Massive Particles (WIMPs)

The neutralino and other supersymmetric particles are examples of WIMPs. WIMP is an umbrella term for all particles that are massive and interact weakly with matter. They are by definition dark matter candidates. WIMPs would have a mass comparable to that of a heavy nucleus and so one method of detection would be through collisions with heavy nuclei. In such a collision, they would exchange a Z^0 boson or a squark. While squarks have not been found, the Z^0 can be detected and would constitute a signature of such an event. The mass of the WIMP would be found by measuring the recoil of the target nucleus. Of course such a collision would be very rare, as WIMPs interact weakly with matter.

4.6 What are axions

While very popular among physicists, SUZY has its weaknesses. It's biggest weakness is its complexity. To avoid the problem of an infinite Higgs boson mass, one has to invoke a score of new particles. The simplest SUZY model, the Minimal Supersymmetric Model (MSSM) involves 24 parameters (Mitchell Symposium 2006, Marco Battaglia "Focus Collider experiment for DM, including LHC"). It is also entirely based on the assumption that the Higgs boson exists, and so far, there is no supporting experimental evidence.

Axions are better motivated than neutralinos as they are the result of an attempt to solve the strong CP problem in the Standard Model, which was raised by experimental results. It is only after axions were proposed that the community realized that they made excellent dark matter candidates (Weinberg, 1989).

4.6.1 Particle physics motivation for axions

CP violation - a bit of history

Before the 50's, physicists believed that nature conserved both charge and parity. But in 1957, Wu et al. found that parity was not conserved in the beta decay of ^{60}Co nuclei. They observed that polarized ^{60}Co nuclei beta decayed preferably with the electrons going against the polarization. If parity were conserved, then Wu et al. should have observed an equal number of electrons going in one direction as in the other.

While weak interactions did not preserve parity, physicists still believed that charge and parity, taken together, were conserved (CP invariance). In a milestone experiment in 1964, Cronin and Fitch (Christenson et al., 1964) found that CP invariance was also violated in weak interactions. Their experiment showed that K_0^2 mesons could decay into a pion-antipion pair with a branching ratio (pion-antipion pair/all other charged modes) equal to 2×10^{-3} . This decay mode is forbidden under the CP invariant theory of weak interactions and was not expected to occur. The discovery earned them a Nobel Prize in Physics in 1980. More recent experiments at CERN and Fermilab, such as the BaBar experiment confirmed CP violation.

Neutrons and CP invariance

There is no evidence that CP is violated in strong interactions. Indeed, there is experimental evidence that it is conserved. If CP were violated in strong interactions, then we would expect the neutron to have a measurable electric dipole moment, but it does not. To see how that is evidence that CP is conserved, consider two simple models of the neutron.

Neutrons are neutral and have a magnetic dipole moment. One way to construct such a particle is to have a positive charge and a negative charge following the same circular path, but in opposite directions (figure 4.3a). Now reverse the parity (figure 4.3b), and perform a charge reversal (figure 4.3c). In the end, the overall charge does not change, and the magnetic dipole moment is conserved. This model of the neutron is CP invariant.

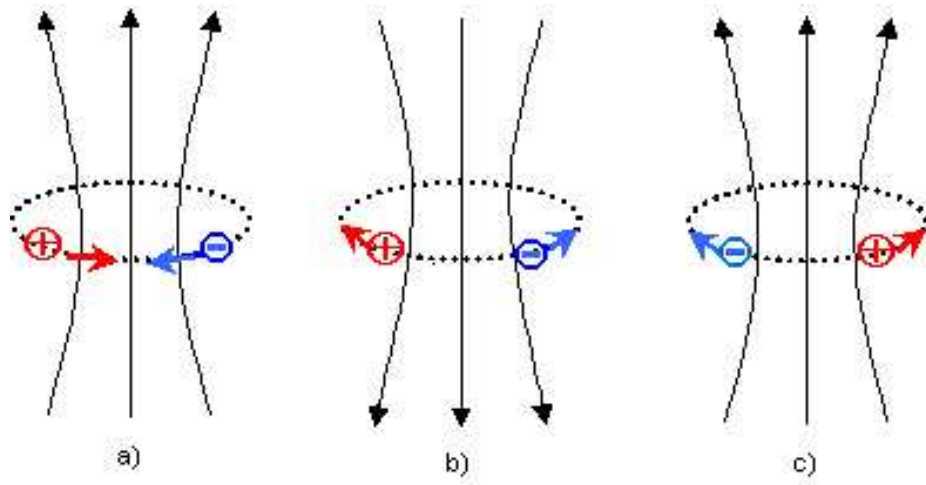


Figure 4.3: A CP conserving model of a neutron.

Now if one adds an electric dipole moment to the neutron, one now has to construct a new model for the neutron, where the two charges follow distinct circular paths. After performing the same set of operations on that new hypothetical particle, one does not recover the original particle: the electric dipole flips. (figure 4.4). CP is violated.

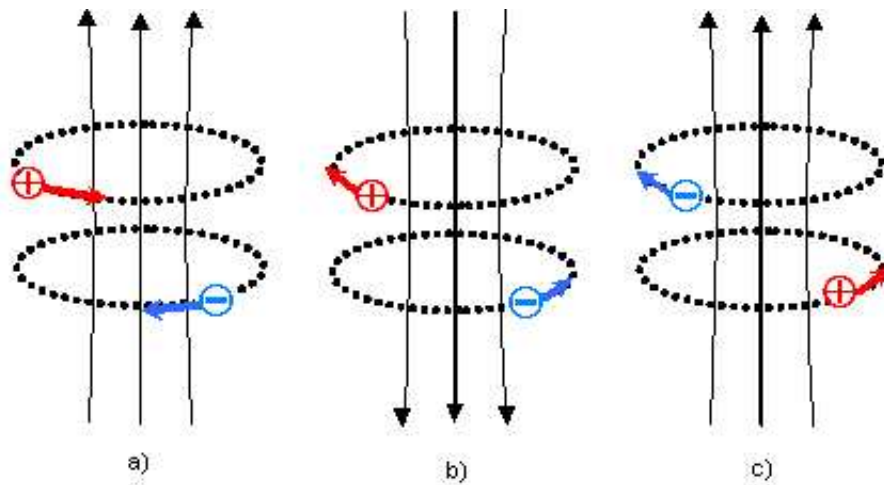


Figure 4.4: A CP violating model of a neutron.

The Standard Model does not explain why CP should be violated in weak interactions and not in strong interactions. One would therefore expect the neutron to have an electric dipole moment. Experiments have placed an upper limit on the neutron's electric dipole of 10^{-25} ecm (electron charge \times length of dipole), 10 orders of magnitude below the predicted value (Turner, 1990).

In more technical terms, in QCD, the neutron electric dipole moment arises from a CP (as well as C and P) violating term in the lagrangian (Turner, 1990). This electric dipole moment is predicted to be of order $5 \times 10^{-16} \bar{\theta}$ ecm, where $\bar{\theta}$ is a free parameter in the theory. The experimental limit of 10^{-25} ecm means that $\bar{\theta}$ is less than 10^{-10} . Theoretical physicists do not understand why $\bar{\theta}$ has to be so small. This is called the strong CP problem and can be solved elegantly by the introduction of a new symmetry.

Peccei-Quinn mechanism

To explain the fact that strong forces do not seem to violate CP conservation, particle physicists came up with a new symmetry. This symmetry, added to the Lagrangian of the fundamental interactions, is called the Peccei-Quinn symmetry (Peccei & Quinn, 1977). It is spontaneously broken by the vacuum expectation value $f_{PQ}/\sqrt{2}$ of the Nambu-Goldstone field Φ , a complex scalar field. The phase of the Nambu-Goldstone field is the axion field. f_{PQ} is the Pecci-Quinn energy scale, an essentially free parameter. It can be anywhere between $f_{\text{weak}} \sim 250 \text{ GeV}$ and the Planck mass, around 10^{19} GeV (Turner, 1990).

The extra term added to the Lagrangian contains the parameter $\bar{\theta} = \theta - \arg(m_1 \dots m_n) - \frac{a(x)}{f_a}$ (Sikivie, 2000). f_a , the axion decay constant, may be expressed in terms of the axion mass:

$$f_a \simeq 10^7 \text{ GeV} \left(\frac{0.6 \text{ eV}}{m_a [\text{eV}]} \right), \text{ e.g. } f_a \propto 1/m_a. \quad (4.8)$$

Axions with very small mass are often referred to as “invisible axions”. “Visible” axions have already been ruled out (Bergstroem, 2000) and current searches all look for invisible axions.

4.6.2 Axion models

Axion models involve axion coupling constants written “g” with subscripts indicating what axions couple to (e.g. $g_{a\gamma\gamma}$ denotes coupling of an axion to two photons). Axions can also couple to electrons and nucleons. Each coupling constant depends on one or more of the PQ charges of the u and d quarks and the electron (denoted X_u , X_d , and X_e respectively.) Those charges can be between 0 and a number of order 1 and are not constrained by the theory. This gives rise to a continuum of axion models. Two simple models include the KVSZ model (Kim, 1979; Shifman et al., 1980), where $X_e = 0$ (no coupling to electrons), and the DFSZ model (Dine et al., 1981; Zhitnitsky, 1980), where $X_u \sim X_d \sim X_e \sim 1$.

Axion-photon coupling

The most common axion production mechanism where axion-photon coupling comes into play is the decay of a photon through the Primakov effect, where a photon turns into an axion after passing in the electro-magnetic field of a nucleus (figure 4.5).

In this model, the axion field is made up of a single electroweak singlet Higgs field with expectation value $f_{PQ}/\sqrt{2}$. There are only two parameters, f_{PQ} and N (the number of exotic quarks), which are related to f_a through $f_a = f_{PQ}/N$.

The axion emission rate depends on the strength of the axion-photon coupling, characterized by the constant $g_{a\gamma\gamma}$ and on the axion mass.

$$g_{a\gamma\gamma} = \left(\frac{1.45 \times 10^{-10}}{\text{GeV}} \right) \left| \frac{E/N - 1.92}{0.75} \right| \left(\frac{m_a}{1 \text{ eV}} \right), \quad (4.9)$$

where E/N , the coefficient of the electromagnetic anomaly, takes on different values depending upon the axion model one adopts. It is often treated like a free parameter of order unity. Searches for axions place constraints in the $m_a - g_{a\gamma\gamma}$ plane.

In that plane, KFSZ axions fall on a line given by the equation above, with E/N set equal to 0, and DFSZ axions on a line with E/N set equal to 8/3. The coupling of DFSZ

axions to photons is 2.7 times weaker than the coupling between KFSZ axions and photons. E/N can take on other values. This gives rise to a continuum of axion models.

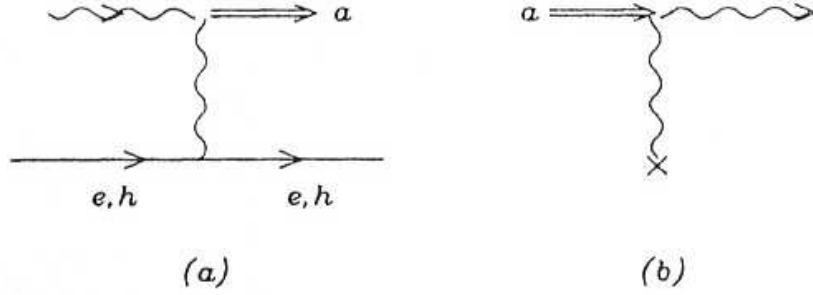


Figure 4.5: Feynman diagrams of the production of axions through the Primakoff effect and the reverse reaction (from Lazarus et al., 1992).

Axion-electron coupling for DFSZ axions

In addition to the singlet scalar field, this model also has two electroweak doublet fields, Φ_1 and Φ_2 , which have expectation values $f_1/\sqrt{2}$ and $f_2/\sqrt{2}$ respectively. One usually defines $x = f_1/f_2$ and $\cos^2 \beta = x^2/(x^2 + 1)$. In this model, $f_a = f_{PQ}/N_f$, where N_f is the number of degenerate vacua. In the Standard Model, $N_f = 3$. We are left with 2 free parameters: β and f_{PQ} . The strength of the axion-electron coupling is

$$g_{ae} = \left(\frac{0.028}{\text{GeV}} \right) \frac{m_a \cos^2 \beta}{1 \text{ eV}}. \quad (4.10)$$

KFSZ axions do not couple to electrons and therefore the above does not apply ($g_{ae} = 0$). For DFSZ axions, the coupling to electrons is 10^8 orders of magnitude greater than the coupling to photons (assuming $\cos^2 \beta \sim 1$). In white dwarfs, where there is a plethora of free electrons in the degenerate interior, the dominant mechanism for axion production is bremsstrahlung (see section 5.3).

Axion-nucleon coupling

The coupling of axions to nucleons comes into play in neutron stars, where axions would be produced in nucleon-nucleon bremsstrahlung events. The strength of the axion-nucleon coupling is given by (Turner, 1990)

$$g_{\text{ann}} = g_{\text{app}} \simeq \frac{0.5 m_N}{f_{\text{PQ}}/N}, \quad (4.11)$$

where $f_{\text{PQ}}/N = f_a$, and m_N is a dimensionless neutron mass.

Comparing equation (8a) in Turner (1990) and equation 4.10, I was able to determine that by his definition, m_e was ~ 4000 so that $m_N \sim 10^7$ and so in the units used for $g_{a\gamma\gamma}$ and g_{ae} above (GeV^{-1}),

$$g_{\text{ann}} = g_{\text{app}} \sim \frac{1}{\text{GeV}} \frac{m_a}{1 \text{ eV}}. \quad (4.12)$$

g_{ann} is weakly dependent on the quantity E/N defined in equation 4.9 so the coupling of axions to nucleons has the same strength, regardless of the axion model one adopts (Turner, 1990). g_{ann} is 2 orders of magnitude stronger than g_{ae} and dominates where nucleon-nucleon-axion interactions are present.

4.7 Axion Cosmology and Dark Matter

Results from WMAP imply that $\Omega_{DM} = \Omega_M - \Omega_B = 0.193$ (Limon et al. , 2006). If axions are to explain dark matter, then one should have $\Omega_a = \Omega_{DM} = 0.193$. Ω_a depends on the mass of the axion (or equivalently on the energy scale f_a , see equation 4.8). The difficulty is that the exact dependence of Ω_a on f_a depends on the cosmological model of the formation of the universe and to be honest, some of it is not very well constrained. In this section, I present the different cosmological models and how an upper bound on m_a can help us constrain each.

Axions were formed when the early universe cooled down to a temperature T_{PQ} , when the PQ symmetry became spontaneously broken (the PQ phase transition). At that time axions were massless and all values of the axion field $\langle a(x) \rangle$ were equally likely. Topological defects in the form of axion strings appeared. Today's axion mass density depends on what happened next.

4.7.1 Inflationary scenario

If there was inflation and the universe subsequently failed to reach T_{PQ} ever again, then the axion strings were destroyed and the axion field in our “corner of the universe” had a unique initial value θ_i , which is unfortunately completely unknown. Subsequently, the axion field relaxed to its equilibrium value $\theta_i = 0$. Axions are the result of coherent oscillations of the axion field. This process is called “vacuum misalignment”.

The mass density of axions in that case is (Shellard & Battye, 1998)

$$\Omega_a h^2 = \theta_i^2 f(\theta_i), \quad (4.13)$$

where θ_i can be anywhere between 0 and 2π . For $\theta_i = 0$ (the equilibrium value), $f(\theta_i) = 1$. For $\theta_i \rightarrow \pi$, $f(\theta_i) \rightarrow -\ln|\pi - \theta_i|$. This means that for $\theta_i \sim \pi$, $f(\theta_i)$ gets very large, allowing arbitrarily large values of m_a for any given axion mass density. As a result, the inflationary scenario is essentially non-constrainable (though limits to the madness do arise from quantum fluctuations and constraints from temperature and density fluctuations in the CMB - see Shellard & Battye (1998) for an overview).

4.7.2 Standard thermal scenarios

If inflation never took place or if the temperature of the universe rose above T_{PQ} after inflation took place, then the axion strings were not destroyed. When the temperature came close to the QCD scale, the axion acquired a mass. At a critical time t_1 , defined by $m_a(t_1) \times t_1 = 1$,

the axion field started to oscillate in response to the turn-on of the axion mass. At that time, the universe had a temperature $T_1 = 1 \text{ GeV}$ (Sikivie, 2000).

In this case, there are two contributions to the axion mass density. One from axions that were radiated by axion strings before time t_1 and one from the decay of walls bounded by strings after time t_1 .

Decay of axion strings and of domain walls bounded by strings

In both cases, the axion mass density is given by an expression of the form

$$\Omega_a h^2 = \left(\frac{6.0 \mu\text{eV}}{m_a} \right)^{7/6} Q. \quad (4.14)$$

The value of Q is model dependent. For the decay of axion strings, estimates from various authors vary from $Q \sim 0.1$ (Battye & Shellard, 1994) to $Q \sim 100,000$ (Frieman & Jaffe, 1992), but most seem to believe that $Q \sim 1 - 100$ (Nagasawa & Kawasaki, 1994; Shellard & Battye, 1998; Yamaguchi et al., 1999). The contribution from the decay of domain walls formed when axions acquired mass is of the same order as the contribution from the decay of strings, or a little smaller. Q for domain wall decay ranges from 0.1 to ~ 3 (Chang et al., 1999; Shellard & Battye, 1998).

An upper limit on the mass of the axion can allow us to place an upper limit on $Q^{tot} = Q^{str} + Q^{DW}$:

$$Q^{tot} \leq x \Omega_{DM} h^2 \left(\frac{m_a^{\max}}{6.0 \times 10^{-3} \text{ meV}} \right)^{7/6}, \quad (4.15)$$

where x is the fraction of dark matter made up of axions. For $x = 1$ and $m_a^{\max} \sim 10 \text{ meV}$, we get an upper bound for Q of ~ 700 .

Thermally produced axions

For sufficiently large axion mass, axions were once in thermal equilibrium in the early universe. The density for thermally produced axions is:

$$\Omega_a^{th} h^2 = 8 \times 10^{-9} \left(\frac{60}{g^*} \right) \left(\frac{6 \times 10^{-6} \text{ eV}}{m_a} \right)^{-1} e^{-t_U/\tau_a}, \quad (4.16)$$

where $g^* \sim 60$ is the effective number of thermally excited degrees of freedom in the early universe at the time the axions froze out, t_U is the age of the universe, and τ_a is the axion life-time, given by

$$\tau_a = 6.8 \times 10^{24} \text{ s} \left(\frac{1 \text{ eV}}{m_a} \right)^5 \left(\frac{0.72}{E/N - 1.95} \right)^2. \quad (4.17)$$

g^* is somewhat of a fudge factor, which can differ from author to author by about an order of magnitude. Raffelt (1990) takes $g^* \sim 60$ and so (for $t_U/\tau_a \ll 1$), he obtains $\Omega_a^{th} h^2 \approx 10^{-3} m_a/\text{eV}$. Turner (1990) on the other hand finds $\Omega_a^{th} h^2 \approx 10^{-2} m_a/\text{eV}$.

Either way, thermally produced axions contribute very little to the axion mass density, unless axions are fairly massive ($\sim 10 \text{ eV}$) and axions that massive have already been ruled out by collider experiments. We can say that this model of axion formation has been ruled out.

4.7.3 Cosmological lower limit on m_a

In the standard thermal scenario, contributions to the relic axion density come from the decay of strings and domain walls. We have, as a function of Q_{\min} and the fraction x of dark matter made up of axions:

$$m_a^{\min} = 6.0 \mu\text{eV} \left(\frac{Q_{\min}^{\text{tot}}}{x \Omega_{\text{DM}} h^2} \right)^{6/7}. \quad (4.18)$$

Assuming $Q_{\min}^{\text{tot}} \sim 0.2$, and requiring that axions make up 100% of the dark matter, we get $m_a^{\min} \sim 8 \mu\text{eV}$. Unfortunately, no current astrophysical observation can probe down to such low energies.

4.8 Non white dwarf axions searches and limits

Both particle physicists and astrophysicists are looking for axions, each on their own turf. In this section, I present the efforts led by particle physicists. Those searches put limits on the free parameters $g_{a\gamma\gamma}$ and m_a . They are all sensitive to axions that would be produced in the Primakoff effect, in which a photon produces an axion as it passes in the neighborhood of a nucleus. The axion is detected in the inverse reaction, an axion decaying into a photon (figure 4.5).

4.8.1 Microwave cavity experiments

Microwave cavity experiments are “table top” experiments that look for axions residing in the Milky Way dark matter halo and should be everywhere around us. Axions entering a resonant cavity immersed in a static magnetic field (acting as a catalyst) convert into microwave photons, which we detect.

Microwave cavity searches are very limited in range. As of today, they have excluded a tiny region in the m_a - $g_{a\gamma\gamma}$ plane. The most recent is the Axion Dark Matter Experiment or ADMX (Kinion et al., 2005). The ADMX rules out KFSZ axions between 1.9 and 3.3 μeV . This result is representative of the kind of results those experiments typically yield. Bradley et al. (2003) review microwave cavity experiments done up to that date. First generation microwave cavity experiments (mainly the Rochester-Brookhaven-Fermilab experiment) were able to exclude a small area of the m_a - $g_{a\gamma\gamma}$ plane with m_a between 10 and 20 μeV (figure 4.7).

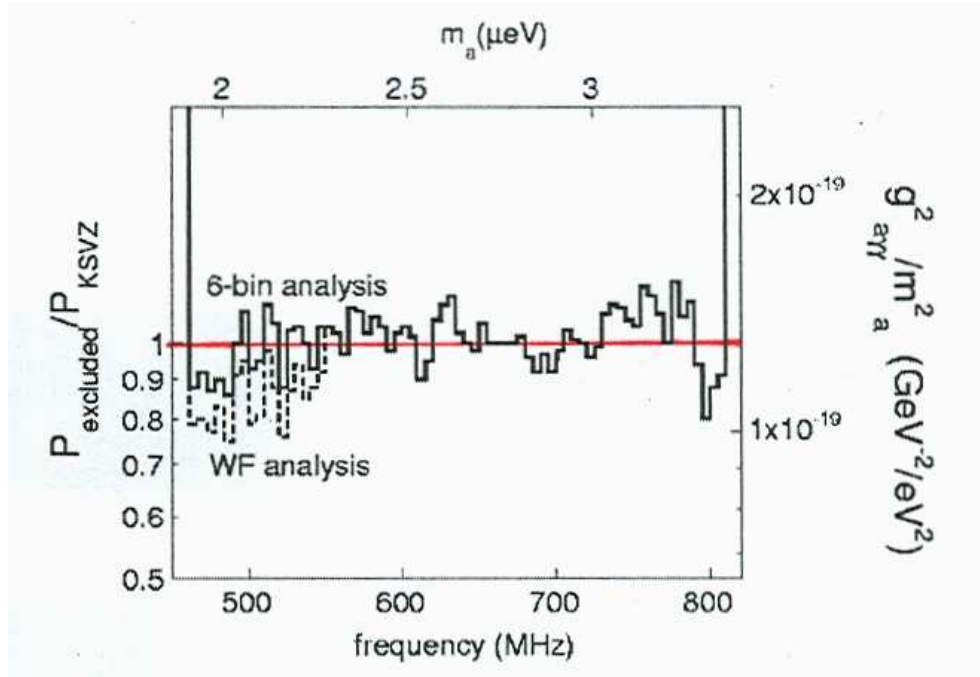


Figure 4.6: Figure 2 from Kinion et al. (2005). The excluded region lies above the curve. The horizontal line (added) shows the relation between $g_{\gamma\gamma}$ and m_a for KSVZ axions (see equation 4.9). Microwave experiments do not place any limits on DFSZ axions.

4.8.2 Solar axions

Searches for solar axions are similar to microwave cavity experiments. They use the reverse Primakoff effect as well, with a static magnetic field as a catalyst. But instead of looking for dark matter halo axions, those searches look for axions produced inside the Sun.

Lazarus et al. (1992) were the first to use such a detector, and were able to place some limits in the m_a - $g_{\gamma\gamma}$ plane. None of them were able to make a dent in the KFSZ axion models. Next came the Tokyo helioscope (Moriyama et al., 1998). This experiment failed in this respect as well (see fig. 4.8). More recently, the CAST experiment at CERN made use of a decommissioned LHC test magnet in its solar axion detector (Eleftheriadis, 2003). The most recent results (CAST Collaboration, 2007) again fall short of the relevant region

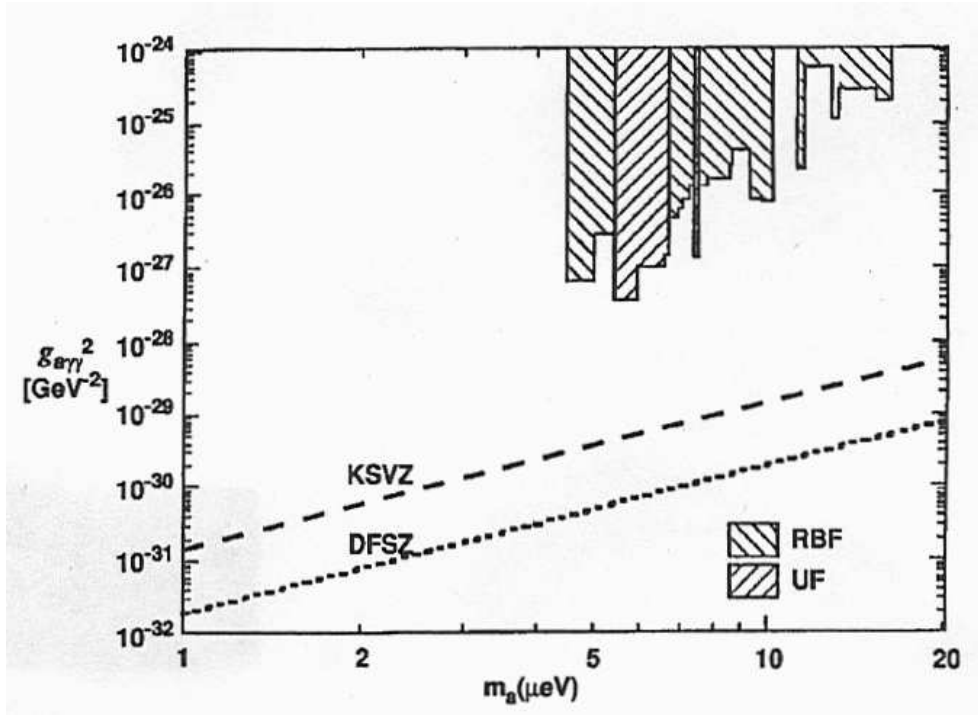


Figure 4.7: Figure 3 from Bradley et al. (2003). Exclusion regions for early microwave cavity experiments (Rochester-Brookhaven-Fermilab and University of Florida).

of parameter space (figure 4.8). The CAST collaboration hopes to improve their sensitivity in the future (Kinion et al., 2005).

The shaded region labeled “Axion models” in figure 4.8 shows the region of the m_a - $g_{aγγ}$ plane consistent with a range of the parameter E/N (equation 4.9). The pictured region should be taken with a grain of salt. It is generously wider than what the most likely values of E/N (~ 1) would give. To be fair, E/N is constrained to be of order 1 or 2 only in theory, and those experiments do make a statement about the maximum value of E/N .

The microwave cavity experiments are fairly solid, but they probe only very narrow ranges of KSVZ axion mass, and the solar axion searches struggle to reach the required sensitivity to test the models. Turner may have been right when he wrote “Does the axion actually exist? I do not know. However, I am very certain that if it does, it will be found in

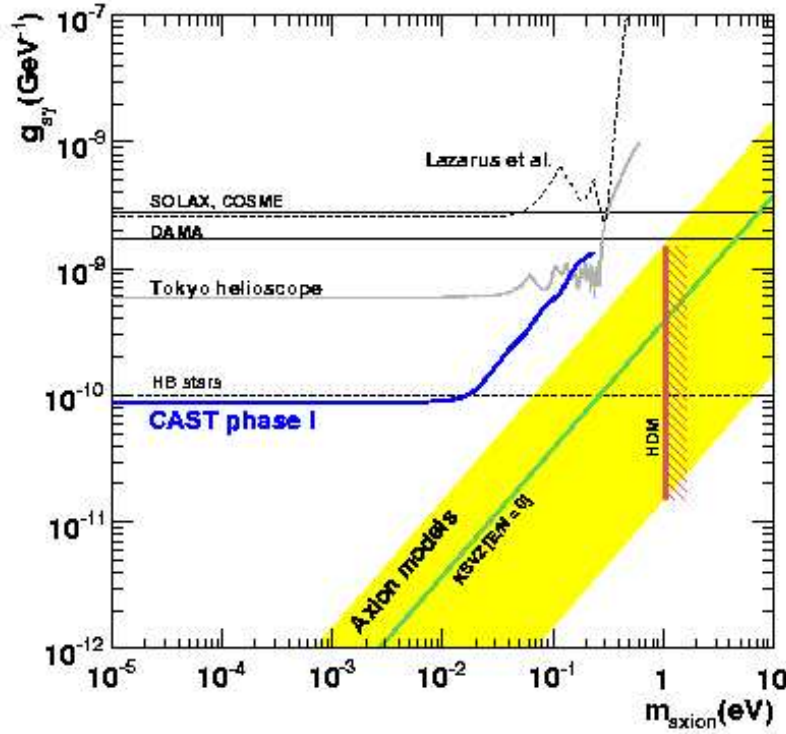


Figure 4.8: The region of parameter space excluded by the CAST experiment. The excluded region lies above the curve labeled “CAST phase I”. The slanted region indicates axion models for which $|E/N - 1.95|$ lies between 0.07 and 7. DFSZ axions ($E/N = 8/3$) lie on a line within that region, below the KSVZ axion model line. None of the solar axion experiments have the required sensitivity to place any limit on those two axion models.

the heavens and not on earth!” (Turner, 1990). The most useful limits so far have been set by astrophysical observations.

4.8.3 “Telescope” searches

One could argue that any astrophysical observation would fall under that category (hence the quotation marks). However, for physicists, telescope searches apply to a very specific observation done with radio telescopes. They look for extra-galactic dark matter halo ax-

ions. Just like the Milky Way dark halo axions which the microwave cavity experiments are attempting to detect, those axions are produced in the Primakoff effect and are expected to decay via the reverse Primakoff effect into nearly monochromatic microwave photons. The result would be narrow emission lines in radio telescope power spectra.

Not very many searches of that kind have been conducted. The first one was done by Bershadsky et al. (1991). They excluded axions between 3 and 8 eV. Ten years later, Blout et al. looked at three Local Group dwarf galaxies Pegasus, Leo I, and LGS 3. They were able to eliminate axion masses between 300 and 365 μeV , for $g_{a\gamma\gamma} > 10^{-9} \text{ GeV}^{-1}$ (figure 4.9).

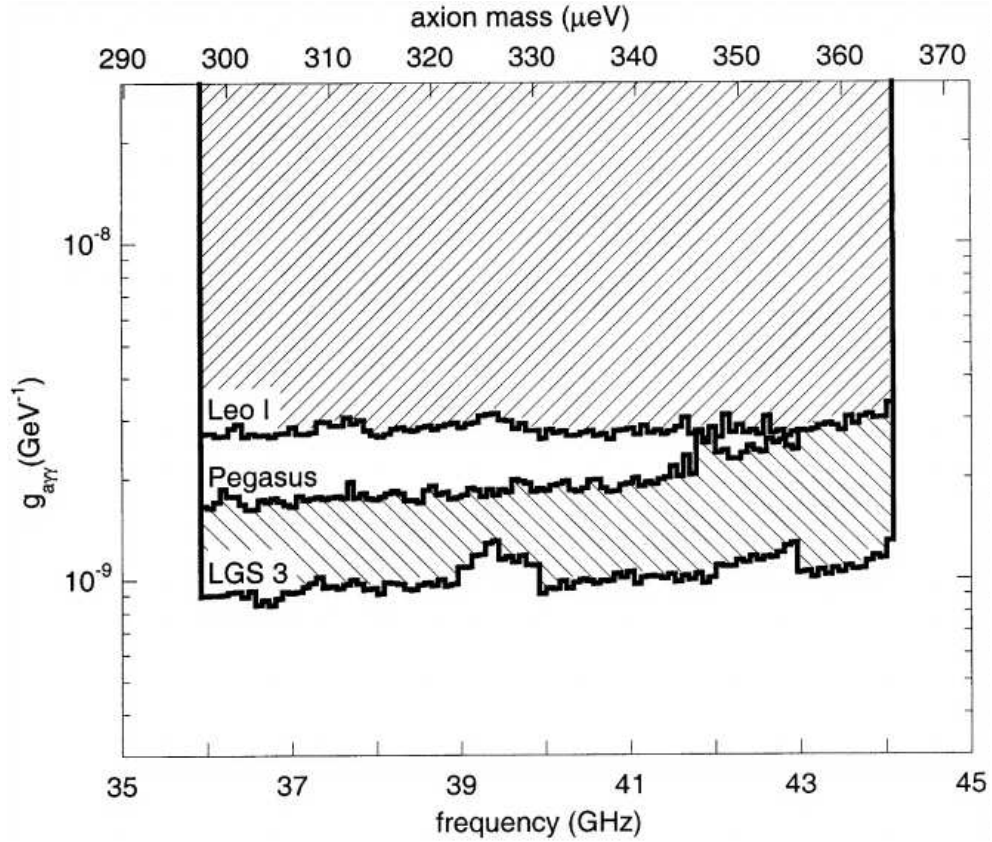


Figure 4.9: Excluded region from telescope search. The telescope searches fails to place any limit on KFSZ or DFSZ axions (for $m_a \sim 300\mu\text{eV}$, $g_{a\gamma\gamma} \sim 10^{-14}$)

4.8.4 Constraints from the Sun's known properties

The rest of the astrophysical constraints on the mass of the axion are all based (directly or indirectly) on the cooling effect axions would have on a heavenly body. Axions interact very little with matter and as a result would stream right out of the core of stars, like neutrinos do, carrying energy away.

If a star like the Sun were losing too much of its energy in the form of axions, it would not be able to remain on the Main Sequence for billions of years like we know the Sun has from radioactive dating of meteorites. Axions, if they were produced, would cool the core efficiently. In response, the core would have to contract. By the virial theorem, half the potential energy gained in the contraction would go into thermal energy and heat up the core. Nuclear reactions rates would increase in response, and raise the luminosity of the Sun, shortening its lifetime.

Frieman et al. (1987) estimated the effect of a non-zero axion luminosity on the Sun's luminosity, radius, central temperature, and Main Sequence lifetime. The main axion production processes in their models was through electron bremsstrahlung and recombination (where instead of photons, axions are produced). In their analytic treatment, Frieman et al. assumed that the Sun, or a star like it, was radiative throughout (an approximation), and that it would contract homologously as a result of the loss of energy from its core. The results are dependent on the initial composition of the Sun (mainly the hydrogen abundance). Since the observed luminosity and radius of the Sun are measured to a high accuracy and can be very well explained by axion-free models, the only room for axions lies in the uncertainties in the initial hydrogen abundance in the core of the Sun.

The total Main Sequence lifetime of the Sun is not a quantity we can measure, but Frieman et al. obtain a conservative limit by requiring that it should be longer than the current (measured) age of the Sun. Combining all the information at hand, they obtain an upper mass limit of ~ 0.3 eV.

4.8.5 Constraints from post Main Sequence evolution

Axion cooling, if present, should have several observable consequences on the post-Main Sequence (post-MS) evolution of stars. Stars leave the MS when they run out of hydrogen to fuse in their core. The now inert core contracts and heats up until it reaches a high enough temperature for the helium to ignite. Models predict that for low mass stars ($M < 2M_{\odot}$), helium ignition takes place under degenerate conditions. A degenerate core being unable to expand in response to an increase in temperature, the ignition is not a peaceful process and happens in what is commonly called the core helium flash.

After helium ignition, stars drop in luminosity and increase in surface temperature and populate the Horizontal Branch (HB) in globular clusters or the Red Giant clump in open clusters. Axion cooling during that stage of evolution, if present, could have two different observational consequences (Raffelt, 1990):

1. Overly efficient cooling during the Red Giant phase could suppress helium ignition until the hydrogen shell burning front reached the surface, at which point the star would leave the Red Giant branch and peacefully become a helium white dwarf. In practice, however, the core of such stars would grow to a higher mass than inferred from the data and the stars would reach very high luminosities we do not observe.
2. Overly efficient cooling during the helium burning phase could reduce the time stars spend on the HB or in the clump and so both observed populations would be reduced.

Constraints from red giants

Dearborn et al. (1986) included axion cooling in a stellar structure code written by Eggleton (1971). In their Red Giant models, axions are mostly produced through Compton scattering at the base of the hydrogen burning shell. Axion emission would cool the outer layers of the helium core and insulate it from conductive heating of the hydrogen burning shell above, slowing down its warming. They find a conservative limit on the DFSZ axion mass

by picking a red giant model that reaches twice the observed maximum luminosity for red giants before its helium core ignites. That limit is $m_a \cos^2 \beta \leq 0.01$ eV.

Raffelt (1986a) includes plasma screening effects in the axion energy loss rates and require that they be less than the helium burning energy generation rate, taken to be 100 erg/g/s. For KFSZ axions, produced through the Primakoff effect, this leads to the limit $m_a \cos^2 \beta < 0.7$ eV. For DFSZ axions, produced mainly through Compton scattering, he finds $m_a \cos^2 \beta < 0.03$ eV, in agreement with Dearborn et al. (1986).

Raffelt & Dearborn (1987) extend axion production rates to degenerate conditions, which are more appropriate deep in the core. They find that electron degeneracy greatly reduces the Primakoff effect emission rates. The rates in the core become low enough that in their models, the axion luminosity never gets large enough to inhibit Helium ignition, unless m_a is unreasonably large (over ~ 10 eV), in conflict with existing bounds on the axion mass known at the time.

Raffelt & Weiss (1995) follow a slightly different approach and derive a constraint by requiring that the model's core mass at the tip of the RGB with axion cooling does not differ too much from what it is inferred to be from observed luminosities. They claim that the core mass is known from observations to within 5% and use that uncertainty to get $m_a \cos^2 \beta < 0.009$ eV, the tightest constraint obtained from stellar evolution. It is, however, heavily dependent on models, as the core mass is not a quantity that can be readily observed.

Constraints from helium burning stars

Raffelt & Dearborn (1987) look at the open cluster M67. Open clusters have young (Pop I, solar metallicity) stars. Their calculations show that for $m_a \sim 0.7$ eV, the number of red giants in the clump is reduced by half. It is reduced by an order of magnitude for $m_a \sim 2$ eV. The latter is a conservative limit on the axion mass.

4.8.6 SN 1987A

SN 1987A surprised and delighted astronomers when it went off in the Large Magellanic Cloud in February 1987. A flow of neutrinos reached the Earth 3 hours before astronomers sighted the exploding star. Of those neutrinos, 19 triggered signals in the Kamiokande II detector and the Irvin-Michigan-Brookhaven nucleon decay detector. The 19 signals occurred all within a 10 second interval (Turner, 1990).

Neutrinos are emitted when the iron core of a massive star collapses and the emission stops when the young neutron star has become so compact that neutrinos can no longer stream out like they usually do (because of the huge opacity). Axions, produced through nucleon-nucleon bremsstrahlung, would accelerate the cooling of the core and contribute to the collapse, cutting short the emission of neutrinos.

The duration of the neutrino pulse from SN 1987A is consistent with standard neutrino emission models. The question then becomes, “how large an axion emission can one hide in the uncertainties of the measurement?” The main difficulty lies in determining the axion rates in a collapsing iron core. This is not an easy task, because the equation of state in those super-nuclear densities is very uncertain.

Early upper bounds of around 1 meV (Turner, 1990; Burrows et al., 1989) were rather optimistic. Theorists later ran into unforeseen additional difficulties in the modeling such as the importance of nuclear mean-field effects in axion production (Turner, 1990), and the limit was relaxed to ~ 10 meV.

Pulsating white dwarfs have the potential to not only bring this limit down, but also to strengthen it, by relying on a solid measurement and much better constrained physics.

4.8.7 Constraints from white dwarfs not based on \dot{P} 's

Raffelt (1986b) made an early attempt to use white dwarf cooling to constrain the axion mass with the data and models available at the time. In that work, Raffelt computes the

following expression for the axion bremsstrahlung emission rate:

$$\varepsilon = 3.30 \times 10^{23} \text{ erg g}^{-1} \alpha \frac{Z^2}{A} T_7^4, \quad (4.19)$$

where $\alpha = g_{ae}^2/4\pi$.

This emission rate is about a factor of 3 larger than the one computed by Nakagawa et al. (1988), which I included in the models I used in the next chapter. Raffelt considers white dwarfs with $10^{-3} L_\odot < L < 1 L_\odot$, a range in which Mestel cooling is a good approximation, according to him. Assuming that axions are the dominant cooling mechanism in that luminosity range, Raffelt derives an expression for the time it takes for a white dwarf to cool from luminosity L_1 down to L_2 :

$$t_2 - t_1 \simeq 1.7 \times 10^7 \text{ yr } \alpha_{26}^{-1} Z^{-2} M^{6/7} \times (L_2^{-6/7} - L_1^{-6/7}), \quad (4.20)$$

where $\alpha_{26} = \alpha/10^{26}$.

Multiplying the above by the white dwarf birth rate yields the number of white dwarfs one would expect to see between L_1 and L_2 . Using a constant white dwarf birth rate of $2 \times 10^{-12} \text{ yr}^{-1} \text{ pc}^{-3}$, Raffelt finds

$$N_{\text{pred}} \simeq 6.1 \times 10^{-4} \alpha_{26}^{-1} (L_2^{-6/7} - L_1^{-6/7}). \quad (4.21)$$

He then derives a number density from pure carbon, $0.6 M_\odot$ white dwarf models, including axion cooling, with the axion mass as a free parameter. Requiring that axions do not have an observable effect on N , Raffelt finds a conservative axion mass upper limit of 30 meV.

4.9 Summary

There is a continuum of axion models, depending upon the PQ charges X of the u and d quark and the electron we adopt. Two simple axion models include the KVSZ model where axions do not couple to electrons and the DFSZ model, where axions couple to the u , d quarks and the electron in about the same amount. Because KVSZ axions do not couple to electrons, they can only be produced through the Primakoff effect, where a photon passing in the neighborhood of a nucleus produces an axion. DFSZ axions can also be produced in processes that involve electrons, such as Compton scattering.

There are three cosmological models for the formation of axions (so far). Under the right conditions, the inflationary model can accommodate any mass axion and is therefore impossible to disprove by placing constraints on the axion mass. For axions to account for all of dark matter, the axion string model requires axions that are at least $8 \mu\text{eV}$ in mass. Axions that were in thermal equilibrium in the early universe would contribute very little to the axion relic density and could account for all of dark matter only if they were at least 11 eV . Such massive axions would have been found by now. I summarize those limits in the top panel of figure 4.10.

In this chapter, I presented a number of searches that each place their own constraint on the axion mass. The axion mass limits are determined by studying the three main interactions of axions with matter and light: the coupling with photons ($g_{a\gamma\gamma}$), with electrons (g_{ae}), and with nucleons (g_{ann} and/or g_{app}). $g_{a\gamma\gamma}$ is related to the axion mass by equation 4.9. Its relation with m_a depends on the axion model one adopts and some of the searches I presented place constraints on axions in the $g_{a\gamma\gamma} - m_a$ plane. I summarize those searches in the main panel of figure 4.10.

Most experiments that use the axion-photon interaction to place limits on axion properties lack the required sensitivity to constrain the KFSZ or DFSZ model. The Axion Dark Matter Experiment (ADMX) barely rules out KFSZ axions ranging in mass between $1.9 \mu\text{eV}$ and $3.3 \mu\text{eV}$. The most stringent upper limit on the axion mass found using axion-

photon interactions comes from the observation of Horizontal Branch stars by Raffelt & Dearborn (1987). For KFSZ axions, Raffelt & Dearborn find $m_a \leq 0.3$ eV and for DFSZ axions, $m_a \leq 0.8$ eV.

The best limit on the mass of DFSZ axions found using axion-electron interactions by searches presented in this chapter is $m_a \leq 9$ meV (Raffelt & Weiss, 1995). SN1987A helped place an upper limit of 10 meV on the axion mass, independently of the axion model chosen (using axion-nucleon interactions). In the next chapter, I attempt to improve those limits, if not by lowering them, at least by strengthening them greatly. In order to be able to rule out the axion string cosmological model, however, one would have to constrain the axion mass to less than $8 \mu\text{eV}$. No search can come near that limit today, but we can at least constrain the parameters of the cosmological models. On the other hand, we should soon be able to tell whether DFSZ axions can be responsible for dark energy.

Axion-photon coupling constraints

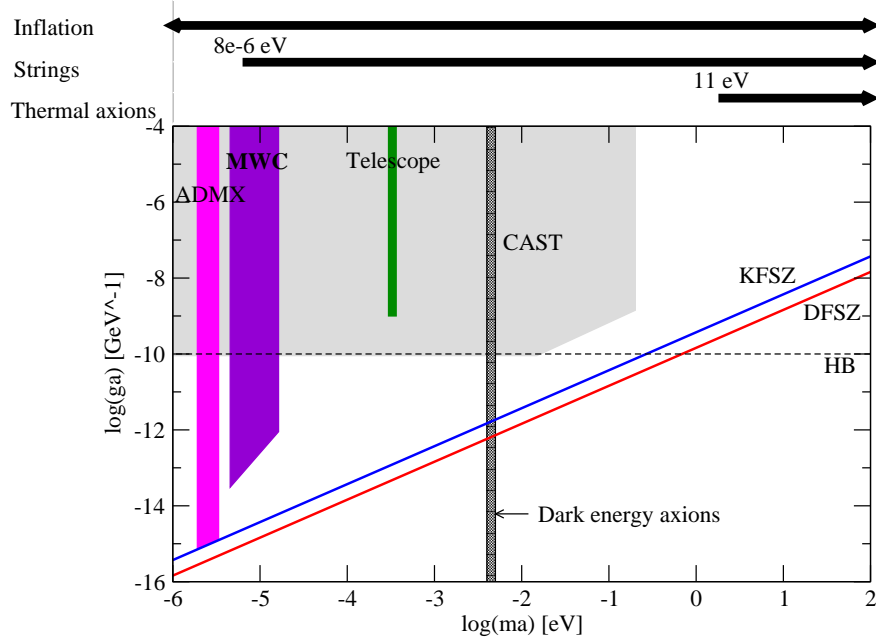


Figure 4.10: A summary of the allowed axion mass range according to the three cosmological models presented in this chapter (top part of the figure) along with the limits set in the $g_{a\gamma} - m_a$ plane by a variety of searches, also presented in this chapter. The shaded regions are exclusion regions. “ADMX” stands for the Axion Dark Matter Experiment and “MWC” for older microwave cavity experiments (see figure 4.7). “Telescope” refers to the most recent telescope search (figure 4.9). The two slanted lines mark the location in this parameter space of the KFSZ and DFSZ axion models (see equation 4.9). The horizontal dashed line labeled “HB” corresponds to the limit found by Raffelt & Dearborn (1987) using observations of Horizontal Branch stars. The dark, narrow vertical region is the allowed mass range for axions to account for dark energy (de Vega & Sanchez, 2007).

Chapter 5

Axion limits from G117-B15A and R548

“The invisible axion must not be too visible.”

Preskill et al. (1983)

5.1 Introduction

Axions, like neutrinos, would accelerate the cooling of white dwarfs, and therefore have an effect on the observed pulsation periods. As a white dwarf cools, its interior becomes more degenerate. As we saw in section 2.3, this leads to an increase in the pulsation periods observed. The faster the star cools, the faster the periods increase. We can make a prediction of how fast the star should be cooling through known sources, e.g. photons (Mestel, 1952) and neutrinos (Itoh et al., 1996a). A higher \dot{P} than expected means that the star is cooling faster than expected, and indicates an extra source of energy loss. \dot{P} provides therefore a measure of the axion emission rate, which in turns depends on the axion mass (see equations 4.8, 5.1).

We determine an upper limit on axion mass by asking the question, “What is the

maximum mass axions can have and not have an observable effect (within uncertainties) on the measured periods?” The strength of that limit depends therefore on the uncertainties involved in the measurement of the \dot{P} and in the modeling.

Observations of a pulsating white dwarf yield its luminosity, mass, effective temperature, and \dot{P} ’s for one or more modes of the star. We then model the star for the given mass and effective temperature, including all the physics we know and the physics we want to test, such as axion emission rates. For our model, we calculate the period spectrum and \dot{P} ’s for each mode. When we include non-zero mass axions, we find $\dot{P}_{\text{model}} > \dot{P}_{\text{observed}}$. We then determine how high we can increase the axion mass (m_a) before \dot{P}_{model} becomes greater than $\dot{P}_{\text{observed}} + \Delta\dot{P}$, where $\Delta\dot{P}$ includes not only the uncertainties in the measurement of \dot{P} , but also other uncertainties, such as those discussed in sections 3.2 and 3.3.

The hunt for axions gives us one reason to conduct a rigorous asteroseismological analysis of G117-B15A, which has a very well determined \dot{P} , and R548, for which we expect an equally well determined \dot{P} in the near future. Studying them in parallel also allows us to make the best of a small number of observed periods. As part of the analysis, I built a fine grid of models that covers the relevant part of parameter space, giving us for the first time a comprehensive view of the shape of the function we wish to minimize (the difference between observed and calculated periods).

5.2 The stars

G117-B15A and R548 have much in common and as we shall see, studying them side by side helps constrain the model parameters. In table 5.1 I list the spectroscopically determined effective temperatures and mass of both stars, along with the modes we observe in those stars (Mukadam, 2004). Those are the clues we have at our disposal to find best fit models to G117-B15A and R548.

By comparing the amplitude of G117-B15A’s pulsations in the ultra violet to those in the visible, Robinson et al. (1995) were able to determine confidently that they were

Table 5.1: Observed properties of G117-B15A and R548

	G117-B15A	R548
T_{eff}	11630 ± 200 (2) 12250 ± 125 (3) 12375 ± 125 (5)	11990 ± 200 (2) 11865 ± 170 (4)
$\log g$ mass [M/M_{\odot}]	7.92 ± 0.05 (1) 0.579 ± 0.074 7.97 ± 0.05 (2) 0.59 ± 0.03 (thick H layer) 0.55 ± 0.03 (thin H layer) 7.94 ± 0.17 (4) 0.57	7.97 ± 0.05 (2) 7.89 ± 0.05 (4) 0.55
Periods [s]) (Amplitudes [mma])	215.22 (19.8) 270.86 (7.1) 304.15 (8.8)	212.77 (4.1), 213.13 (6.7) 274.25 (4.1), 274.78 (2.9) 187.27 (1.0) 318.08 (0.9) 333.65 (1.0)

(1) Bergeron et al. (1995b). (2) Bergeron et al. (1995a). (3) Koester et al. (1994). (4) Koester & Holberg (2001). (5) Robinson et al. (1995)

$\ell = 1$ modes. R548's higher amplitude modes are close to the 215s and 271s modes in G117-B15A and are very likely $\ell = 1$ modes as well.

5.3 Axion production in White Dwarfs

We would expect axions in White Dwarfs to be produced through electron bremsstrahlung, where an electron radiates an axion instead of a photon (figure 5.1). Nakagawa et

al. (1988) fit the axion emission rate resulting from Bremsstrahlung in dense interiors with

$$\epsilon_a = 1.08 \times 10^{23} \text{ ergs g}^{-1} \alpha \frac{Z^2}{A} T_7^4 F(T, \rho), \quad (5.1)$$

where $\alpha = \frac{g_{ae}^2}{4\pi}$ and g_{ae} is given by equation 7. $F(T, \rho)$ is a numerical fit, of order 1 throughout most of the interior of a typical white dwarf model (see figure 5.2). This is the fit I included in the White Dwarf Evolution code to determine an upper mass limit for the axion in section 5.7. I detail the changes made to the code to include axions in appendix A.

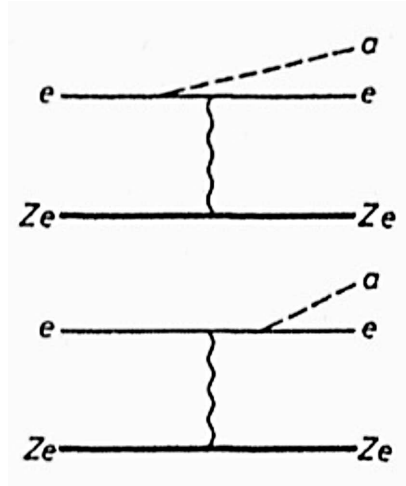


Figure 5.1: Feynman diagram of the production of axions through electron-ion bremsstrahlung (figure 2.a in Raffelt, 1986a)

5.4 Review of work done on the subject

Isern et al. (1992) first used G117-B15A's \dot{P} to obtain a limit on the axion mass. At the time, the \dot{P} measured ($12.0 \pm 3.5 \times 10^{-15}$ s/s, Kepler et al., 1991b) for that star was uncertain, and much higher than the one expected from simple Mestel cooling. Using models available at the time (Wood, 1990; D'Antona & Mazzitelli, 1989) and a simple semi-analytical treatment, Isern et al. found an average axion mass of 8 meV. Individual values, depending upon

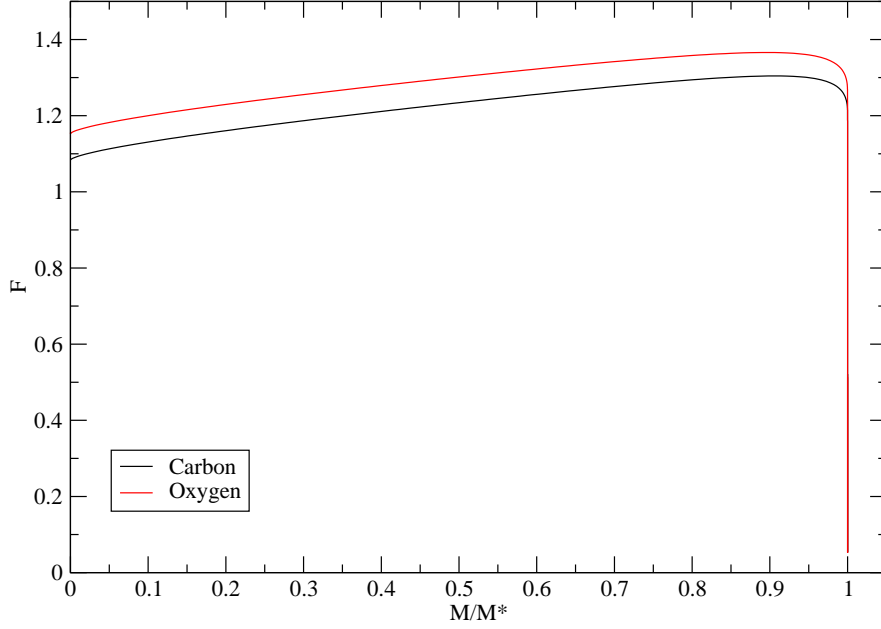


Figure 5.2: Value the quantity $F(\rho, T)$ in equation 5.1 takes on in the interior of a typical DAV white dwarf model ($0.6 M_{\odot}$, 11000K).

the model chosen and value of observed \dot{P} considered ($\dot{P} - \Delta\dot{P}$, \dot{P} , and $\dot{P} + \Delta\dot{P}$) allowed a range between 0 meV and 20 meV for the axion mass.

Córsico et al. (2001) revisited the problem with a new value of \dot{P} , that had come down to what was expected from simple Mestel cooling: $(2.3 \pm 1.4) \times 10^{-15} \text{s/s}$ (Kepler et al., 2000). In their work, Córsico et al. performed an asteroseismological study of G117-B15A to find its mass, helium layer mass, and hydrogen layer mass. To reduce the number of parameters to fit, they fixed the internal composition to that found from stellar evolution by Salaris et al. (1997), and the effective temperature to the latest spectroscopic estimate at the time, 11,620 K (Bergeron et al., 1995a). Their best fit model had a mass of $0.55 M_{\odot}$

and a helium layer mass $M_{He} = 10^{-2}$.

Córsico et al. (2001) considered only small uncertainties in effective temperature (200 K) and found that they led to a 4% uncertainty in the calculated \dot{P} 's. They also considered larger uncertainties in mass and central oxygen abundance and found that those had less of an effect on the model's \dot{P} 's than the effective temperature. A mass uncertainty of $.02 M_{\odot}$ (3%) led to a 6% uncertainty in \dot{P} 's. And considering a full range of core composition (0% carbon to pure carbon) changed the \dot{P} 's only by 5%. They concluded that uncertainties other than the one in the measured \dot{P} were insignificant and could be ignored altogether. This gave a fairly tight constraint on the axion mass: 4 meV.

There are problems with Córsico et al. (2001)'s analysis. First of all, their fit to G117-B15A is not very good. On the average, their model's periods differ from the observed periods by 4.3 seconds. With only three observed periods, it is possible to obtain a fit whose periods are less than one second away from the observed periods (e.g. Bradley 1998 and section 5.6 of present work). It is likely that the effective temperature they chose was not very good for their models. The same authors revisited their fit to G117-B15A a year later (Benvenuto et al., 2002). This time they performed a full 4 parameter asteroseismological analysis. They were not able to improve the quality of their fit.

We also now have a new value of \dot{P} to fit, $3.57 \pm 0.82 \times 10^{-15} \text{s/s}$ (Kepler et al., 2005c), with a smaller error, which could help constrain the axion mass better. On the other hand, we also want to include the relevant uncertainties in our analysis.

5.5 The observables: periods, temperature and mass

The most solid observables listed in table 5.1 are the periods. For both G117-B15A and R548, periods are determined to better than a second. The 215s mode in G117-B15A and the 213s in R548 are extremely stable and determined to extremely high accuracy. For both stars, we can not only list the value of those periods with confidence, but also measure how fast they are changing with time. In the asteroseismological fits detailed in section 5.6, I use

the periods rounded to the second, and do not distinguish a model period that fit within 0.5 seconds from one that fits within 1 second. The reason for doing so is not the observational uncertainties, but the theoretical uncertainties discussed in section 3.3.

Effective temperature is a much more poorly determined quantity. For G117-B15A, there are three recent (nearly) independent studies that derive its effective temperature from spectra. Bergeron et al. (1995a) analyze high signal to noise optical spectra obtained in the Palomar-Green survey and find a temperature of 11630 ± 200 K. Koester et al. (1994) analyze a UV spectrum of G117-B15 taken with the Faint Object Spectrograph on the Hubble Space Telescope. Using different atmospheric models than Bergeron et al., they derive a temperature of 12250 ± 125 K. Robinson et al. (1995) used multichannel high speed photometry, in two UV bands from the HST and in the U,B,V, and R band from the 2.1 m telescope at McDonald observatory. Assuming a $\log g$ of 7.97 from Bergeron et al., they find an effective temperature of 12375 ± 125 K, consistent with Koester et al. (1994), but not with Bergeron et al. (1995a). For R548, Bergeron et al. (1995a) derive a temperature of 11990 ± 200 K. Koester & Holberg (2001), using HST UV data with visual magnitude constraints and their own atmospheric models derive $T_{\text{eff}} = 11865 \pm 170$ K.

Bergeron et al. (1995b) examined the effect of gravitational redshift on the Balmer lines in G117-B15A's spectrum and derived a mass of $0.579 \pm 0.074 M_{\odot}$, using published values of velocities based on evolutionary models of Wood (1990), the ancestors of the models I used in my analysis. Wood's models stand behind all the mass determinations from $\log g$'s in table 5.1. From their spectroscopically determined $\log g$, Bergeron et al. (1995a) find a mass of $0.59 \pm 0.03 M_{\odot}$ for models with $\log(M_{\text{H}}) = -4$ and 0.55 ± 0.03 for models with negligible hydrogen layer masses ($\sim 10^{-10}$ and thinner). Koester & Holberg (2001) derive a mass of $0.57 M_{\odot}$, based on their own determination of $\log g$ (7.94 ± 0.17) and on absolute V magnitudes derived in Bergeron et al. (1995a). The latter find that R548 is indistinguishable in mass from G117-B15A. Koester & Holberg (2001) find that it is slightly less massive ($0.55 M_{\odot}$).

Because the mass determinations depend on models very similar to the ones I am using in my analysis, it would be circular to rely too heavily on those mass determinations for G117-B15A and R548. From spectroscopy, all we can really say is that G117-B15A and R548 have average gravities, so we would expect their masses to be around the average, $0.60 M_{\odot}$.

5.6 Four-parameter fit to G117-B15A and R548

I performed a four-parameter search for best fit models to G117-B15A and R548. The 4 parameters are: effective temperature, stellar mass, the location of the transition from pure carbon to pure helium (M_{He}), and the location of the transition from pure helium to pure hydrogen (M_{H}). I fixed the core carbon and oxygen abundance profiles to those calculated from stellar evolution by Salaris et al. (1997) (figure 5.3).

5.6.1 Broad search on a not so fine grid

I started with a search of all the reasonable parameter space for DAVs. While computers have grown more powerful, time is not a commodity to be wasted, so I limited the resolution of this large grid. In table 5.2 I list the region of parameter space covered by the grid (including the grid spacing). I ran a total of 19635 models, 14382 of which were successful. I obtained a uniform coverage of the parameter space considered. I did not extend the grid to thinner helium layers for two reasons. First, stellar evolution calculations and previous asteroseismological calculations (see Bradley 1998 and Benvenuto et al. 2002 for instance) all point to thicker helium layers ($\log(M_{\text{He}}) \sim -2$). A more pragmatic reason was that models with thinner helium layers had trouble converging.

For each model, the code computed a period spectrum and wrote it out to a file. The period spectra included $\ell = 1$ and $\ell = 2$ modes, and the periods ranged between 50 and 1500 seconds. Once I had a large file containing period lists for each model of the grid, I could compare it to any set of observed periods. This turned out not to be as trivial as it

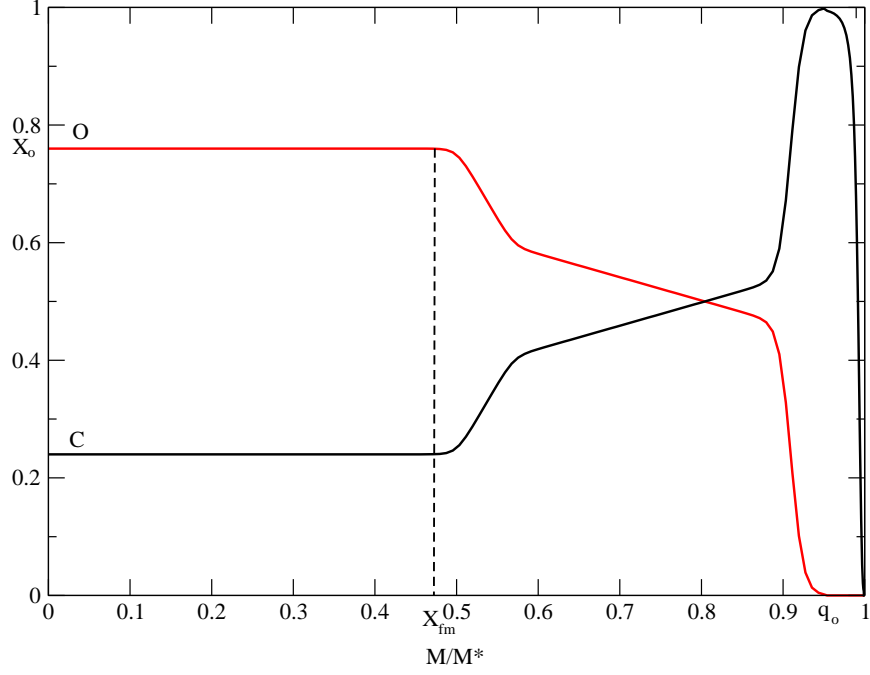


Figure 5.3: Core composition profiles for the models in the four-parameter grid.

Table 5.2: Region of parameter space covered in the broad four-parameter fit and step sizes.

Parameter	Range (inclusive)	Step size
T_{eff}	10800K to 13000K	200K
M_*	$0.46 M_{\odot}$ to $0.80 M_{\odot}$	$0.02 M_{\odot}$
$-\log(M_{He})$	2.0 to 2.8	0.02
$-\log(M_h)$	$[-\log(M_{He}) + 2.0]$ to 8.4	0.02

sounds. I had to make sure my routine paired up the periods in a way that minimized Φ (see equation 3.1) for that particular model, without reusing the same model period for two

different observed periods. I list and discuss the relevant routine in appendix D. I had my fitting routines compute A in equation 3.1 by finding the largest number of periods listed for any single model in the table (n_{\max}). For any model in the table, A was set equal to n/n_{\max} so that models with more periods listed were penalized.

5.6.2 Constraints from mode identification

For G117-B15A, I further narrowed down the list of possible best fits by limiting the list of candidates to those that fit the observed periods successfully with $\ell = 1$ modes, consistent with mode identification work done by Robinson et al. (1995). For R548, I required that the two high amplitude modes, which also seem to be present in G117-B15A (see table 5.1), be $\ell = 1$ modes. I did not place any constraints on the identification of the other three modes. I display the results for G117-B15A and R548 side by side in the $T_{\text{eff}} - M_{\star}$ plane in figure 5.4; and in the $\log(M_{\text{H}}) - \log(M_{\text{He}})$ plane in figure 5.5. In figure 5.4, I also indicated the spectroscopic mass and temperature determinations for both stars.

In section 3.3, we gained a feel for how a number of modeling uncertainties influenced the calculated periods. From table 3.1, we learn that if we set our significance limit to $\langle \Delta P \rangle = 1\text{s}$, we do not need to worry about a large number of modeling uncertainties.

I also ran two simple tests to determine the effect of pure numerical noise on the asteroseismological fits. In the first test, I introduced random noise in the calculated periods (1s at most) and looked for the models that satisfied $\langle \Delta P \rangle < 1\text{s}$. In a more radical, second test, I introduced a systematic shift of +1 second in the calculated periods and repeated the exercise.. I found with some relief that the results of my broad grid asteroseismological analysis did not change significantly.

From their observed properties (table 5.1), we expected G117-B15A and R548 to be best fit by similar models. We do see that in our results. It also comes as no surprise that the $\ell = 1$ identification requirement does not limit model fits to R548 as much as they do for G117-B15A. To obtain the dotted circles in figures 5.4, I discarded fits that did not obey

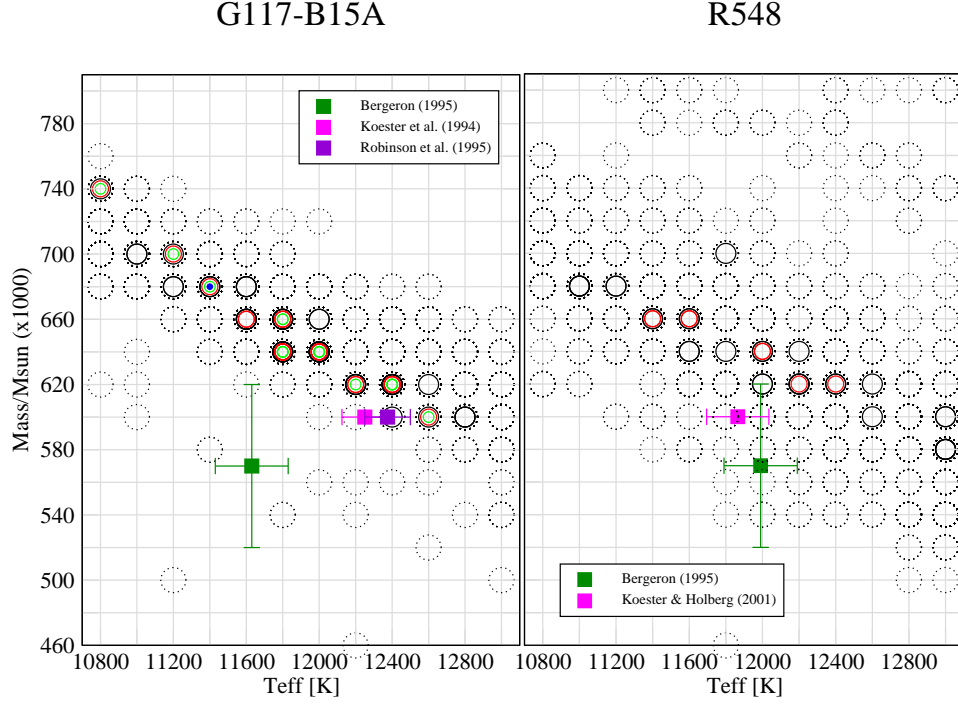


Figure 5.4: The valley of best fit models (4 parameters) for G117-B15A and R548 in the $M_* - T_{\text{eff}}$ plane. The dashed circles mark the location of the subset of models that fit the $\ell = 1$ mode identification criterion (see text). Of those, the progressively filled-in circles indicate better and better fits ($\Phi < 2.5\text{s}, 2\text{s}, 1.5\text{s}, 1\text{s}$ respectively). For G117-B15A, the one model that fits to better than 1 second is not significantly better than the next model down the list. The colored squares indicate the spectroscopically determined temperatures and mass for G117-B15A and R548, according to the legend. Koester et al. 1994 and Robinson et al. 1995 do not quote a mass, but both find an average $\log g$ for G117-B15A so I placed their values at the average white dwarf mass ($0.6 M_{\odot}$).

the $\ell = 1$ mode identification for G117-B15A's 3 modes and for R548's 2 high amplitude modes. Because this first cut is based on a constraint on a fewer number of modes in the case of R548, it does not eliminate as many models. On the other hand, we have 3 additional modes to fit and they allow us to narrow down the best fit models to a small region of

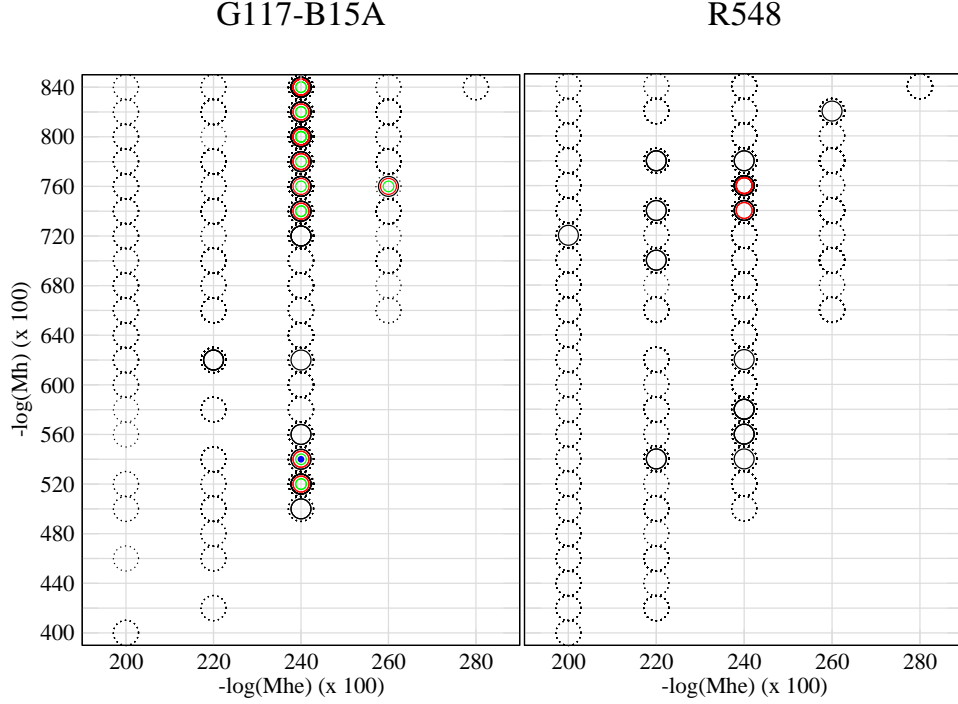


Figure 5.5: The valley of best fit models (4 parameters) for G117-B15A and R548 in the $\log(M_H) - \log(M_{He})$ plane. Like in figure 5.4, the dashed circles mark the location of the subset of models that fit the $\ell = 1$ mode identification criterion (see text) and the progressively filled-in circles indicate better and better fits.

parameter space. We do not have that luxury with G117-B15A, as the 3 $\ell = 1$ modes is all we have. We also obtain better fits to G117-B15A's 3 periods than we do to R548's 5 periods, as it should be.

For G117-B15A, the thickness of the helium layer is entirely determined by the 215s mode. If we do not include that mode in the fit, M_{He} is unconstrained. If we change it by as little as 5 seconds (e.g. 215s to 210s), the helium layer mass changes from $10^{-2.4}$ to $10^{-2.3}$. This is a very interesting result that we can explore further with the semi-analytic formalism developed by Montgomery et al. (2003), based on an analogy with a non-uniform

vibrating string.

Unfortunately, we are unable to determine a unique point in parameter space that matches G117-B15A and/or R548. Instead, we find families of solutions. There is a tight correlation between the mass and the effective temperature, anticipated from earlier work (Bradley, 1998). Decreasing either the temperature or the mass decreases the spatial average of the Brunt-Väisälä frequency in a similar way, and therefore yields similar sets of periods. The helium layer mass seems to be fairly well constrained to be around $10^{-2.4}$.

The effective temperature of R548 appears to be constrained in a range between 11400 and 12400 K, in the hotter half of the DAV instability strip. G117-B15A's effective temperature is even less well constrained. Assuming that G117-B15A is similar to R548, we can discard the best fit model (it is indeed only one model) at 10800 K and adopt a comparable range of effective temperatures and masses as for R548 for a more detailed grid search.

5.6.3 Zooming in - A finer, narrower grid

Next I refined my solution for G117-B15A and R548 by focusing on the region of parameter space detailed in table 5.3. The new grid is 5757 models strong.

Table 5.3: Region of parameter space covered in the narrowed four-parameter fit and step sizes.

Parameter	Range (inclusive)	Step size
T_{eff}	11400K to 12600K	100K
M_*	$0.60 M_{\odot}$ to $0.70 M_{\odot}$	$0.01 M_{\odot}$
$-\log(M_{\text{He}})$	2.3-2.5	0.1
$-\log(M_{\text{h}})$	$[-\log(M_{\text{He}}) + 2.0]$ to 8.0	0.2

I present the results in figures 5.6 and 5.7. The solutions in the $M_* - T_{\text{eff}}$ plane separate out by hydrogen layer masses (figure 5.8). For G117-B15A, the thin hydrogen so-

G117-B15A

R548

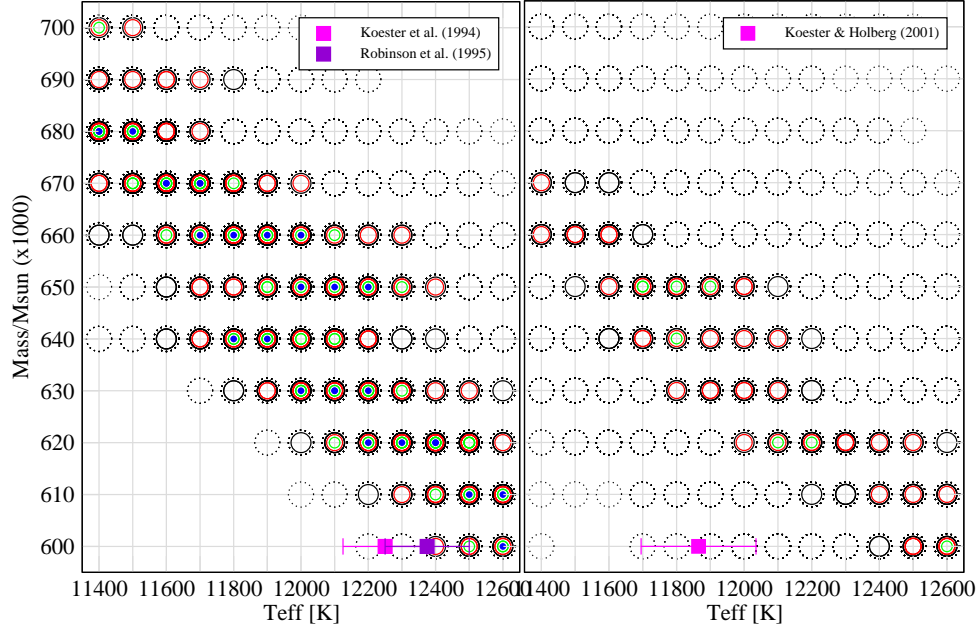


Figure 5.6: Same as figure 5.4 for the finer grid.

lutions ($-\log(M_H) > 6.4$) match the spectroscopy better. R548 has only one thick hydrogen solution at a rather high effective temperature.

Previous asteroseismological studies of G117-B15A (Bradley, 1998; Benvenuto et al., 2002) identified the three modes as consecutive $\ell = 1$ modes, with the 215s mode being either a $k = 1$ or a $k = 2$ mode. Bradley found equally good fits with either mode identification. While Benvenuto et al.'s best fit model was consistent with a $k = 1,2,3$ mode identification, they also found good fit models with $k = 2,3,4$ modes. Among the 27 models in the fine grid that matched the observed periods to better than 1 second on the average, 13 matched the observed periods with $k = 1,2,3$ modes and 14 with $k = 2,3,4$ modes. The former family of models all have ($-\log(M_H) > 6.4$) and the latter ($-\log(M_H) < 6.4$).

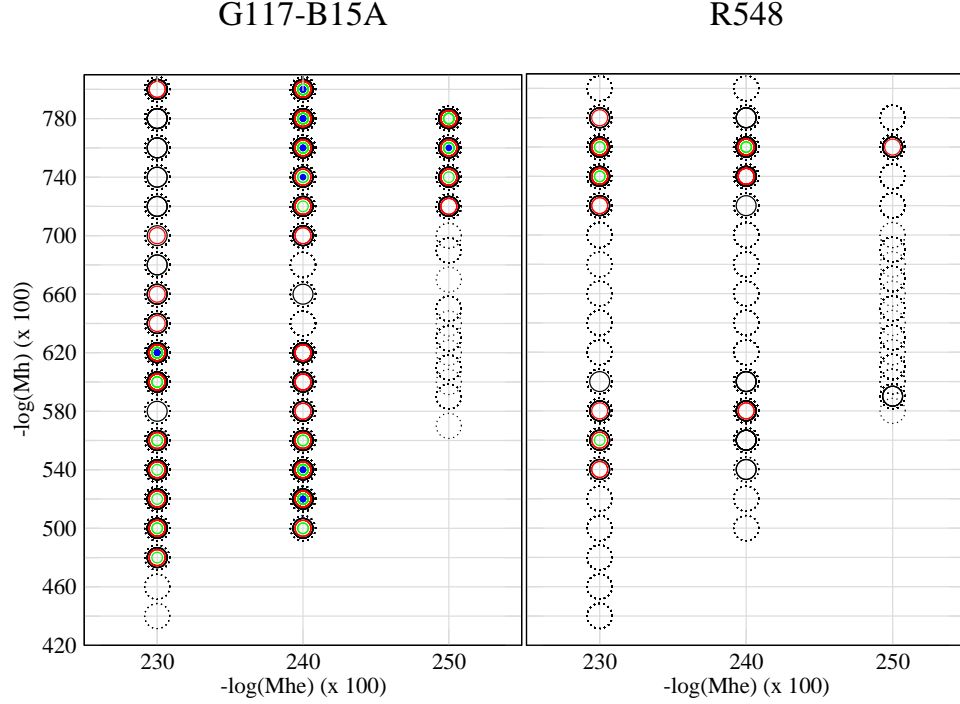


Figure 5.7: Same as figure 5.5 for the finer grid.

For R548, Bradley (1998) determined from its rotational splitting that the 213s mode was more likely to be a $k = 2$ mode ($\ell = 1$). Among the top 20 best fit models in the present study, I find that the most likely mode identification (17 out of 20 models) is $\ell = 1, k = 1, 2, 4$ respectively for the 213s, 274.5, and 318s modes and $\ell = 2, k = 4$ and 8 for the 187s and 334s modes. Recall that we required the 213s and 274.5s modes to be $\ell = 1$ modes, but did not place any constraints on the other modes. The $\ell = 2, k = 4$ identification for the 187s mode is very robust (20/20). Two out of the three models which disagree with this mode identification are thick hydrogen models (while the 17 models with the most common mode identification are thin hydrogen models).

The main reason we are studying G117-B15A and R548 side by side is that they

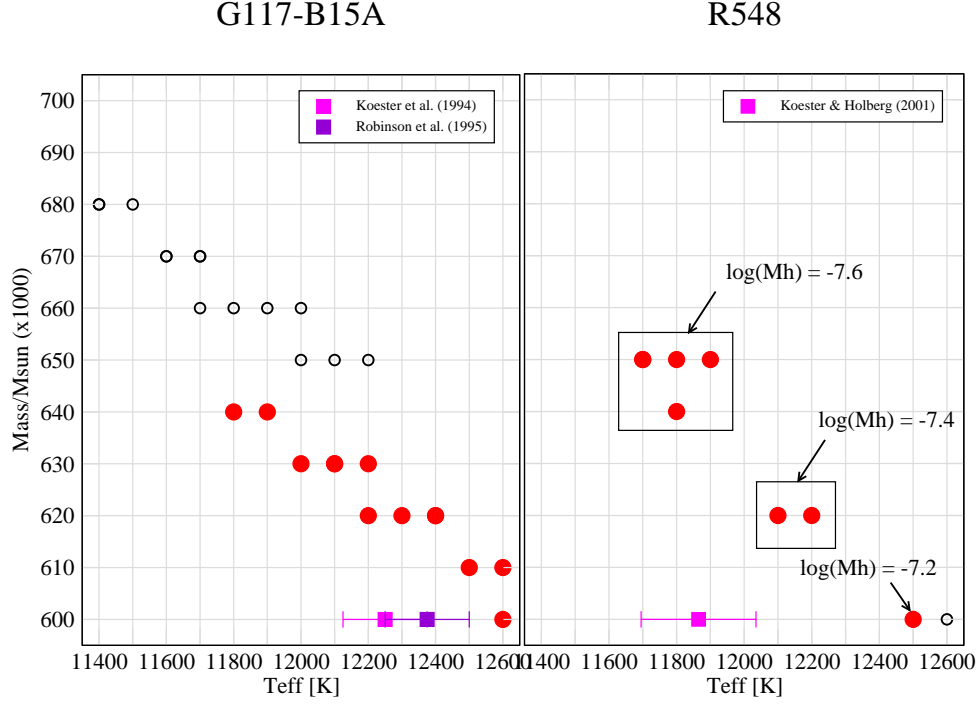


Figure 5.8: Best fit models in the $M_* - T_{\text{eff}}$ plane for different layer masses. For G117-B15A, I isolated the solutions for which $\Phi < 1\text{s}$ and for R548, those for which $\Phi < 1.5\text{s}$. The open circles correspond to thick hydrogen solutions ($-\log(M_H) < 6.4$), while the filled circles correspond to thin hydrogen solutions ($-\log(M_H) > 6.4$).

are observationally similar and we therefore expect them to also be structurally similar. If that is the case, then the mode identification results for R548 suggest that the correct mode identification for G117-B15A is $k = 1, 2$ and 3, in favor of the thin hydrogen layer solutions ($-\log(M_H) > 6.4$).

5.6.4 Summary of the results

While we have not been able to find a single best fit model for G117-B15A or R548, we have achieved what we set out to do. We have constrained the solutions to narrow regions

of parameter space and we can assess the uncertainties in effective temperature, mass, helium layer mass and hydrogen layer mass. I compile the constraints we have on those 4 parameters for both stars in table 5.4. The values indicated are inclusive. I present a view of the 5 families of solutions listed in table 5.4 in figure 5.8.

Table 5.4: Regions of the 4 parameter space occupied by the best fit models for G117-B15A and R548 and mode identification.

G117-B15A			
	Family 1 Thick H layer	Family 2 Medium H layer	Family 3 Thin H layer
T_{eff} [K] M_*/M_{\odot}	11300 to 12300 $a = 4.04075 \times 10^{-5}$ $b = 1.1441$		11700 to 12700 $a = 4.36769 \times 10^{-5}$ $b = 1.1576$
$-\log(M_{\text{He}})$ $-\log(M_{\text{h}})$	2.35 to 2.45 5.10 to 5.50	2.25 to 2.35 6.10 to 6.30	2.35 to 2.55 7.20 to 8.10
Mode identification $P[s](\ell, k)$	215(1,2), 271(1,3), 304(1,4)		215(1,1), 271(1,2), 304(1,3)

R548			
	Family 1 $\log(M_{\text{H}}) = -7.6$	Family 2 $\log(M_{\text{H}}) = -7.4$	Family 3 $\log(M_{\text{H}}) = -7.2$
T_{eff} [K] M_*/M_{\odot} $-\log(M_{\text{He}})$ $-\log(M_{\text{h}})$	12400 to 12600 0.590 to 0.610 2.25 to 2.35 7.15 to 7.25	12000 to 12300 0.610 to 0.630 2.25 to 2.35 7.35 to 7.45	11600 to 12000 0.635 to 0.655 2.25 to 2.45 7.50 to 7.70
Mode identification $P[s](\ell, k)$	213(1,1), 274.5(1,2), 318(1,4) 187(2,4), 334(2,8)		

To obtain the constraints listed in table 5.4, I trusted that G117-B15A and R548 could not be much hotter than 12600 K (consistent with the broad grid search and spec-

troscopy). To get the relation between the stellar mass and the effective temperature for G117-B15A, I simply did a linear fit to the points corresponding to the chosen hydrogen layer thicknesses. Judging from figure 5.8, the vertical scatter about the $M_* - T_{\text{eff}}$ relation is roughly $0.02 M_{\odot}$.

Now that we have identified the most likely parameters for G117-B15A and R548's models, we are ready to calculate \dot{P} 's for those models. But first, let us wander off the grid and explore the shape of Φ in parameter space.

5.6.5 Breaking free from grid points - Simplex search

While the grids seem to be reasonably resolved, I implemented a way to zero in on a solution, without being tied to grid points. I tested the method on the fit to G117-B15A. Having identified the regions of parameter space likely to contain the solution, I proceeded with a simplex search (see Appendix E) to find real local minima. I retained the best 50 models from the fine grid search and performed a simplex search for a minimum around each of them. In figure 5.9 I show how the distribution of the top 50 models in the $M_* - T_{\text{eff}}$ plane changes after the simplex search.

With the simplex search, I found that the valley of best fits became significantly narrower, but also that I was losing the strong preference for a particular range of mass and effective temperature. Figure 5.10 illustrates that fact. The simplex search was able to find solutions with $\Phi \sim 0.1 s$, even around grid points for which Φ exceeded 2 seconds. This does not necessarily mean that grid searches (or genetic algorithm searches) are meaningless, especially if we are careful to treat all solutions with $\Phi < 1$ equally. The numerical noise level appears to be below 0.5 seconds (figure 5.10). Figure 5.10 also shows why a grid search works. A grid search finds solutions where there is a high concentration of very good solutions. If there is not a high concentration of very good fits, the grid search is most likely to miss those isolated minima. It also explains why once in a while a grid search will find a solution away from the families of solutions. A grid search is useful in that respect

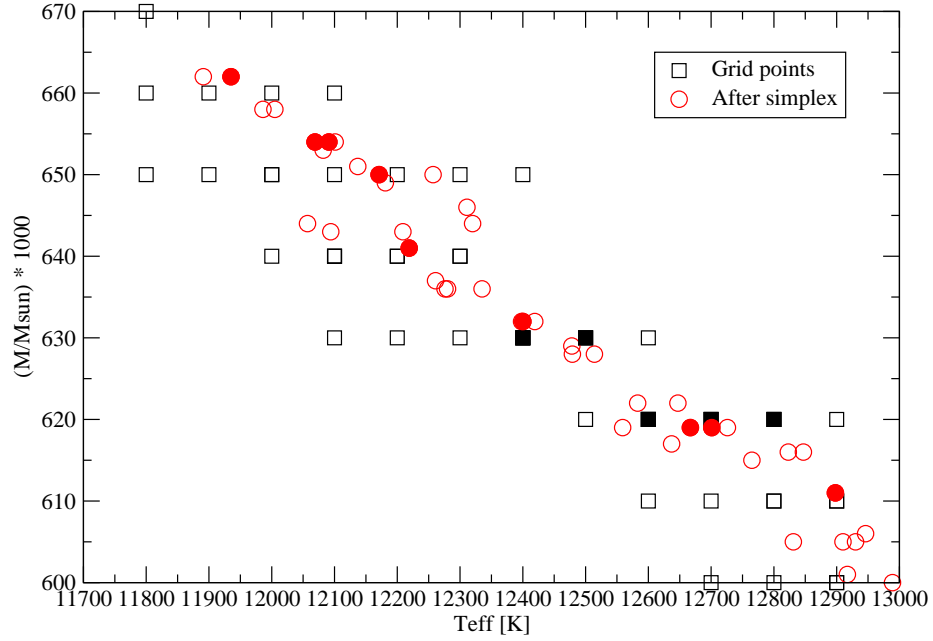


Figure 5.9: The migration of the best solutions for a model like G117-B15A after a simplex search. The filled squares correspond to solutions that satisfy $\Phi < 1$ s and the filled circles to those that satisfy $\Phi < 0.1$ s.

because it allows us to detect entire regions of good fits and we can be assured that those fits are not merely a numerical accident.

One benefit of the simplex exercise is that it tightens all the correlations that are present in the parameter space. In figure 5.11 I plotted the best fit models in the $M_H - T_{\text{eff}}$ plane and the $M_{\text{He}} - T_{\text{eff}}$ planes. Clear trends appear for G117-B15A. The hydrogen layer mass in particular seems to be strongly correlated with effective temperature. I found that this strong relation only existed if I included the 215s mode in the fit.

While the simplex searches gave a better picture of parameter space and suggested

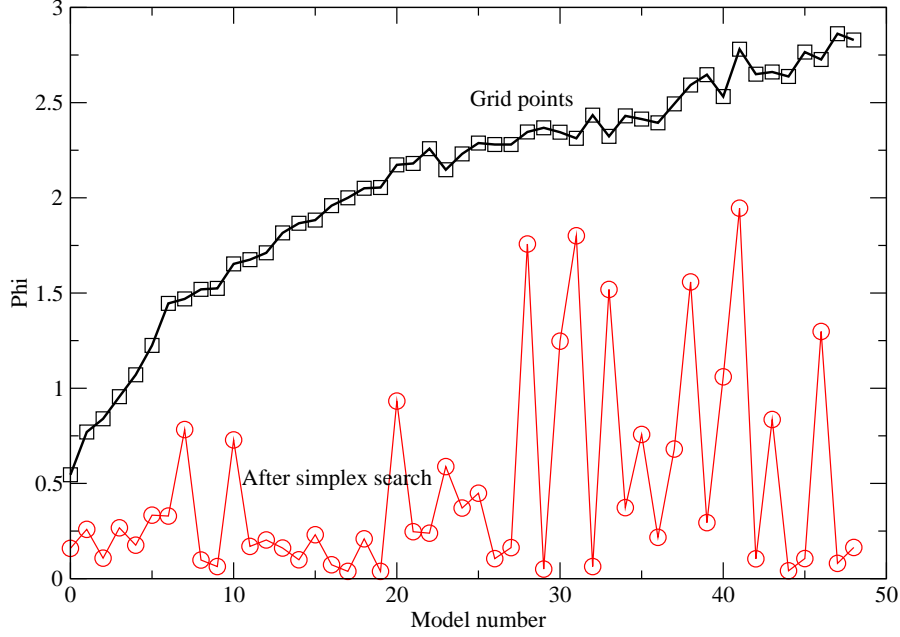


Figure 5.10: The value of the function Φ (equation 3.1) for the 50 best fit models from the grid, before and after a simplex search for a nearby true minimum.

new lines of investigation, I decided not to rely on them to compute the \dot{P} 's in the next section and obtain a constraint on the axion mass.

5.7 Constraint on the axion mass from \dot{P} 's

Having narrowed down the regions of parameter space occupied by best fit models for G117-B15A and R548, the next and last step is to derive rates of period change for those models along with the associated uncertainties. This is a classic Monte Carlo problem. Based on the results listed in table 5.4, I defined the 4 independent variables as being T_{eff} ,

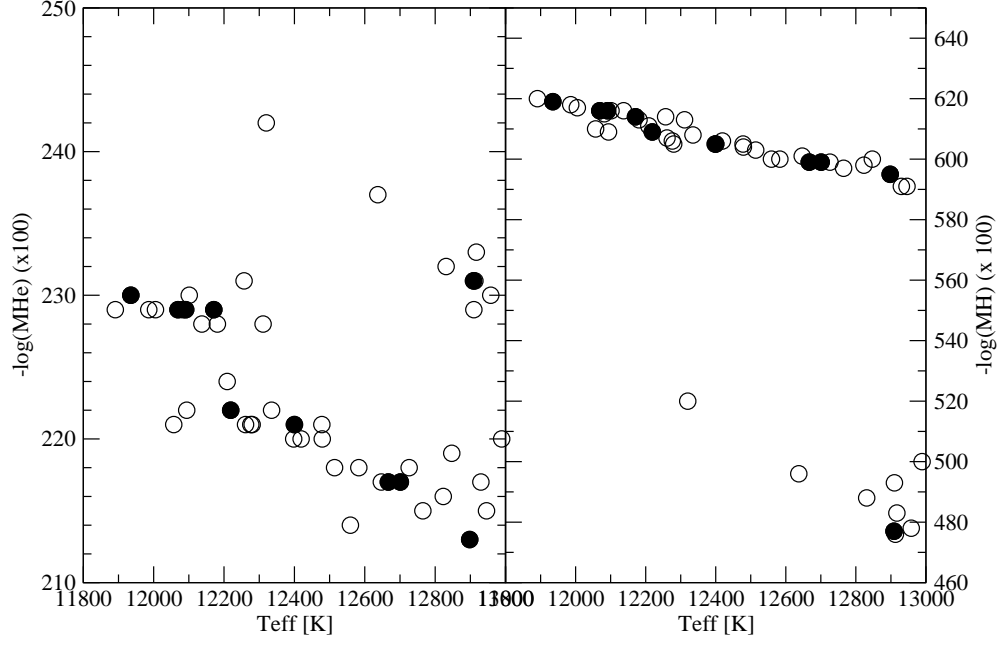


Figure 5.11: Best fit models after the simplex search in the $M_H - T_{\text{eff}}$ plane and the $M_{\text{He}} - T_{\text{eff}}$ planes. The filled circles, like in figure 5.9 mark the location of the models for which $\Phi < 0.1$ s.

ΔM (instead of M_*), M_{He} , and M_H . I set

$$M_* = b - a T_{\text{eff}} + \Delta M, \quad (5.2)$$

where a and b take on the values listed in table 5.4 and $|\Delta M| \leq 0.02$, as determined in section 4.6.5.

5.7.1 A sanity check: 0 meV axion results

For each family of solutions listed in table 5.4, without including axions just yet, I generated a random population ($N=500$). We have a total of 6 families of solutions and therefore 6 populations of 500 models, 3 for G117-B15A and 3 for R548. I display the distribution of the models of each of the 6 populations in figures 5.12 and 5.13. For each model in each population, I proceeded with calculating a \dot{P} . This involved computing in each case one model slightly cooler and one slightly hotter. I picked a step in temperature of $\pm 100K$, comfortably above the resolution limit of the WDEC ($\simeq 50K$) and small enough to give a meaningful time derivative of the periods.

I checked that the period and \dot{P} distribution for each of the 6 (0 meV axions) populations were close to gaussian and found that they were. For each population (family of solutions) I calculated the mean period and \dot{P} . I list the results in table 5.5 with one sigma error bars. Remember that those results assume axions do not exist and that the cooling is due entirely to photons.

For G117-B15A, we know that the period for the mode of interest is 215.2s and that the \dot{P} for that mode is $3.57 \pm 0.82 \times 10^{-15} \text{s/s}$. Family 1 has a low period, inconsistent with the measured period. This indicates that it is not a good fit to G117-B15A and we can discard thick hydrogen layer solutions. Family 2's \dot{P} is inconsistent with the observed value. It is lower. Based on this fact alone, we cannot discard that solution, however, as we can always increase the cooling rate and therefore raise the value of \dot{P} by adding in axions.

We are left with two possible families of fits for G117-B15. Family 2's fits have a medium hydrogen layer thickness ($M_H = 10^{-6.2}$) and occupy the high mass, low effective temperature region of the $M_* - T_{\text{eff}}$ plane. Family 3's fits have a thin hydrogen layer ($M_H < 10^{-7.2}$) and they lie at higher effective temperature (lower mass) in the $M_* - T_{\text{eff}}$ plane. Family 3's fits to G117-B15A are very similar to the fits to R548. While this makes family 3 more attractive than family 2, we cannot discard family 2 as a viable possibility on that basis alone and in the next section, we consider both families when constraining the axion

Table 5.5: Average periods and \dot{P} 's for G117-B15A and R548, without axions.

G117-B15A

	Family 1 Thick H layer	Family 2 Medium H layer	Family 3 Thin H layer
P [s] \dot{P} [10^{-15} s/s]	213.1 ± 1.9 2.76 ± 0.14	214.9 ± 2.5 1.92 ± 0.26	215.7 ± 2.0 2.98 ± 0.17

R548

	Family 1 $\log(M_H) = -7.6$	Family 2 $\log(M_H) = -7.4$	Family 3 $\log(M_H) = -7.2$
P [s] \dot{P} [10^{-15} s/s]	213.0 ± 1.5 2.75 ± 0.43	212.7 ± 1.6 3.01 ± 0.12	213.5 ± 2.2 2.95 ± 0.08
P [s] (combined) \dot{P} [10^{-15} s/s]	213.1 ± 1.8 2.91 ± 0.29		

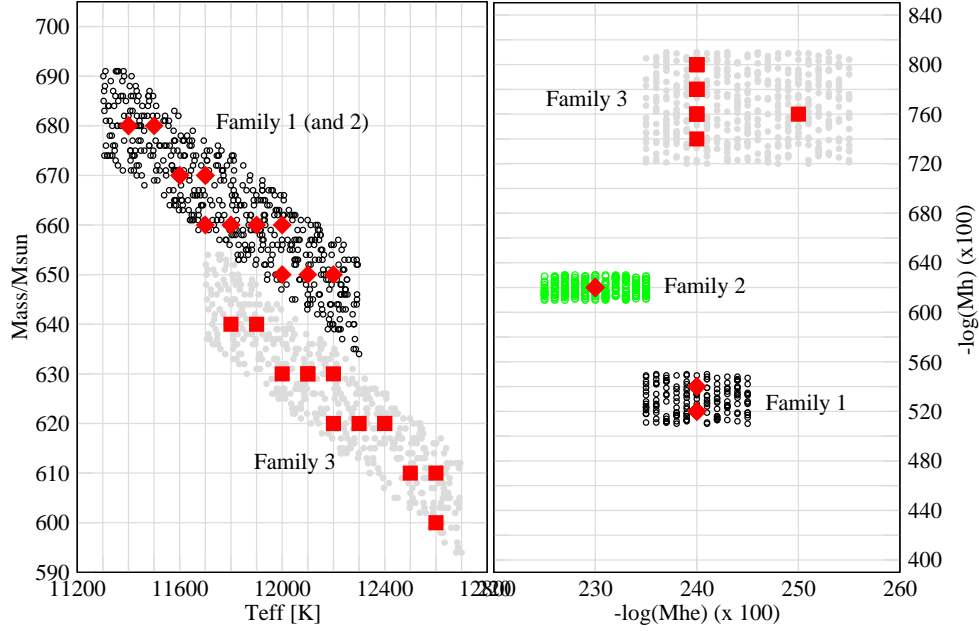


Figure 5.12: A sample simulated random population within the bounds defined in table 5.4 for G117-B15A. The small circles show the location in parameter space of the simulated population, while the squares and diamonds are best fit grid models. In the $M_* - T_{\text{eff}}$ plane, family 1 and 2 lie on top of each other.

mass.

All three families of best fit models for R548 have periods close to the observed 213s and they all have similar \dot{P} 's. We do not have a precise measurement of \dot{P} for this mode in R548 yet, but we can already say that the values in table 5.5 are consistent with the observed \dot{P} ($\dot{P} < 5.5 \pm 1.9 \times 10^{-15} \text{s/s}$). In the last 2 rows of table 5.5, I combined all three families of best fits for R548 because, unlike the classes of best fit models for G117-B15A who differ in fundamental ways, the three families of fits for R548 appear to belong to one unique family.

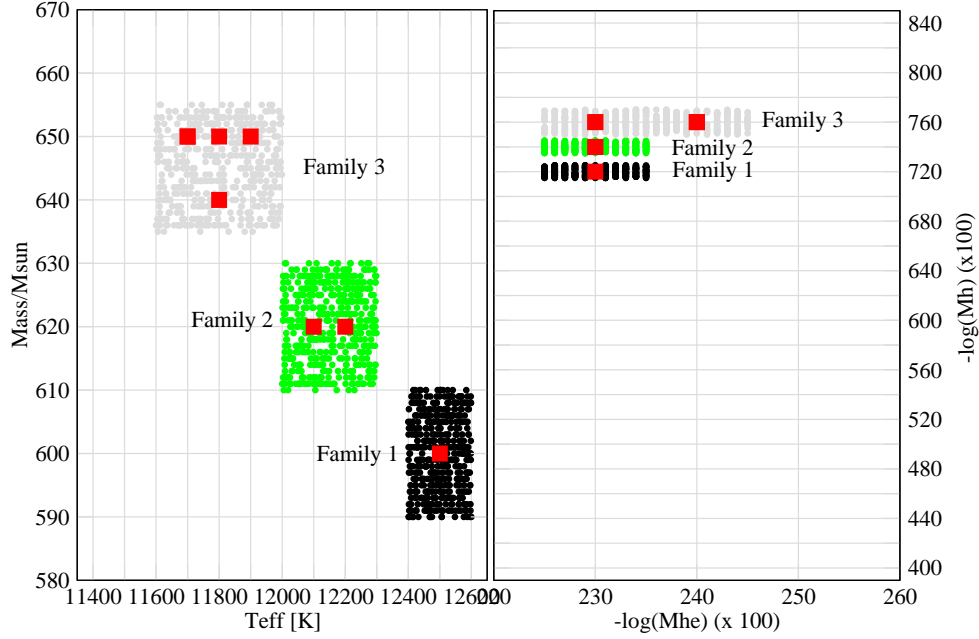


Figure 5.13: A sample simulated random population within the bounds defined in table 5.4 for R548. The small circles show the location in parameter space of the simulated population, while the squares are best fit grid models.

5.7.2 Axion mass limit

I repeated the procedure described in the previous section for axions of different masses (up to 30 meV). When I increased the axion mass, the period for a given family of solution remained very nearly identical to the 0 meV axion period listed in table 5.5 (figure 5.14), and \dot{P} increased with increasing axion mass as a result of the higher and higher cooling rate. In figure 5.15 I show \dot{P} as a function of axion mass for G117-B15A (family 2 and 3) and R548 (all 3 families). For R548, I plot the \dot{P} 's for each of the 3 families of fits individually and also show a combined likelihood region.

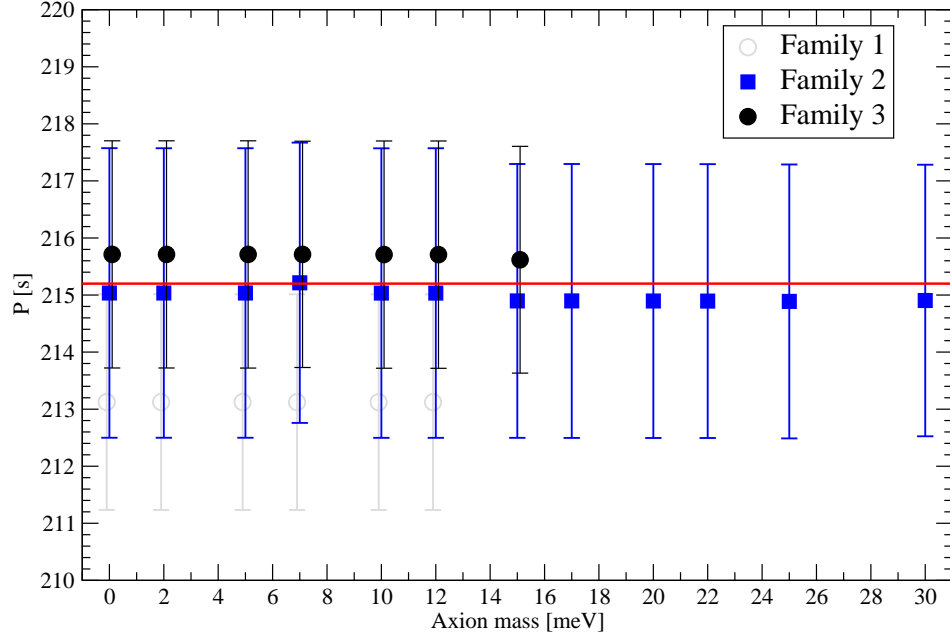


Figure 5.14: Period of the 215.2s mode as a function of axion mass for all three families of fit to G117-B15A’s period spectrum. Family 1’s period is too low and I did not use that family to place a constraint on the axion mass. Family 2 has a low \dot{P} and as a result, can accommodate higher mass axions before the calculated \dot{P} becomes too large to be consistent with the observed value.

The limit on \dot{P} for R548 does not allow us to constrain the axion mass nearly as well as the measured \dot{P} for G117-B15A. For the latter, family 1 places an upper limit of 13.5 meV on the axion mass and family 2 (taken alone) requires the existence of axions. According to family 2, the axion mass should be between 10.4 and 26.5 meV. Combining the two families together, we can place a conservative upper limit of 26.5 meV on the axion mass. What makes this limit unique is not the fact that it is an order of magnitude or more lower than previous limits. It is not. What makes it unique is its strength. It is based

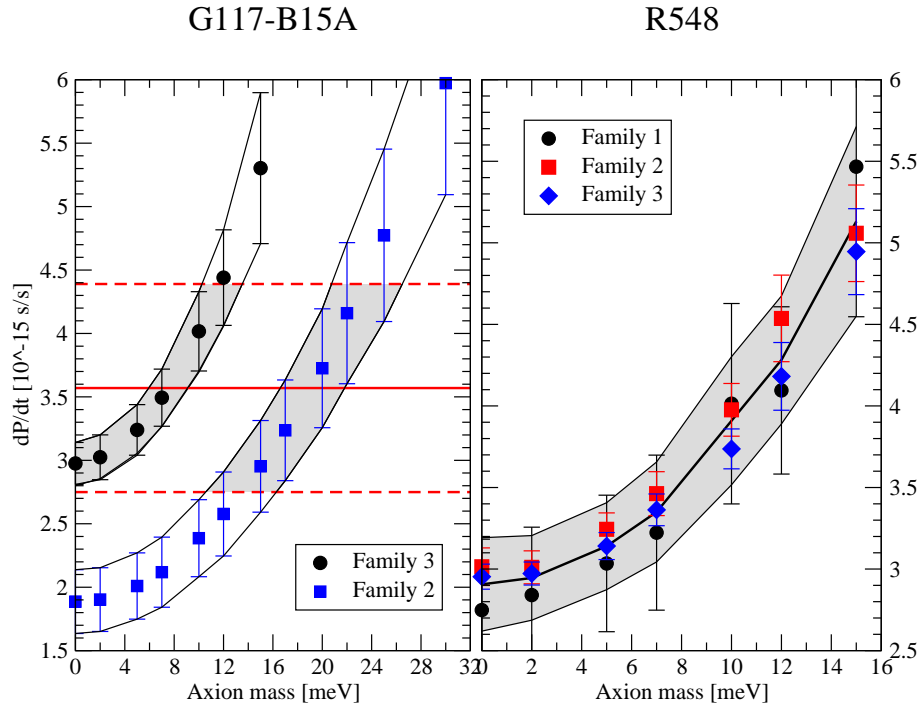


Figure 5.15: \dot{P} 's as a function of axion mass for G117-B15A and R548. The observed \dot{P} for G117-B15A is indicated by the horizontal solid line and its 1 sigma error bars by the dashed lines above and below it. The shaded regions inside the dashed horizontal lines indicates the range of calculated \dot{P} 's consistent with the observed value (to 1 sigma). For R548, the symbols with error bars indicate the \dot{P} calculated for each family of fits listed in table 5.5, and are labeled in the legend. The bold curve and shaded region combines all three families.

on a naive, rigorous analysis and well known physics. Compared to the axion searches I presented in chapter 4, the present analysis involved relatively small uncertainties and we considered all of them systematically. Like always, there is room for improvement and I discuss what we can do better in the conclusion.

Chapter 6

EC20058 and Plasmon neutrinos

6.1 Introduction

In the previous chapter, we assumed that the theory adequately described plasmon neutrino emission rates so that neutrinos did not contribute to the cooling of DAVs. We further assumed that the only source of cooling other than photons was due to axions. In this chapter, we take the opposite approach. We assume that axions do not exist, or if they do, interact so weakly with matter that the only significant source of cooling in white dwarfs (aside from radiation) comes from plasmon neutrinos. For plasmon neutrinos we have a more solid foundation theoretically than we did with axions, but we do not have as much data at our disposal to test the theory. We already know neutrinos exist, and plasmon decay is solidly predicted by the same theory that predicts neutrino emission through better known processes such as those taking place in the Sun.

From the predicted neutrino emission rates, we would expect plasmon decay to be the dominant mode of neutrino production in white dwarfs. Furthermore, neutrinos should account for half the energy loss in white dwarfs hotter than $\sim 25000\text{K}$ (figure 1.2). In that temperature range, we find DBV pulsating white dwarfs. EC20058 is the only stable DBV we know and for now we must rely on the measured \dot{P} for that star. Sullivan (2004) has

collected over 10 years of data on EC20058, but has not published a \dot{P} yet. In this chapter, after I give a thorough introduction to plasmon neutrinos, I present an asteroseismological study of EC20058 following a method similar to the one I followed in the previous chapter for G117-B15A and R548, and make a prediction of how tightly we can constrain the plasmon neutrino emission rates given a measured \dot{P} for EC20058.

6.2 Plasmon neutrinos

6.2.1 Description of the basic physical process

Plasmon neutrinos result from the decay of a plasmon into a neutrino-antineutrino pair. Classically, one thinks of a plasmon as an electromagnetic wave propagating through a dielectric medium. It is made up of an oscillating electromagnetic field coupled with electrons oscillating with the same frequency. The frequency, ω , of such a wave obeys the dispersion relation

$$\omega^2 = \omega_0^2 + k^2 c^2, \quad (6.1)$$

where ω_0 is the plasma frequency (see next section). Quantizing the field, the equation above yields

$$E^2 = \hbar^2 \omega_0^2 + p^2 c^2. \quad (6.2)$$

In effect, a plasmon is a particle similar to a photon, except it has a non-zero rest mass.

In free space, photons cannot decay into a neutrino-antineutrino pair without violating conservation of four-momentum. In a plasma, the electrons coupled to the photon allow conservation of energy and momentum and so plasmons can decay into a neutrino-antineutrino pair.

One can readily see from equation 6.1 that plasmons can only exist if $\omega > \omega_0$. This means that more plasmon neutrinos will be produced if the plasma has a high temperature relative to its frequency, i.e. $kT > \hbar\omega_0$. However, ω should not be too large either because

otherwise, the coupling with the electrons does not occur and plasmons do not exist.

6.2.2 Plasma frequency inside white dwarfs

In a plasma, electrons displaced from equilibrium oscillate with frequency ω_0 , the plasma frequency. The restoring force is the coulomb force between the electrons and the ions.

Under normal conditions, the plasma frequency is given by

$$\omega_0^2 = \frac{4\pi n_e e^2}{m_e}. \quad (6.3)$$

In a degenerate plasma, the plasma frequency is (Inman & Ruderman, 1964)

$$\omega_0^2 = \frac{4\pi n_e e^2}{m_e} \left[1 + \left(\frac{\hbar}{m_e c} \right)^2 (3\pi^2 n_e)^{\frac{2}{3}} \right]^{-\frac{1}{2}}. \quad (6.4)$$

Note that the degeneracy correction brings ω_0 *down*. For the temperatures and densities of a typical DBV interior, the correction is relatively small and the plasma frequency is not depressed by very much (less than a factor of 2) compared to the non-degenerate value. On the other hand, the densities inside a white dwarf are very high. This leads to a large value of ω_0 . In an average DBV, ω_0 is around 30 keV. As a comparison, ω_0 is about 400 eV in the center of the Sun.

For our purposes, it is useful to express the plasma frequency as a function of the local density. To that end, we make the simplifying assumption that the interior is fully degenerate. This begs the question “How far out in radius is that a good assumption?” Electrons obey Fermi statistics. Their energy distribution, originally worked out by Lev Landau is given by the Fermi-Dirac distribution (Hansen & Kawaler, 1994)

$$f(E, T) = \frac{1}{\exp \left[\frac{E_f}{kT} \left(\frac{E}{E_f} - 1 \right) \right] + 1}. \quad (6.5)$$

Figure 6.1 shows $f(E, T)$ for different values of the parameter E_f/kT . Full degeneracy is

characterized by the fact that the energy levels with $E < E_f$ where E_f is the Fermi energy are fully occupied, while the levels with $E > E_f$ are vacant. E_f/kT greater than a thousand or so indicates full degeneracy.

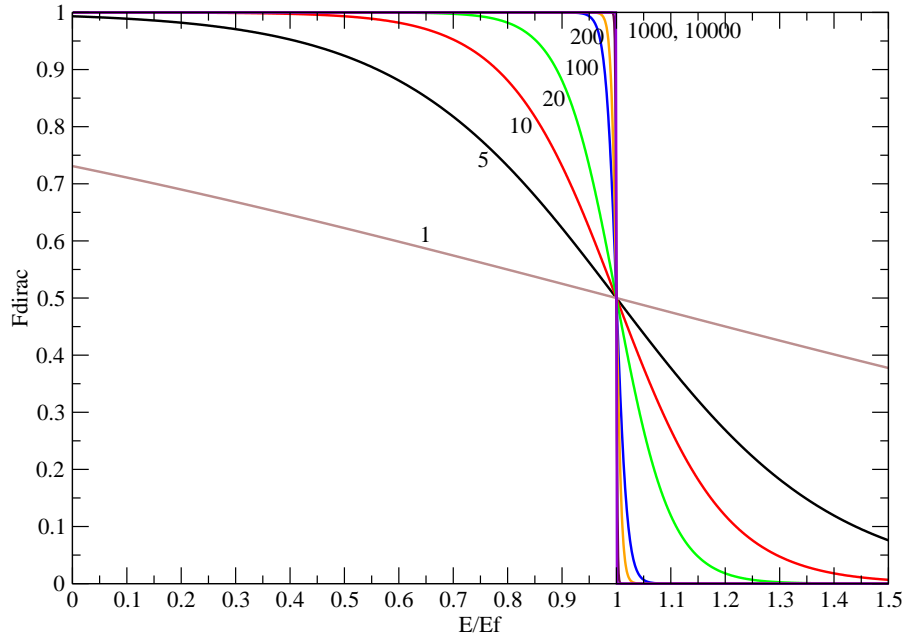


Figure 6.1: Fermi-dirac distribution for different values of E_f/kT (values listed next to the curves.)

Hansen & Kawaler (1994) derive a criterion for degeneracy (equation 3.66 in Hansen & Kawaler) based on $E_f/kT \sim 1$:

$$\frac{\rho}{\mu_e} \sim 6.0 \times 10^{-9} T^{3/2} \text{ g cm}^{-3}. \quad (6.6)$$

It is useful to obtain the same criterion for different values of E_f/kT , e.g. obtain an expression that allows us to decide how degenerate conditions should be in order to be considered

degenerate. To that end, we can repeat the simple derivation Hansen & Kawaler (1994) used to get equation 6.6, keeping E_f/kT as a variable instead of setting it ~ 1 . The resulting criterion is

$$\frac{\rho}{\mu_e} \sim 6.0 \times 10^{-9} \frac{E_f}{kT}^{3/2} T^{3/2} \text{ g cm}^{-3}. \quad (6.7)$$

If ρ/μ_e is greater than the right hand side, then the electrons are degenerate. The degree of degeneracy is set by the value of E_f/kT we pick. In figure 6.2, I show a plot of ρ/μ_e in the interior of a $0.6 M_\odot$, 28000K model and the degree of degeneracy of different parts of the model. The model is very nearly fully degenerate out to $M_r \simeq 0.93M_*$ ($E_f/kT \geq 200$), and still very much degenerate ($E_f/kT \geq 100$) out to $M_r \simeq 0.98M_*$. On the same graph, I also plotted the plasmon neutrino emission rate ϵ_n . The figure clearly shows that assuming complete degeneracy throughout the model is a very good approximation. We proceed with confidence.

For a fully degenerate plasma, the electron density is given by (Hansen & Kawaler, 1994)

$$n_e = 5.865 \times 10^{29} x_F^3 \text{ cm}^{-3}, \quad (6.8)$$

where

$$x_F^3 = \frac{\rho}{B\mu_e}. \quad (6.9)$$

$B = 9.739 \times 10^5 \text{ g cm}^{-3}$ for electrons and μ_e , the mean molecular weight per free electron is 2 in the interior of a white dwarf made up of carbon and oxygen. Plugging those values in 6.4, we obtain:

$$\hbar\omega_o = 20.4 \rho^{1/2} (1 + 6.41 \times 10^{-5} \rho^{2/3})^{-1/4} [\text{eV}], \quad (6.10)$$

consistent with Inman & Ruderman (1964). Clayton (1983) derives a similar expression, but finds:

$$\hbar\omega_o = 40.8 \rho^{1/2} (1 + 1.6155 \times 10^{-4} \rho^{2/3})^{-1/4} [\text{eV}]. \quad (6.11)$$

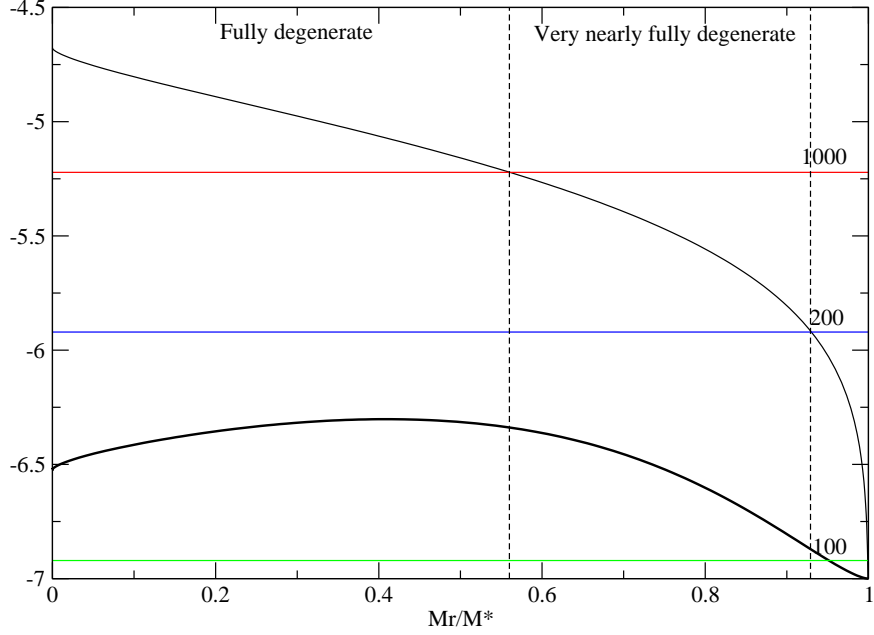


Figure 6.2: Degree of degeneracy of a $0.6 M_{\odot}$, 28000K model. The thin solid black curve is the ρ/μ_e profile. The horizontal lines correspond to the right hand side of equation 6.7, evaluated for different values of E_f/kT (corresponding E_f/kT listed for each above the line). The bold curve is a plot of the plasmon neutrino emission in the model. Full degeneracy becomes a poorer approximation out at $M_r \simeq 0.98M_*$, where neutrino rates are small and do not contribute much to the neutrino luminosity.

I compare the two different results in the next section.

6.2.3 Approximate expressions for plasmon neutrino rates

Approximate neutrino rates are useful to gain further insight into plasmon neutrino processes in white dwarfs. The following derivation is based on Adams et al. (1963). Similar derivations may also be found in Inman & Ruderman (1964) and Clayton (1983). We focus on transverse plasmon neutrino rates. Longitudinal plasmon neutrino rates are negligible

inside white dwarfs.

For most of the following derivation we set fundamental constants such as c , \hbar , and m_e equal to 1. We begin with the neutrino-pair emission rate per unit volume from plasmons (also called “emissivity”). Note that astronomers like to use energy emission rates per unit mass. We adopt the notation Q for the emissivity and ϵ_n for the neutrino energy emission rate per unit mass.

$$Q = \int \tau^{-1} \omega [e^{\omega\beta} - 1] (2\pi)^{-3} (8\pi) k^2 dk \quad (6.12)$$

where ω is the frequency of the plasmon and $\beta = (kT)^{-1}$ (k here is the Boltzman constant). τ^{-1} is the decay rate of a plasmon. It is given by

$$\tau^{-1} = \frac{8}{3} g^2 (4\pi e)^{-2} \left[\omega \left(2\epsilon + \omega \frac{\partial \epsilon}{\partial \omega} \right) \right]^{-1} (\omega^2 - k^2) [\omega^2 (\epsilon - 1)]^2 \quad (6.13)$$

where $\epsilon = 1 - \frac{\omega_0^2}{\omega^2}$ and g is the strength of the coupling between photons and plasmons. $g = 3.08 \times 10^{-12} \frac{\hbar^3}{m_e^2 c}$ (Inman & Ruderman, 1964) is a constant. k is related to ω by the dispersion relation 6.1. Eliminating ϵ and k from equation 6.13, we have

$$\tau^{-1} = \frac{4}{3} g^2 (4\pi e)^2 \omega_0^6 \omega^{-1}. \quad (6.14)$$

Equation 6.12 then becomes

$$Q = 2g^2 (3\pi e^2)^{-1} (2\pi)^{-3} \omega_0^6 \int_0^\infty k^2 (e^{\omega\beta} - 1)^{-1} dk. \quad (6.15)$$

The integrand may be rewritten (using geometric series)

$$Q = 2g^2 (3\pi e^2)^{-1} (2\pi)^{-3} \omega_0^6 \sum_{n=1}^{\infty} \int_0^\infty e^{-n\omega\beta} k^2 dk. \quad (6.16)$$

The integrand becomes very nearly zero before k gets a chance to come anywhere near ω_0 .

For $k \ll \omega_0$, $\omega \approx \omega_0 + \frac{k^2}{2\omega_0}$. We now have

$$Q \approx 2g^2(3\pi e^2)^{-1}(2\pi)^{-3}\omega_0^6 \sum_1^\infty e^{-n\omega_0\beta} \int_0^\infty e^{-\frac{n\beta k^2}{2\omega_0}} k^2 dk. \quad (6.17)$$

Evaluating the integral, we find

$$Q \approx (2\pi)^{\frac{1}{2}} \frac{g^2}{3\pi e^2} \frac{\omega_0^{7.5}}{(2\pi)^3} \beta^{-\frac{1}{5}} \sum_1^\infty n^{-\frac{3}{2}} e^{-n\omega_0\beta}. \quad (6.18)$$

The sum converges very quickly and we only keep the first term:

$$Q \approx (2\pi)^{\frac{1}{2}} \frac{g^2}{3\pi e^2} \frac{\omega_0^{7.5}}{(2\pi)^3} \beta^{-\frac{1}{5}} e^{-\beta\omega_0}. \quad (6.19)$$

Putting back the values of all the relevant physical constants through a careful unit analysis, and grouping constants, we finally have

$$Q = 9.43 \times 10^{76} (kT)^9 x^{7.5} e^{-x}, \quad (6.20)$$

where $x = \frac{\hbar\omega_0}{kT}$ (note the temperature dependence of x). $\hbar\omega_0$ is given by equation 6.10. The energy generation rate per unit mass ϵ_n may be easily obtained from the emissivity by multiplying Q by the local density.

Adams et al. (1963) derive the same result. Clayton (1983) follows a similar derivation but finds

$$Q = 2.36 \times 10^{76} (kT)^9 x^{7.5} e^{-x}. \quad (6.21)$$

This emissivity is about one quarter that in equation 6.20. According to Clayton, $\hbar\omega_0$ is given by equation 6.11. I show the two different results in figure 6.3, along with the exact neutrino emissivity from Itoh et al. (1996a). While both approximate expressions for Q miss the mark by quite a bit, 6.20 combined with 6.10 seem to reproduce the general behavior of the neutrino emissivity. It also means that we can use equation 6.20 to gain a better

qualitative understanding of neutrino emission inside white dwarfs. We do so in the next section.

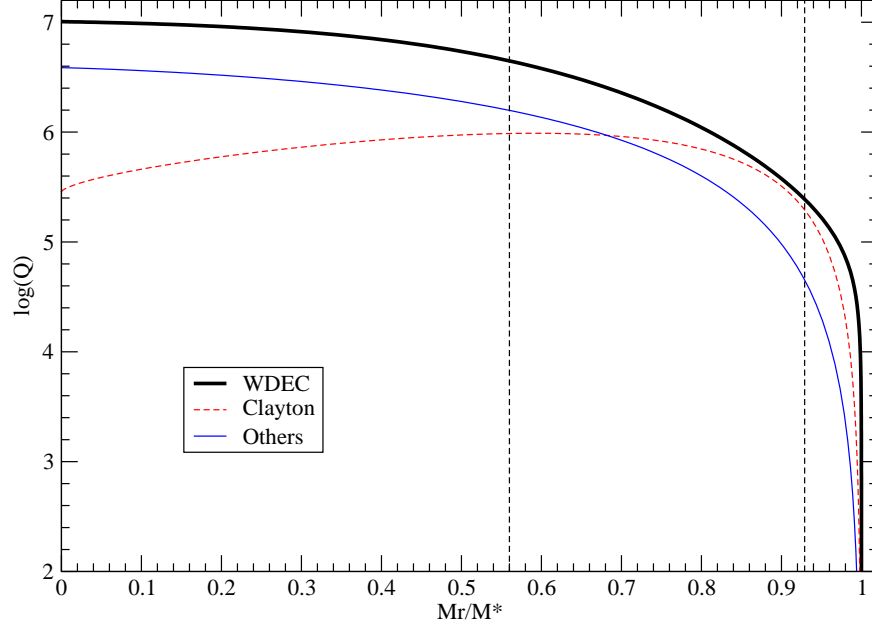


Figure 6.3: A comparison of approximate emissivities with the exact result for a $0.6 M_{\odot}$, 28000K model. The vertical dashed lines were borrowed from figure 6.2 and indicate the degree of degeneracy of the model. The assumption of full degeneracy is very good out to the rightmost vertical dashed line.

6.2.4 Plasmon neutrino rates in white dwarfs - A physical understanding

Figure 6.4 shows the value of x in the interiors of two different mass DBV models at 28000K and 24000K, according to equation 6.10. For reference, I display their respective temperature profiles in figure 6.5. Note that the model interiors are roughly isothermal and that the higher mass model has a *lower* central temperature. Figure 6.6 shows the neutrino rates for

the same models.

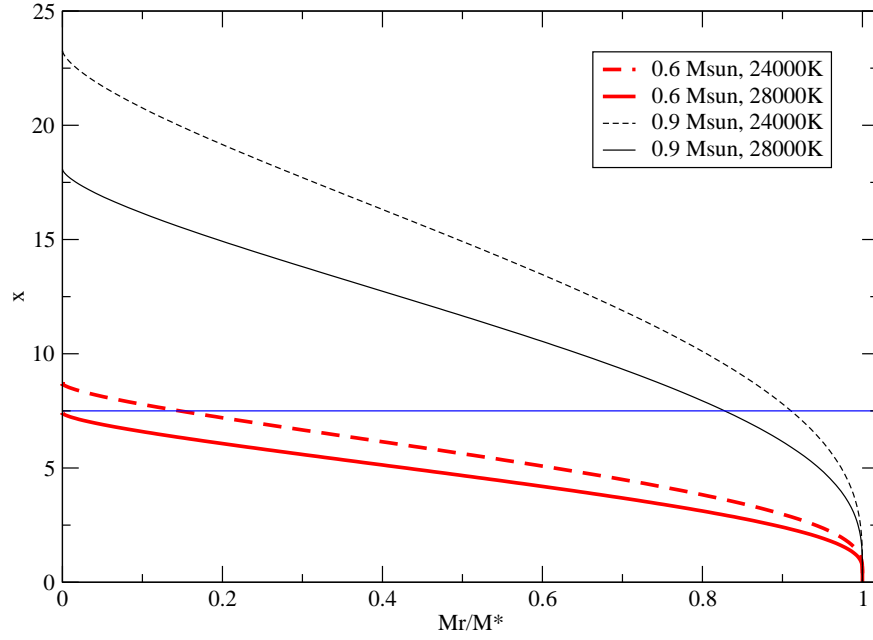


Figure 6.4: The $x = \frac{\hbar\omega_0}{kT}$ profiles for different mass and effective temperature models. The horizontal line corresponds to $x = 7.5$ (see text).

We now have all the elements to better understand plasmon neutrino rates in white dwarfs. Figure 6.7 shows the neutrino luminosity as a function of effective temperature for different mass models. First let us follow the evolution of a model as it cools. For any given mass, the neutrino luminosity decreases with effective temperature. An obvious reason for this is the steep dependence of ϵ_n on temperature (see equation 6.20). However, the density dependence, embedded in the x term, also has a large effect on the neutrino luminosity. As can be easily worked out from equation 6.20, ϵ_n is maximum for $x = 7.5$. As the model cools, neutrino production peaks further and further away from the center, where the density is lower. For instance, the $0.9 M_\odot$ model at 28,000K has $x = 7.5$ at $M_r/M_* \sim 0.83$, where

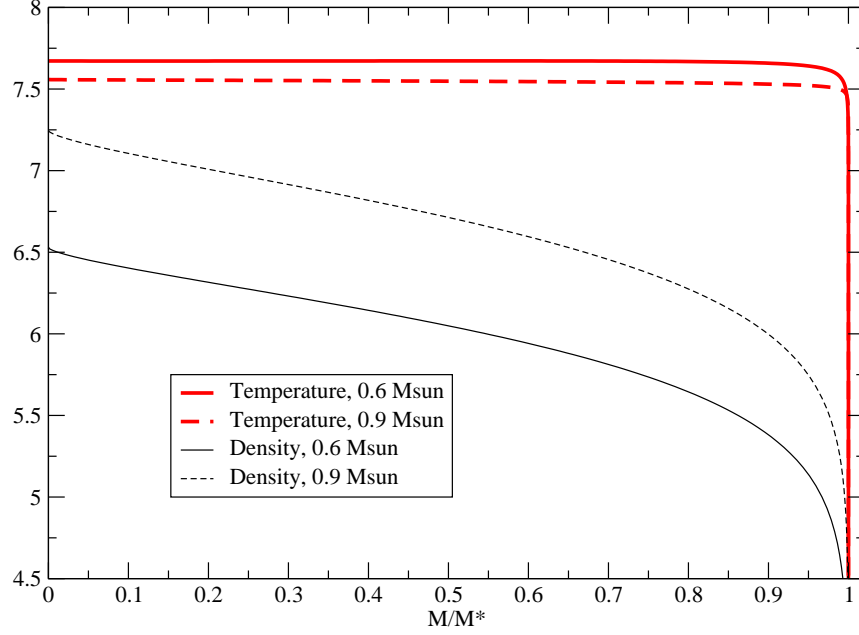


Figure 6.5: Temperature and density profiles for different mass models. Both are 28000K models.

the maximum in ϵ_n also occurs (figure 6.6).

While high densities enhance plasmon neutrino production rates for a time (e.g. the $x^{7.5}$ term in equation 6.20), densities that are too high are not favorable to plasmon neutrino production. The exponential term in equation 6.20 kills plasmon neutrino production when x becomes large. x becomes large when the density rises and when the temperature drops, both of which occur in a cooling model.

Now let us compare a massive model ($0.9 M_\odot$) with an average mass model ($0.6 M_\odot$). Figure 6.7 shows that at high effective temperature, the $0.9 M_\odot$ model has a slightly higher neutrino luminosity, while the opposite is true for lower effective temperatures. It is interesting to note that ϵ_n is lower for the $0.9 M_\odot$ model through the whole effective

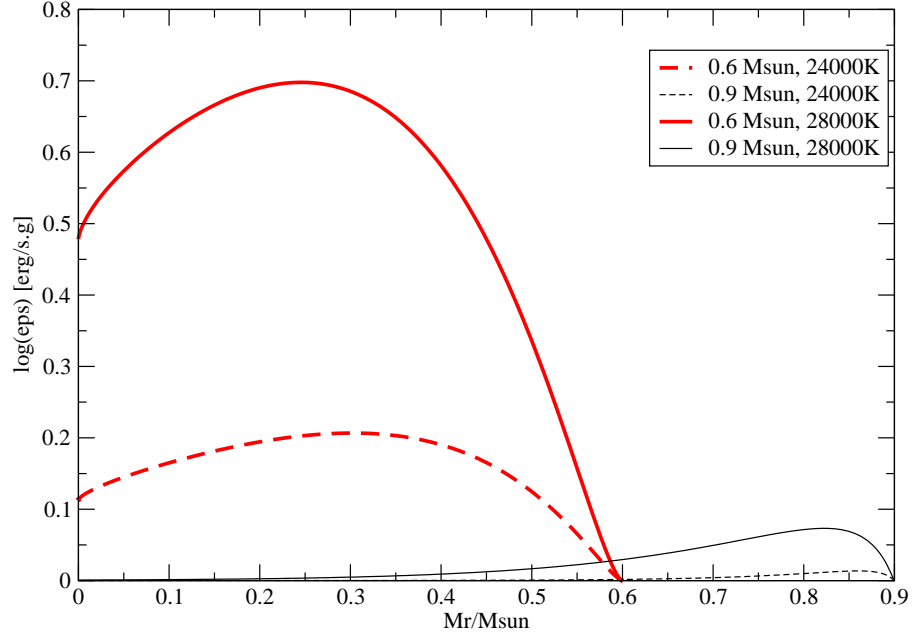


Figure 6.6: Plasmon neutrino rates (according to Itoh et al., 1996a) for different mass models at different effective temperatures. The neutrino luminosity is simply $L_\nu = \int_0^{M_*} \epsilon_n dM$. The horizontal axis was chosen so that the area under each curve is proportional to the neutrino luminosity.

temperature range, because of its high internal densities and lower central temperature. Neutrino production also peaks further out from the center than for the $0.6 M_\odot$ model. In fact, the $0.9 M_\odot$ model is not as favorable to plasmon neutrino production as the $0.6 M_\odot$ model. The only reason it has a higher neutrino luminosity at very high effective temperatures is simply because there is more mass present to produce plasmon neutrinos (see figure 6.8). At lower effective temperatures, plasmon neutrino rates inside the $0.9 M_\odot$ model drop so low that it can no longer compete with the $0.6 M_\odot$ model. This is because $kT \lesssim \hbar\omega_0$, so that few photons are energetic enough to be plasmons.

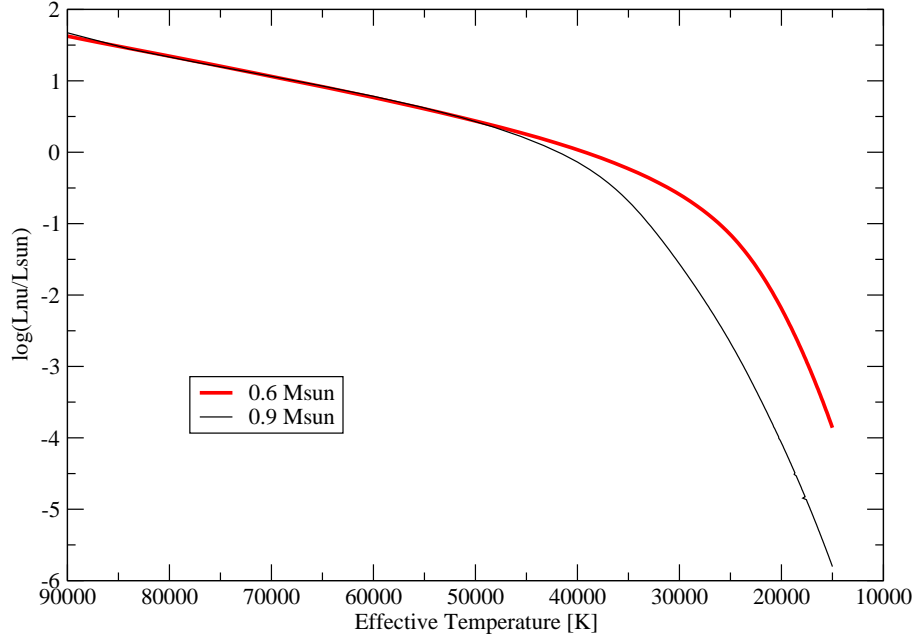


Figure 6.7: Neutrino luminosity as a function of effective temperature for two different mass models.

6.3 Plasmon neutrino rates used in code

6.3.1 Outline of how plasmon neutrino rates are evaluated

The plasmon neutrino rates in the codes are those calculated Itoh et al. (1992, 1996a). They are an improvement over older neutrino rates (Beaudet et al., 1967; Munakata et al., 1985; Itoh et al., 1989) as they use more accurate plasmon dispersion relations, appropriate for ultrarelativistic degenerate electrons as well as non-relativistic degenerate electrons (the latter relevant for the white dwarf interiors). We outline the main steps of the calculation below.

The first step is to evaluate the dielectric function $\omega(q)$, where q is the plasmon

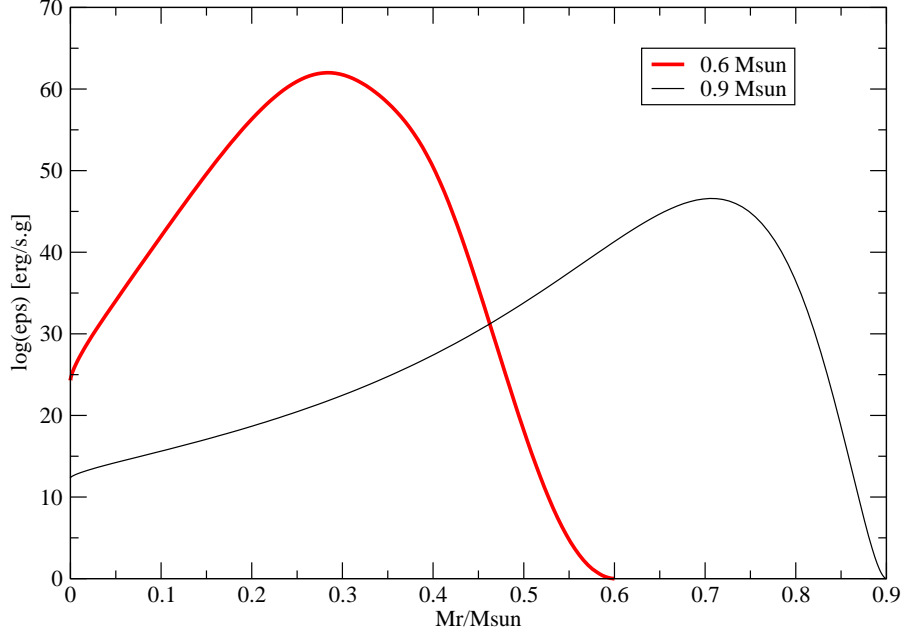


Figure 6.8: Plasmon neutrino rates for the same models as figure 6.6, but for a higher effective temperature (70000K). The $0.9 M_{\odot}$ model has a slightly higher neutrino luminosity than the $0.6 M_{\odot}$ model, only because the integration gets carried out over a larger mass range, not because the neutrino rates are higher.

wavenumber in units of the electron mass m_e . This is done by solving the dispersion relation $\epsilon(q, \omega) = 0$, both for transverse and longitudinal plasmons. The dispersion relations were derived by Jancovici (1962). $\epsilon_l(q, \omega_l)$ and $\epsilon_t(q, \omega_t)$ are very messy expressions. We refer the interested reader to Jancovici's paper.

Once we have $\omega(q)$ we can evaluate the residue functions given by

$$Z_l^{-1} = (\omega_l^2 - q^2) \frac{\partial \epsilon_l}{\partial \omega_l^2} \quad (6.22)$$

$$Z_t^{-1} = \frac{\partial(\omega_t^2 \epsilon_t)}{\partial \omega_t^2} \quad (6.23)$$

for longitudinal and transverse plasmons respectively. Finally, the dielectric functions and the residue functions go into the integral expressions for the longitudinal and transverse contributions to the plasmon neutrino rates, Q_l and Q_t :

$$Q_l = \frac{1}{2} A_o \int_0^\infty q^2 Z_l(q) [\omega_l(q)^2 - q^2]^3 n_B[\omega_l(q)] dq \quad (6.24)$$

$$Q_t = A_o \int_0^\infty q^2 Z_t(q) [\omega_t(q)^2 - q^2]^3 n_B[\omega_t(q)] dq. \quad (6.25)$$

In the above expressions, A_o is a constant and $n_b[\omega(q)]$ is the Bose distribution function

$$n_B[\omega(q)] = \frac{1}{e^{\omega/T'} - 1}, \quad (6.26)$$

where $T' = kT/m_e$. The plasmon neutrino rate is given by

$$Q_{pl} = (C_V^2 + n C_V'^2) Q_V, \quad (6.27)$$

where

$$Q_V = Q_l + Q_t, \quad (6.28)$$

$$C_V = \frac{1}{2} + 2 \sin^2 \theta_w, \quad (6.29)$$

$$C_V' = 1 - C_V, \quad (6.30)$$

and

$$\sin^2 \theta_w = 0.23. \quad (6.31)$$

θ_w is the Weinberg angle and n is the number of neutrino flavors other than the electron neutrino (we set $n = 2$ to account for the known τ neutrinos and μ neutrinos).

The exact calculation outlined above is numerically demanding, and Itoh et al. (1996a) offer an analytical fit for ease of use in computing models of dense stellar interiors. That analytical fit is what I have included in the White Dwarf Evolution Code (see appendix F). For interior conditions in white dwarfs ($\log T \sim 7$ and $\log \rho / \mu_e \sim 6$), the accuracy of the fitting formula is around 1% (Itoh et al., 1996b). I verified that this was the case for our models.

6.4 Observed properties of EC20058

EC20058 is the shortest period known DBV and the only one with stable pulsation periods. It is observable from the southern hemisphere and was first discovered to pulsate by Koen et al. (1995) from the South African Astronomical Observatory. Koen et al. detected 6 independent frequencies in the period spectrum. There was a Whole Earth Telescope (WET) run on this star in 1997, that resulted in the discovery at least 11 independent modes (Sullivan, 2004). Since the WET run, Sullivan observed EC20058 regularly at Mt John Observatory in New Zealand. He reports results in Sullivan & Sullivan (2000) and Sullivan (2004, 2005). I list EC20058's 5 highest amplitude modes in table 6.1. The two highest amplitude modes have periods of 257s and 281s.

Table 6.1: Observed properties for EC20058

	$\log(y) = -3.5$ (1)	No hydrogen
T_{eff}	27100 ± 1500 K	28400 ± 1500
$\log g$	7.80 ± 0.10	7.86 ± 0.10
Periods[s]	195, 204, 257*, 281*, 333	

(1) $y \equiv \text{NHe}/\text{NH}$

* High amplitude modes

In the table, I also list the spectroscopically determined properties of EC20058 (Beauchamp et al., 1999). They will serve as clues for our asteroseismological analysis,

though they do not offer very tight constraints. Beauchamp et al. obtained a high resolution spectrum from the Cerro Tololo Inter-American Observatory 4m telescope. EC20058's effective temperature is even less well-determined spectroscopically than that of G117-B15A or R548. DB spectra are more challenging to study than DA spectra, mainly because they do not show hydrogen lines. It is, however, possible to “hide” a trace amount of hydrogen in the noise of the spectra. This is a problem because stellar atmospheres are sensitive to even a small amount of hydrogen (Beauchamp et al., 1999). With the exception of GD358, the brightest DBV, for which we have high signal-to-noise spectra, the effective temperatures of DBVs are uncertain by more than a thousand degrees. For EC20058, Beauchamp et al. are able to hide an amount of hydrogen equal to $\log(\text{NHe}/\text{NH}) = \log(y) = -3.5$, leading to the allowable range for the effective temperature and $\log g$ given in table 6.1. According to my models (described in section 3.1), those values correspond to masses ranging between 0.46 and 0.60 M_{\odot} . Based on those numbers, we do not expect EC20058 to be exceedingly massive.

6.5 Asteroseismological analysis of EC20058

From the spectroscopy (table 6.1), we know we are likely to find a fit between 25600K and 29900K in effective temperature and 0.46 M_{\odot} and 0.60 in mass. And in section 3.3.2, we learned that the five most important factors in determining the periods of the models are the effective temperature, the total mass, the location of the base of the helium layer (M_{He}), the location of the edge of the homogeneous carbon and oxygen core (X_{fm}), and whether we adopt a double layer helium profile or not (table 3.2). I decided to consider all five factors and built two 4 parameter (T_{eff} , M_{\star} , M_{He} , X_{fm}) grids, one with single helium layer profiles and one with double helium layer profiles. I fit the 5 periods listed in table 6.1.

6.5.1 Broad 4 parameter grid search

As I did earlier for G117-B15A and R548, I started with coarse grids to cover a broader region of parameter space. Knowing from the work done in chapter 5 that our best fit asteroseismological models tend to be hotter and/or more massive than what the spectroscopy predicts, I extended my grids to higher temperatures and higher masses. For the double layer helium profiles, I varied M_{He} and set $\log(M_{\text{He}2}) = \log(M_{\text{He}}) - 3$. I computed a total of 13860 single layer models and the same number of double layer models. 13664 single layer models and 13751 double layer models were successful.

Table 6.2: Region of parameter space covered in the broad four-parameter fit and step sizes

Parameter	Range (inclusive)	Step size
T_{eff}	26000K to 30000K	400K
M_*	0.48 to 0.66 M_{\odot}	0.02 M_{\odot}
$-\log(M_{\text{He}})$	2.0 to 7.2	0.4
X_{fm}	0.10 to 0.90	0.1

I show the results of the broad grid search in figures 6.9, 6.10, and 6.11. By and large, in all three planes (M_* vs T_{eff} , M_{He} vs T_{eff} and X_{fm} vs T_{eff}), the two families of solutions show the same features, but the fits with single layer helium abundance profiles are slightly better. We also notice (figure 6.9) that we did not look for solutions at high enough temperatures.

Since we know little about the interior a priori, we want to keep our models as simple as possible. We tried the double layer helium profiles predicted by time dependent diffusion calculations, but since they do not fit outstandingly better than the single layer models (in fact they are slightly worse), there is no reason to use those models for the fine grid search and we proceed with single helium layer models.

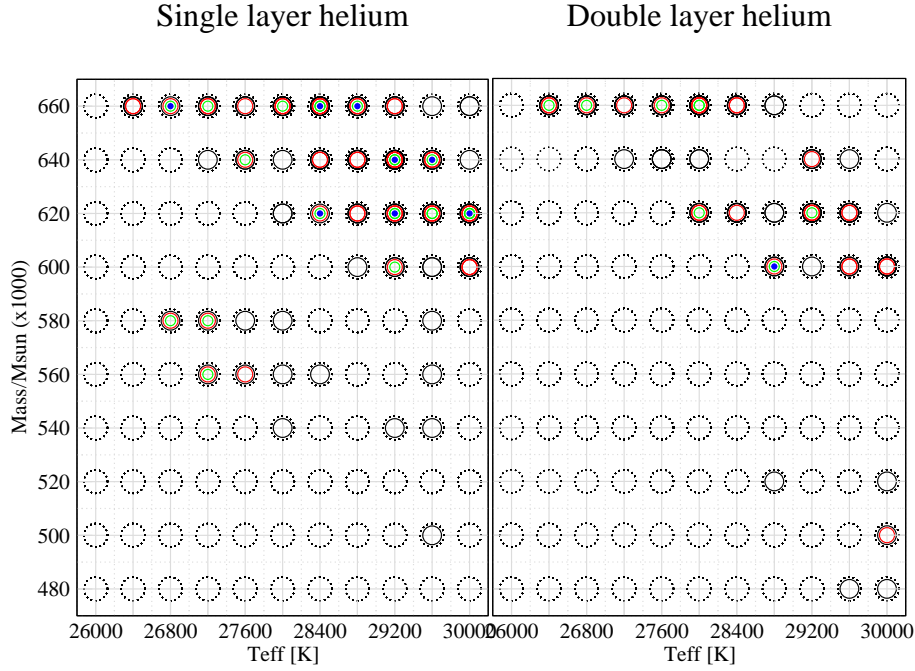


Figure 6.9: The best fit solutions in the M_* – T_{eff} plane for EC20058. The dotted circles mark the location of the grid points. The progressively filled in circles correspond to better and better fits ($\Phi < 1.75\text{s}$, 1.50s , 1.25s , and 1.00s) respectively, where Φ is defined by equation 3.1.

6.5.2 Fine grid search

From the broad grid search, we also learned that we need to extend our grid to higher T_{eff} (figure 6.9). I detail the region of parameter space I explored in table 6.3. The grid in the $M_* - T_{\text{eff}}$ plane is not square. To save computing time, I considered higher masses at lower effective temperatures and lower masses at higher effective temperatures. For a visual representation of the grid, see figure 6.12. Out of the 68580 models run, 65655 were successful and I obtained a uniform coverage of parameter space.

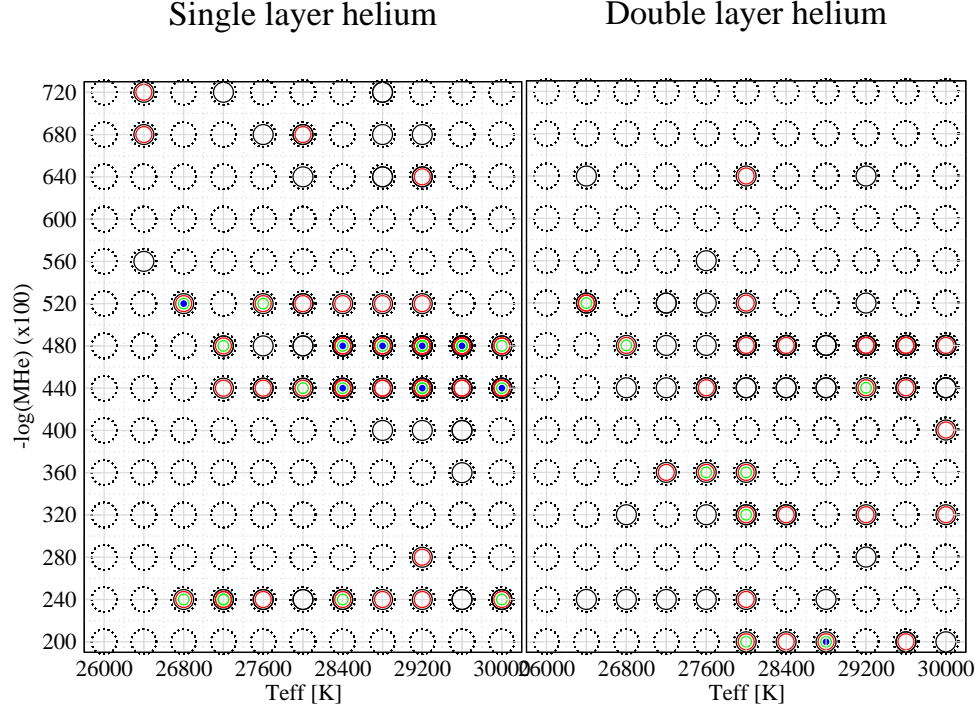


Figure 6.10: Same as figure 6.9, but in the $\log(M_{\text{He}}) - T_{\text{eff}}$ plane.

Table 6.3: Region of parameter space covered in the fine four-parameter fit and step sizes

Parameter	Range (inclusive)		Step size
T_{eff}	26600K to 30000K	30200K to 32000K	200K
M_*	0.59 M_{\odot} to 0.66 M_{\odot}	0.53 M_{\odot} to 0.63 M_{\odot}	0.01 M_{\odot}
$-\log(M_{\text{He}})$	2.0 to 5.4		0.2
X_{fm}	0.10 to 0.80		0.05

6.5.3 Results

I show the results of the fine grid search in figures 6.12, 6.13 and 6.14. For clarity, I only show the models for which $\Phi < 1$ s. The location of the best fit models in the $M_* - T_{\text{eff}}$

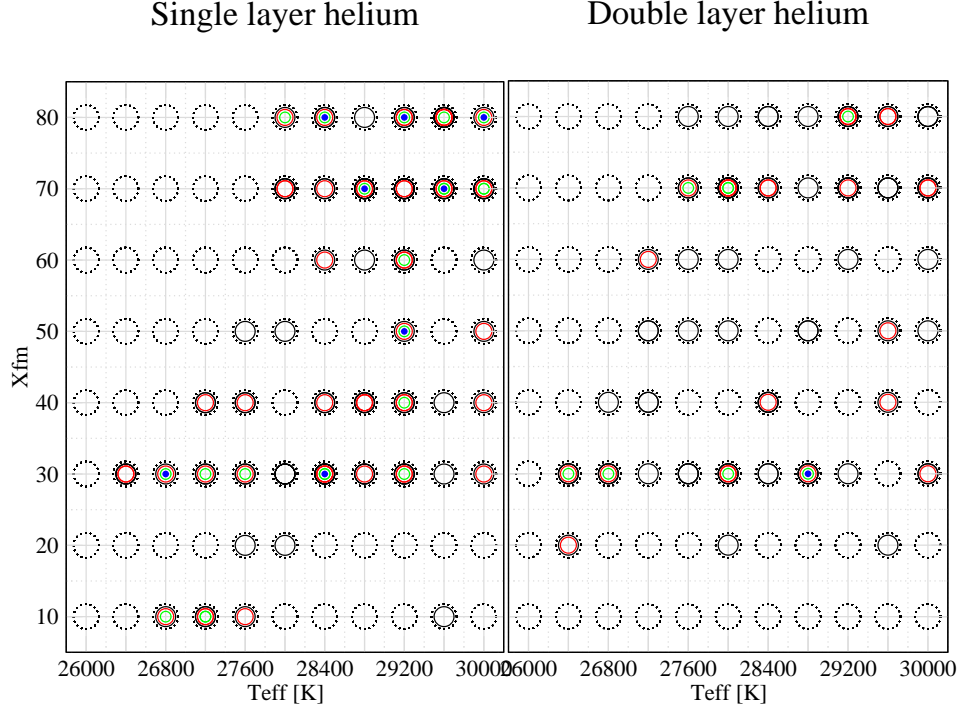


Figure 6.11: Same as figure 6.9, but in the $X_{\text{fm}} - T_{\text{eff}}$ plane.

plane depends on what X_{fm} is (compare figures 6.12 and 6.14). I color coded the models according to where they lay in the $X_{\text{fm}} - T_{\text{eff}}$ plane. The solid filled circles correspond to thin helium solutions while the shaded circles correspond to thick helium solutions (see figure 6.13). As was the case for G117-B15A and R548, we find families of best fit models, not a unique fit.

From the density of best fits, the thin helium, high X_{fm} models appear to be better. They also reach lower Φ 's, though the level of our uncertainties both in the observed periods and in the models does not allow us to draw strong conclusions from that fact. It is just another sign that those models may be better. What we can say for sure is that the helium layer mass lies between $10^{-5.3}$ and $10^{-4.1}$. For the purpose of computing \dot{P} 's for EC20058,

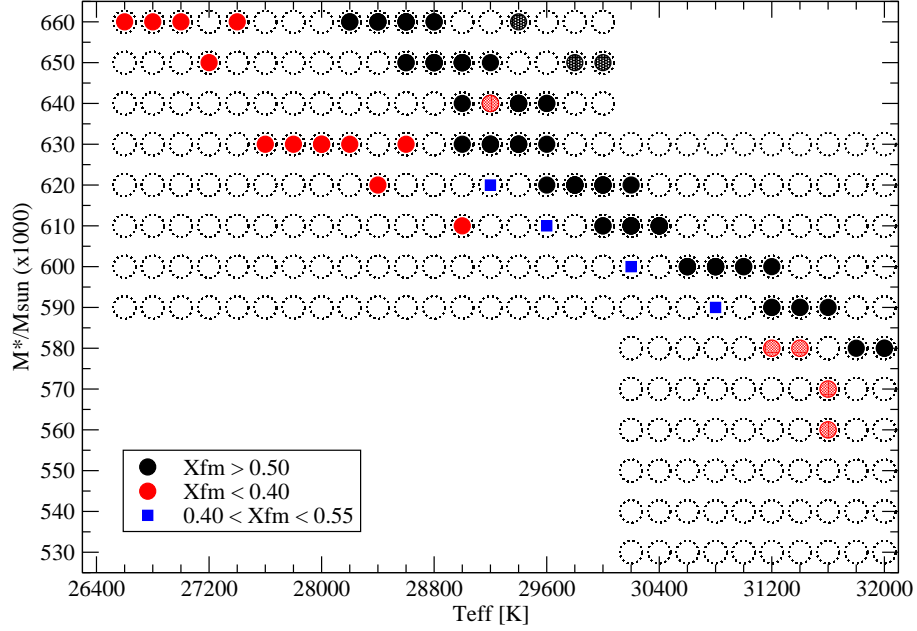


Figure 6.12: The location of the best fit models in the $M_* - T_{\text{eff}}$ plane. The dotted circles indicate the location of the grid points. Only the very best fit models are shown ($\Phi < 1\text{s}$). The circles are color coded by the models' X_{fm} value. The solid circles correspond to thin helium solutions ($-\log(M_{\text{He}}) > 3.6$) while the shaded circles correspond to thick helium solutions ($-\log(M_{\text{He}}) < 3.6$).

I define the two families of models detailed in table 6.4. Once again, I reproduce the trend in the $M_* - T_{\text{eff}}$ plane by fitting a function, quadratic this time, to the best fit models in figure 6.12.

In table 6.4, I also list the preferred mode identification for each family of models. The dominant mode identification for family 1 is $\ell = 1$, $k = 3, 5, 7$ respectively for the 195s, 257s, and 333s modes; $\ell = 2$, $k = 6$ and 10 for the 204s and 281s modes. This is the mode identification for 21 out of the top 26 models in the fine grid. The deciding factor in

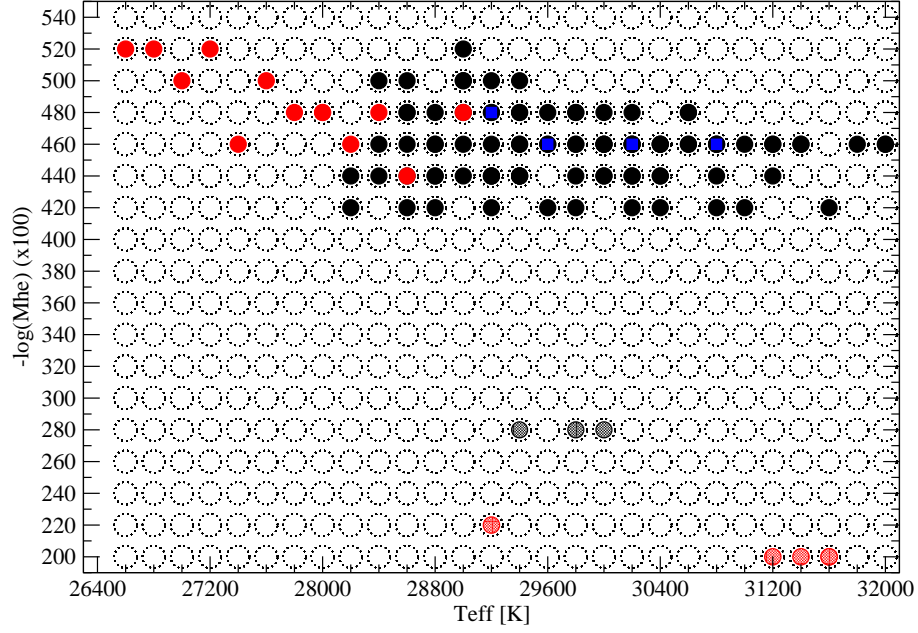


Figure 6.13: Same as figure 6.12, but in the $\log(M_{\text{He}}) - T_{\text{eff}}$ plane.

Table 6.4: The two families of best fit solutions for EC20058

	Family 1	Family 2
T_{eff} M_*/M_{\odot} $-\log(M_{\text{He}})$ X_{fm}	28100K to 32100K $= 3.30 - 1.55 \times 10^{-4} T_{\text{eff}}$ $+ 2.18 \times 10^{-9} T_{\text{eff}}^2$ 4.10 to 5.10 0.60 to 0.80	26300K to 29100K $= 2.55 - 1.16 \times 10^{-4} T_{\text{eff}}$ $+ 1.69 \times 10^{-9} T_{\text{eff}}^2$ 4.30 to 5.30 0.25 to 0.35
Mode Identification $P[s](l,k)$	195(1,3), 257(1,5), 333(1,7) 204(2,6), 281(2,10)	195(1,3), 333(1,7) 204(2,6), 257(2,9), 281(2,10)

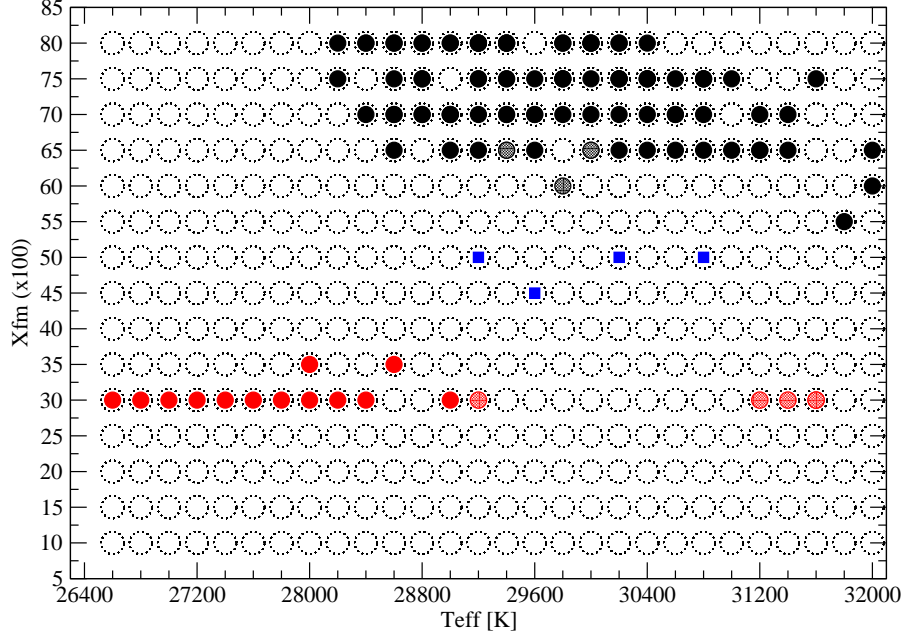


Figure 6.14: Same as figure 6.12, but in the $X_{\text{fm}} - T_{\text{eff}}$ plane.

the mode identification for family 1 appears to be the parameter X_{fm} . The 5 models that do not yield the same mode identification all have $X_{\text{fm}} \simeq 0.65$, while the majority of the models have $X_{\text{fm}} > 0.65$. The mode identification for those 5 models is also $\ell = 1, k = 3$ and 7 for the 195s and 333s mode, but $\ell = 2, k = 6, 9$ and 10 for the 204s, 257s, and 281s modes. This second mode identification is the preferred one for family 2 (10/13). The odd 3 models in family 2 follow the dominant mode identification for family 1. They all have $\log(M_{\text{He}}) \geq -4.6$.

In short, the 195s and 333s periods are $\ell = 1$ modes, $k = 3$ and 5 and the 204s and 281s periods $\ell = 2, k = 6$ and 10 modes, regardless of which family of fits we consider. The 257s mode is an $\ell = 1, k = 5$ mode for $X_{\text{fm}} > 0.65$ or $X_{\text{fm}} \simeq 0.30$ and $\log(M_{\text{He}}) \geq -4.6$.

Otherwise, it is an $\ell = 2$, $k = 9$ mode. In other words, we recover the same mode identification and therefore asteroseismologically indistinguishable models by compensating a smaller homogeneous core (X_{fm}) with a thicker helium layer. This may be a manifestation of a core-envelope symmetry in EC20058, to which the 257s mode is sensitive. Montgomery et al. (2003) describe the existence of such a symmetry, where features in the Brunt-Väisälä due to composition transitions in the core mirror the effect of such features in the envelope.

For EC20058, this symmetry is not perfect and family 1 (large homogeneous core, thin helium layer) appears to be a stronger fit. Also the 257s mode is a high amplitude mode and as such, more likely to be an $\ell = 1$ mode (geometrical effects tend to cancel out brightness variations across the surface of the star for higher ℓ modes). The deciding factor between the families will likely be the measured value of the \dot{P} for the 257s mode.

6.6 Prospective limits on plasmon neutrino rates

Having defined families of best fit models for EC20058, I proceeded with a Monte Carlo simulation to obtain the corresponding \dot{P} 's and uncertainties. According to Sullivan (2004), there is strong evidence that the two dominant modes in EC20058 (257s and 281s) are very stable and can therefore be used to measure cooling timescales for EC20058. I focused on those two modes in what follows.

6.6.1 Method

I started by generating a random population for each family of best fits detailed in table 6.4, adding a ± 0.10 scatter in mass. An example of the random populations generated is shown in figures 6.15, 6.16 and 6.17. Each population contains 500 models. For each member in the simulated populations, I also computed a model 100K hotter and one 100K cooler to allow the computation of \dot{P} 's for each mode.

In order to study the effect of varying the plasmon neutrino rates, I defined the

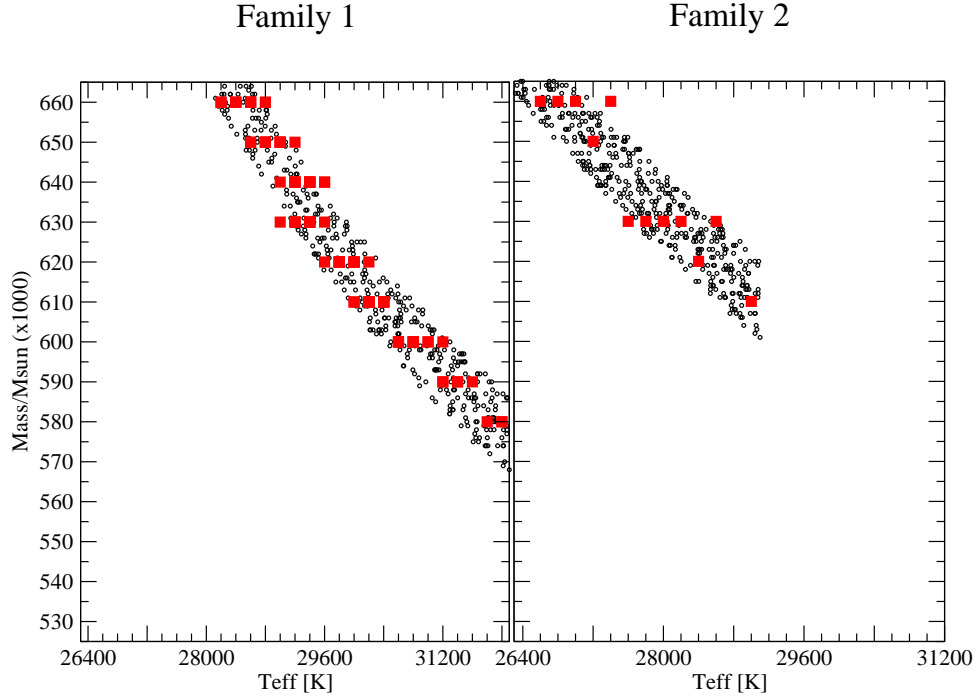


Figure 6.15: The simulated populations (small circles) for each family of best fit models listed in table 6.4 in the $M_* - T_{\text{eff}}$ plane. Each population contains 500 members. The big squares are the best fit models from the grid search ($\Phi \leq 1s$).

parameter λ as:

$$\varepsilon'_\nu = \lambda \varepsilon_\nu, \quad (6.32)$$

where ε_ν is the plasmon neutrino emission rates the theory predicts and ε'_ν is the changed rate used in the models. I varied λ between 0 and 10 and each time, generated 500 models for each family, along with hotter and cooler models to compute \dot{P} 's.

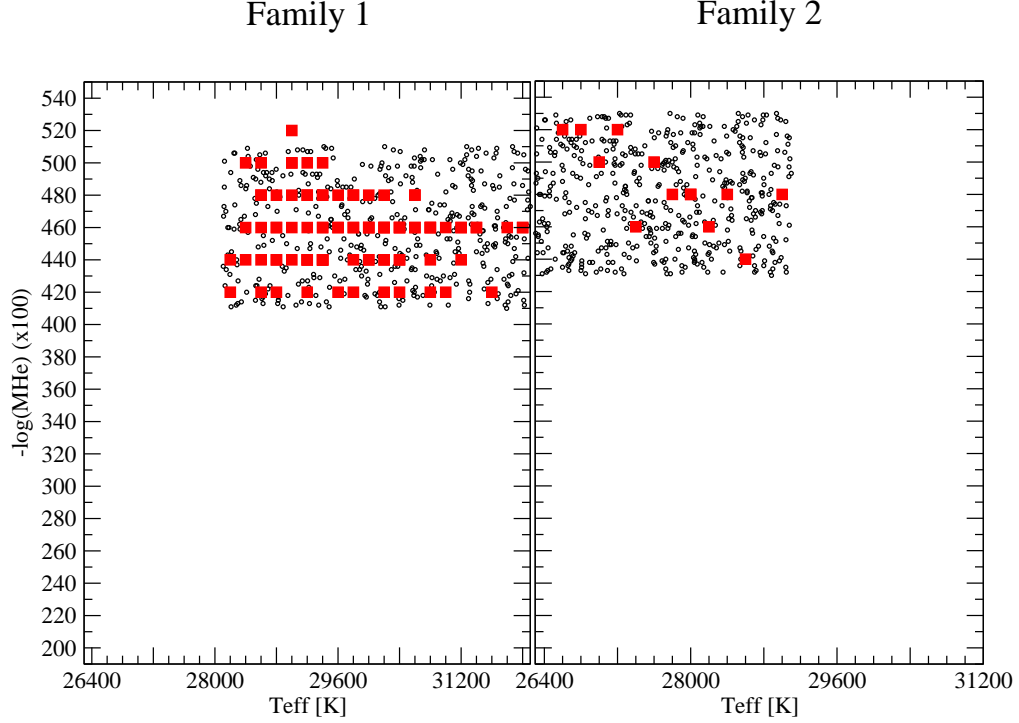


Figure 6.16: Same as figure 6.15 in the $\log(M_{\text{He}}) - T_{\text{eff}}$ plane

6.6.2 Results

To check the quality of each population, I calculated the average period each model had for the 257s mode and the 281s mode, for varying values of λ . For $\lambda = 1$, I list the periods and \dot{P} 's I find for each mode and both families of fits in table 6.5.

We get yet another hint that family 2 is not as strong a fit as family 1. For family 2, the models are 3 seconds off the 257s mode on the average, and 257s is 2 sigmas away from the sample mean. I tested the idea that this discrepancy could be due to the fact that my sample population for family 2 contained many members who were

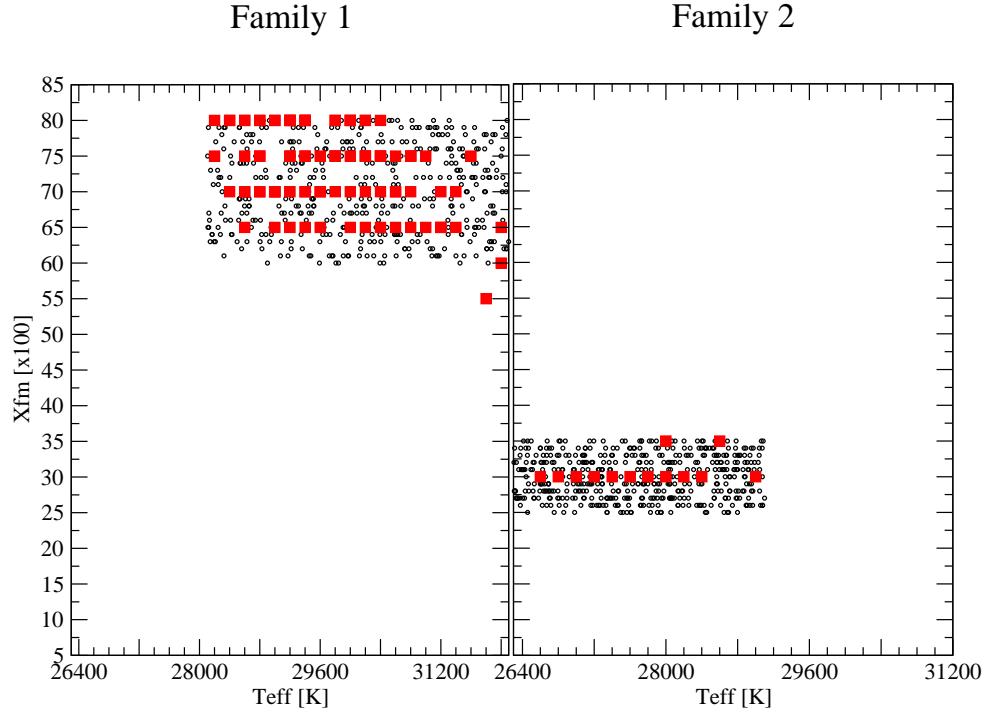


Figure 6.17: Same as figure 6.15 in the $X_{\text{fm}} - T_{\text{eff}}$ plane

Table 6.5: Average periods and \dot{P} 's for EC20058, with plasmon neutrino rates given in Itoh et al. (1996a).

Mode	Family 1		Family 2	
	257s	281s	257s	281s
P [s]	258.0 ± 2.5	280.7 ± 2.5	259.8 ± 1.6	282.6 ± 2.5
\dot{P} [10^{-14} s/s]	4.06 ± 1.08	4.63 ± 1.20	2.70 ± 0.47	3.06 ± 0.54

fairly different from the grid best fit models (see figure 6.16). I generated a new population, with helium layer masses correlated to the effective temperature through the relation

$-\log(M_{\text{He}}) = 11.9 - 2.54 \times 10^{-4} T_{\text{eff}} \pm \Delta$, where Δ was randomly chosen to be between 0 and 0.3. Doing this produced a population more tightly clustered around the grid best fit models in the $\log(M_{\text{He}}) - T_{\text{eff}}$ plane. This had a very small effect on the average period and standard deviation and failed to solve the discrepancy.

In figure 6.18, I show the periods as a function of λ for each family of best fit models, with one sigma error bars. Figure 6.18 strikingly illustrates the fact that varying the plasmon neutrino rates has little effect if any on the period spectrum.

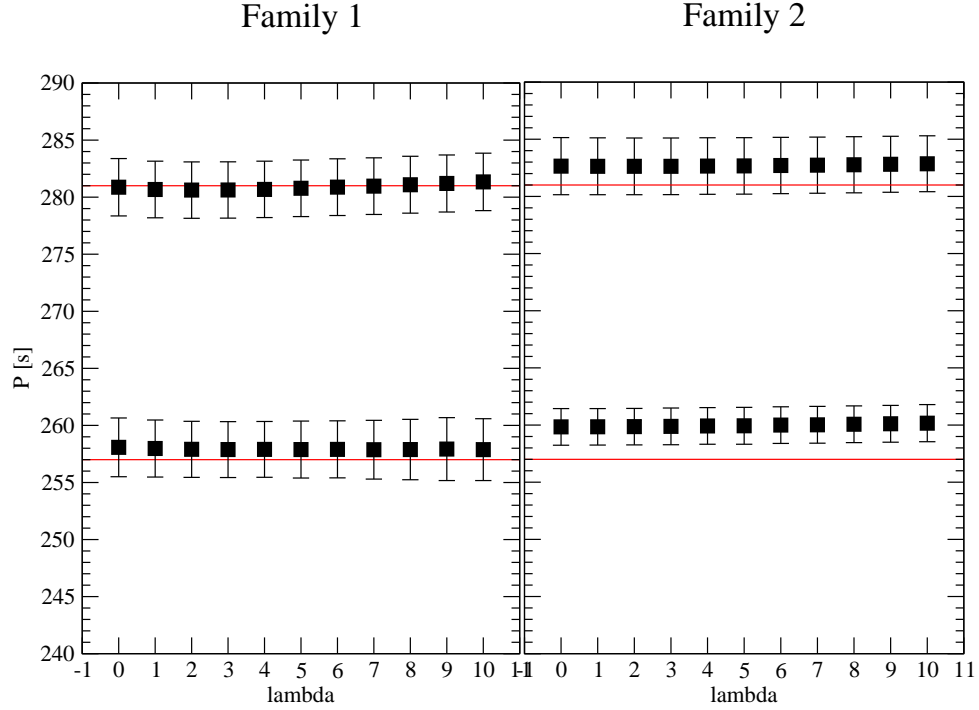


Figure 6.18: The average period for the 257s mode and 281s mode for each family of best fit models. The horizontal lines show the observed values of those two modes. Each point is shown with 1 sigma error bars.

In figure 6.19, I display the \dot{P} 's for each family of models as a function of the

parameter λ . I am including family 2 solutions for completeness, though at this point we have good reasons to trust family 1 solutions more. Each point in figure 6.19 was obtained assuming gaussian distributions and I did not include those that could not be fit reasonably well with a gaussian. The error bars are again 1 sigma error bars. To obtain the gray shaded region, I performed linear fits to the top of the error bars and to the bottom of the error bars.

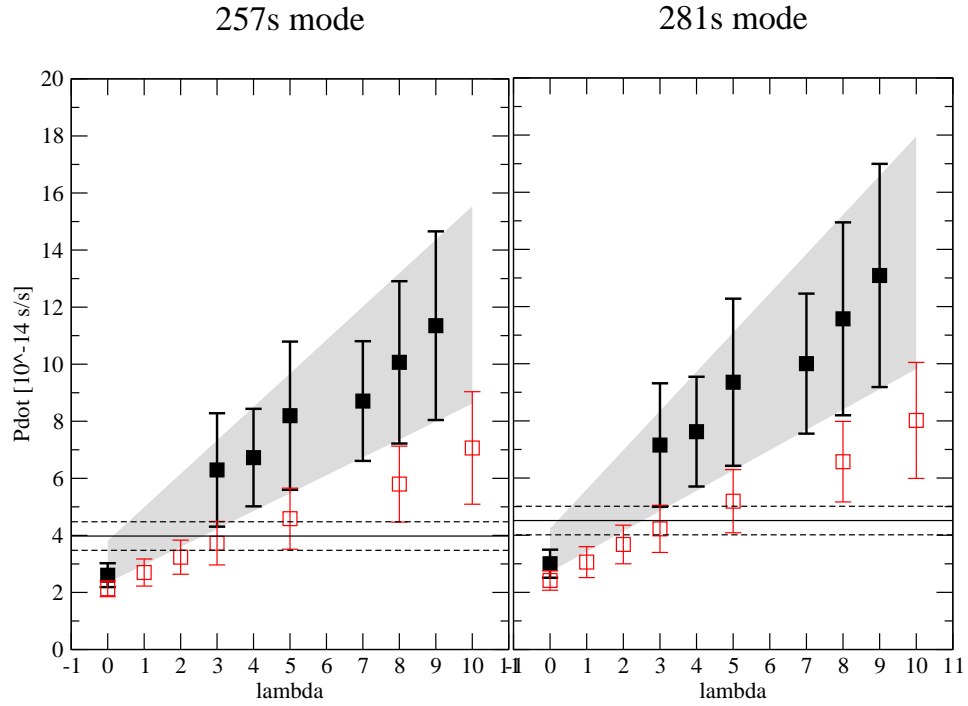


Figure 6.19: The \dot{P} 's predicted for each mode with 1 sigma error bars. The filled symbols correspond to family 1 best fit models and the open symbols to family 2. The horizontal lines are an example of a measured \dot{P} we could obtain for EC20058.

We have set the stage to constrain plasmon neutrino rates from EC20058's \dot{P} . While we do not have a value for that quantity yet and therefore cannot draw conclusions on whether the plasmon neutrino rates are what we think they should be (e.g. whether $\lambda = 1$),

we can make a statement about how tightly we will be able to constrain those rates once we know \dot{P} for EC20058. Assuming the timing errors on EC20058 are comparable to those for G117-B15A, we can estimate that the error bars on the measured \dot{P} should be comparable to those we had on G117-B15A's \dot{P} . To take into account that we do not have 30 years of data on EC20058 (though early data on G117-B15A was taken with phototubes and was of lower quality than later data taken with CCD's), let us assume error bars of 0.5×10^{-14} s/s, based on the ones we had in 1991 for G117-B15A (0.35×10^{-14} s/s, Kepler et al., 1991b).

As an illustration, let us assume that the measured \dot{P} is just as we expect it. I included the corresponding lines in figure 6.19. With error bars of 0.5×10^{-14} , we would be able to tell that the neutrino rates are correct to within a factor of 3 or 4, but we would not be able to rule out the possibility that plasmon neutrinos are not being emitted by the star. To establish the existence of plasmon neutrinos in this scenario, we would require error bars smaller than $\sim 0.2 \times 10^{-14}$ s/s, an achievable goal.

Chapter 7

Conclusions

7.1 The big picture

We set out to place constraints on the emission rates of plasmon neutrinos and axions, both weakly interacting particles that carry energy away from white dwarf interiors and contribute to their cooling. While we know neutrinos exist, plasmon neutrinos are a special breed of neutrinos, yet unobserved. Axions are even more mysterious. They have not been detected conclusively, but if they exist and have the right mass, they could account for the dark matter and perhaps even the dark energy that pervade our universe. Their emission rate depends on their mass and constraining the former determines the latter.

We saw that the pulsating periods of white dwarfs become longer as the stars cool. Some pulsating white dwarfs are very stable clocks, losing less than a second every 8 million years, that is 1 “tick” (one 215s cycle) every 1.7 billion years. For such white dwarfs, we can measure rates of period change (\dot{P} 's) very accurately. We have a well measured \dot{P} , based on over 30 years of data for G117-B15A. We used that number to constrain the axion mass to be less than 26.5 meV. EC20058, a hotter pulsating white dwarf than G117-B15A, also shows stable modes. Its \dot{P} may be used to constrain the plasmon neutrino rates. We made a prediction of how well EC20058's \dot{P} will allow us to constrain the plasmon neutrino

rates once we know its \dot{P} .

In order to constrain the axion and plasmon neutrino emission rates, we had to produce believable models of the relevant stars. To that end, we performed the asteroseismological analysis of G117-B15A and its sister R548 and of EC20058, using fine grid searches. This method, while simple, had not been tried before because of the large amount of computing time involved. Along the way, we learned about the behavior of the function to minimize, the difference between the observed and the calculated periods. We found that we cannot, with period matching alone, single out a unique best match model. We have to rely on additional information, such as the \dot{P} 's themselves, and spectroscopy.

7.2 What we found

7.2.1 Asteroseismology of G117-B15A and R548 and the axion mass

In chapter 5, we studied the two similar DAVs, G117-B15A and R548. We find best fit models for both between 11600 and 12700K and between 0.59 and 0.66 M_{\odot} . In both cases, the region occupied by the best fit models in the $M_{*} - T_{\text{eff}}$ plane is related to the thickness of the hydrogen layer. The lowest period mode for each star (215s for G117-B15A and 213s for R548) singlehandedly sets the helium layer mass to $10^{-2.4}$ for both star. Both stars are well fit with thin hydrogen layer models ($10^{-7} < M_H < 10^{-8}$). For G117-B15A, we find a second family of solutions between 11300 and 12300K and between 0.65 and 0.68 M_{\odot} . Those fits have slightly thicker hydrogen layers ($M_H = 10^{-6.2}$).

For R548 we find a unique, robust mode identification. The dominant modes (213s and 274.5s) are $\ell = 1, k = 1, 2$ modes. The 318s mode is also an $\ell = 1$ mode, with $k = 4$. The last two modes (187s and 334s) are $\ell = 2, k = 4$ and 8 respectively. For G117-B15A, we find two distinct families of best fit models. Models with $-\log(M_H) < 6.4$ all have the same mode identification, namely $k = 2, 3$ and 4 for G117-B15A's three observed periods (215s, 271s, and 304s). The latter are all identified as $\ell = 1$ through multi-wavelength high

speed photometry (Robinson et al., 1995). Models with $-\log(M_H) > 6.4$ are consistent with G117-B15A's periods being $k = 1, 2$ and 3. R548 and G117-B15A have similar observed properties and based on that fact, it is likely that they have similar structures. In this case, the second class of models seems better. However, we cannot discard the first class of models based on a hunch alone.

I concluded chapter 5 by computing \dot{P} 's for the 215s mode in G117-B15A and the 213s mode in R548 for axion free models at first, and then including axions of different masses. The zero axion model for G117-B15A have a \dot{P} of $2.98 \pm 0.17 \times 10^{-15}$ s/s, consistent with the observed value of $3.57 \pm 0.82 \times 10^{-15}$ s/s. The zero axion models for R548 have a similar \dot{P} ($\sim 3 \times 10^{-15}$ s/s), also consistent with the best current limit on \dot{P} for R548's 213s mode. If we believe that G117-B15A must be similar to R548, then we find an upper limit on the axion mass of 13.5 meV. Otherwise, a second family of solution requires the existence of axions with a mass ranging between 10.4 and 26.5 meV. Together, those constraints point to an upper mass limit of 26.5 meV for axions. While this limit may not be as low as we would like it to be, it is a very sound limit. An even longer data baseline for G117-B15A will reduce the size of the error bars on the measured \dot{P} . It is merely a question of time until we can place an even tighter constrain on the axion mass.

7.2.2 Asteroseismology of EC20058 and plasmon neutrino rates

For EC20058, we found two families of fits. Each family lies on distinct, clearly defined trends in the $M_* - T_{\text{eff}}$ plane. We are unable to constrain the effective temperature and mass of EC20058 better than spectroscopy does. All we can say is that the best fit models are between 23600K and 32100K, and more likely between 28100K and 32100K. The corresponding mass bounds are $0.58 M_\odot - 0.66 M_\odot$. The upper mass limit is influenced by the spectroscopic bounds ($\sim 0.5 - 0.6 M_\odot$) and most astronomers in the field (including me) would feel uncomfortable considering higher masses for EC20058. In retrospect, knowing now that our asteroseismological models tend to be hot and/or massive, perhaps we should

play the naive game all the way and include the whole range of good asteroseismological fits.

The two families of solutions separate out according to the value of the parameter X_{fm} , the size of the homogeneous carbon-oxygen core. Family 1 has a large core ($X_{\text{fm}} \geq 0.60$), while family 2 has a rather small, precisely determined $X_{\text{fm}} \simeq 0.3$. Family 1 appears to be a stronger minimum in parameter space than family 2 is, but considering modeling and observing uncertainties, we cannot discard family 2 on that basis alone.

We get another clue that family 2 may not be a real solution from mode identification. For both families, the 195s and 333s modes are $\ell = 1, k = 3$ and 7 modes and the 204s and 281s modes $\ell = 2, k = 6$ and 10 respectively. For family 1, the 257s mode is an $\ell = 1, k = 5$ mode, while for family 2, it is an $\ell = 2, k = 9$ mode. We also found that we recovered the $\ell = 1, k = 5$ identification for the 257s mode if we took a family 2 model ($X_{\text{fm}} \simeq 0.3$) and made the helium layer thicker. This is strong evidence that the 257s mode in EC20058 is sensitive to a core-envelope symmetry and it suggests that family 2 may be a reflection of family 1, not a real solution.

A Monte Carlo simulation gives an additional clue that something may be amiss with family 2. The 257s mode for the simulated population has a period of 259.8 ± 1.6 s, 3 seconds off. For family 1, the \dot{P} we find from the Monte Carlo simulation is 4.06 ± 1.08 s/s for the 257s mode and 4.63 ± 1.20 s/s for the 281s mode (with the plasmon neutrino rates of Itoh et al., 1996a). The \dot{P} 's for family 2 are $2.70 \pm 0.47 \times 10^{-14}$ s/s and $3.06 \pm 0.54 \times 10^{-14}$ s/s respectively. Once we have a value for the observed \dot{P} 's of those two modes, we should be able to constrain the plasmon neutrino rates to within a factor of 3 or 4, but with the baseline of data we have so far and if I estimated the size of the error bars correctly, we are unlikely to be able to rule out models with no neutrino emission. Measured \dot{P} 's may also put the final nail in the family 2 coffin.

7.3 What now?

While some interesting results came out of this work, there are lingering questions and problems.

1. What are EC20058's \dot{P} 's and what do they imply for plasmon neutrino rates?
2. Why are the asteroseismological fits systematically too massive and/or hot?
3. Can we narrow down the asteroseismological fits further?
4. If we measure a \dot{P} higher than expected for a given white dwarf, how do we know whether it is due to cooling by axions or by neutrinos, or that our models are predicting \dot{P} correctly in the first place?

As I mentioned numerous times, we have the data at hand to determine \dot{P} 's for the 257 and 281s modes in EC20058. Once we have those results, we can use the results of chapter 6 (figure 6.19) to constrain the plasmon neutrino rates. Nature may surprise us yet again.

In chapters 5 and 6 I explored a number of factors that could influence the location of the best fit models in the $M_* - T_{\text{eff}}$ plane. They included the thickness of the hydrogen and helium layer masses, the shape of the helium abundance profile, and the shape of the core composition profiles. Varying those factors within reasonable bounds merely changed the location of the best fit models along a stubborn trend in the $M_* - T_{\text{eff}}$ plane, that lied at masses and effective temperatures higher than those predicted by spectroscopy.

In chapter 3, I systematically compared the effect of all the modeling uncertainties I could think of (or at least those I could test) on the periods. I did not include in my analysis the core equation of state and the opacities. Both have the potential to significantly alter the structure of the models and the fact that our models appear to be systematically too hot and/or massive may be indicative of a problem with the core equation of state or the opacities. Just recently, Cassisi et al. (2007) published new electron-conduction opacities

that treat the partially degenerate regime relevant in white dwarf envelopes better. While according to Cassisi et al., the new opacities differ only by about a factor of 2 at most in white dwarf envelopes and have very little effect on the mass-radius relation or white dwarf ages, it would be worth checking what effect new opacities would have on our models. It would also be good to test the effect of the core equation of state. We are working on including new equation of state tables from Los Alamos National Lab.

White dwarf asteroseismology allows us to constrain best fit models to small regions of parameter space, and also to place limits on quantities we cannot determine by any other means. If we want to further constrain the models, we need to use additional clues. Spectroscopy gives effective temperatures and surface gravities. For DAs, spectroscopically determined temperatures are known to within 600 degrees or better. While those are fairly large uncertainties, they at least help narrow down the allowable range of asteroseismological fits. For DBVs, spectroscopy is not as successful. The uncertainties on spectroscopically determined effective temperatures for DBVs can be as high as 2000K. In order to use clues from spectroscopy, we need to calibrate our models to the spectroscopy. The precision of the calibration and of future asteroseismological fits depend on how tightly we can determine effective temperatures and gravities from spectroscopy.

We now come to question number 4. If our model's \dot{P} 's do not match the observed ones, how do we know whether it is due to an unseen source of energy loss or a problem with the models? Of course if the calculated \dot{P} is too high, then the only explanation is that the models are not right. Any unseen source of energy loss would only increase the calculated \dot{P} and make matters worse. If it is too low, then we have to rely on additional clues to assess the quality of our models, such as the periods themselves, their spacing if we have a rich enough period spectrum and spectroscopy, and use our best scientific judgment.

The second part of the question is, assuming we trust our models, how can we tell that the extra source of energy loss is due to neutrinos or axions or both? Looking at a single star, we have to make an educated guess of what the physical process is responsible

for the extra source of cooling and we draw conclusions on the details of that physical process based on how the calculated \dot{P} compares with the observed one. For G117-B15A, we assumed that the predicted plasmon neutrino rates were close enough to the actual ones so that if G117-B15A was cooling because of weakly interacting particles streaming out they could not be neutrinos and we assumed, for the sake of argument, that they were axions. Since plasmon neutrino rates are solidly rooted in the Standard Model, this was not a big leap to make. Any results we obtained with G117-B15A will be greatly strengthened by the analysis of other DAVs. In section 2.4.2, I gave a progress report on where we stand with measuring \dot{P} 's. In the near future, we can expect at least 9 new \dot{P} 's. Even if only a fraction of them prove to be evolutionary timescales useful for this study, they will help us place unprecedented limits on the axion mass.

For EC20058 and DBVs in general, the situation is not as clear-cut, as axions and neutrinos are both possible sources of energy loss. In chapter 6, I made the somewhat non-scientific assumption that axions did not contribute to the cooling of EC20058. One could easily turn the argument around, assume that the predicted plasmon neutrino rates are right, and that any extra source of cooling is due to axions. This approach could potentially help us place a strong upper limit on the axion mass, as the axion luminosity is a function of the axion mass squared, and is higher than the neutrino luminosity in hot DBV models even for relatively low axion mass (~ 6 meV).

The key to untangling the effect of plasmon neutrinos from the effect of axions is to study more than one star. As we saw in chapter 6, plasmon neutrino emission is heavily dependent on the mass of the star, with massive models being less favorable to plasmon neutrino emissions. For instance, we do not expect massive DBVs to emit any neutrinos at all. This presents us with the challenge of finding more stable DBVs. Recently Nitta et al. (2005) reported the discovery of 4 new DBVs. At least one of them has short period modes, like EC20058, and could be stable. It would be worth performing follow-up observations of that star and of the other 3 as well. Eisenstein et al. (2006) report the discovery of about

6000 new white dwarfs from the Sloan Digital Sky Survey archive (fourth data release), multiplying by 3 the number of known white dwarfs and bringing the number of known DBs up to 700. If we search that sample for pulsating DBs, we can expect to triple the number of known DBVs and find about 20 new ones.

Appendix A

Axions in the White Dwarf Evolution Code

A.1 Modifications to the WDEC to include axions

The simplest way to include axions in the WDEC was to treat them as an extra neutrino emission process. Physically, it is after all another source of energy loss. We called the axion emission rate per unit mass “fa” and added it to “fn”, the neutrino emission rate per unit mass. I list below the changes made to the WDEC itself. Most of them involve the inclusion of fa as a common block variable and extra source of energy loss. We also want to write it out to the relevant files (which means changing a few format and write statements). At some point we call the subroutine “axions” to compute fa. To compute the axion emission rate, we need the axion mass. This is given in the standard WDEC input file, on a new line right after line 11.

In subroutines `calc`, `cshell`, `homo`, `interp`, `ledouxc`, and `read2`, add the variable `fa` to common block `thermo`.

```
common/thermo/u2,up2,ut2,e2,ep2,et2,psi2,pg,o2,op2,ot2,fp,ft,
```

1


```
en2(5),fn,fcc,ce,ci,cif,w,nu,fa
```

In subroutine `istat1`, add the variable `fa2` to common block `thermo`.

```
common/thermo/u2,up2,ut2,e2,ep2,et2,psi2,pg,o2,op2,ot2,fp,ft,      1
en2(5),fn,fcc,ce,ci,cif,w,nu,fa2
```

In subroutine `calc`, add axion emission to the neutrino loss rate.

```
c      qn2=(fcc-fn)*qx
      qn2=(fcc-fn-fa)*qx
```

In subroutines `istat1`, `istatco`, `neu`, `neutrino`, and `gnutrino`, add the variable `fa` to common block `neut`

```
common/neut/en(5),fn,fa
```

In subroutines `istat1` and `istatco` call the axions subroutine right after the neutrino routines calls and add the axion energy loss to the total emission rate.

```
      if (nu .le. 0) then
          fn=0
      elseif(nu .eq. 1)then
call venerable BPS neutrino rates
          call neu(d,t)
      elseif(nu .eq. 2)then
call Munkata etal Plasmon, Photo, and Pair rates
          call neutrino(d,t)
      elseif(nu .eq. 3)then
call Itoh etal neutrino rates
          call gnutrino(d,t)
      endif
-->      call axions(xc,d,t,epsaxion)
-->      fa=epsaxion
-->      f=fn-fcc*w + fa
```

In subroutines `istat1` and `istatco` after the line

```
fn2=fn
```

Add the line

```
fa2=fa.
```

In subroutine `read2` add the common block `ax`.

```
common/ax/amaxion
```

In subroutine `read2` modify format statement number 333 to include one more float.

```
333      format(9(1x,f8.4))
```

In subroutine `read2`, after line 11 of the input file is read and processed, read and save the axion mass.

```
read *,ip5,ip6,ip7,nmod,nitel,m,md,nu,ip8,ip1,irdold,ip40
```

```
print *, ' nmod:',nmod
```

```
print *, ' ip40:',ip40
```

```
if(nu .le. 0)then
```

```
    print *, 'neutrino-less models'
```

```
elseif(nu .eq. 1)then
```

```
    print *, 'old BPS neutrino rates'
```

```
elseif(nu .eq. 2)then
```

```
    print *, 'Munkata etal neutrino rates'
```

```
elseif(nu .eq. 3)then
```

```
    print *, 'Itoh etal neutrino rates'
```

```
endif
```

```
write(20,*) ' nmod:',nmod
```

```
write(20,*) ' ip40:',ip40
```

```
C.....
```

```
c new in input file:  read in axion mass in eV
```

```
C.....
```

```

      read *,amaxion
      print *, 'amaxion =', amaxion

```

In subroutine write1 (entry write1 in subroutine read2), initialize the axion luminosity at the same time as the neutrino luminosity.

```

      bnt=1.e-10
      bax =1.e-10

```

In subroutine write2 (entry write2 in subroutine read2), compute the axion luminosity after the neutrino luminosity.

```

      bnt=bnt+fn*xr
      bax=bax+fa*xr

```

In subroutine write3 (entry write3 in subroutine read2), take the log of the axion luminosity after taking that of the neutrino luminosity.

```

      bnt=dlog10(bnt)
      bax =dlog10(bax)

```

In subroutine write3 (entry write3 in subroutine read2), output the axion luminosity next to the neutrino luminosity.

```

      write(51, 333) (bn(i),i=1,5),bnt,bgrav,bl,bax
      write(1,161) modnr,sg,p2,t2,ucent,rm,tel,bl,bnt,bax,
      write(9,161) modnr,sg,p2,t2,ucent,rm,tel,bl,bnt,bax,
      write(1,161) modnr,sg,p2,t2,ucent,rm,tel,bl,bnt,bax,10.**amxc
      write(9,161) modnr,sg,p2,t2,ucent,rm,tel,bl,bnt,bax,10.**amxc
      write(20,161) modnr,sg,p2,t2,ucent,rm,tel,bl,bnt,bax,10.**amxc
      write(50,161) modnr,sg,p2,t2,ucent,rm,tel,bl,bnt,bax,10.**amxc

```

In the same subroutine, also modify format 161 to accommodate one more float.

```

      161 format(i4,1p,e12.4,0p,f7.3,2f6.3,f7.3,f9.6,3f9.4,2f7.3)

```

A.2 Subroutine axions

I used the fits to numerically evaluated axion emission rates given in Nakagawa et al. (1987, 1988). The fitting formulae used depend on the state of the interior, determined by the parameter

$$\Gamma = 2.275 \times 10^{-1} \frac{Z^2}{T_8} \left(\frac{\rho_6}{A} \right). \quad (\text{A.1})$$

For an average carbon core white dwarf model, $A = 12$ and $Z = 6$, in the center $T \sim 10^7 K$ ($T_8 = 0.1$) and $\rho \sim 10^6 g/cc$ ($\rho_6 = 1$), so that $\Gamma \sim 36$. Lattice and phonon contributions to the axion emission rate become important only when $\Gamma > 178$. We would not expect such conditions to exist anywhere in most of the models we run (especially not pulsating white dwarfs, which do not go below $\sim 11,000$ K in effective temperature), but we nonetheless include lattice and phonon contributions, for completeness.

```

C*****
c Axion rates according to Nakagawa, Kohyama and Itoh (1987),
c Ap.J. 322, 291 and Nakagawa, Adachi, Kohyama and Itoh (1988),
c Ap.J. 326, 241 (phonon contributions). Coupling constant g given in
c Isern, Hernanz and Garcia-Berro (1992), Ap.J. 392, L23.
C*****
c June 2004, Agnes.
C*****

```

```

subroutine axions(Xc, d, t, epsaxion)

```

```

c amaxion is actually  $m_a * \{\cos^2(\beta)\}$ , the "mass" of the
c axion in eV. It is an input parameter, defined in the input file.

```

```

implicit none
double precision pi,T8,T7,rho,rho6,gamma,g,alphaa,epsaxion,
1      d,t,Fliquid,Flatrice,Fphonon,Xc,F12,F16,Zc,Zo,Ac,Ao,
2      gammc,gammo,eps\_c,eps\_o,Xo
common/ax/amaxion
double precision amaxion

```

```

pi = 3.14159265

```

```

Xo=1.-Xc

```

```

Zc=6.

```

```

Zo=8.

```

```

Ac=12.

```

```

Ao=16.

```

c First calculate gamma, which is a measure of the degree of
c crystallization

```

T8 = 10**t/1.d8

```

```

T7 = 10**t/1.d7

```

```

rho = 10**d

```

```

rho6 = 10**d/1.d6

```

```

gammc = 2.275d-1 * Zc**2/T8 *(rho6/Ac)**(1./3.)

```

```

gammo = 2.275d-1 * Zo**2/T8 *(rho6/Ao)**(1./3.)

```

```

gamma = Xc*gammc + Xo*gammo

```

c For gamma < 178 (non-crystallized), contribution from Fliquid

```

    if (gamma .le. 178.) then
        call calcFliquid12(rho, gammc, Fliquid)
        F12 = Fliquid
        call calcFliquid16(rho, gammo, Fliquid)
        F16 = Fliquid
    end if

c For gamma > 178 (crystallized), contribution from Flattice and
c Phonon
    if (gamma .ge. 178.) then
        call calcFlattice12(rho, gammc, Flattice)
        call calcFphonon12( rho, gammc, Fphonon)
        F12 = Flattice + Fphonon
        call calcFlattice16(rho, gammo, Flattice)
        call calcFphonon16( rho, gammo, Flattice)
        F16 = Flattice + Fphonon
    end if

    g = 8.5e-11/3.*amaxion
    alphas = g**2/(4*pi)
    eps\_c = 1.08d23 * alphas * Zc**2/Ac * T7**4 * F12
    eps\_o = 1.08d23 * alphas * Zo**2/Ao * T7**4 * F16
    epsaxion = Xc*eps\_c + Xo*eps\_o

end

```

Subroutine axions calls the following subroutines:

C*****

```

subroutine calcFliquid12(rho, gamma, Fliquid)

implicit none
integer i
double precision c,d,g,h,rho,gamma,Fliquid,rho6,u,v,F1,F160,
1      logFliquid,pi

```

Coefficients for C12

```

double precision a(0:4),e(0:4),b(4),f(4),alpha(0:3)
data a / 2.7337,-0.8648,-0.2367,-0.0715,-0.0477 /
data e / 3.1029,-1.0355,-0.247, -0.0551,-0.0558 /
data b      /-0.345, -0.0135, 0.0132, 0.0022 /
data f      /-0.3332, 0.0271, 0.005, -0.0026 /
data alpha /-0.3423, 2.2053,-2.1415, 1.3474 /

```

```

pi = 3.14159265

```

```

c=-0.1395

```

```

d=-1.3894

```

```

g=-0.3146

```

```

h=-1.3409

```

```

rho6 = rho/1.e6

```

```

u = 2.*pi*(log10(rho)+5.)/18.

```

```

v = 0

```

```

do i=0,3

```

```

        v = v + alpha(i) * gamma**(-real(i)/3.)
    enddo

    F1 = a(0)/2. + c*u + d
    F160 = e(0)/2. + g*u + h

    do i=1,4
        F1 = F1 + a(i)*cos(real(i)*u) + b(i)*sin(real(i)*u)
        F160 = F160 + e(i)*cos(real(i)*u) + f(i)*sin(real(i)*u)
    enddo

    logFliquid = v*F1 + (1.-v)*F160
    Fliquid = 10**logFliquid

end

c*****
subroutine calcFliquid16(rho, gamma, Fliquid)

implicit none
integer i
double precision c,d,g,h,rho,gamma,Fliquid,rho6,u,v,F1,F160,
1    logFliquid,pi

Coefficients for O16
double precision a(0:4),e(0:4),b(4),f(4),alpha(0:3)

data a / 2.7258,-0.862, -0.2375,-0.0717,-0.0468 /

```



```

data e / 3.1015,-1.0292,-0.2499,-0.0572,-0.0553 /
data b      /-0.3408,-0.0139, 0.0142, 0.0029 /
data f      /-0.34  , 0.0218 ,0.0077,-0.003  /
data alpha /-0.1407, 0.4307, 1.9644,-1.2932 /

pi = 3.14159265

c = -0.1258
d = -1.4084
g = -0.2959
h = -1.3475

rho6 = rho/1.e6
u = 2.*pi*(log10(rho)+5.)/18.
v = 0
do i=0,3
    v = v + alpha(i) * gamma**(-real(i)/3.)
enddo
F1 = a(0)/2. + c*u + d
F160 = e(0)/2. + g*u + h
do i=1,4
    F1 = F1 + a(i)*cos(real(i)*u) + b(i)*sin(real(i)*u)
    F160 = F160 + e(i)*cos(real(i)*u) + f(i)*sin(real(i)*u)
enddo

logFliquid = v*F1 + (1.-v)*F160
Fliquid = 10**logFliquid

```

end

C*****

subroutine calcFlattice12(rho, gamma, Flattice)

implicit none

integer n

double precision k,l,r,s,rho,gamma,Flattice,rho6,u,w,F180,

1 F5000,logFlattice,pi

Coefficients for C12

double precision i(0:4),p(0:4),j(4),q(4),beta(0:3)

data i / 3.565, -1.1495, -0.2968, -0.0738, -0.0694 /

data p / 3.621, -1.1746, -0.297, -0.0745, -0.0696 /

data j / -0.4141, 0.0072, 0.0007, -0.003 /

data q / -0.4223, 0.012, 0.0007, -0.0033 /

data beta / 0.1906, -5.6458, 32.461, 142.6 /

pi = 3.14159265

k=-0.3664

l=-1.7456

r=-0.4079

s=-1.4663

rho6 = rho/1.e6

```

u = 2.*pi*(log10(rho)+5.)/18.
w = 0
do n=0,3
    w = w + beta(n) * gamma**(-real(n)/3.)
enddo
F180 = i(0)/2. + k*u + l
F5000 = p(0)/2. + r*u + s
do n=1,4
    F180 = F180 + i(n)*cos(real(n)*u) + j(n)*sin(real(n)*u)
    F5000 = F5000 + p(n)*cos(real(n)*u) + q(n)*sin(real(n)*u)
enddo

logFlattice = w*F180 + (1.- w)*F5000
Flattice = 10**logFlattice

end

C*****
subroutine calcFlattice16(rho, gamma, Flattice)

implicit none
integer n
double precision k,l,r,s,rho,gamma,Flattice,rho6,u,w,F180,
1      F5000,logFlattice,pi

Coefficients for 016
double precision i(0:4),p(0:4),j(4),q(4),beta(0:3)

```

```

data i / 3.3487,-1.0898, -0.2755, -0.067 , -0.063 /
data p / 3.3263,-1.0877, -0.2682, -0.0686, -0.0621 /
data j      / -0.3875, 0.0113, 0.0049, -0.0042 /
data q      / -0.4107, 0.0197, 0.003 , -0.0036 /
data beta   / 0.2263, -7.7843, 66.147, 13.781 /

pi = 3.14159265

k=-0.3303
l=-1.6563
r=-0.4079
s=-1.1416

rho6 = rho/1.e6
u = 2.*pi*(log10(rho)+5.)/18.
w = 0
do n=0,3
    w = w + beta(n) * gamma**(-real(n)/3.)
enddo
F180 = i(0)/2. + k*u + l
F5000 = p(0)/2. + r*u + s
do n=1,4
    F180 = F180 + i(n)*cos(real(n)*u) + j(n)*sin(real(n)*u)
    F5000 = F5000 + p(n)*cos(real(n)*u) + q(n)*sin(real(n)*u)
enddo

logFlattice = w*F180 + (1.- w)*F5000

```

```

    Flattice = 10**logFlattice

end

C*****
    subroutine calcFphonon12(rho, gamma, Fphonon)

    implicit none
    integer n
    double precision k,l,rho,gamma,Fphonon,rho6,x,F180,u,
1      logFphonon,pi

    Coefficients for C12

    double precision i(0:4),j(4),gama(0:3)
    data i      / 3.8289, -1.1987, -0.3269, -0.0939, -0.0787 /
    data j      / 0.5103, -0.0101, -0.0034, -0.0018 /
    data gama   / 12.118, -197.1, 1253.6, -2804.8 /

    pi = 3.14159265

    k=-0.4501
    l=-1.9453

    rho6 = rho/1.e6
    u = 2.*pi*(log10(rho)+5.)/18.
    x = 0
    do n=0,3

```

```

        x = x + gama(n) * gamma**(-real(n)/3.)
    enddo
    F180 = i(0)/2. + k*u + 1
    do n=1,4
        F180 = F180 + i(n)*cos(real(n)*u) + j(n)*sin(real(n)*u)
    enddo

    logFphonon = x*F180
    Fphonon = 10**logFphonon

end

c*****
subroutine calcFphonon16(rho, gamma, Fphonon)

implicit none
integer n
double precision k,l,rho,gamma,Fphonon,rho6,x,F180,u,
1    logFphonon,pi

Coefficients for O16
double precision i(0:4),j(4),gama(0:3)
data i    / 3.3882, -1.0837, -0.2774, -0.0776, -0.0683 /
data j    / -0.4482, 0.0079, -0.0036, -0.0035 /
data gama / 13.343, -219, 1381.9, -3053.7 /

pi = 3.14159265

```

```

k=-0.4237
l=-1.5933

rho6 = rho/1.e6
u = 2.*pi*(log10(rho)+5.)/18.
x = 0
do n=0,3
    x = x + gama(n) * gamma**(-real(n)/3.)
enddo
F180 = i(0)/2. + k*u + l
do n=1,4
    F180 = F180 + i(n)*cos(real(n)*u) + j(n)*sin(real(n)*u)
enddo

logFphonon = x*F180
Fphonon = 10**logFphonon

end

```

Appendix B

Smoothing of abundance profiles and Salaris-like profiles

B.1 Overview

I experimented with core composition profiles that were improved in two ways: I used smooth core chemical profiles and in some instances also modified their shapes according to Salaris et al. (1997). Figure B.1 summarizes the changes made.

B.2 Smoothing of the core abundance profiles

B.2.1 Introduction

Core chemical composition profiles inside white dwarfs depend on the progenitor evolution up to that stage and are fairly uncertain. However, a number of authors agree on a general shape for the chemical composition profiles (Salaris et al., 1997; Metcalfe et al., 2002). The version of WDEC I inherited treated those profiles in a crude way (figure B.1). One striking feature of the simple profile in figure B.1 is the discontinuous slope where the oxygen abundance first starts to decrease. This is likely unphysical, but we do not know to what

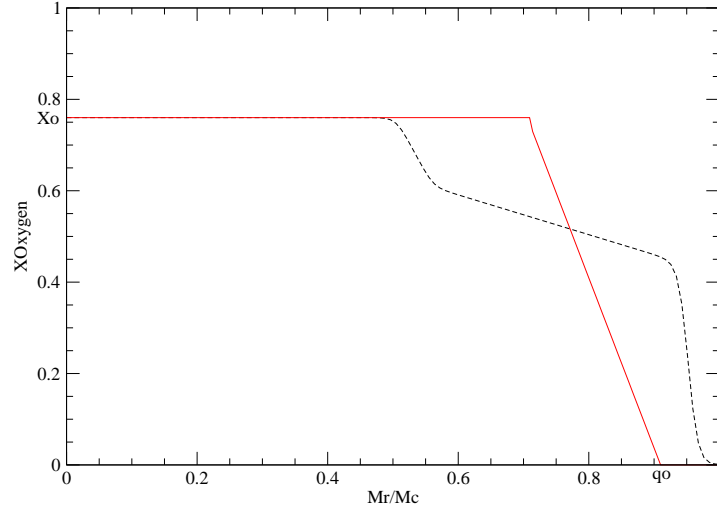


Figure B.1: Oxygen abundance profile for a $0.606 M_{\odot}$ white dwarf model according to Salaris et al. 1997 (black dashed curve) and a WDEC chemical profile (solid red curve). The WDEC chemical profile is defined by two parameters: X_o , the central oxygen abundance, and q_o , the point in the star at which the oxygen abundance drops to zero.

extent. Another striking feature is that it is a poor approximation of the evolved chemical profiles.

In the late stages of its pre-white dwarf life, the progenitor burns helium to produce carbon and oxygen in a convective core. This leads to a chemical profile that is flat within the convective core (homogeneous composition), but enriched in oxygen right above that (Althaus et al., 2002). Because oxygen is heavier than carbon, this means that there is a dense region lying over a region that is less dense. When fusion shuts down and the core is no longer convective, Rayleigh-Taylor instability sets in and mixes the carbon and the oxygen until the mixture is homogeneous throughout the core.

One would guess that some diffusion might happen at the edge of the homogeneous core, but whether diffusion does take place and if it does, how much, is completely un-

known. The details of the transition should matter little to most modes, as such a sharp feature would be “invisible” to all but the shortest wavelength modes. In that respect, it would make sense to leave the sharp edge as it is. However, it does pose problems in numerical computations and when we look at the Brunt-Väisälä frequency, we can tell that it looks odd (figure B.2). Because the modes care little about the exact shape of the transition, it seems sensible to smooth it out and see how that changes the Brunt-Väisälä frequency and the pulsation periods. I test the effect of smoothing the core composition profiles in section 3.3.

B.2.2 Results

In figure B.2, I show how the chemical profiles and the Brunt-Väisälä frequency compare for a model with the original chemical profiles and the smoothed version of the chemical profiles. The modes of the two models differ by 0.1 % on average.

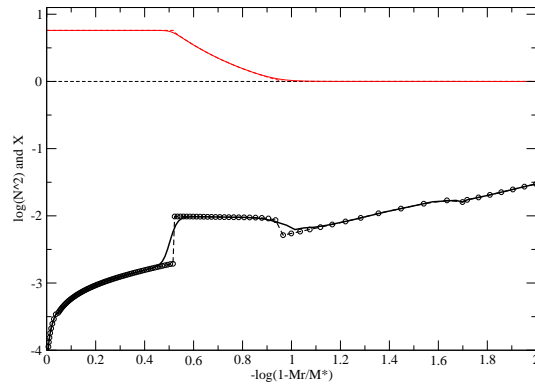


Figure B.2: The oxygen abundance profile (solid curve on top) and the Brunt-Väisälä frequency both for the original abundance profile (dashed with circles) and the smoothed profile (bold line).

B.2.3 Code

The following subroutine (written by Mike Montgomery) smooths out the carbon and oxygen chemical profiles.

```
C*****
C
C          subroutine profsm
C When irdold is set to 3, this routine uses the profile specified
C in the header in ams() and corat() and computes a smoothed version
C of it so that the derivatives of this profile are also smooth.
C The parameter "a" controls the sharpness of the changes in
C slope, where a larger "a" means a more rapid change in slope
C (MHM March 2006)
C*****

      subroutine profsm(amr,ams,corat,ndim,xc2)
      implicit none
      integer ndim,i,npoints
      real*8 ams(ndim),corat(ndim),amr,xc2,am(ndim-1),dm(ndim-2),a,
1      efac,emax

      a=100.d0
      emax=25.d0

      do i=1,ndim
         if (ams(i).ge.0.99999999) goto 10
      enddo
10    continue
      npoints = i
```

```

do i=1,npoints-1
    am(i) = (corat(i+1)-corat(i))/(ams(i+1)-ams(i))
enddo
do i=1,npoints-2
    dm(i) = am(i+1)-am(i)
enddo

xc2=corat(1)
do i=1,npoints-2
    efac=a*(amr-ams(i+1))
    if (efac.lt.-emax) then
        xc2 = xc2 + 0.0
    elseif (efac.gt.emax) then
        xc2 = xc2 + efac*dm(i)/a
    else
        xc2 = xc2 + log(1.d0+exp(efac))*dm(i)/a
    endif
enddo

return
end

```

irdold is a flag set in the input file. The function version of WDEC uses a database of input files, which all have irdold set equal to 1. Instead of modifying every single one of them in order to trigger the smoothing, I allowed the code to read in irdold (=1) and then reset it to 3. That change and a few others are listed below, including the call statement.

After the line

```
read(7,*)ip5,ip6,ip7,nmod,nitel,m,md,nu,ip8,ipl,irdold,ip40
```

Add the lines

```
* Forcibly set irdold to 3 for smooth profiles
```

```
irdold = 3
```

Replace

```
if ( irdold .eq. 1 .or. irdold .eq. 0 ) then
```

with

```
if ( irdold .eq. 1 .or. irdold .eq. 0 .or. irdold .eq. 3 ) then
```

After

```
elseif ( irdold .eq. 2 ) then
```

```
*** read from input file ***
```

```
read(7, 7) jb,((y(j,i),i=1,7),j=1,jb)
```

```
do i = 1,jb
```

```
amr = 10.**y(i,1)
```

```
if ( i .ne. jb ) then
```

```
xo2 = .5 * ( 1. + alph ) * ( 1. - amr )**alph
```

```
else
```

```
xo2 = 0.
```

```
endif
```

```
xc2 = 1 - xo2
```

```
xc(i) = xc2
```

```
if ( xc2 .gt. .000001 .and. xc2 .lt. .999999 ) then
```

```
call istatco(p(i),t(i),0,.false.)
```

```
elseif ( xc2 .ge. .999999 ) then
```

```

        call istat1(p(i),t(i),0,12,.false.)
    elseif ( xc2 .le. .000001) then
        call istat1(p(i),t(i),0,16,.false.)
    endif
    e(i) = e2
enddo
corat(1) = xc(1)
corat(2) = xc(jb)
ncore = 2

```

Add the condition block

```

elseif ( irdold .eq. 3 ) then
    read(7, 7) jb,((y(j,i),i=1,7),j=1,jb)
    ndim=10
    do i = 1,jb
        amr = 10.**y(i,1)
        call profsm(amr,ams,corat,ndim,xc2)
        xo2 = 1 - xc2
        xc(i) = xc2
        if ( xc2 .gt. .00001 .and. xc2 .lt. .99999)then
            call istatco(p(i),t(i),0,.false.)
        elseif ( xc2 .ge. .999999) then
            call istat1(p(i),t(i),0,12,.false.)
        elseif ( xc2 .le. .000001) then
            call istat1(p(i),t(i),0,16,.false.)
        endif
    e(i) = e2

```

enddo

B.3 Salaris-like core abundance profiles

To get the chemical profiles to look more like the ones derived from stellar evolution is tricky because we want to keep the number of free parameters to a minimum. The more free parameter we have, the more it becomes computationally demanding to find best fit models to a set of periods. I designed a parameterization that allowed me to replicate Salaris profiles for different white dwarf masses with only two free parameters.

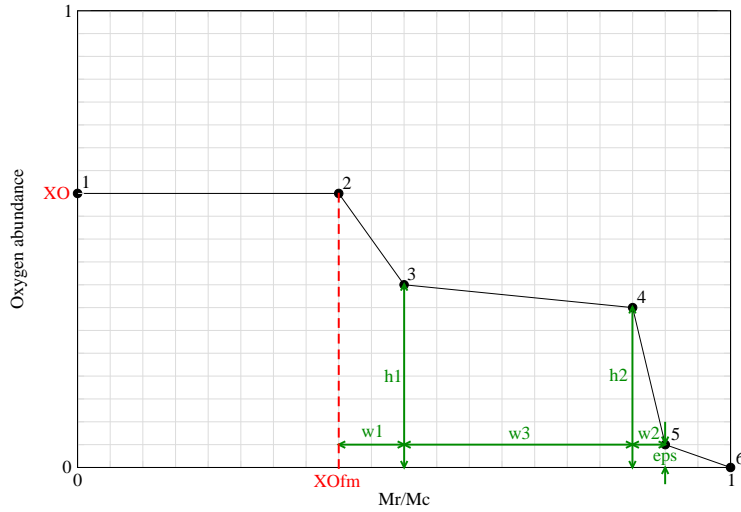


Figure B.3: Basic structure of an evolved chemical profile. XO and $XOfm$ are input parameters that may be changed in order to obtain a best fit to the periods. One can also set them to the values that best correspond to the Salaris chemical profiles (see table B.2). All other parameters on the figure are fixed for a given mass range. Table 1 lists the coordinates of each of the points in terms of the parameters.

In figure B.3, I show the basic structure of the evolved chemical profiles and the

Table B.1: Coordinates of the points that make up the chemical abundance profile. The second column header line lists the names each variable is given in the code.

Point number	M_r/M_c	X_O
i	ams(i)	corat(i)
1	0	XO
2	XOfm	XO
3	ams(2)+w1	h1
4*	ams(3)+w3	h2
5	ams(4)+w2	eps
6	1	0

*To ensure that the oxygen abundance drops down to zero well inside the core, the x coordinate of point number 4 is constrained to be no larger than $rmax = 1 - w2 - b \cdot eps$. The numerical value of b appears in table B.2.

Table B.2: Parameters that fit the Salaris profiles best. $w1$ and $w2$ are limited by the smoothing done by subroutine `profsm`. Any value smaller than 0.01 does not do anything as we cannot make the profile any steeper than `profsm` will allow. The $0.606 M_\odot$ profile and above meet the $rmax$ limit (see text) and so the value of $w3$ for those models is irrelevant. This is what “saturated” means.

Mass [M_\odot]	0.538	0.551	0.606	0.682	0.768	0.867	1.000
w1	0.07	0.05	0.07	0.04	0.04	0.01	0.01
h1/XO	0.72	0.81	0.78	0.77	0.81	0.83	0.90
w2	0.02	0.01	0.01	0.01	0.01	0.01	0.01
h2	0.47	0.47	0.46	0.46	0.48	0.505	0.59
w3	0.31	0.37	saturated	saturated	saturated	saturated	saturated
eps	1.e-3	1.e-3	1.e-3	1.e-3	1.e-3	1.e-3	1.e-3
b	30	30	85	85	85	85	85
XO	0.85	0.81	0.76	0.73	0.71	0.68	0.655
XOfm	0.53	0.50	0.50	0.54	0.47	0.63	0.75

parameters needed in order to fully define such profiles. The initial chemical profile is defined by six points, given in terms of the parameters in table B.1. XO and XOfm are input parameters that can vary, but all other parameters are fixed for a given mass range. I

chose the values for all those other parameters by fitting the profiles given by Salaris et al. (1997), for which Salaris kindly provided data files. The best fit parameters for each model are listed in table B.2. The initial chemical profiles are then smoothed, using subroutine `profsm`. In figures B.4 to B.10, I show how the profiles thus obtained compare with the Salaris profiles.

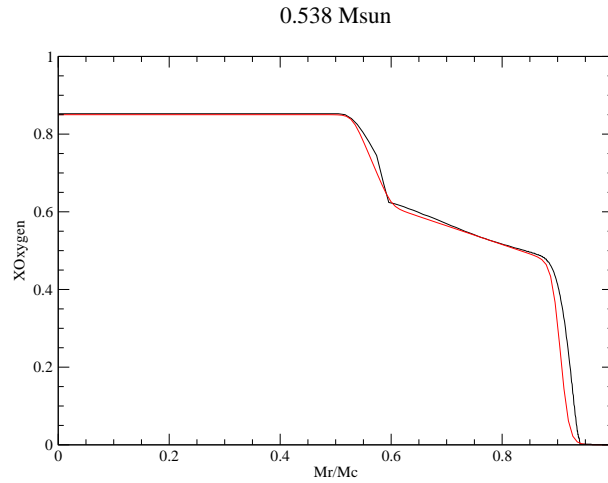


Figure B.4:

In figure B.11, I show how the chemical profiles and the Brunt-Väisälä frequency compare for a model with the original chemical profiles and the smooth Salaris chemical profiles. The periods of the two models differ by 1.5 % on average.

B.3.1 Code

The changes I made in order to include the Salaris profiles occur in the first part of subroutine `read2`, which is the part where the input chemical profiles are read. The code also includes the changes detailed in section 2. The input profiles look like the one in figure B.3. The code then calls the subroutine `profsm`, which interpolates and smooths the input

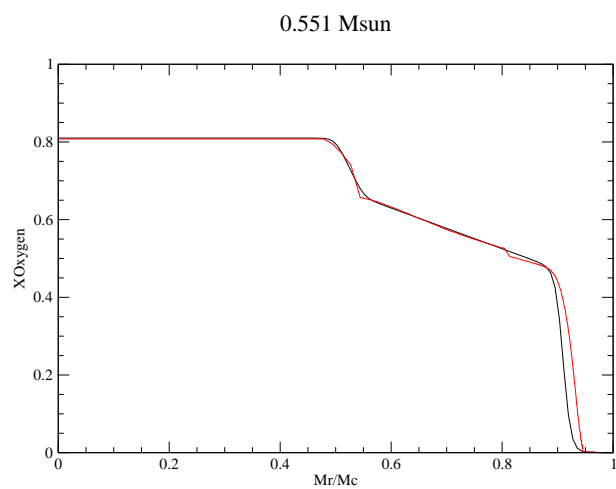


Figure B.5:

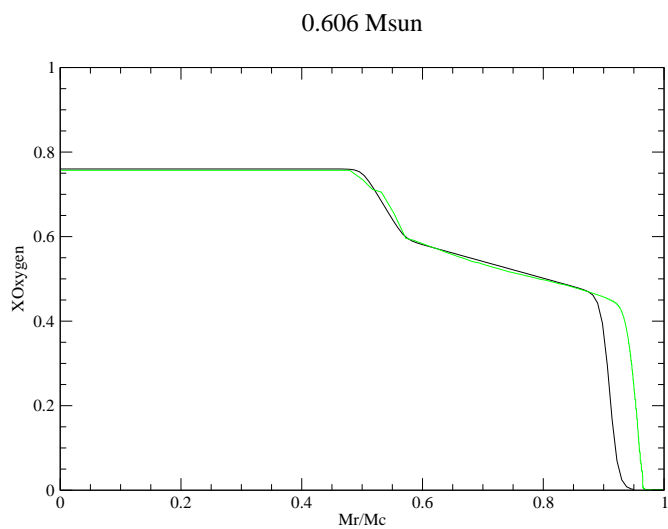


Figure B.6:

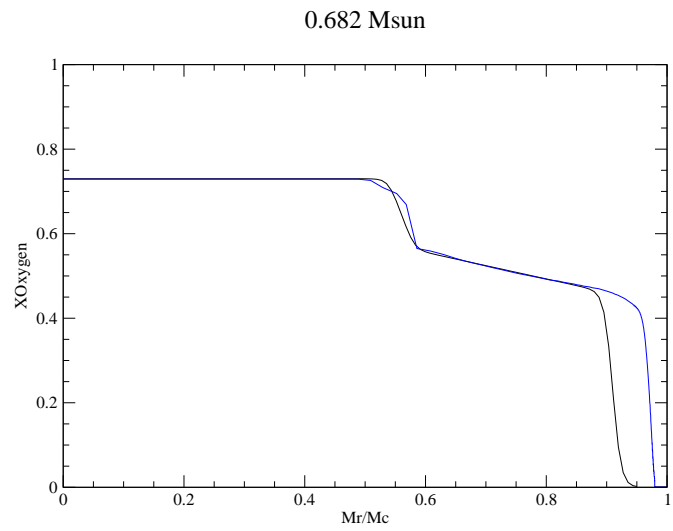


Figure B.7:

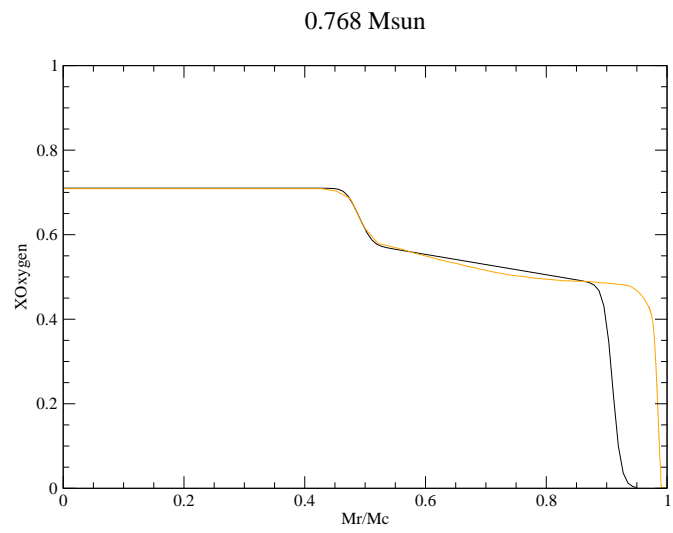


Figure B.8:

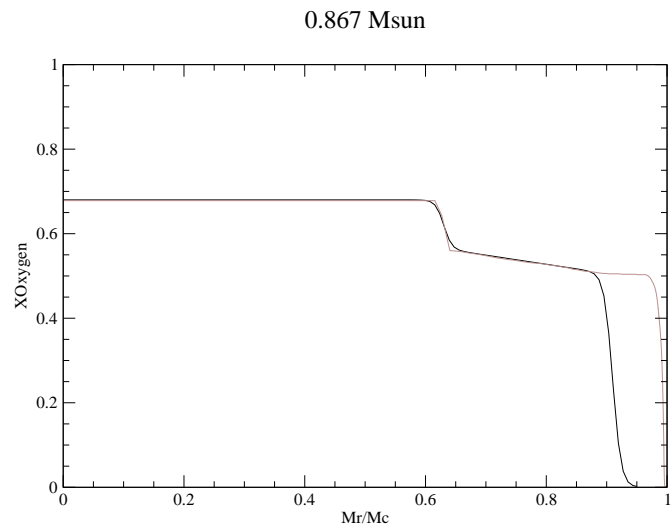


Figure B.9:

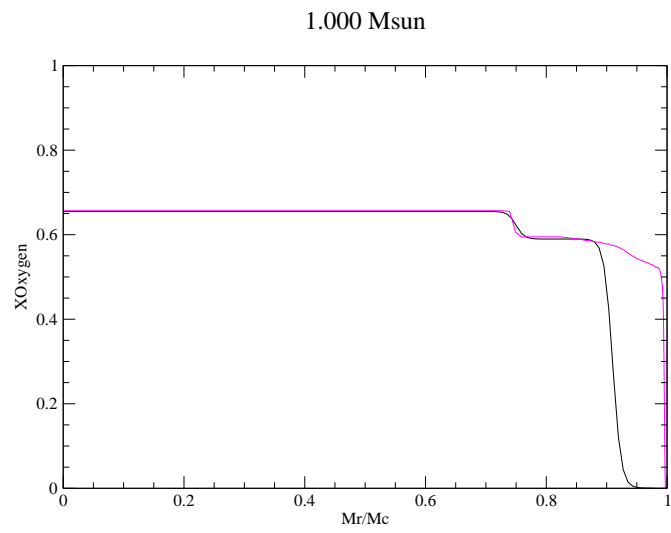


Figure B.10:

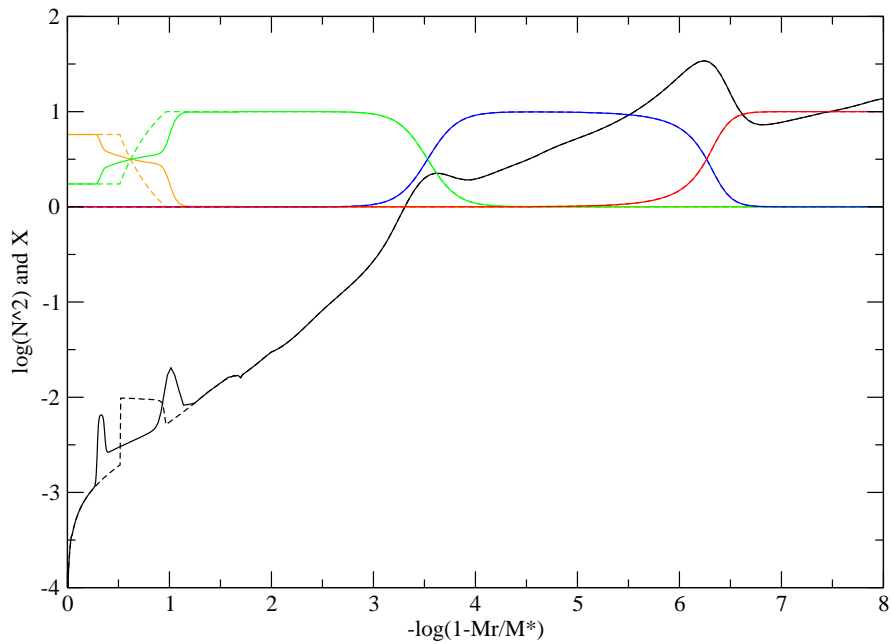


Figure B.11:

profile. For inspection purposes, the input profile is written out to the file “initprof.dat”, and the smoothed profile is written out to the file “x.dat”.

The following includes the relevant part of read2 (modified to include Salaris profiles).

```
c Here is where we read in the model.  if we are reading in
c an old model, then we also have to specify the run of the
c desired c/o profile.  (corat = 1 ==> pure c).
c if irdold = 1, then do linear interpolation between the specified
c   mass points
```

```

c  if irdold = 2, then use the relation given in Barrat, Hansen,
c      \& Mochkovitch 1988, A+A, 199, L15
c  if irdold = 3, then cleverly smooth the profiles

      if ( irdold .eq. 1 ) then

*** read from input file ***
      read(7, 7) jbr,((y(j,i),i=1,7),j=1,jbr)
      do 1000 i = 1,jbr
          amr = 10.**y(i,1)
          iii = 2
999      if ( amr .gt. ams(iii) ) then
          iii = iii + 1
          goto 999
      endif
      xc2 = dcorat(iii) / delmass(iii) * (amr - ams(iii-1))
1      + corat(iii-1)
      xo2 = 1 - xc2
      xc(i) = xc2
      if ( xc2 .gt. .00001 .and. xc2 .lt. .99999)then
          call istatco(p(i),t(i),0,.false.)
      elseif ( xc2 .ge. .999999) then
          call istat1(p(i),t(i),0,12,.false.)
      elseif ( xc2 .le. .000001) then
          call istat1(p(i),t(i),0,16,.false.)
      endif
      e(i) = e2

```

```

1000      continue

      elseif ( irdold .eq. 2 ) then

*** read from input file ***
        read(7, 7) jb,((y(j,i),i=1,7),j=1,jb)
        do i = 1,jb
            amr = 10.**y(i,1)
            if ( i .ne. jb ) then
                xo2 = .5 * ( 1. + alph ) * ( 1. - amr )**alph
            else
                xo2 = 0.
            endif
            xc2 = 1 - xo2
            xc(i) = xc2
            if ( xc2 .gt. .000001 .and. xc2 .lt. .999999 ) then
                call istatco(p(i),t(i),0,.false.)
            elseif ( xc2 .ge. .999999 ) then
                call istat1(p(i),t(i),0,12,.false.)
            elseif ( xc2 .le. .000001 ) then
                call istat1(p(i),t(i),0,16,.false.)
            endif
            e(i) = e2
        enddo
        corat(1) = xc(1)
        corat(2) = xc(jb)
        ncore = 2

```

```

elseif ( irdold .eq. 3 ) then
c Salaris-like Oxygen profile
c First fix a few parameters. Those are based on Salaris (1997)
c profiles.
c Mass dependent parameters
smoms = 10**sm/1.989e33
w2 = 0.01
w3 = 0.40
beps = 85.
if (smoms .lt. 0.5445) then
w1 = 0.07
hlfrac = 0.72
w2 = 0.02
h2 = 0.47
w3 = 0.31
b = 30.
endif
if (smoms .ge. 0.5445 .and. smoms .lt. 0.5785) then
w1 = 0.05
hlfrac = 0.81
h2 = 0.47
w3 = 0.37
b = 30.
endif
if (smoms .ge. 0.5785 .and. smoms .lt. 0.6440) then
w1 = 0.07

```



```

        hlfrac = 0.78
        h2 = 0.46
        w3 = 0.38
endif
    if (smoms .ge. 0.6440 .and. smoms .lt. 0.7250) then
        w1 = 0.04
        hlfrac = 0.77
        h2 = 0.46
    endif
    if (smoms .ge. 0.7250 .and. smoms .lt. 0.8175) then
        w1 = 0.04
        hlfrac = 0.81
        h2 = 0.48
    endif
    if (smoms .ge. 0.8175 .and. smoms .lt. 0.9335) then
        w1 = 0.01
        hlfrac = 0.83
        h2 = 0.505
    endif
    if (smoms .ge. 0.9335) then
        w1 = 0.01
        hlfrac = 0.90
        h2 = 0.59
    endif
endif

```

c The best fit for X0 and X0fm for each mass are the following. You
c can hardwire them if you like.

```

c      M*/Msun  XO      XOfm
c      0.538    0.85    0.53
c      0.551    0.81    0.50
c      0.606    0.76    0.50
c      0.682    0.73    0.54
c      0.768    0.71    0.47
c      0.867    0.68    0.63
c      1.000    0.655  0.75

c Mass independent parameters
      eps = 1.e-3
      rmaxx = 1 - w2 - beps*eps

c Now set the oxygen profile
      ams(1) = 0.0
      corat(1) = XO\_tmp
      ams(2) = XOfm\_tmp
      corat(2) = XO\_tmp
      ams(3) = ams(2) + w1
      corat(3) = hlfrac * XO\_tmp
      ams(4) = ams(3) + w3
      if (ams(4) .ge. rmaxx) then
        ams(4) = rmaxx
      endif
      corat(4) = h2
      ams(5) = ams(4) + w2

```

```

corat(5) = eps
ams(6) = 1.
corat(6) = 0.

open (2000, file="initprof.dat")
do i=1,6
    write(2000,*) ams(i), corat(i)
enddo
close(2000)

```

c The code uses the Carbon profile so we have to translate

```

do i=1,6
    corat(i) = 1 - corat(i)
enddo

open (3000,file="x.dat")
read(7, 7) jb,((y(j,i),i=1,7),j=1,jb)
ndim=10

do i = 1,jb
    amr = 10.**y(i,1)
    call profsm(amr,ams,corat,ndim,xc2)
    xc2 = 1 - xc2
    xc(i) = xc2
    if ( xc2 .gt. .00001 .and. xc2 .lt. .99999)then
        call istatco(p(i),t(i),0,.false.)
    elseif ( xc2 .ge. .999999) then

```

```

        call istat1(p(i),t(i),0,12,.false.)
    elseif ( xc2 .le. .000001) then
        call istat1(p(i),t(i),0,16,.false.)
    endif
    e(i) = e2
    rmassfrac = amr
    write (3000,*) rmassfrac, xo2, xc(i)
enddo
close(3000)
else

*** read from input file ***
    read(7, 7) jb,((y(j,i),i=1,7),j=1,jb)
    do j=1,jb
        xc(j)=y(j,7)
    enddo
endif

close(7)

```

Appendix C

Smoothing of the Brunt-Väisälä frequency

C.1 Overview of the problem and quick solution

In its current state, the WDEC computes models piece-wise. It treats separately the core, the envelope, and the atmosphere. Different physics go in each region. The whole model gets stitched together at the end. This is the only way we have found so far to deal with the many orders of magnitude changes in quantities such as the density. The stitching gives rise to a small discontinuity at the core-envelope boundary. For most quantities, the discontinuity is non-existent or without consequence, but for one of them, it is a nuisance when trying to compute periods of pulsation of the model. This significant discontinuity occurs in the Brunt-Väisälä frequency, which sets the pulsation periods. A discontinuity in the Brunt-Väisälä frequency modifies the periods of the modes. I test the effect of the discontinuity in the Brunt-Väisälä frequency on the periods in section 3.3.

The real solution to the problem would be to merge the interior and the envelope into one region. This is work in progress. Meanwhile, I implemented a quick fix, which is simply to remove the discontinuity in the Brunt-Väisälä frequency after the fact. The

discontinuity is usually small, and removing it involves changing the value of the Brunt-Väisälä slightly for a dozen of shells (figures C.1 and C.2).

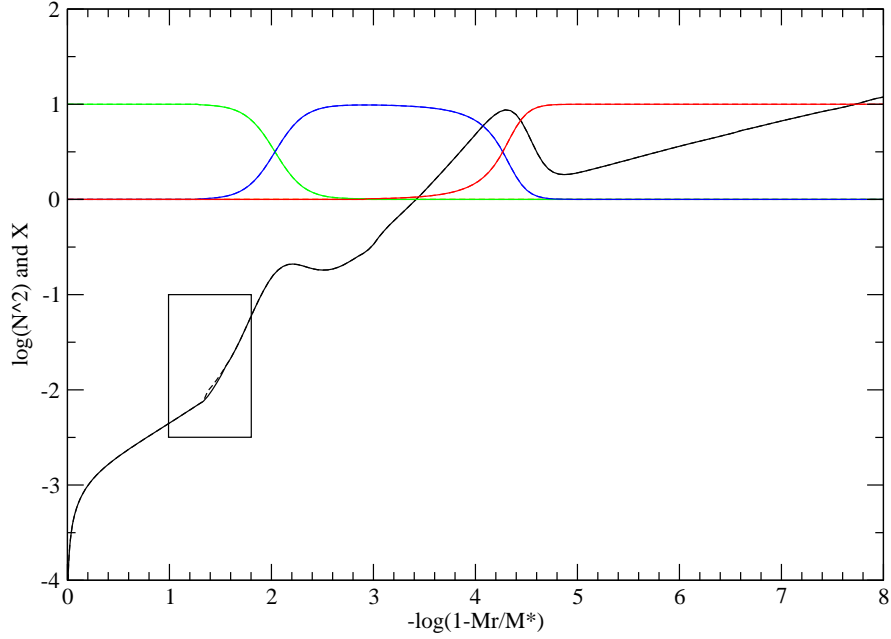


Figure C.1: The Brunt-Väisälä frequency and composition profiles for an average DA model (11500K, $0.6 M_{\odot}$, $M_{He} = 10^{-2}$, $M_H = 10^{-4}$). The dotted line shows the original curve, while the solid line shows the smoothed version of the curve. The region inside the box is blown up in figure C.2.

A discontinuity means that the core calculation and the envelope calculation disagree on the value of the basic physical quantities at (nearly) the same point in the model. The first step is to decide which one to trust. We have good reasons to trust the core calculation. We have good equation of state tables for the core (Lamb, 1974), more physics (e.g. oxygen in the chemical make-up and neutrinos), and at the core-envelope boundary, we are still well within the region of parameter space that is valid for the core EOS. The basic

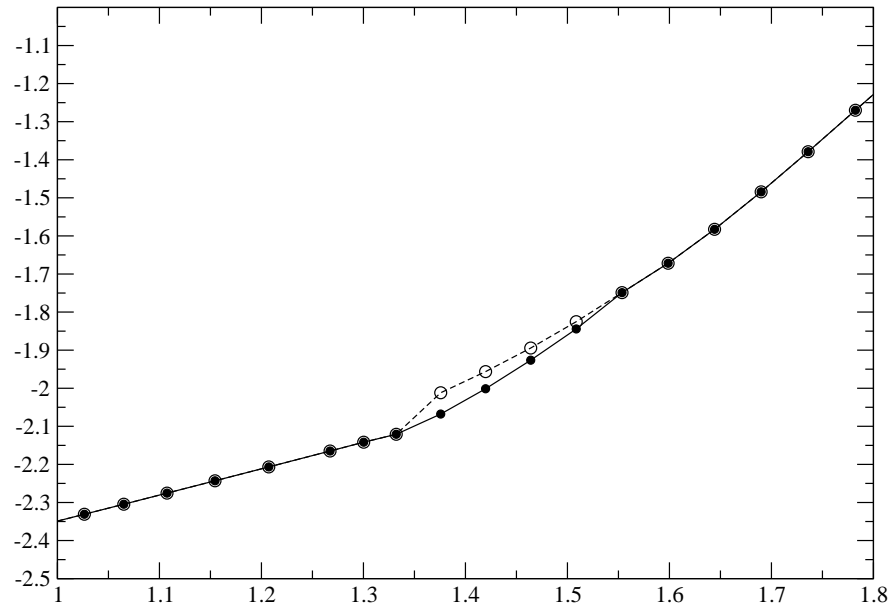


Figure C.2: A blow up of the smoothed part of the Brunt-Väisälä frequency.

idea is then to bring the value of the Brunt-Väisälä frequency right past the core-envelope boundary to where we would expect it to be if we had never left the core region. The method is simple:

- 1) find the core-envelope boundary (get that from an input quantity, $stpm_s$)
- 2) look at the slope before and after the discontinuity (see figure C.3)
- 3) take the average of the two
- 4) move the point to its new position
- 5) keep going, until we rejoin, or until we've modified way too many points.

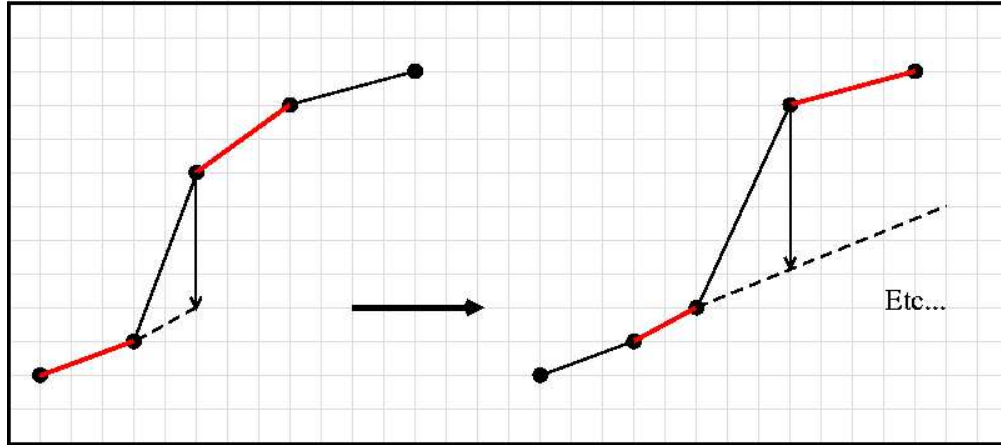


Figure C.3: Illustration of the smoothing algorithm. The program averages the slope right before and right after the discontinuity (in this case $\frac{1/3+2/3}{2} = \frac{1}{2}$) and moves the point to the right of the discontinuity on the line that has that average slope. It repeats the process until it rejoins the original curve or after a set number of iterations have occurred.

C.2 Implementation

In practice, the discontinuous quantity to smooth occurs in y_3 (section 13 in Unno et al., 1989):

$$y_3 = \frac{r}{g} N^2, \quad (\text{C.1})$$

where N^2 is the Brunt-Väisälä frequency.

In the original WDEC, y_3 is computed by the prep code and gets written out to file tape29. Travis Metcalfe (Metcalfe, 2001) recast WDEC as a fortran function to be called by the genetic algorithm code. I have implemented the smoothing of y_3 in one version of that function, because that is where I needed it ultimately. It would be very easy to implement it in the original WDEC as well. The main difference is that instead of writing out y_3 to a file, the function saves y_3 as a one dimensional array (with as many elements as there are shells).

I wrote a subroutine, `smoother3`, that takes in array y_3 , smooths it, and saves it to

array y3s. For monitoring purposes, I have the program write out y3 and y3s to two files so one can compare the two and make sure the smoothing went as planned.

The smoothing gets done in subroutine pulsate. The smoothing routine needs to know the stop mass so the first thing to do is to add the common block terp, which contains the variable stpms to the list of common blocks under subroutine pulsate.

```
common/terp/stpms, rat1
```

The smoothing routine gets called right before subroutine pulse. Insert the following lines before the call to pulse.

```
call smoothy3(stpms, mstar, mr, y3, y3s, np)
open (unit=10000, file="y3.dat")
open (unit=10001, file="y3s.dat")
do i = 1, np
    write (10000,*) partt(i), y3(i), mr(i)
    write (10001,*) partt(i), y3s(i), mr(i)
    y3(i) = y3s(i)
enddo
close(10000)
close(10001)
```

Subroutine smoothy3

```
! *****
!
!      SUBROUTINE SMOOTHY3
!
! smoothes the "kink" caused by the core/envelope boundary in the
! quantity y3 (basically the B-V frequency).
!
! ABK March 2006
! *****
subroutine smoothy3(stms, mstar, mr, y3, y3s, np)
```

```

real*8, dimension(np), intent(out) :: y3s
real*8 :: avgslope, slope, maxdiff
real*8 :: mrstms, diff1
real*8, intent(in) :: stms, mstar
real*8, dimension(np), intent(in) :: mr, y3
real*8, parameter :: msun = 1.989e33
real*8, parameter :: eps = 1.e-5
!*****epsilon determines when to quit smoothing*****
real*8, parameter :: epsilon = 0.2
real*8, dimension(4) :: x2, y2
real*8, dimension(3) :: xk, yk
real*8 :: yprime, delta
real*8, dimension(10) :: x,y,diff
integer, dimension(10) :: shapeofkink
integer :: i, j, position, smposition, start, lambda, failed,shape
integer, intent(in) :: np

failed = 0 !we start out optimistic
mrstms = 10**stms * mstar * msun
! print 40, mrstms

10 format(2E20.12E2)
20 format(I5)
30 format(I5, ES20.12E2)
40 format(ES20.12E2)
50 format(F10.4)
60 format(4E16.8E2)

```

```

70 format(8E20.12E2)

!Go through until we find stop mass discontinuity
do i=1,np
    diff1 = abs(mrstms/mr(i) - 1)
!When stopmass point found, begin smoothing
    if (diff1 .le. eps) then
!        print *, "Stop mass found at mr="
!        print 40, mr(i)
        y3s(i) = y3(i)
        position = i
        goto 3
    end if
    y3s(i) = y3(i)
end do

!If all goes well, the following doesn't happen.
print *, "Failed: could not find stop mass point"
stop

3 continue

!print *, "kink on line: ", position

!Let the fun begin

!First make sure of where we are. The stop mass doesn't always
!correspond to the exact same shell w.r.t the discontinuity. This

```

!routine works from the shell right before the jump and that's where
!we need to be.

!The following saves 6 points around the stopmass discontinuity to
!the arrays x and y.

```
start = position - 2
```

```
do i=1,6
```

```
    x(i) = mr(start+i-1)
```

```
    y(i) = y3(start+i-1)
```

```
end do
```

```
do i=1,4
```

```
    xk = x(i:i+2)
```

```
    yk = y(i:i+2)
```

```
    call findkink(xk, yk, diff(i),start,shapeofkink(i))
```

```
end do
```

!The kink is where the before and after slopes differ the most.

```
maxdiff = diff(1)
```

```
do i=2,4
```

```
    if (diff(i) .gt. maxdiff) then
```

```
        maxdiff = diff(i)
```

```
        smposition = i
```

```
    end if
```

```
end do
```

```

shape = shapeofkink(smposition)

!print *, "kink found at ", smposition

!OK, now we have found where the kink is exactly. Save the 2 points
!before the jump and the 2 points after the jump to (x2,y2). If we
!have a dip, need to start one point earlier.

if (shape == -1) then
    smposition = smposition -1
end if

4 do i=1,4
    x2(i) = mr(start + smposition + i - 2)
    y2(i) = y3(start + smposition + i - 2)
end do

!Compute where we want the point to be to make things smooth.
!lambda is an iteration counter. It also tells how many points are
!smoothed.

lambda = 0

!Book-keeping: copy the point right before the one we want to modify
!over. If we have a dip, start one point earlier.

```

```

y3s(start + smposition + lambda) = y3(start + smposition + lambda)
call displace(x2, y2, yprime, avgslope)
y3s(start + smposition + lambda+1) = yprime

!Process the points after that in the same manner. Quit when they are
!close to where we would them to be (the curve is smoothed from that
!point on).
do
    lambda = lambda + 1

!First reassign values (we are moving one point to the right)
!The first two points are from the new, smoothed array, y3s.
    do i=1,2
        x2(i) = mr(start + smposition + i - 3 + lambda)
        y2(i) = y3s(start + smposition + i - 3 + lambda)
    end do
!The last two points are from the original array y3.
    do i=3,4
        x2(i) = mr(start + smposition + i - 3 + lambda)
        y2(i) = y3(start + smposition + i - 3 + lambda)
    end do

    call displace(x2, y2, yprime, avgslope)
    y3s(start + smposition + lambda) = yprime

!Exit clauses
!Compare the average slope (see subroutine displace) with the actual

```

```

!slope. If they are close enough, exit.
    slope = (y2(3) - y2(2))/(x2(3) - x2(2))
    diff1 = abs(1 - slope/avgslope)
    if (diff1 .le. epsilon) then
        goto 6
    end if
!If the average slope never gets close enough to the actual slope,
!exit no matter what when we get to the 30th shell (or the one of our
!choice). The first time we get to that point, give it one more try
!The second time we get to that point, we've tried all we could and
!we quit.
    if (lambda .ge. 30) then
        if (failed .eq. 1) then
            print *, "Alright, enough! Either something went horribly &
                wrong or the epsilon you picked is too small.      &
                Smoothing stopped at"
            print 40, x2(3)
            goto 6
        end if
        failed = 1
!try again, from the other side of the detected discontinuity
        smposition = smposition - 1
        goto 4
    end if
end do

```

```

6 continue

!print *, "Number of points smoothed, nr of last point smoothed:"

!print 30, lambda, x2(2)

!We have rejoined the original curve. Merely write out the rest of
!the file as is.

do i = start + smposition + lambda, np
    y3s(i) = y3(i)
end do

end subroutine smoothy3

!Compares the slopes of 2 successive segments. If the slopes differ
!by a lot, then we have a discontinuity in slope and we found the
!kink. shape tells the shape of the kink. If the slopes before and
!after the kink both have the same sign, then shape = +1. If the
!slopes are opposite in sign (we have a dip) then shape = -1. It
!matters for where we begin the smoothing (for reasons I don't fully
!understand anymore).

subroutine findkink(x,y,diff,start,shape)

    real*8, dimension(3), intent(in) :: x,y
    real*8, intent(out) :: diff
    integer, intent(out):: shape
    real*8 :: slope1, slope2

```



```

integer :: sign1, sign2
integer :: start

slope1 = (y(2) - y(1))/(x(2) - x(1))
slope2 = (y(3) - y(2))/(x(3) - x(2))

if (abs(slope1) == slope1) then
    sign1 = 1
else
    sign1 = -1
end if

if (abs(slope2) == slope2) then
    sign2 = 1
else
    sign2 = -1
end if

if (sign1 == sign2) then
    shape = 1
else
    shape = -1
end if

diff = abs(slope1-slope2)
return

```

```

end subroutine findkink

!Computes where the point after (x2, y2) should be if it
!lied on a line going through y2 with a slope that is the average
!between the slope right before y2 and the slope right after y3.
!Returns the new value yprime and the average slope computed.

subroutine displace(x, y, yprime,slope)

  real*8, dimension(4), intent(in) :: x, y
  real*8 :: slope1, slope2
  real*8, intent(out) :: yprime, slope

  slope1 = (y(2)-y(1))/(x(2)-x(1))
  slope2 = (y(4)-y(3))/(x(4)-x(3))
  slope = 1/2.*(slope1 + slope2)
  yprime = slope*(x(3)-x(2)) + y(2)
  return

end subroutine displace

```

Appendix D

Period fitting

D.1 Overview

The purpose of the routine I describe in this appendix is to compare a given set of periods (e.g. the observed period spectrum of a star) with a list of periods calculated for a given model. The routine needs to find best matching pairs (without reusing the same model period twice) and proceeds to compute the fitness function Φ (equation 3.1). In essence this is a traveling salesman problem (Numerical recipees, 1987), where a salesman has to visit a number of towns and wants to minimize the distance traveled. I considered treating the problem as such and use the full machinery developed in Numerical Recipes to solve it, but realized that it was not necessary. There are two kinds of models: those that fit reasonably well and those that fit poorly (e.g. a period is missing altogether). Among the models that fit poorly, it does not matter exactly how poorly each fits compared to the other. While the fitting routine may look complicated, it follows a fairly simple process. The rest is book keeping.

D.2 How the routine works with an example

Suppose we have the following observed periods to match up with the following list of calculated periods:

P_{obs}	$P_{\text{calc}} (\ell)$
161	226 (1)
172	287 (1)
203	133 (2)
217	170 (2)
282	193 (2)
	205 (2)
	245 (2)
	270 (2)
	285 (2)

In a first, naive pass, the routine looks for the best matching pair among the list of calculated periods for each observed period:

160	170
172	170
203	205
217	226
282	285

If one calculated period matches more than one observed periods, the program tries
 1) keeping the first pair and rematching the second 2) keeping the second pair and rematch-
 ing the first one. It retains the most advantageous combination of the two.

keep	160	170		rematch	160	133
rematch	172	193		keep	172	170
	203	205	or		203	205
	217	226			217	226
	282	285			282	285

The second pairing leads to a smaller residual. In rare cases where they are equivalent, the default is to retain the first pair.

If there are more than one degenerate pair, then the program simply saves the best matching pair, removes that calculated period from the race, and rematch the rest of the observed periods, this time without worrying about reusing the same period twice. This is rather crude, but if there is a need to reuse calculated periods so many times, it means the model is a poor fit anyway and we do not worry about finding out exactly how bad it is. This worse case scenario rarely occurred in my grids. There is another test that helps us eliminate bad models and that is the following.

For each model, the routine computes the average period spacing. It then looks at the matched pairs and counts how many of them match to within better than half an average period spacing. The percentage of periods that match well is called `goodfits`. In all my grids, I made a first cut by keeping only the models for which `goodfits` was 100%. This ensured the quality of the fits and also that the fitness function Φ was a meaningful quantity.

D.3 Fitness routine

```
program calcfits
```

```
implicit none
```

```
real, dimension(:), allocatable :: obsper
```

```
real, dimension(:,:), allocatable :: calcper, fitper, fitpersorted
```

```
real, dimension(:,:), allocatable :: repeatper, repeatpersorted, &  
    fitpertmp
```

```
real :: dum, fit, omcmin, omc, omc1, omc2, omctot1, omctot2, &  
    pfitttwice
```

```

real :: fitper11, fitper12, fitper21, fitper22
real :: P1, P2, deltaP, deltaPsum, avgdP, goodfits, kmax, sigma
integer :: nobs, ncalc, i, j, k, jbest, klmax, ifitprev, ifitnext, &
           ifitstart
integer :: teff, mass, mhe, mh
integer :: counter, reused, best, ifit1, ifit2, resume
integer :: istart, jbest1, jbest2, degen, numl2P, minncalc

10 format(4I6,F12.6,F5.0,2I4,F5.0)
20 format(F4.0,F12.6,2F4.0,2F12.6)
30 format(3F8.1,I4)

open(unit=1, file="obsperiods")
open(unit=2, file="calcperiods")
open(unit=3, file="fitnesspars.dat")
open(unit=4, file="periods.dat")

!Fill the observed period array

read(1,*) nobs
allocate(obsper(nobs))
allocate(fitper(nobs,7), fitpersorted(nobs,7), fitpertmp(nobs,7))

do i = 1, nobs
    read(1,*) obsper(i)
    fitper(i,2) = obsper(i)
end do

```

```

counter = 0

!First run through calculated periods file: find the minimum number
!of calculated periods among all the models listed in the file

minncalc = 1000.
do
    ncalc = 0

    read(2,*,end=3) teff, mass, mhe, mh
    do
        read(2,*,end=3) dum
        if (dum .eq. 100000) exit
        ncalc = ncalc + 1
    end do
    ncalc = ncalc - 1
    if (ncalc .lt. minncalc) minncalc = ncalc
end do

3 continue

rewind(2)

do
    ncalc = 0

```

```

!Fill the calculated period array
!First figure out how many calculated periods there are and allocate
!array
      read(2,*,end=2) teff, mass, mhe, mh
      do
        read(2,*,end=2) dum
        if (dum .eq. 100000) exit
        ncalc = ncalc + 1
      end do

      ncalc = ncalc - 1
      allocate(calcper(ncalc,4))

!Rewind to the correct spot and read again, this time filling the
!array. Column 1 = index number, column 2 = l, column 3 = k (first
!period of a given l has k=1, the next one k=2, etc... this is not
!the formal indentification, just there to give a notion of low k vs
!high k), column 4 = period .Use this opportunity to compute a
!representative period spacing (use l=2 modes because it is smaller
!for those).

      do i = 1,ncalc+2
        backspace(2)
      end do

      do i=1,ncalc

```



```

        calcper(i,1) = real(i)
        calcper(i,3) = real(i)
        read(2,*,end=2) calcper(i,2), calcper(i,4)
        if (calcper(i,2) .eq. 2.) then
            klmax = i - 1
            exit
        end if
    end do
end do

```

```

backspace(2)

```

```

P1 = calcper(i,4)
numl2P = 1
deltaPsum = 0.
do i = klmax+1, ncalc
    calcper(i,1) = real(i)
    calcper(i,3) = real(i-klmax)
    read(2,*,end=2) calcper(i,2), calcper(i,4)
    P2 = calcper(i,4)
    deltaP = abs(P2 - P1)
    deltaPsum = deltaPsum + deltaP
    numl2P = numl2P + 1
    P1 = P2
end do
avgdP = deltaPsum/numl2P

```

!Build the first fitness matrice. Naively lists the best matching

!mode for each observed period. A given calculated period may be used
!more than once. Also lists how close each best match is to the
!observed period.

```

do i = 1,nobs
  omcmin= 100000000.
  do j = 1,ncalc
    omc = abs(obsper(i)-calcper(j,4))
    if (omc .LT. omcmin) then
      omcmin=omc
      fitper(i,1) = calcper(j,1)
      fitper(i,3) = calcper(j,2)
      fitper(i,4) = calcper(j,3)
      fitper(i,5) = calcper(j,4)
      fitper(i,6) = omc
    end if
  end do
end do

```

!Sort the fitness matrice by index (first column) so that we can
!readily see if calculated periods got used more than once.

```

do i=1,nobs
  best = ncalc+1
  do j=1,nobs
    fit = fitper(j,1)
    if (fit .lt. best) then

```

```

        best = fit
        jbest = j
        do k=1,6
            fitpersorted(i,k) = fitper(j,k)
        end do
    end if
end do
fitper(jbest,1) = ncalc+1
end do

```

!Run through fitpersorted line by line from top to bottom and futher
!process modes that match the same calculated. Keep track of how many
!modes are fighting for the same calculated period. That's an
!indication of how bad the fit is.

```

reused = 1
resume = 1
degen = 1

1 ifitprev = fitpersorted(resume,1)
  calcper(ifitprev,4) = 10000.
  do i=resume+1,nobs
      ifitnext = fitpersorted(i,1)
      if (ifitnext .eq. ifitprev) then
          reused = reused + 1
          ifit1 = ifitnext
          ifit2 = fitpersorted(i+1,1)
      end if
  end do

```

```

        istart = i - 1
    end if
    if (ifitnext .ne. ifitprev) calcper(ifitprev,4) = 10000.
    ifitprev = ifitnext
end do

!If we found a set of two observed periods matching the same
!calculated period. Find the most advantageous combination without
!reusing periods already used.

    if (reused .eq. 2) then
        pfittwice = fitpersorted(istart,5)
        calcper(ifitnext,4) = 10000.

!CASE 1: keep the first pair, rematch the second one.
        fitper11 = fitpersorted(istart,5)
        omc1 = fitpersorted(istart,6)
        omcmin= 100000.
        do j = 1,ncalc
            omc2 = abs(fitpersorted(istart+1,2)-calcper(j,4))
            if (omc2 .LT. omcmin) then
                omcmin=omc2
                jbest1 = j
                fitper12 = calcper(j,4)
            end if
        end do
        omc2 = omcmin

```

```

omctot1 = omc1 + omc2

!CASE 2: keep the second pair, rematch the first one.
fitper21 = fitpersorted(istart+1,5)
omc2 = fitpersorted(istart+1,6)

omcmin= 100000.
do j = 1,ncalc
    omc1 = abs(fitpersorted(istart,2)-calcper(j,4))
    if (omc1 .LT. omcmin) then
        omcmin=omc1
        jbest2 = j
        fitper22 = calcper(j,4)
    end if
end do
omc1 = omcmin
omctot2 = omc1 + omc2

!Save the most advantageous combination
if (omctot1 .le. omctot2) then
!Don't touch fitpersorted(istart,:), save proper values in
!fitpersorted(istart+1,:)
    fitpersorted(istart+1,1) = jbest1
    fitpersorted(istart+1,3) = calcper(jbest1,2)
    fitpersorted(istart+1,4) = calcper(jbest1,3)
    fitpersorted(istart+1,5) = calcper(jbest1,4)
    fitpersorted(istart+1,6) = omc2

```

```

else
!Opposite. Keep second line as is, change first one.
    fitpersorted(istart,1) = jbest2
    fitpersorted(istart,3) = calcper(jbest2,2)
    fitpersorted(istart,4) = calcper(jbest2,3)
    fitpersorted(istart,5) = calcper(jbest2,4)
    fitpersorted(istart,6) = omc1
end if

resume = istart + 1
degen = degen + 1
reused = 1
goto 1
end if

!If we find more than two observed periods matching the same
!calculated period, things get complicated. Run through again, this
!time saving the reused periods
if (reused .gt. 2) then
    degen = reused
    allocate(repeatper(reused,7),repeatpersorted(reused,7))

    ifitprev = fitpersorted(1,1)
    do i=2,nobs
        ifitnext = fitpersorted(i,1)
        if (ifitnext .eq. ifitprev) then
            ifitstart = i-1

```

```

        exit
    end if
    ifitprev = ifitnext
end do

do i=1,reused
    do k=1,7
        repeatper(i,k) = fitpersorted(ifitstart+i-1,k)
    end do
end do

```

!Sort the repeat period subarray from best match to worse. Keep
!the best match, rematch the rest in a rather crude way. At this
!point we don't care much anymore, if we get to this point, the
!model is not very good.

```

do i=1,reused
    best = 10000.
    do j=1,reused
        fit = repeatper(j,6)
        if (fit .lt. best) then
            best = fit
            jbest = j
            do k=1,6
                repeatpersorted(i,k) = repeatper(j,k)
            end do
        end if
    end do
end do

```

```

        end do
        repeatper(jbest,6) = 10000.
    end do

!Remove best matching calcper from the race
    best = int(repeatpersorted(1,1))
    calcper(best,4) = 10000.

!Find best matches to the rest of the observed periods in the array
    do i=2,reused
        omcmin= 100000.
        do j = 1,ncalc
            omc = abs(repeatpersorted(i,2)-calcper(j,4))
            if (omc .LT. omcmin) then
                omcmin=omc
                jbest = j
                repeatpersorted(i,1) = calcper(j,1)
                repeatpersorted(i,3) = calcper(j,2)
                repeatpersorted(i,4) = calcper(j,3)
                repeatpersorted(i,5) = calcper(j,4)
                repeatpersorted(i,6) = omc
            end if
        end do
        calcper(jbest,4) = 10000.
    end do

!Modify the original sorted fitper array

```



```

do i=1,reused
  do k=1,7
    fitpersorted(iffitstart+i-1,k) = repeatpersorted(i,k)
  end do
end do

```

!Of course now fitpersorted is no longer sorted by index. Sort it
!again before looping through.

```

do i=1,nobs
  best = ncalc+1
  do j=1,nobs
    fit = fitpersorted(j,1)
    if (fit .lt. best) then
      best = fit
      jbest = j
      do k=1,6
        fitpertmp(i,k) = fitpersorted(j,k)
      end do
    end if
  end do
  fitpersorted(jbest,1) = ncalc+1
end do

```

```

do i=1,nobs
  do j=1,7
    fitpersorted(i,j) = fitpertmp(i,j)
  end do
end do

```

```

        end do
    end do

    deallocate(repeatper,repeatpersorted)
    resume = 1
    reused = 1
    goto 1

end if

!Phew! Now we have an array with (nearly) the best possible matching
!pairs in it. Use it to compute a number of fitness indicators.
!degen = number of calculated periods reused. Already calculated
!goodfits = number of periods that match to better than half the
!average period spacing, scaled by 100/nobs (to get a normalized
!percentage).
!sigma = average period difference normalized by multiplying by
!ncalc/minncalc.

sigma = 0.
numl2P = 0
kmax = 0.
goodfits = 0.
do i=1,nobs
    sigma = sigma + fitpersorted(i,6)
    if (fitpersorted(i,6) .le. avgdP/2.) then
        goodfits = goodfits + 1
    end if
end do

```

```

        end if
        if (fitpersorted(i,3) .eq. 2.) then
            numl2P = numl2P + 1
        end if
        if (fitpersorted(i,4) .ge. kmax) then
            kmax = fitpersorted(i,4)
        end if
    end do

    goodfits = goodfits * 100./nobs
    sigma = sigma * ncalc/minncalc *1./real(nobs)

!Write out the files
    write(3,10) teff, mass, mhe, mh, sigma, goodfits, degen, numl2P,&
        kmax
    write(4,10) teff, mass, mhe, mh, sigma, goodfits, degen, numl2P,&
        kmax
    do i=1,nobs
        omc = abs(fitpersorted(i,5) - fitpersorted(i,2))
        write(4,30) fitpersorted(i,2), fitpersorted(i,5), omc,&
            int(fitpersorted(i,3))
    end do
    write(4,*), "100000"

    counter = counter + 1
    print *, counter

```

```
        deallocate(calcper)

!Reposition ourselves at beginning of next period listing
        read(2,*)
        read(2,*)
end do
2 continue

end program calcfit
```

Appendix E

Simplex method

E.1 Brief description of the downhill simplex method and implementation

In section 5.6.5 I used a downhill simplex search for the minima in the quantity Φ (equation 3.1), the average departure between the observed periods and the model's periods. The downhill simplex method is computationally robust because, unlike most minimization routines, it does not require numerical evaluation of derivatives. As we saw in section 5.6.5, this is particularly valuable for the function we were trying to minimize in that section. The simplex method is fully described in section 10.4 of Numerical Recipes for Fortran 77 and I used the subroutine given in that section, `amoeba.f`. A simplex is a geometrical figure with $N+1$ vertices, where N is the number of parameters in the function to minimize.

Travis Metcalfe 2001 recast all the elements of the WDEC in one single fortran function (`ff`), for use with the Genetic Algorithm. `ff` accepts the regular input given to the first program in WDEC, `evol` and in addition, a list of periods the model should match. The function computes a white dwarf model and the corresponding pulsation spectrum. It outputs a list of periods and most importantly, a fitness parameter, the quantity we want to minimize.

One limitation of the function `ff` was that it could only compute models of discrete masses. The mass was set in the input file (which included a starter model) and so if one wanted to change the mass, one had to generate a new input file. There was an easy way around that. I found that one could easily use the existing input files and simply change the mass to the value one wanted after the fact. Having a starter model with the wrong mass does not really matter. The starter models are initial guesses anyway, and with a grid of starter models $0.005 M_{\odot}$ apart, the mass of any given starter model is never more than $0.0025 M_{\odot}$ away from the specified mass.

E.1.1 Input

To start a simplex search for a minimum, we need to specify the $N+1$ vertices of the starting simplex, and the values of the function at those $N+1$ vertices. The former are saved in the array $p(1:N+1,1:N)$, while the latter are saved in the array $y(1:N+1)$. With 4 parameters ($N=4$), p is a (5×4) matrix and y is a column vector with 5 rows. Equation E.1 shows the form p and y take for our present purposes.

$$p = \begin{pmatrix} T_{\text{eff}}^1 & M_*^1 & M_{\text{He}}^1 & M_{\text{H}}^1 \\ T_{\text{eff}}^2 & M_*^2 & M_{\text{He}}^2 & M_{\text{H}}^2 \\ T_{\text{eff}}^3 & M_*^3 & M_{\text{He}}^3 & M_{\text{H}}^3 \\ T_{\text{eff}}^4 & M_*^4 & M_{\text{He}}^4 & M_{\text{H}}^4 \\ T_{\text{eff}}^5 & M_*^5 & M_{\text{He}}^5 & M_{\text{H}}^5 \end{pmatrix} \quad (\text{E.1})$$

$$y = \begin{pmatrix} \text{ff}(T_{\text{eff}}^1, M_*^1, M_{\text{He}}^1, M_{\text{H}}^1) \\ \text{ff}(T_{\text{eff}}^2, M_*^2, M_{\text{He}}^2, M_{\text{H}}^2) \\ \text{ff}(T_{\text{eff}}^3, M_*^3, M_{\text{He}}^3, M_{\text{H}}^3) \\ \text{ff}(T_{\text{eff}}^4, M_*^4, M_{\text{He}}^4, M_{\text{H}}^4) \\ \text{ff}(T_{\text{eff}}^5, M_*^5, M_{\text{He}}^5, M_{\text{H}}^5) \end{pmatrix} \quad (\text{E.2})$$

In my implementation of the simplex method, I specify $(T_{\text{eff}}^1, M_*^1, M_{\text{He}}^1, M_{\text{H}}^1)$ and

$\text{delta}(1:4) = (\Delta_1, \Delta_2, \Delta_3, \Delta_4)$, and define the starting simplex in the following way:

$$p = \begin{pmatrix} T_{\text{eff}}^1 & M_*^1 & M_{\text{He}}^1 & M_{\text{H}}^1 \\ T_{\text{eff}}^1 + \Delta_1 & M_*^1 & M_{\text{He}}^1 & M_{\text{H}}^1 \\ T_{\text{eff}}^1 & M_*^1 + \Delta_2 & M_{\text{He}}^1 & M_{\text{H}}^1 \\ T_{\text{eff}}^1 & M_*^1 & M_{\text{He}}^1 + \Delta_3 & M_{\text{H}}^1 \\ T_{\text{eff}}^1 & M_*^1 & M_{\text{He}}^1 & M_{\text{H}}^1 + \Delta_4 \end{pmatrix} \quad (\text{E.3})$$

The code then proceeds to evaluate the function at each vertex of the simplex and saves it in the array $y(1:5)$, which it then feeds into the `amoeba` routine.

E.1.2 Convergence criterion

As in all minimization problems, we need to decide how close is close enough. In successive iterations, the subroutine `amoeba` computes simplexes that are smaller and smaller (i.e. the $N+1$ points of the simplex come closer and closer together) as the code converges on a solution. We need to specify how close those points have to come together before we consider the solution fully converged. Below is an example of a converged simplex.

12482.	0.618	2.26	7.87
12480.	0.617	2.25	7.88
12471.	0.618	2.25	7.88
12477.	0.617	2.25	7.88
12486.	0.618	2.25	7.87

Each row in the array above is one corner of the simplex. This example immediately suggests a very simple test for convergence: average the five values found for each parameter and compare each corner of the simplex with the average. If all of them are close to the average, then the simplex has converged to a solution.

E.2 Code and input files

E.2.1 Main program

The main program is called `main.f`. It obtains $(T_{\text{eff}}^1, M_*^1, M_{\text{He}}^1, M_{\text{H}}^1)$, builds the starting simplex, and calls the subroutine `amoeba`, which actually does the minimization. The example below reads $(T_{\text{eff}}^1, M_*^1, M_{\text{He}}^1, M_{\text{H}}^1)$ off a file called “inputdata”.

```
program main

implicit none

double precision data(36),ff, sum(4), average(4), sig
double precision funk, y(5), p(5,36), a(4), delta(4), ftol
integer npar,i,j,m
integer ndim, mp, np, iter, failedflag

10  format(f8.0, f8.3, 2f8.2)

open (unit=1, file="delta.dat")
open (unit=2003, file="inputdata")
open (unit=2001, file="simplex.dat")
open (unit=2002, file="shortoutput")

npar = 4
failedflag = 0

c Define delta, tolerance, and number of parameters
```



```

read (1,*) ftol
read(1,*)

do i=1,npar
    read (1,*) delta(i)
enddo

ndim = npar
mp = npar + 1
np = npar

close(1)

do
    read(2003,*) data(1), data(2), data(3), data(4), sig
    if (sig.gt.1.5) exit
    write(2001,10) data(1), data(2), data(3), data(4)
    write(2002,10) data(1), data(2), data(3), data(4)

    write(*,*) 'begin simplex fit'

c Define the starting simplex
c a(i) IS THE FIT WE ARE TRYING TO REFINE
c It is one corner of our starting simplex

    write (2001,*) 'starting simplex'

```

```

do i=1, ndim
    a(i) = data(i)
enddo

do i=1,np
    p(1,i) = a(i)
enddo
do j=5,36
    p(1,j) = 0.
enddo

p(2,1) = a(1) + delta(1)
p(2,2) = a(2)
p(2,3) = a(3)
p(2,4) = a(4)
do j=5,36
    p(2,j) = 0.
enddo

p(3,1) = a(1)
p(3,2) = a(2) + delta(2)
p(3,3) = a(3)
p(3,4) = a(4)
do j=5,36
    p(3,j) = 0.
enddo

```

```

p(4,1) = a(1)
p(4,2) = a(2)
p(4,3) = a(3) + delta(3)
p(4,4) = a(4)
do j=5,36
    p(4,j) = 0.
enddo

p(5,1) = a(1)
p(5,2) = a(2)
p(5,3) = a(3)
p(5,4) = a(4) + delta(4)
do j=5,36
    p(5,j) = 0.
enddo

do i = 1,mp
    write (2001,10) p(i,1:4)
enddo

do i=1,mp
    y(i) = ff(npar, p(i,:),2)
enddo

write(*,*) 'call amoeba'
call amoeba(p,y,mp,np,ndim,ftol,ff,npar,iter,failedflag)

```

```

write(*,*) 'number of iterations', iter
write(2001,*) 'end simplex'

c Writes out the 5 points of the simplex, which are all within
c rtol of the minimum.

do i = 1,mp
    write (*,10) p(i,1:4)
enddo

do i = 1,mp
    write (2001,10) p(i,1:4)
enddo

sum = (/0.,0.,0.,0./)
do j = 1,4
    do i = 1,mp
        sum(j) = sum(j) + p(i,j)
        average(j) = sum(j)/real(mp)
    enddo
enddo

write(2001,*) "Average"
write(2001,10) average
write(2001,*) ""
write(2002,10) average

```

```

        write(2002,*)
        print 10, average
        write(*,*) 'tolerance', ftol
        write (*,*)

    enddo

end

```

E.2.2 The minimizing routine

I list below the modifications made to the `amoeba` subroutine. The two significant changes is the passing of the variable `npar` from `main.f` and a redefinition of the convergence criterion. `npar` specifies the number of parameters we have. I also had to add a kludge to prevent `amoeba` from evaluating the same models over and over again, sometimes preventing it from converging. The best way to break it lose was to give a “kick” to the effective temperatures the routine was trying. This is a problem specific to how the WDEC works. In each block of changes, unless specified otherwise, the modified version follows the original version.

```

*****

subroutine amoeba(p,y,mp,np,ndim,ftol,funk,iter)
---

subroutine amoeba(p,y,mp,np,ndim,ftol,funk,npar,iter,
1          failedflag)
*****

integer iter,mpndim,np,NMAX,ITMAX

```

```

real ftol,p(mp,np),y(mp),funk,TINY
---
integer iter,mp,ndim,np,NMAX,ITMAX,npar
real ftol,p(mp,np),rtol(mp,np),sum2(np),average(np),y(mp),funk
real rtolsum(np), TINY

iter=0
*****

integer i,ih,i,ilo,inhi,j,m,n
real rtol,sum,swap,ysave,ytry,psum(NMAX),amotry
---
integer i,ih,i,ilo,inhi,j,m,n,failedflag,toocloseflag
real sum,swap,ysave,ytry,ytryold,psum(NMAX),amotry

10  format(f8.0, f8.3, 4f8.2)
20  format(f8.0, f8.3, 2f6.2)

iter=0
toocloseflag=0
ytry = 0.
*****

```

The following is the modified convergence condition.

```

rtol=2.*abs(y(ih)-y(ilo))/(abs(y(ih))+abs(y(ilo))+TINY)
if (rtol.lt.ftol) then
---
do j = 1,mp

```

```

        write (*,10) p(j,:)
    enddo

    write (*,*) ""
!Condition for quitting : quit when each rows of p(:, :) are nearly
!identical. We've converged to a solution.

!Compute averages of each column of P(:, :)

    sum2 = (/0.,0.,0.,0./)
    do j = 1,4
        do i = 1,mp
            sum2(j) = sum2(j) + p(i,j)
            average(j) = sum2(j)/real(mp)
        enddo
    enddo

!Let rtol(:, :) be the difference between the average of each column
!and the individual members in each column

    do j = 1,4
        do i = 1,mp
            rtol(i,j) = abs(average(j) - p(i,j))
        enddo
    enddo

!Add up those departures column by column. If any total is too big,
!at least one member in that column is straying too far and we need

```

```

!to keep going.
    rtolsum = (/0.,0.,0.,0./)
    do i=1,np
        do j=1,mp
            rtolsum(i) = rtolsum(i) + rtol(j,i)
        enddo
    enddo

    write(*,10) rtolsum(:)

    if (rtolsum(2).le.0.002 .and. rtolsum(3).le.0.02 .and.
1    rtolsum(4).le.0.02) then
        swap=y(1)
        y(1)=y(ilo)
        y(ilo)=swap
        do n=1,ndim
            swap=p(1,n)
            p(1,n)=p(ilo,n)
            p(ilo,n)=swap
        enddo
        return
        if (rtolsum(1).ge.200) failedflag=1
    endif

*****

    ytry=amotry(p,y,psum,mp,np,ndim,funk,ihl,-1.0)
---

    ytryold = ytry

```



```

        ytry=amotry(p,y,psum,mp,np,ndim,funk,npar,ihl,-1.0,
1          toocloseflag)
        if (ytryold.eq.ytry) toocloseflag=1
*****

        ytry=amotry(p,y,psum,mp,np,ndim,funk,ihl,2.0)
---

        ytryold = ytry
        ytry=amotry(p,y,psum,mp,np,ndim,funk,npar,ihl,2.0,
1          toocloseflag)
        if (ytryold.eq.ytry) toocloseflag=1
*****

        ytry=amotry(p,y,psum,mp,np,ndim,funk,ihl,0.5)
---

        ytryold = ytry
        ytry=amotry(p,y,psum,mp,np,ndim,funk,npar,ihl,0.5,
1          toocloseflag)
        if (ytryold.eq.ytry) toocloseflag=1
*****

        y(i)=funk(psum)
---

        y(i)=funk(npar,psum,2)

```

Subroutine amoeba calls the function amotry . I list the changes made to that function below.

```

*****

FUNCTION amotry(p,y,psum,mp,np,ndim,funk,ihl,fac)

```

```

---
      FUNCTION amotry(p,y,psum,mp,np,ndim,funk,npar,ihi,fac,
1          toocloseflag)
*****
      integer ihi,mp,ndim,np,NMAX
---
      integer ihi,mp,ndim,np,NMAX,npar,toocloseflag
*****

```

Add the following format statement after the declaration block

```

20    format(f8.0, f8.3, 2f6.2)
*****
      ytry=funk(ptry)
---
      if (toocloseflag.eq.1) then
          write(*,*) "toocloseflag = 1"
          ptry(1) = ptry(1) + 100.
      endif

      ytry=funk(npar,ptry,2)
*****

```

E.2.3 Input file

`ftol` and `delta(1:4)` are specified in the file “delta.dat”, which looks like the following. The first line is `ftol`. The modified version of `amoeba` no longer uses it. The conditions for convergence are hardwired in `amoeba.f`, but could easily be reinstated as input.

1.e-1

dTeff, dM, dMHe, dMH (each on a separate line)

100.

0.002

0.05

0.05

Appendix F

New Plasmon Neutrino Rates

F.1 Comparison between the older rates and the new ones

Itoh et al. (1996a) provide fortran routines to compute neutrino rates. The routines are published in the AAS CD-ROM Series (now out of print, but still available from the AAS website). I included the plasmon neutrino routine in the White Dwarf Evolution Code (WDEC). To check that the rates were accurately calculated in the code, I compared the rates calculated by the WDEC with the plasmon neutrino rates obtained by feeding the same model directly into Itoh's routine and found perfect agreement.

I also compared the new plasmon neutrino rates with the previous rates (Itoh et al., 1989). In figures F.1-F.3, I show a comparison of the neutrino rates in models covering a broad range in mass and effective temperature. The new rates seem significantly higher than the old neutrino rates. However, when integrated over the mass of the star to give neutrino luminosities, the effect is small (figure F.4).

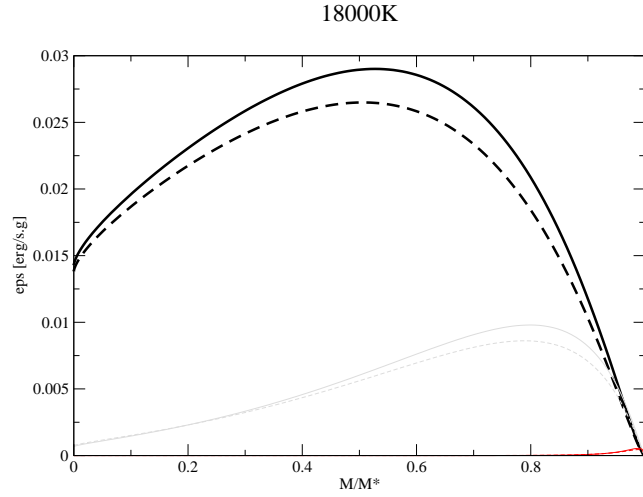


Figure F.1: New plasmon neutrino rates (solid lines) compared with old rates (dashed lines) for a low mass model ($0.5 M_{\odot}$, bold), a medium mass model ($0.6 M_{\odot}$, grey), and a high mass model ($0.9 M_{\odot}$, lowest curves). All models have $T_{eff} = 18000K$.

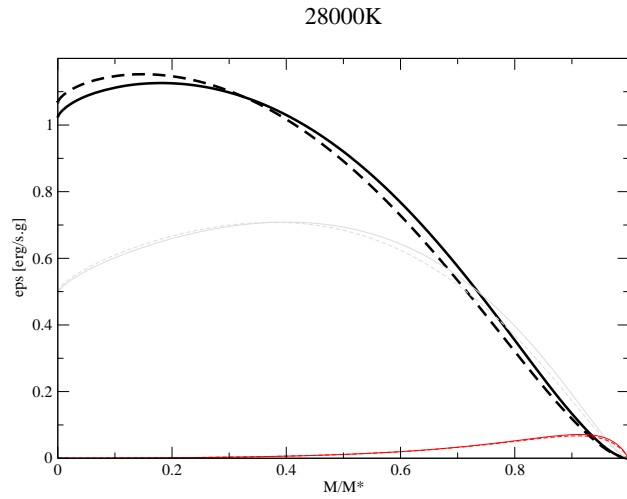


Figure F.2: Same as figure F.1 for hotter models (28000K)

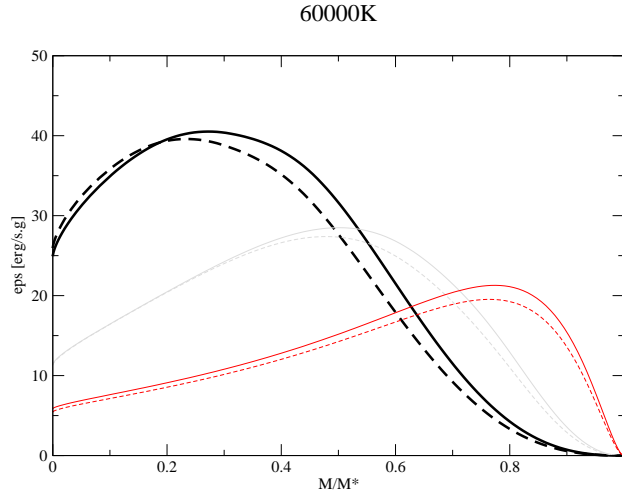


Figure F.3: Same as figure F.1 for even hotter models (60000K)

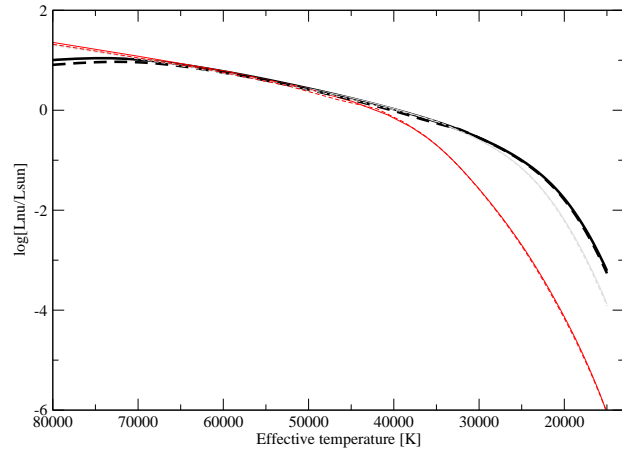


Figure F.4: The plasmon neutrino luminosity for the same 3 different mass models as a function of effective temperature.

F.2 Relevant subroutines

I replaced the old “plasmon” subroutine with the following routine. I had to change the call statement in the subroutine “gnutrino” from

```
call plasmon(flam,rho,t2,mue,cv,cvp,ca,cap,qplas)
```

to

```
call plasmon(t2, rhomooe, qplas)
```

Subroutine plasmon:

```
c*****
c Plasmon Neutrinos according to Itho et al. 1996, APJS, 102, 411
c According to Itoh et al. 1996, ApJ, 470, 1015, those rates are
c numerically more accurate than the ones from 1992 (which
c are the same as the ones from 1989 except for ultra-relativistic
c electrons).
c Replaces Paul's plasmon routine.
c ABK 2005
c*****
      subroutine plasmon(t2, rhomooe, qplas)
      implicit double precision (a-h, o-z)
      double precision logrhomooe
      logrhomooe = dlog10(rhomooe)
      call formulae(t2, logrhomooe, qplas)
      return
      end
```

Subroutine plasmon calls the following routine, written by Itoh et al., 1996.

```
c*****
c Plasma process fitting formulae as written by Itoh et al. 1996
```

c Given in AAS CD-ROM series, volume 7, 1996 December.

c*****

```
subroutine formulae ( t, r, qn)
implicit real*8 (a-z)

tn      = 1.d1**t
rn      = 1.d1**r
rdouble = dlog10(2*rn)

x = ( 1.75d1 + rdouble - 3.d0*t )/6.d0
y = ( -2.45d1 + rdouble + 3.d0*t )/6.d0

if ( dabs(x).gt.7.d-1.or.y.lt.0.d0 ) then
    fxy = 1.d0
elseif (y-1.6d0+1.25d0*x.lt.0.d0) then
    fxy = 1.05d0 +(0.39d0 -1.25d0*x - 0.35d0*dsin(4.5d0*x)
&          -0.3d0*dexp(-1.d0*(4.5d0*x + 0.9d0)**2.d0))
&          *dexp(-1.d0*((y-1.6d0+1.25d0*x)
&          /(0.57d0-0.25d0*x))**2.d0)
else
    fxy = 1.05d0 +(0.39d0 - 1.25d0*x - 0.35d0*dsin(4.5d0*x)
&          -0.3d0*dexp(-1.d0*(4.5d0*x + 0.9d0)**2.d0))
endif

lamb = (1.686d-10)*tn
```



```

gamd = 1.1095d11*rn/((tn**2.d0)*
&      ((1.d0+(1.019d-6*rn)**(2.d0/3.d0))** 0.5d0))
ft    = 2.4d0 + 0.6d0*(gamd**0.25d0) + 0.51d0*(gamd**0.5d0) +
&      1.25d0*(gamd**0.75d0)
fl    = (8.6d0*gamd + 1.35d0*(gamd**(7.d0/4.d0)))/(2.25d2 -
&      1.7d1*(gamd**0.5d0) + gamd )

if (dabs(gamd**0.5d0).gt.700) then
    gap=0.d0
else
    gap = fxy*(fl+ft)*dexp(-1.d0*gamd**0.5d0)*(gamd**3.d0)*
&      (lamb**9.d0)*3.d21
endif

cvd   = ( 0.5d0 + 2.d0*0.2319d0)**2.d0 + n*(0.5d0 -
&      2.d0*0.2319d0)**2.d0

if ( gap*cvd.le.0.d0 ) then
    q = 9.9999999d-99
else
    q    = dlog10(gap*cvd)
    qn   = gap*cvd
endif
return
end

```

Bibliography

- Adams, J. B., Ruderman, M. A., & Woo, C.-H. 1963, *Physical Review* , 129, 1383
- Althaus, L. G., Serenelli, A. M., Córscico, A. H., & Benvenuto, O. G. 2002, *MNRAS*, 330, 685
- Atre, A., Barger, V., & Han, T. 2005, *Phys. Rev. D*, 71, 113014
- Battye, R. A., & Shellard, E. P. S. 1994, *Physical Review Letters*, 73, 2954
- Beauchamp, A., Wesemael, F., Bergeron, P., Fontaine, G., Saffer, R. A., Liebert, J., & Brassard, P. 1999, *ApJ*, 516, 887
- Beaudet, G., Petrosian, V., & Salpeter, E. E. 1967, *ApJ*, 150, 979
- Bennett, J. O., Donahue, M., Schneider, N., & Voit, M. 2004, *The Cosmic Perspective*, 3rd Edition, by J.O. ennet, M. Donahue, N. Schneider, and M. Voit. Benjamin Cummings, 2004. ISBN 0-8053-8738-2.,
- Benvenuto, O. G., Córscico, A. H., Althaus, L. G., & Serenelli, A. M. 2002, *MNRAS*, 332, 399
- Bergeron, P., Wesemael, F., Lamontagne, R., Fontaine, G., Saffer, R. A., & Allard, N. F. 1995, *ApJ*, 449, 258
- Bergeron, P., Liebert, J., & Fulbright, M. S. 1995, *ApJ*, 444, 810

- Bergstroem, L. 2000, Reports of Progress in Physics, 63, 793
- Bershady, M. A., Ressel, M. T., & Turner, M. S. 1991, Physical Review Letters, 66, 1398
- Bischoff-Kim, A., Montgomery, M. H., Winget, D. E. 2007, ApJ, submitted
- Blout, B. D., Daw, E. J., Decowski, M. P., Ho, P. T. P., Rosenberg, L. J., & Yu, D. B. 2001, ApJ, 546, 825
- Bohm, K. H., & Cassinelli, J. 1971, A&A, 12, 21
- Bradley, P. A., & Winget, D. E. 1991, ApJ Supp., 75, 463
- Bradley, P. A. 1993, Ph.D. Thesis,
- Bradley, P. A. 1998, ApJ Sup., 116, 307
- Bradley, R., Clarke, J., Kinion, D., Rosenberg, L. J., van Bibber, K., Matsuki, S., Mück, M., & Sikivie, P. 2003, Reviews of Modern Physics, 75, 777
- Burrows, A., Turner, M. S., & Brinkmann, R. P. 1989, Phys. Rev. D, 39, 1020
- Cassisi, S., Potekhin, A. Y., Pietrinferni, A., Catelan, M., & Salaris, M. 2007, ArXiv Astrophysics e-prints, arXiv:astro-ph/0703011
- CAST Collaboration 2007, ArXiv High Energy Physics - Experiment e-prints, arXiv:hep-ex/0702006
- Castanheira, B. G., Kepler, S. O., Koester, D., & Handler, G. 2005, ASP Conf. Ser. 334: 14th European Workshop on White Dwarfs, 334, 557
- Castanheira, B. G., et al. 2006, A&A, 450, 227
- Chang, S., Hagmann, C., & Sikivie, P. 1999, Nuclear Physics B Proceedings Supplements, 72, 99

- Christenson, J. H., Cronin, J. W., Fitch, V. L., & Turlay, R. 1964, *Physical Review Letters*, 13, 138
- Clayton, D. D. 1983, Chicago: University of Chicago Press, 1983,
- Coc, A., Angulo, C., Vangioni-Flam, E., Descouvemont, P., & Adahchour, A. 2005, *Nuclear Physics A*, 752, 522
- Cooperstock, F. I., & Tieu, S. 2006, *ArXiv Astrophysics e-prints*, arXiv:astro-ph/0610370
- Córsico, A. H., Benvenuto, O. G., Althaus, L. G., Isern, J., & García-Berro, E. 2001, *New Astronomy*, 6, 197
- Cowling, T. G. 1941, *MNRAS*, 101, 367
- Cox, J. P. 1980, Research supported by the National Science Foundation Princeton, NJ, Princeton University Press, 1980. 393 p.
- D’Antona, F., & Mazzitelli, I. 1989, *ApJ*, 347, 934
- Dearborn, D. S. P., Schramm, D. N., & Steigman, G. 1986, *Physical Review Letters*, 56, 26
- Dehner, B. T., & Kawaler, S. D. 1995, *ApJ Lett.*, 445, L141
- de Vega, H. J., & Sanchez, N. G. 2007, *ArXiv Astrophysics e-prints*, arXiv:astro-ph/0701212
- Dine, M., Fischler, W., & Srednicki, M. 1981, *Physics Letters B*, 104, 199
- Dominguez, I., Chieffi, A., Limongi, M., & Straniero, O. 1999, *ApJ*, 524, 226
- Eggleton, P. P. 1971, *MNRAS*, 151, 351
- Eleftheriadis, C. 2003, *ArXiv Astrophysics e-prints*, arXiv:astro-ph/0305534
- Eisenstein, D. J., et al. 2006, *ApJS*, 167, 40

- Englmaier, P., & Gerhard, O. 2006, *Celestial Mechanics and Dynamical Astronomy*, 94, 369
- Fabian, A. C., & Allen, S. W. 2003, *Texas in Tuscany. XXI Symposium on Relativistic Astrophysics*, 197
- Fontaine, G., & Brassard, P. 2002, *ApJ Lett.*, 581, L33
- Frieman, J. A., Dimopoulos, S., & Turner, M. S. 1987, *Phys. Rev. D*, 36, 2201
- Frieman, J. A., & Jaffe, A. H. 1992, *Phys. Rev. D*, 45, 2674
- Gianninas, A., Bergeron, P., & Fontaine, G. 2006, *ArXiv Astrophysics e-prints*, arXiv:astro-ph/0612043
- Gough, D. O. 2007, *Astronomische Nachrichten*, 328, 273
- Hansen, C. J., & Kawaler, S. D. 1994, *NASA STI/Recon Technical Report N*,
- Inman, C. L., & Ruderman, M. A. 1964, *ApJ*, 140, 1025
- Isern, J., Hernanz, M., & Garcia-Berro, E. 1992, *ApJ Lett.*, 392, L23
- Itoh, N., Adachi, T., Nakagawa, M., Kohyama, Y., & Munakata, H. 1989, *ApJ*, 339, 354
- Itoh, N., Mutoh, H., Hikita, A., & Kohyama, Y. 1992, *ApJ*, 395, 622
- Itoh, N., Hayashi, H., Nishikawa, A., & Kohyama, Y. 1996, *ApJ Supp.*, 102, 411
- Itoh, N., Nishikawa, A., & Kohyama, Y. 1996, *ApJ*, 470, 1015
- Izotov, Y. I., Chaffee, F. H., Foltz, C. B., Green, R. F., Guseva, N. G., & Thuan, T. X. 1999, *ApJ*, 527, 757
- Jancovici, B., 1962, *Il Nuovo Cimento*, 25, 2

- Jordan, S., Aznar Cuadrado, R., Napiwotzki, R., Schmid, H. M., & Solanki, S. K. 2007, *A&A*, 462, 1097
- Kawaler, S. D. 1986, Ph.D. Thesis,
- Kawaler, S. D. 2003, ArXiv Astrophysics e-prints, arXiv:astro-ph/0301539
- Kepler, S. O., Nather, R. E., McGraw, J. T., & Robinson, E. L. 1982, *ApJ*, 254, 676
- Kepler, S. O., Winget, D. E., Robinson, E. L., & Nather, R. E. 1988, *IAU Symp.* 123: *Advances in Helio- and Asteroseismology*, 123, 325
- Kepler, S. O., Vauclair, G., Nather, R. E., Winget, D. E., & Robinson, E. L. 1989, *LNP Vol. 328: IAU Colloq. 114: White Dwarfs*, 328, 341
- Kepler, S. O., et al. 1990, *ApJ*, 357, 204
- Kepler, S. O., et al. 1991, *NATO ASIC Proc. 336: White Dwarfs*, 143
- Kepler, S. O., et al. 1991, *ApJ Lett.*, 378, L45
- Kepler, S. O., et al. 1995, *Baltic Astronomy*, 4, 221
- Kepler, S. O., Nather, R. E., & Metcalfe, T. S. 1998, *Baltic Astronomy*, 7, 175
- Kepler, S. O., Mukadam, A., Winget, D. E., Nather, R. E., Metcalfe, T. S., Reed, M. D., Kawaler, S. D., & Bradley, P. A. 2000, *ApJ Lett.*, 534, L185
- Kepler, S. O., Costa, J. E. S., Mukadam, A., Mullally, F., Winget, D. E., Nather, R. E., & Sullivan, D. 2005b, *ASP Conf. Ser. 334: 14th European Workshop on White Dwarfs*, 334, 501
- Kepler, S. O., et al. 2005, *ApJ*, 634, 1311
- Kepler, S. O., Kleinman, S. J., Nitta, A., Koester, D., Castanheira, B. G., Giovannini, O., Costa, A. F. M., & Althaus, L. 2007, *MNRAS*, 375, 1315

- Kim, J. E. 1979, *Physical Review Letters*, 43, 103
- Kinion, D., Irastorza, I. G., & van Bibber, K. 2005, *Nuclear Physics B Proceedings Supplements*, 143, 417
- Kirkman, D., Tytler, D., Suzuki, N., O'Meara, J. M., & Lubin, D. 2003, *ApJ Supp.*, 149, 1
- Koen, C., O'Donoghue, D., Stobie, R. S., Kilkenney, D., & Ashley, R. 1995, *MNRAS*, 277, 913
- Koester, D., Allard, N. F., & Vauclair, G. 1994, *A&A*, 291, L9
- Koester, D., & Holberg, J. B. 2001, *ASP Conf. Ser.* 226: 12th European Workshop on White Dwarfs, 226, 299
- Kutter, G. S., & Savedoff, M. P. 1969, *ApJ*, 156, 1021
- Lamb, D. Q. J. 1974, Ph.D. Thesis,
- Lamb, D. Q., & van Horn, H. M. 1975, *ApJ*, 200, 306
- Lasker, B. M., & Hesser, J. E. 1971, *ApJ Letters*, 163, L89
- Lazarus, D. M., Smith, G. C., Cameron, R., Melissinos, A. C., Ruoso, G., Semertzidis, Y. K., & Nezzrick, F. A. 1992, *Physical Review Letters*, 69, 2333
- Luridiana, V., Esteban, C., Peimbert, M., & Peimbert, A. 2003, *IAU Symposium*, 212, 730
- McGraw, J. T., & Robinson, E. L. 1976, *ApJ Letters*, 205, L155
- Meléndez, J., & Ramírez, I. 2004, *ApJ Letters*, 615, L33
- Mestel, L. 1952, *MNRAS*, 112, 583
- Metcalf, T. S. 2001, Ph.D. Thesis,

- Metcalf, T. S., Salaris, M., & Winget, D. E. 2002, ASP Conf. Ser. 259: IAU Colloq. 185: Radial and Nonradial Pulsations as Probes of Stellar Physics, 259, 602
- Metcalf, T. S., Montgomery, M. H., & Kawaler, S. D. 2003, MNRAS, 344, L88
- Milgrom, M. 1983, ApJ, 270, 365
- Montgomery, M. H. 1998, Ph.D. Thesis,
- Montgomery, M. H., Metcalf, T. S., & Winget, D. E. 2003, MNRAS, 344, 657
- Montgomery, M. H. 2005, ApJ, 633, 1142
- Montgomery, M. H. 2007, Proceedings of the 15th European Workshop on White Dwarfs, submitted.
- Moriyama, S., Minowa, M., Namba, T., Inoue, Y., Takasu, Y., & Yamamoto, A. 1998, Physics Letters B, 434, 147
- Mukadam, A. S., et al. 2003, ApJ, 594, 961
- Mukadam, A. S. 2004, Ph.D. Thesis
- Mukadam, A. S., & Nather, R. E. 2005, Journal of Astrophysics and Astronomy, 26, 321
- Mullally, F., Winget, D. E., & Kepler, S. O. 2006, ASP Conf. Ser. 352: New Horizons in Astronomy: Frank N. Bash Symposium, 352, 265
- Mullally, F., Winget, D. E., Jeffery, E. J., DeGennaro, S., & Kepler, O., ApJ, submitted
- Munakata, H., Kohyama, Y., & Itoh, N. 1985, ApJ, 296, 197
- Nakagawa, M., Kohyama, Y., & Itoh, N. 1987, ApJ, 322, 291
- Nakagawa, M., Adachi, T., Kohyama, Y., & Itoh, N. 1988, ApJ, 326, 241
- Nagasawa, M., & Kawasaki, M. 1994, Phys. Rev. D, 50, 4821

- Nitta, A., et al. 2005, ASP Conf. Ser. 334: 14th European Workshop on White Dwarfs, 334, 585
- Numerical recipes in Fortran 77: the art of scientific computing / William H. Press ... [et al.]. - 2nd ed.
- O'Donoghue, D., & Warner, B. 1987, MNRAS, 228, 949
- Olive, K. A., & Skillman, E. D. 2004, ApJ, 617, 29
- Peccei, R. D., & Quinn, H. R. 1977, Physical Review Letters, 38, 1440
- Preskill, J., Wise, M. B., & Wilczek, F. 1983, Physics Letters B, 120, 127
- Raffelt, G. G. 1986, Phys. Rev. D, 33, 897
- Raffelt, G. G. 1986, Physics Letters B, 166, 402
- Raffelt, G. G., & Dearborn, D. S. P. 1987, Phys. Rev. D, 36, 2211
- Raffelt, G. G. 1990, Phys. Rep., 198, 1
- Raffelt, G., & Weiss, A. 1995, Phys. Rev. D, 51, 1495
- Reuter, M., & Weyer, H. 2004, Phys. Rev. D, 69, 104022
- Richer, H. B., & Ulrych, T. J. 1974, ApJ, 192, 719
- Robinson, E. L., et al. 1995, ApJ, 438, 908
- Ryan, S. G., Beers, T. C., Olive, K. A., Fields, B. D., & Norris, J. E. 2000, ApJ Lett., 530, L57
- Salaris, M., Dominguez, I., Garcia-Berro, E., Hernanz, M., Isern, J., & Mochkovitch, R. 1997, ApJ, 486, 413
- Saumon, D., Chabrier, G., & van Horn, H. M. 1995, ApJS, 99, 713

- Shellard, E. P. S., & Battye, R. A. 1998, COSMO-97, First International Workshop on Particle Physics and the Early Universe, 233
- Shifman, M. A., Vainshtein, A. I., & Zakharov, V. I. 1980, Nuclear Physics B, 166, 493
- Sikivie, P. 2000, Nuclear Physics B Proceedings Supplements, 87, 41
- Spergel, D. N. et al. 2007, ApJ, in press
- Sullivan, D. J. 1998, ASP Conf. Ser. 135: A Half Century of Stellar Pulsation Interpretation, 135, 62
- Sullivan, D. J., & Sullivan, T. 2000, Baltic Astronomy, 9, 81
- Sullivan, D. J. 2004, ASP Conf. Ser. 310: IAU Colloq. 193: Variable Stars in the Local Group, 310, 212
- Sullivan, D. J. 2005, ASP Conf. Ser. 334: 14th European Workshop on White Dwarfs, 334, 495
- Tolstoy, I. 1963, Reviews of Modern Physics, 35, 207
- Tolstoy, I. 1973, Wave Propagation (N. Y.: McGraw-Hill) (1,5.4b, 17.2, 17.9, 17.10)
- Tremaine, S., & Gunn, J. E. 1979, Physical Review Letters, 42, 407
- Turner, M. S. 1990, Phys. Rep., 197, 67
- Unno, W., Osaki, Y., Ando, H., Saio, H., & Shibahashi, H. 1989, Nonradial oscillations of stars, Tokyo: University of Tokyo Press, 1989, 2nd ed.,
- Weinberg, S. 1989, Reviews of Modern Physics, 61, 1
- Wilkinson Microwave Anisotropy Probe (WMAP): Three-Year Explanatory Supplement, editor M. Limon et al. (Greenbelt, MD. NASA/GSFC)

- Winget, D. E. 1981, Ph.D. thesis, University of Rochester
- Winget, D.E., and Fontaine, G. (1982). In *Pulsations in Classical and Cataclysmic Variables*, edited by J.P. Cox and C.J. Hansen (University of Colorado, Boulder), p. 142.
- Winget, D. E., van Horn, H. M., Tassoul, M., Hansen, C. J., & Fontaine, G. 1983, ApJ. Letters, 268, L33
- Winget, D. E., Sullivan, D. J., Metcalfe, T. S., Kawaler, S. D., & Montgomery, M. H. 2004, ApJ. Letters, 602, L109
- Wood, M. A. 1990, Ph.D. Thesis,
- Wu, C. S., Ambler, E., Hayward, R. W., Hoppes, D. D., & Hudson, R. P. 1957, Physical Review, 105, 1413
- Yamaguchi, M., Kawasaki, M., & Yokoyama, J. 1999, Physical Review Letters, 82, 4578
- Zhitnitsky, A. R. 1980, Sov. J. Nucl. Phys. 31, 260
- Zwicky, F. 1933, Helvetica Physica Acta, 6, 110

Vita

Agnès Kim was born on a chilly spring day, June 18, 1975 in Geneva, Switzerland. She is the daughter of Paulette and Pierre Bischoff. She grew up in Juvigny, an unremarkable little French village on the border with Switzerland. She started schooling in France, but left after her first year in high school to spend an academic year in Baltimore, Maryland. There she attended Mount de Sales Academy and perfected her English. She finished high school in Collège Calvin in beautiful old town Geneva. She graduated with a science Matura in June 1995. In need of adventure and wanting to see more cold and snow (and tornadoes), she came back to the US in August 1996 to attend Iowa State University as a Meteorology student. Her first week at ISU, she met her future husband, Tchi Mhan Kim, known affectionately to her as “Ryan”. As a freshman, she took her first Astronomy class, taught brilliantly by Dr. Steve Kawaler. The class revived her interest in the subject and she switched her major to Physics with an emphasis on Astronomy. She was awarded the Bernice Black Durand Scholarship to do undergraduate research and worked with Dr. Kawaler on pulsating white dwarfs. She graduated with a Bachelor of Science in Physics in December 1999 and married Ryan Kim. She went on to earn a Masters of Science in Astrophysics, still at ISU, in August 2003.

Permanent Address: 5203 Downs Drive
Austin, TX 78721

This dissertation was typeset with L^AT_EX 2_ε¹ by the author.

¹L^AT_EX 2_ε is an extension of L^AT_EX. L^AT_EX is a collection of macros for T_EX. T_EX is a trademark of the American Mathematical Society. The macros used in formatting this dissertation were written by Dinesh Das, Department of Computer Sciences, The University of Texas at Austin, and extended by Bert Kay, James A. Bednar, and Ayman El-Khashab.